

**Unveiling the Wind Structure of the Vela X-1  
High-Mass X-ray Binary: Insights from *XMM-Newton*  
and *NuSTAR* observatories**

**Dissertation**

der Mathematisch-Naturwissenschaftlichen Fakultät  
der Eberhard Karls Universität Tübingen  
zur Erlangung des Grades eines  
Doktors der Naturwissenschaften  
(Dr. rer. nat.)

vorgelegt von  
Camille Diez  
aus Nancy/Frankreich

Tübingen  
2023

Gedruckt mit Genehmigung der Mathematisch-Naturwissenschaftlichen Fakultät der Eberhard Karls Universität Tübingen.

Tag der mündlichen Qualifikation:

24.05.2023

Dekan:

Prof. Dr. Thilo Stehle

1. Berichterstatterin:

Dr. Victoria Grinberg

2. Berichterstatter:

Prof. Dr. Andrea Santangelo

3. Berichterstatter:

Prof. Dr. Klaus Werner

# Zusammenfassung

Röntgendoppelsternsysteme mit massereichen Begleitern (High Mass X-ray Binaries, HMXBs) sind wertvolle Laboratorien, um die Akkretion auf kompakte Objekte zu verstehen und Rückschlüsse auf das interstellare Medium zu ziehen. Außerdem können sie aufgrund ihrer hohen Leuchtkraft aus großer Entfernung beobachtet werden, was ihre Entdeckung erleichtert. Bei der Untersuchung von HMXBs gibt es eine Reihe offener Fragen, deren Beantwortung das gesamte Gebiet voranbringen würde. Eine einzigartige Möglichkeit, die Akkretionsmechanismen zu untersuchen, besteht darin, die Struktur der Sternwinde zu studieren, indem man die spektralen und zeitlichen Eigenschaften der HMXBs betrachtet. Die Struktur der Akkretions- und Photoionisationsschleppe im Wind und ihre Eigenschaften sind noch wenig bekannt und wurden bisher nicht systematisch untersucht. Das archetypische HMXB Vela X-1 ist eines der wichtigsten Systeme für solche Untersuchungen. Es besitzt einen komplexen, klumpigen Sternwind, ausgeprägte Zyklotronlinien und ist von der Erde aus von der Seite sichtbar, was die zeitliche und spektrale Analyse erleichtert.

In dieser Arbeit analysieren wir zwei neue Beobachtungen von *NuSTAR* und *XMM-Newton* zu den Bahnphasen  $\sim 0,36-0,52$  (kurz bevor sich der Neutronenstern in der unteren Konjunktion befindet, d.h. zwischen dem Beobachter auf der Erde und dem begleitenden Überriesen) und  $\sim 0,68-0,78$ . Wir modellieren die Variabilität des Kontinuums und der lokalen Absorption, indem wir die Entwicklung der spektralen Parameter auf der Zeitskala der Pulsperiode verfolgen.

In [Diez et al. \(2022\)](#) modellieren wir die *NuSTAR*-Daten unter Verwendung eines partiellen Bedeckungsmodells mit einem absorbierten Potenzgesetz-Kontinuum, das durch einen hochenergetischen Abknick modifiziert wird, um die Absorption sowohl durch den Wind als auch durch das interstellare Medium zu berücksichtigen. Die Verwendung eines Modells mit partieller Bedeckung erlaubt es, die lokale Variation der

Absorption zu verfolgen und zu untersuchen, ob der Wind Klumpen enthält. Die starke Variabilität der Absorption, die während der Bewegung des Neutronensterns entlang seiner Bahn beobachtet wird, hängt mit Akkretions- und Photoionisationsschleppen zusammen. Wir beobachten eine flussabhängige Korrelation der spektralen Parameter des Kontinuums, was auf eine Änderung der Plasmaeigenschaften und des Akkretionsregimes hindeutet.

Die wichtigsten Merkmale, die die Natur und Struktur des Sternwindes beschreiben, liegen jedoch bei niedrigeren Energien, die von *NuSTAR* nicht erfasst werden. In [Diez et al. \(2023\)](#) stellen wir Analysen von Beobachtungen bei  $\phi_{orb} \approx 0,36-0,52$  vor, die gleichzeitig von *NuSTAR* und *XMM-Newton* erfasst wurden. Letzteres ermöglicht eine Energieabdeckung bis hinunter zu 0,5 keV und damit den Zugang zu einer Vielzahl von Emissionslinien. Aufbauend auf unseren Modell- und Kontinuumsergebnissen aus der vorangegangenen *NuSTAR*-Analyse können wir erstmals das Einsetzen der Schleppe mit hoher zeitlicher Auflösung verfolgen. Wir untersuchen auch das Vorkommen von hochionisierten Atomen im Plasma zusammen mit quasi-neutralen Ionen, was auf Temperaturänderungen im Plasma hinweist.

# Abstract

High-mass X-ray binaries (HMXBs) are fundamental laboratories to understand accretion onto compact objects and provide feedback on the interstellar medium. Moreover, they can be observed at far distances thanks to their high luminosities that facilitate their detection. There are several open questions surrounding the study of HMXBs, answering which would bring the whole field forward. In particular, a unique opportunity to investigate the accretion mechanisms is through stellar wind structure studies provided by the spectral and timing characteristics of HMXBs. The structure of the accretion and photoionisation wakes in the wind and their properties are still poorly understood and have so far not been systematically studied. The archetypical HMXB Vela X-1 is one of the key systems for such studies. It has a complex clumpy stellar wind, prominent cyclotron lines and it is seen edge-on from the Earth thus facilitating timing and spectral analyses.

In this work, we analyse two new observations taken with *NuSTAR* and *XMM-Newton* at orbital phases  $\sim 0.36$ – $0.52$  (shortly before the neutron star is in inferior conjunction, i.e. is located between the observer on Earth and the supergiant companion star) and  $\sim 0.68$ – $0.78$ . We model the continuum and local absorption variability by following the evolution of spectral parameters down to the pulse period timescale.

In [Diez et al. \(2022\)](#), we model *NuSTAR* data using a partial covering model with an absorbed powerlaw continuum modified by a high-energy cutoff to account for the absorption from both the wind and the interstellar medium. The use of a partial coverer allows us to follow local absorption variability and to probe the presence of clumps in the wind. The strong absorption variability observed as the neutron star moves along the orbit is associated to the presence of the accretion and photoionisation wakes. We observe a flux dependent correlation of the continuum spectral parameters which indicates a change in the properties of the plasma and accretion regime.

However, the main features describing the nature and the structure of the stellar wind are imprinted at lower energies that are not covered by *NuSTAR*. In [Diez et al. \(2023\)](#), we present the analyses of the observation at  $\phi_{\text{orb}} \approx 0.36\text{--}0.52$  simultaneously covered by *NuSTAR* and *XMM-Newton*. The latter enables an energy coverage down to 0.5 keV giving us access to a plethora of emission lines. Building on our model and continuum results from the previous *NuSTAR* analysis, we are able to trace the onset of the wakes for the first time with high-time resolution. We also probe the presence of highly ionised atoms in the plasma together with near-neutral ions thus indicating changes in temperature of the plasma.

# Contents

<b>1</b>	<b>Introduction</b>	<b>1</b>
1.1	Endpoints of stellar evolution . . . . .	1
1.1.1	Stellar evolution and formation of neutron stars . . . . .	1
1.1.2	High-mass X-ray binaries . . . . .	5
1.1.3	Accreting neutron star high-mass X-ray binaries . . . . .	6
1.2	The case of Vela X-1 . . . . .	7
1.2.1	Properties and description of the system . . . . .	7
1.2.2	Stellar wind in Vela X-1 . . . . .	8
1.3	X-ray spectrum of Vela X-1 . . . . .	10
1.3.1	Accretion column geometry . . . . .	11
1.3.2	X-ray continuum: seed soft photons & Comptonisation . . . . .	13
1.3.3	Accretion regime . . . . .	15
1.3.4	Photoelectric absorption . . . . .	17
1.3.5	Line emission . . . . .	19
1.3.6	10-keV feature . . . . .	21
<b>2</b>	<b>Aim of the thesis and open questions</b>	<b>23</b>
2.1	Investigation of X-ray emission... . . . .	24
2.2	... and absorption . . . . .	24
<b>3</b>	<b>X-ray observatories</b>	<b>27</b>
3.1	<i>NuSTAR</i> . . . . .	27
3.2	<i>XMM-Newton</i> . . . . .	29
3.2.1	EPIC-pn . . . . .	30

<b>4</b>	<b>Summary of the original publications</b>	<b>33</b>
4.1	Continuum, cyclotron line, and absorption variability in the high-mass X-ray binary Vela X-1 (Diez et al., 2022)	33
4.2	Observing the onset of the accretion wake in Vela X-1 (Diez et al., 2023)	36
<b>5</b>	<b>Results &amp; Discussion</b>	<b>37</b>
5.1	Continuum shape and accretion regime in Vela X-1	37
5.1.1	Spectral shape	37
5.1.2	Accretion regime	42
5.2	Variable absorber	46
5.2.1	Large-scale changes	47
5.2.2	Small-scale changes	52
<b>6</b>	<b>Conclusion &amp; Outlook</b>	<b>59</b>
	<b>Appendix</b>	<b>61</b>
	<b>Bibliography</b>	<b>99</b>
	<b>Abbreviations</b>	<b>109</b>
	<b>Acknowledgements</b>	<b>111</b>



“ Things not to ask a PhD student: When will you graduate? Are you writing your thesis? How is your research going? Did your paper get published yet? What year are you again?

— Friends, colleagues, family

In this Chapter, we will address the formation of a High-Mass X-ray Binary (HMXB): from the ignition of a star to the formation of those binary systems composed of a massive star and a compact object. More specifically, we will review the final stages of stellar evolution leading to the birth of a particular type of compact object: neutron stars. We will then describe the physics that can be studied in accreting neutron star HMXBs with a special focus on Vela X-1, the neutron star HMXB of interest for this thesis.

## 1.1 Endpoints of stellar evolution

### 1.1.1 Stellar evolution and formation of neutron stars

When stars ignite, they begin their life on the main sequence in the Hertzsprung-Russell diagram (Rosenberg, 1910; Hertzsprung, 1911; Russell, 1914). They spend most of their life on the main sequence phase (see Fig. 1.1) burning hydrogen in the core to helium by nuclear fusion in hydrostatic equilibrium, where the gravitational force is balanced by the radiation pressure released during the fusion. The main sequence

lifetime of stars depends on the initial mass: the more massive the star is, the faster it burns hydrogen and the faster it evolves outside the main sequence. When stars die, they leave a remnant called "compact object" which can be classified into three main categories. Endpoints of stellar evolution is a very complex field and we will give a basic and simple overview focusing on neutron stars. For a more detailed discussion, we refer to [Guidry \(2019\)](#) that we also use as the main source for this Sect. 1.1.

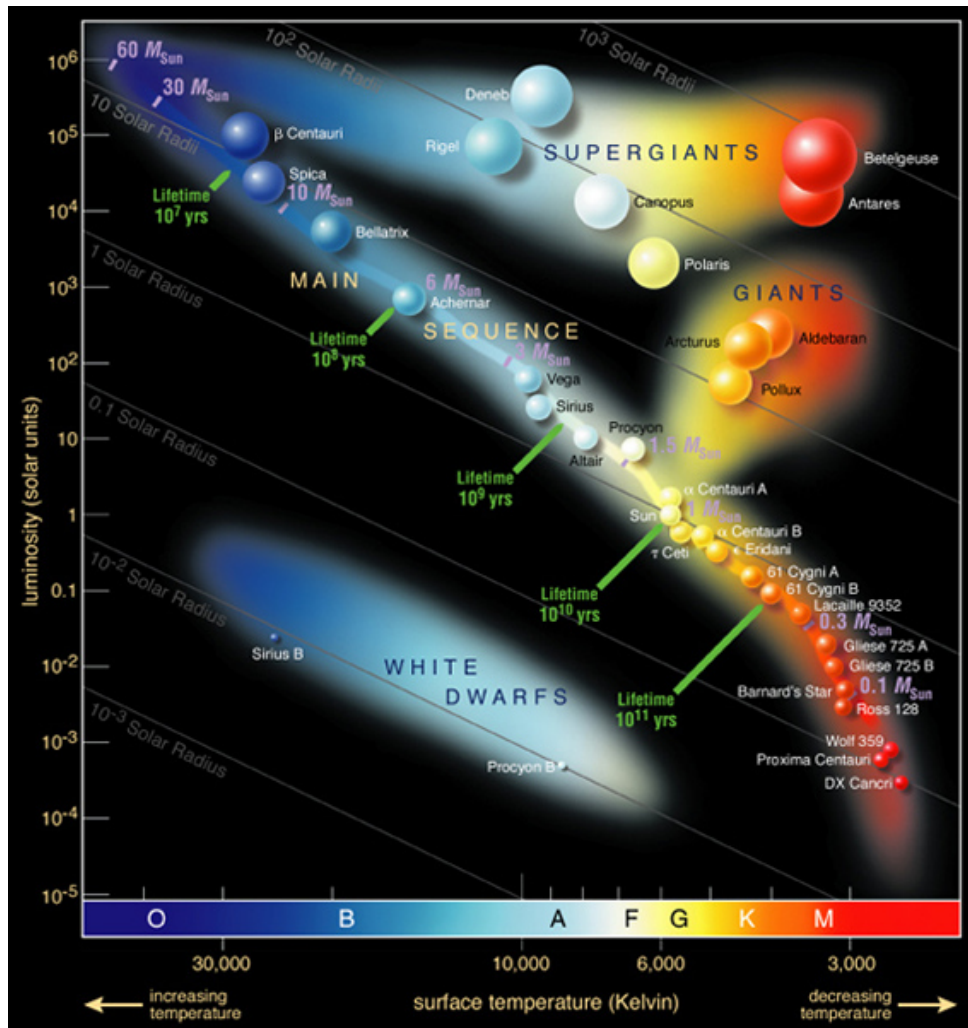


**Fig. 1.1:** Hertzsprung-Russell diagram showing luminosity of stars (in  $L_{\odot}$ ) against temperature (in K), with corresponding spectral type (from the hottest O to the coolest M). Radius, lifetime and mass on the main sequence are also shown. This diagram indicates the position of a star depending on its life-stage. Credit: ESO/ESA <https://www.cosmos.esa.int/web/cesar/the-hertzsprung-russell-diagram>.

Low-mass stars with an initial mass of less than about  $\sim 8 M_{\odot}$  become white dwarfs at the end of their life. This commonly cited limit can vary because of several parameters such as the metallicity of the star, its angular momentum, the mass losses or simply because of our limited knowledge on stellar evolution. Once the hydrogen in the core of a low-mass star is exhausted, the radiation pressure is not sufficient to balance the inward gravitational force and the hydrostatic equilibrium breaks. The star enters into the red giant branch phase, the core contracts and becomes denser and hotter. Helium burning to heavier elements starts in the core. The outer layers are repelled by the intense radiation pressure that is generated, causing the luminosity and radius of the star to increase. As the star's outer layers are ejected, it loses mass. However, the core temperature of low-mass stars is not high enough for carbon burning. They undergo gravitational collapse, shedding their outer layers away into a planetary nebula and leading to the formation of a white dwarf. The core pressure in white dwarfs is so high that it forces the electrons to fill the lowest energy quantum states. When the lowest energy state is filled, the other electrons are forced to reach higher energy states because of the Pauli exclusion principle (Pauli, 1925), creating a repulsive force called electron degeneracy pressure (Fowler, 1926). The electron degeneracy pressure balances the gravitational forces if the mass of the white dwarf reaches a maximum of  $1.44 M_{\odot}$ , also known as the Chandrasekhar limit (Chandrasekhar, 1931a,b).

## Neutron stars

Neutron stars are the end products of stellar evolution of massive stars of more than about  $\sim 8 M_{\odot}$ . They evolve similarly to low-mass stars but much faster, directly initiating helium core fusion after the exhaustion of hydrogen. They start on the top-left part of the main sequence and continue to the supergiant branch on the Hertzsprung-Russell diagram. Contrary to low-mass stars, the core pressure and temperature of high-mass stars is high enough to proceed to carbon and heavier elements burning in the core. After several burning stages, an iron core forms. The fusion stops at iron production because its fusion would require more energy than what it would release. The newly

created iron core of the star however exceeds the Chandrasekhar limit and the electron degeneracy pressure cannot stop the gravitational collapse. The collapsed core is so dense that electrons and protons are forced to combine into neutrons through inverse  $\beta$ -decay resulting in additional production of a huge amount of neutrinos. When the core pressure and temperature become too high, the trapped neutrinos escape during a massive explosion called a core-collapse supernova (Colgate & White, 1966). The outer layers are blown-off and a remnant is left behind: a neutron star is born. The neutron degeneracy pressure (the equivalent of electron degeneracy pressure for neutrons) counterbalances further gravitational collapse, thus stabilising the neutron star.

Neutron stars are fast rotating objects due to the conservation of angular momentum after the core collapse and can reach one rotation per ms (Hessels et al., 2006). The upper mass limit of a neutron star to maintain the equilibrium between neutron degeneracy pressure and gravitational collapse is called the Tolman-Oppenheimer-Volkoff limit (Oppenheimer & Volkoff, 1939). On the contrary to the Chandrasekhar limit, the Tolman-Oppenheimer-Volkoff limit is more difficult to estimate because of the limited understanding of the dense nuclear matter. It is commonly admitted that it does not exceed  $\sim 3 M_{\odot}$ . Using gravitational wave observations of the merger of a binary neutron star system called GW170817, Rezzolla et al. (2018) estimated the maximum mass to be between  $2.01_{-0.04}^{+0.04} M_{\odot}$  and  $2.16_{-0.15}^{+0.17} M_{\odot}$  although Romani et al. (2022) recently found the heaviest known galactic neutron star PSR J0952-0607 to be  $2.35 \pm 0.17 M_{\odot}$ . For neutron star masses ranging between  $1 M_{\odot}$  and  $3 M_{\odot}$ , and typical radii of about 10 to 12 km (Özel & Freire, 2016), mean densities are  $\sim 10^{14} \text{ g cm}^{-3}$ . This makes a neutron star one of the densest objects in the Universe. The exact values of the aforementioned properties depend strongly on the equation of state of neutron stars, which is still unknown as of today. The equation of state of neutron stars describes the relation between density and pressure to determine the internal structure of those objects. Theoretical models predict a matter mostly constituted of a neutron-degenerate matter with possible strange matter. Constraints on the equation of state of neutron stars require mass and radius measurements and is beyond the scope of this thesis. For more details, see Lattimer & Prakash (2007).

For extremely massive progenitor stars, the remnant core exceeds the Tolman-Oppenheimer-Volkoff limit. The neutron degeneracy pressure cannot halt the infall anymore and further gravitational collapse occurs, leading to the formation of a black hole (see the review by [Woosley et al., 2002](#), and references therein). It has to be noted that the metallicity of the progenitor plays a role as well in the question of how massive a star should be to create a black hole and not a neutron star since it tends to enhance the mass lost by stellar winds. According to [Meynet et al. \(2006\)](#), more than 40% of the total mass of non-rotating massive stars with solar metallicity is ejected by winds. Therefore, even very massive stars can form neutron stars. White dwarfs exceeding the Chandrasekhar limit (e.g. through accretion from another star) undergo further gravitational collapse as the electron degeneracy pressure is not sufficient to withstand the gravitational forces leading to the formation of a neutron star or a black hole as well. Another possible scenario for the formation of black holes and neutron stars is the merging of two compact objects.

### 1.1.2 High-mass X-ray binaries

Most of the stars of our Universe are found in binary systems due to the presence of "star nurseries" in clouds of gas and dust, also known as nebulae (see the review by [Lada & Lada, 2003](#)). The probability of a star to be born in a binary system is positively correlated to the stellar mass (see e.g. [Moe & Di Stefano, 2017](#)). Hence, most massive stars are in binary or other multiple systems by gravitational bounding and co-rotating around their centre of mass.

Because neutron stars and black holes are endpoints of the evolution of massive stars, many of them are in a binary system too. If the compact object accretes matter from the companion, these systems are called "X-ray binaries" as high energy radiation is produced via accretion processes. If the mass of the companion star exceeds  $\sim 8 M_{\odot}$  ([Bhattacharya & van den Heuvel, 1991](#)), those binary systems are called High-Mass X-ray Binaries (HMXBs). The companion star is usually an early O or B type star (see Fig. 1.1), meaning

that HMXBs are young systems (less than  $10^7$  years). Such stars are meant to experience the same fate as their compact companion, leading to binary systems with two compact objects and which are sources of gravitational wave events (e.g. GW170817 in [Rezzolla et al., 2018](#)).

An X-ray binary system where the mass of the companion star is smaller than the mass of the compact object is called a Low-Mass X-ray Binary (LMXB). An Intermediate-Mass X-ray Binary (IMXB) is a "hybrid" system and shows characteristics of both LMXBs and HMXBs. For this thesis, we focus on neutron star HMXBs.

### 1.1.3 Accreting neutron star high-mass X-ray binaries

Isolated neutron stars are very faint when observed from a far distance. In HMXBs, the young and highly magnetic neutron stars accrete material from the companion star (also called donor star) that is channelled along the magnetic field lines onto the poles and release intense X-ray radiation (see Sect. 1.3.2 for the mechanisms of X-ray production). This radiation is observed as beams of light emitted along the magnetic axis. Accreting neutron stars in HMXBs are strongly magnetised, ranging from  $\sim 10^{10}$  to  $\sim 10^{15}$  G ([Igoshev et al., 2021](#)). If the magnetic axis is misaligned with the rotation axis, the emitted beams are detected as periodic variations in X-ray. Accreting neutron stars with such properties are also called X-ray pulsars.

In binary systems, the Roche lobe delimits the region gravitationally bound to the two components. In LMXBs, the low-mass companion fills its Roche lobe: the material is accreted onto the compact object via the Lagrangian point  $L_1$  through Roche lobe overflow and an accretion disc is formed. In HMXBs, the massive companion does not fill its Roche lobe and the material is ejected from the star through stellar winds (see Sect. 1.2.2). The presence of the compact object influences the accretion geometry: almost spherical and/or focusing of the wind towards the compact object via  $L_1$  with a transient disc ([Lamb et al., 1973](#)).

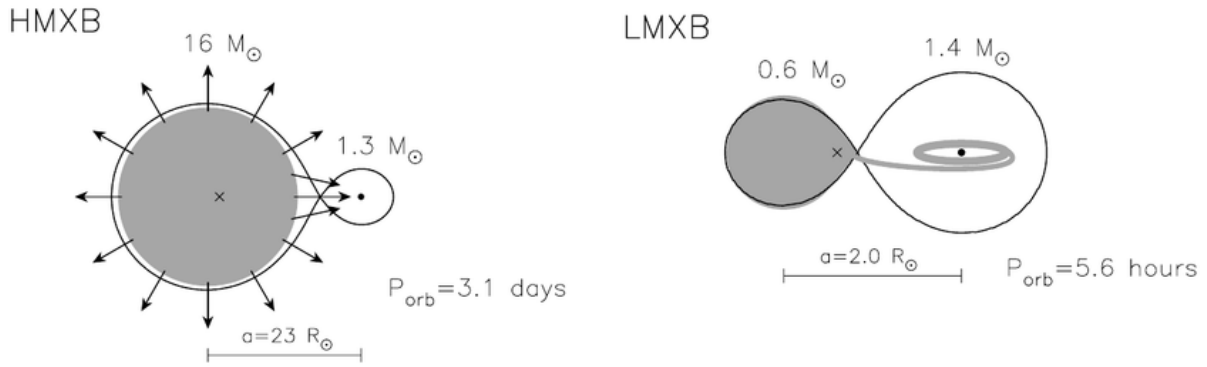


**Fig. 1.2:** Schematic representation of the Roche lobes in HMXBs and LMXBs with typical stellar and orbital parameters. Figure from [Tauris & van den Heuvel \(2006\)](#).

## 1.2 The case of Vela X-1

### 1.2.1 Properties and description of the system

The archetypical Vela X-1 is the perfect key source for studying HMXBs. Its relatively close distance of  $1.99_{-0.11}^{+0.13}$  kpc ([Kretschmar et al., 2021](#)) and mean intrinsic luminosity of  $\sim 5 \times 10^{36}$  erg s $^{-1}$  ([Fürst et al., 2010](#)) makes Vela X-1 one of the brightest and persistent X-ray sources in the sky. This HMXB consists of a B0.5 Ib supergiant called HD 77581 ([Hiltner et al., 1972](#)) with an accreting neutron star. It orbits the supergiant in an almost circular orbit ( $e \approx 0.0898 \pm 0.0012$  [Bildsten et al., 1997](#)) in  $\sim 8.96$  d ([Kreykenbohm et al., 2008](#); [Falanga et al., 2015](#)) and with a pulse period of  $\sim 283$  s ([McClintock et al., 1976](#)). The mass of HD 77581 is of  $\sim 20$ – $26 M_{\odot}$ , its radius of  $\sim 27$ – $32 R_{\odot}$  and the mass of the neutron star is of  $\sim 1.7$ – $2.1 M_{\odot}$  following different estimates (see Table 4 in the review paper by [Kretschmar et al., 2021](#)).

The convenient orbital parameters of Vela X-1 – such as a high inclination of  $> 73^{\circ}$  ([Joss & Rappaport, 1984](#); [van Kerkwijk et al., 1995](#)), small orbital separation of  $\sim 1.7 R_{\star}$  ([van Kerkwijk et al., 1995](#); [Quaintrell et al., 2003](#)) and eclipses in the light curve ([Sato et al., 1986](#); [Sako et al., 1999](#)) – facilitate the study of the system. It allows us to perform observations of the system at different orbital phases to probe different structures in the stellar wind as modified by the presence of the neutron star, which is deeply embedded

into the stellar wind. To derive the orbital phases mentioned during this work, we use the ephemeris listed in Table 1.1. In soft X-rays, the boundaries of the eclipse can be hard to define. Moreover, the orbit is not exactly circular therefore the use of the time of mean longitude equal to  $\pi/2$  ( $T_{90}$ ) is preferred to the mid-eclipse time ( $T_{\text{ecl}}$ ) to derive orbital phases for the Vela X-1 system.

**Tab. 1.1:** Ephemeris used. Table from [Diez et al. \(2022\)](#).

Orbital parameter	Value	Units
Time of mean longitude equal to $\pi/2$ ( $T_{90}$ )	$52974.001 \pm 0.012^{(a)}$	MJD (day)
Mid-eclipse time ( $T_{\text{ecl}}$ )	$52974.227 \pm 0.007^{(a)}$	MJD (day)
Orbital period ( $P_{\text{orb}}$ )	$8.964357 \pm 0.000029^{(a)}$	day
Semi-major axis ( $a \sin i$ )	$113.89 \pm 0.13^{(b)}$	lt-sec
Eccentricity ( $e$ )	$0.0898 \pm 0.0012^{(b)}$	
Longitude of periastron ( $\omega$ )	$152.59 \pm 0.92^{(b)}$	
Inclination ( $i$ )	$> 73^{(b)}$	°

<sup>(a)</sup> ([Kreykenbohm et al., 2008](#)), <sup>(b)</sup> ([Bildsten et al., 1997](#)), <sup>(c)</sup> ([van Kerkwijk et al., 1995](#)).

## 1.2.2 Stellar wind in Vela X-1

Apart from emitting radiation, hot and massive stars also release particles, which is known as the stellar wind. It consists mostly of free electrons, ionised hydrogen and ionised species of more complex atoms ([Lamers & Cassinelli, 1999](#)). Those outflows of moving material are driven by radiation pressure of UltraViolet (UV) photons on the resonant absorption lines of heavy ions ([Lamers & Cassinelli, 1999](#)). In other words, if a photon has the needed energy to excite a bound electron in an ion to a higher energy level, it gets absorbed. However, the excited electron falls back to its original energy level quickly and a photon is re-emitted. Kinetic energy is thus transferred to the ion, creating a radiative acceleration in the wind ([Lamers & Cassinelli, 1999](#)). In Vela X-1, this so-called line-driven wind (first identified in this source by [Castor et al., 1975](#)) can reach a terminal velocity  $v_{\infty}$  ranging from  $< 400 \text{ km s}^{-1}$  to  $1700 \text{ km s}^{-1}$  ([Kretschmar et al., 2021](#)). The mass loss rate of the supergiant HD 77581 is  $\sim 10^{-6} M_{\odot} \text{ yr}^{-1}$  ([Giménez-García et al., 2016](#)) approximately corresponding to the total mass of the Earth every three years. This



significant mass loss impacts the overall structure of the wind and the evolution of HD 77581, hastening its death.

### Accretion and ionisation wakes

Inside the wind, filamentary structures are visible. As a result of the gravitational field of the neutron star, an unstable shock forms. The stellar wind focuses into a trailing accretion wake as the neutron star orbits its supergiant companion and accretes material from it (see hydrodynamical simulations from [Manousakis, 2011](#), and right Fig. 1.3). The X-ray ionisation (see Sect. 1.3.4) of these structures by the neutron star creates a shock between the acceleration of the wind and the slowing down of the photoionised plasma ([Fransson & Fabian, 1980](#)). This results in a trailing spiral structure known as the photoionisation wake (see right Fig. 1.3). The donor star also undergoes tidal deformation possibly causing an increase in wind flux ("tidal stream" in [Blondin et al., 1991](#)) towards the neutron star, even if it does not fill its Roche Lobe, and which may lead to the formation of a transient accretion disc ([El Mellah et al., 2019](#); [Liao et al., 2020](#)). The presence of those large scale structures on our line of sight significantly affects the observed data on ks-timescales as will be discussed in Chap. 5.

On a much larger scale, as the Vela X-1 system moves at a supersonic space velocity of  $90 \text{ km s}^{-1}$  ([Kaper et al., 1997](#)), its line-driven wind causes instabilities with the surrounding interstellar medium gas leading to the formation of a bow shock (see left Fig. 1.3) located at  $\sim 0.48 \pm 0.05 \text{ pc}$  from HD 77581 ([Kaper et al., 1997](#)).

### Clumps

On smaller scales, hydrodynamical simulations in [Owocki et al. \(1988\)](#) and [Feldmeier et al. \(1997\)](#) demonstrate that wind instabilities create rapidly-growing perturbations causing internal shocks and confining the wind mass in local overdense regions, called clumps (see Fig. 1.4). Considering spherical clumps, [Martínez-Núñez et al. \(2014\)](#) estimated the size of the clumps to be of the order of  $10^{10} \text{ cm}$  or  $0.02 R_{\text{HD 77581}}$ , which is in

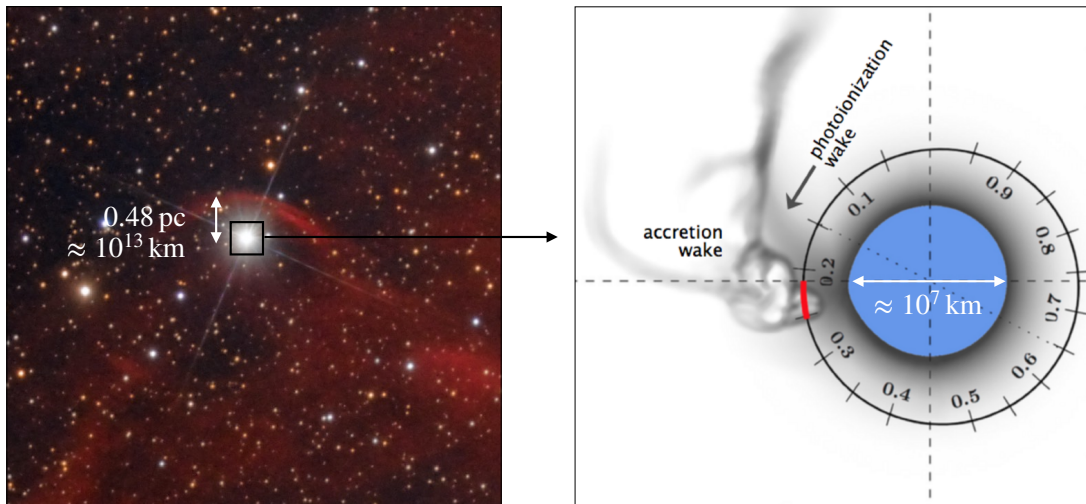


**Fig. 1.3:** *Left:* Optical image of Vela X-1 with the bright giant star HD 77581 in the centre and its optically invisible neutron star. The bow shock can be seen as a red parabola due to hydrogen emission and whose apex is located at approximately 0.48 pc (Kaper et al., 1997) from the star. Credit: Rolf Olsen. *Right:* Sketch of the Vela X-1 system with the representation of the accretion and photoionisation wakes. The position of the neutron star is shown by the red arc interval. Note the scale of the figure in comparison with the left panel. Figure from (Grinberg et al., 2017).

agreement with simulations (Oskinova et al., 2011; Driessen et al., 2019). Those clumps of different densities, velocities and temperatures alter the observed orbital evolution of light curves and spectra of the source on short timescales as will be discussed in Chap. 5. Simulations from Sundqvist & Owocki (2013) show the presence of those clumps at one stellar radius  $R_{\text{HD77581}}$  above the photosphere. It is in better agreement with observations of O-type stars, which typically indicate strong clumping near the wind base.

### 1.3 X-ray spectrum of Vela X-1

Neutron star HMXBs emit on a broad range of the electromagnetic spectrum depending on their intrinsic properties but are mostly known for their bright X-ray emission due to accretion of material from the stellar wind onto their surface. In the following

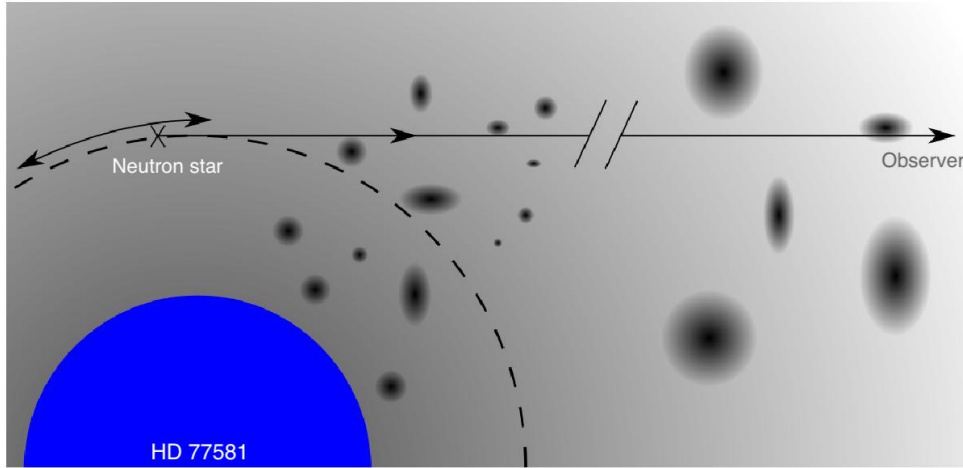


**Fig. 1.4:** Illustration (not to scale) of the clumps in Vela X-1 as radially fading black ellipses/spheres to account for varying densities. The clumps are ejected from the supergiant HD 77581 (blue giant sphere) and accreted by the neutron star (black cross). Clumps may cross the line of sight (solid black line) of the observer. Figure from [Grinberg et al. \(2017\)](#).

section, we will focus on the mechanisms of X-ray production in the bright Vela X-1 and how these features are imprinted in the observed spectrum.

### 1.3.1 Accretion column geometry

Since the neutron star is strongly magnetised, the accreted ionised plasma is channelled along the magnetic field lines at the magnetic poles. The gravitational potential energy of this incoming flow is converted into kinetic energy and then transferred into radiation. A region of high temperature (electron temperature  $T_e$  of  $\sim 10^7$  K for typical accreting pulsars, e.g. [Coburn et al., 2002](#)) on the neutron star's surface called the thermal mound ([Davidson, 1973](#)) appears and is delimited by the magnetic field lines, overall forming the accretion column (see Fig. 1.5). As material keeps accumulating on the dense thermal mound (also called hot spot), soft X-ray seed photons with a black-body distribution are produced and local thermodynamic equilibrium prevails. However, observed spectra of X-ray pulsars are highly non-thermal indicating the contribution of non-thermal processes such as cyclotron and bremsstrahlung seed photons' emission in

the accretion columns (Becker & Wolff, 2007). More details about the X-ray production are given in the following section.

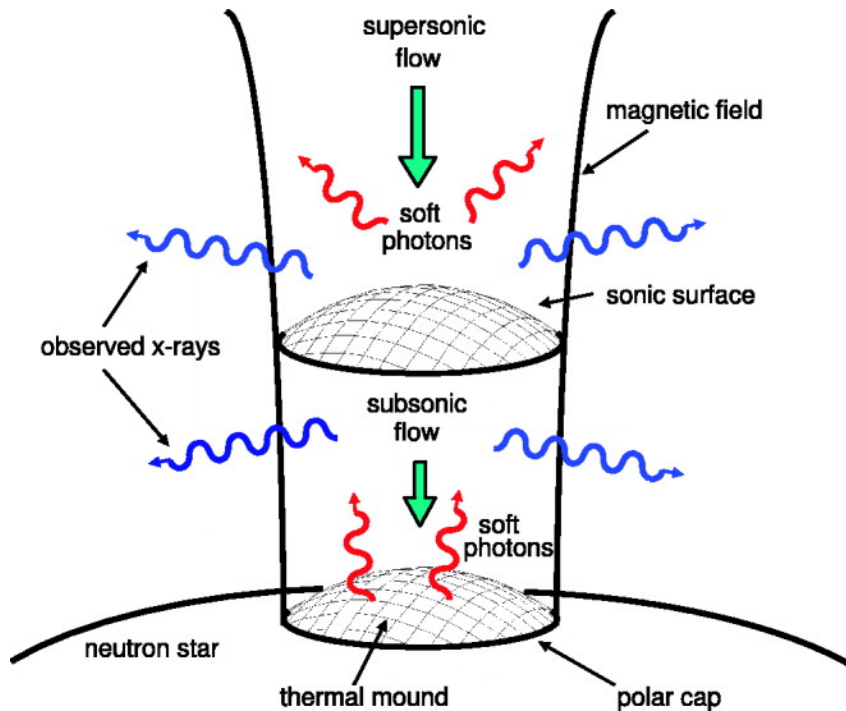


**Fig. 1.5:** Scheme of an accretion column onto the polar cap of a neutron star under the dipole approximation. Soft blackbody seed photons are emitted from the thermal mound, cyclotron and bremsstrahlung seed photons from higher in the accretion column. The description of the geometry structure and the X-ray production mechanisms can be found in Sect. 1.3.2 and Sect. 1.3.3. Figure from Becker & Wolff (2007).

The exact geometry of the accretion columns depends mainly on the mass accretion rate (Mushtukov et al., 2015) and the magnetic field structure in the vicinity of the neutron star (Brice et al., 2021). It is nevertheless possible to understand the basic mechanisms, that we will explain below.

## 1.3.2 X-ray continuum: seed soft photons & Comptonisation

### Blackbody and bremsstrahlung radiation

Thermal photons are emitted from the hot spot ( $T_e \approx 10^7$  K) with a blackbody distribution and have typical energies around 3–4 keV following the Wien's displacement law. Bremsstrahlung seed photons are emitted due to ions slowing down the motion of the electrons in the infalling gas (also called radiation braking). The characteristic bremsstrahlung emission has an exponential cutoff determined by the temperature of the plasma which is  $\sim 1$  keV ( $kT_e$ ).

### Cyclotron radiation

The electrons are accelerated off the neutron star surface through the intense magnetic field of  $\sim 10^{12}$  G (see e.g. [Kreykenbohm et al., 2002](#)). Their energy distribution is continuous in the direction of the magnetic field but quantised into Landau levels in the perpendicular direction (e.g. [Arons et al., 1987](#)). Electrons that are at the ground state do not have a gyrational motion around the magnetic field lines. However, electrons excited to higher Landau levels have larger orbits and spiral around the magnetic field lines. Their circular orbital motion leads to constant changes in the direction of the velocity (i.e. acceleration) and they emit photons as cyclotron radiation. This radiation is emitted at a range of energies with the peak of the emission at the frequency (or energy) of the orbit of the electron known as the cyclotron energy.

The majority of the electrons are at the ground state but they can be excited to higher Landau levels ( $n \geq 1$ ) by incoming X-ray photons with energies corresponding to the cyclotron energy. There is a "resonance" between the energy of the incoming photon and the energy difference between the Landau levels. This resonance is visible as an absorption line, called Cyclotron Resonant Scattering Feature (CRSF) or cyclotron line,

at the cyclotron energy in the observed X-ray spectrum (see [Staubert et al., 2019](#), for a review). The CRSFs are called fundamental if the resonance is between the ground state and the first Landau level  $n = 1$ , harmonics for  $n > 1$ . The cyclotron line energy depends strongly on the magnetic field which can cause a broadening of the line in the observed spectrum. Changes in the temperature of the plasma, changes in the motion of the electrons, relativistic effects and collisional broadening can also modify the shape of the line (e.g. [Schönherr et al., 2007](#); [Schwarm et al., 2017](#)).

Theoretical calculations ([Schönherr et al., 2007](#)) have shown that the fundamental cyclotron line becomes shallower as the number of harmonic lines increases, to the point of being almost undetectable due to spawned photons filling the fundamental line. Indeed, when an electron undergoes resonant scattering and remains in an excited Landau state, it can produce another photon of similar energy by direct radiative deexcitation back to the Landau level of origin. The resulting photon has the same energy as the incoming photon but is re-emitted in random directions. It eventually escapes the magnetic field and reaches the detector resulting in a photon spawning at the cyclotron energy, particularly if its energy is located at the edges of the fundamental line ([Schönherr et al., 2007](#)).

In Vela X-1, two CRSFs have been confirmed (e.g. [Kreykenbohm et al., 2002](#)): a prominent harmonic line at  $\sim 55$  keV and a weaker fundamental line at  $\sim 25$  keV. Studying the CRSF energy variability is important to determine the physical properties of Vela X-1 and will be discussed in Chap. 5.

## Comptonisation

To summarise, the three sources of mostly soft X-ray photons in HMXBs are blackbody photons emitted from the thermal mound, cyclotron photons and strong bremsstrahlung in the accretion column. To explain the observed hard X-rays, we need up-scattering of soft seed photons by energetic electrons to higher energies, through inverse Compton collisions.

There are two known types of Comptonisation: bulk and thermal (Becker & Wolff, 2007). Bulk Comptonisation corresponds to kinetic energy transfers from energetic electrons to photons by scatterings in the shock region. Thermal Comptonisation also corresponds to up-scattering of photons but this time, it is due to the local thermal motion of the electrons. Since the velocity of the infalling gas is larger than the thermal motion of the electrons, bulk Comptonisation dominates and the resulting spectrum is well described by a power law with a spectral index higher than 2. However, for very bright sources such as Vela X-1, thermal Comptonisation dominates for the highest seed photons energies (Titarchuk et al., 1996). More up-scattered photons are produced, thus flattening the power law (relatively compared to a pure bulk Comptonisation). Additionally, there is a characteristic exponential high-energy cutoff of the power law due to Compton down-scattering of high-energy photons via electron recoil (Becker & Wolff, 2007).

In Fig. 1.6, we show a spectrum of the neutron star HMXB Cen X-3 with theoretical model from Becker & Wolff (2007). The spectrum is clearly dominated by Comptonised bremsstrahlung emission, with a CRSF at  $\sim 30$  keV visible in absorption in the cyclotron radiation. The overall shape can be well described by a power law with a high-energy cutoff showing the contribution of both bulk and thermal Comptonisation as explained before.

### 1.3.3 Accretion regime

In the supercritical accretion regime, the neutron star luminosity exceeds a certain threshold called the critical luminosity  $L_{\text{crit}}$  (equivalent to a local Eddington luminosity) as defined in Becker et al. (2012). In such luminous neutron stars ( $L_X \sim 10^{37-38} \text{ erg s}^{-1} \gtrsim L_{\text{crit}}$ ), the radiation pressure from the hot spot dominates the ram pressure of the supersonic infalling gas. Thus, a radiation-dominated shock forms (Basko & Sunyaev, 1976), indicated by "sonic surface" in Fig. 1.5. The infalling material first decelerates to subsonic velocities when encountering the shock and most of the kinetic energy is carried

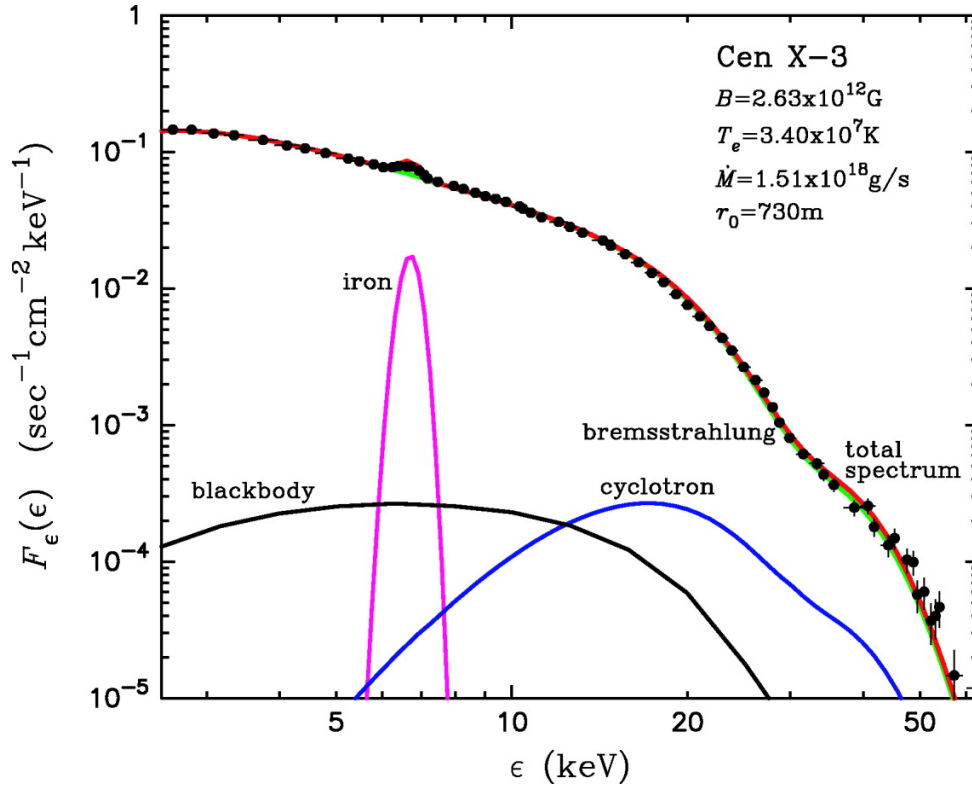


**Fig. 1.6:** Spectrum of the HMXB Cen X-3. Data (black circles and crosses) reported by [dal Fiume et al. \(1998\)](#) with the total spectrum model (red) from [Becker & Wolff \(2007\)](#) showing the individual contributions of Comptonised bremsstrahlung radiation (green), Comptonised cyclotron radiation (blue), Comptonised blackbody radiation (black) and the iron emission line (pink). Figure from [Becker & Wolff \(2007\)](#).

away by scattered X-rays ([Langer & Rappaport, 1982](#)) escaping the accretion column thus cooling down the plasma. Once it has passed the shock, the infalling gas decelerates to rest at the neutron star's solid surface with radiation braking ([Basko & Sunyaev, 1976](#)). The optically thin region above the thermal mound and below the radiation dominated shock is the photosphere of the neutron star. Seed photons (blackbody, bremsstrahlung and cyclotron) are confined by downward advection at a certain altitude in the photosphere (see Fig. 1 in [Becker et al., 2012](#)) and eventually diffuse through the walls of the accretion column in a so-called "fan beam" by Compton up-scattering due to collisions with infalling electrons ([Davidson, 1973](#); [Harding, 1994](#)). The higher the luminosity of the neutron star, the further away from the surface are the shock and the emission region where the photons diffuse.



In a subcritical accretion regime ( $L_X \sim 10^{36-37} \text{ erg s}^{-1} \lesssim L_{\text{crit}}$ ), the infalling gas still passes through a radiation-dominated shock. However, the radiative pressure is not sufficient to bring the infalling material to rest. In this case, Coulomb collisions, due to the repulsive electrostatic forces between two particles of the same charge, fully decelerate the gas to rest just above the surface. [Becker et al. \(2012\)](#) estimated the characteristic emission height  $h_c$  at which Coulomb interactions begin to decelerate the infalling gas and where photons escape the accretion column walls (see Fig. 1.7). They found in their Eq. 51 that  $h_c$  is anti-correlated with increasing mass accretion rate and luminosity in subcritical sources. Still following [Becker et al. \(2012\)](#), above this emission height, advection prevents the photons to escape on time. Conversely, below the characteristic emission height, radiation is confined within the column causing the emission through the walls to gradually diminish as the surface is reached. Thus, [Becker et al. \(2012\)](#) assume that in the subcritical scenario, the CRSF energy is imprinted at the altitude  $h_c$  where strong Coulomb deceleration starts. Vela X-1 has been classified as a subcritical accreting source in the past (e.g. [Fürst et al., 2014b](#)). This will be discussed in Chap. 5 together with CRSF energy variability.

For very low luminosities ( $L_X \lesssim 10^{34-35} \text{ erg s}^{-1} \ll L_{\text{crit}}$ ), it is expected that there is no radiation-dominated shock. The infalling plasma directly strikes the neutron star's surface ([Langer & Rappaport, 1982](#)) and X-rays can escape along the magnetic field lines in a "pencil-beam" ([Burnard et al., 1991](#); [Nelson et al., 1993](#)).

### 1.3.4 Photoelectric absorption

On their way to the observer, photons emitted from the neutron star experience several interactions, impacting the observed data. In particular, there is absorption from the stellar wind close to the neutron star and from the interstellar medium at a larger scale. X-ray photons can be absorbed by the material (atoms or ions) and transfer energy to an electron which is either excited to a higher state (excitation) or ejected from the atom (ionisation). This is called the photoelectric absorption effect and its probability

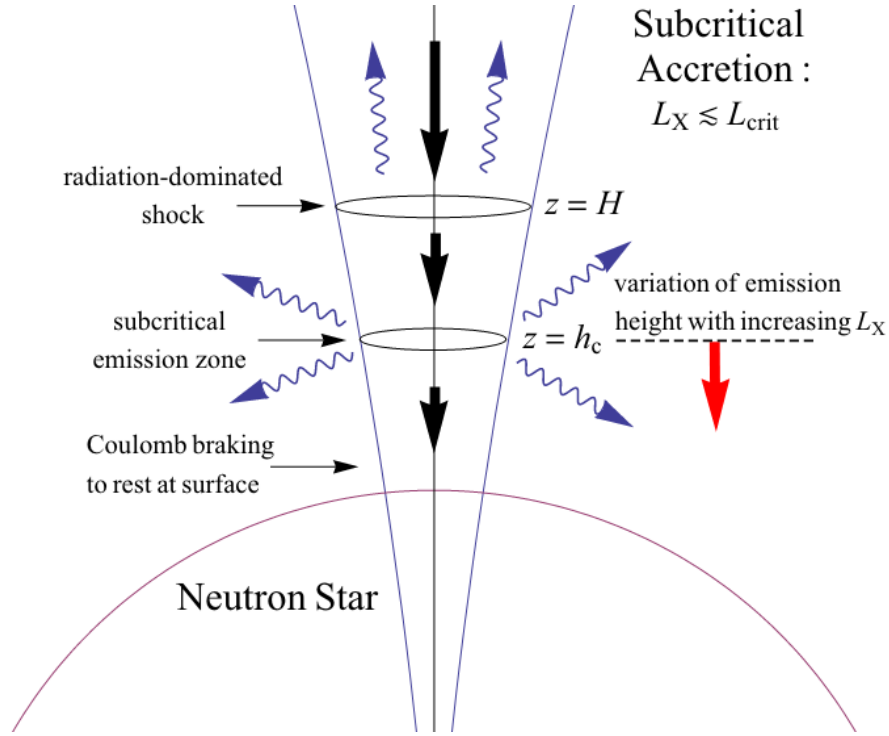


**Fig. 1.7:** Illustration of the geometry of the accretion column in the subcritical accretion regime. Figure from [Becker et al. \(2012\)](#).

to happen is determined by the cross-section  $\sigma(E)$  which depends on the nature of the considered atom, its abundance, its ionisation state and the energy  $E$  of the photon ([Wilms et al., 2000](#)). Since the cross-section  $\sigma(E)$  is proportional to  $E^{-3.5}$  ([Verner et al., 1993](#)), the X-ray absorption mainly impacts the soft photons resulting in a "bending" of the X-ray spectrum at low energies (i.e. absorbed power law). The observed absorbed X-ray spectrum  $I_{\text{obs}}$  is given by ([Wilms et al., 2000](#)):

$$I_{\text{obs}}(E) = I_{\text{source}}(E) \exp^{-\sigma(E)N_{\text{H}}} \quad (1.1)$$

where  $I_{\text{source}}$  is the X-ray spectrum as emitted from the neutron star and  $N_{\text{H}}$  is the number density or absorption column density of hydrogen (molecular, neutral or ionised) in  $\text{cm}^{-2}$ . The parameter  $N_{\text{H}}$  accounts for the number of absorbing hydrogen atoms per cross-section area and is commonly used in X-ray applications to normalise  $\sigma(E)$  ([Wilms et al., 2000](#)).

The dependency between  $\sigma$  and  $E$  is not continuous as the energy levels of the electrons in an atom are quantised into energy levels (also called shells). Therefore, there are "jumps" of the cross-section  $\sigma$  at energies where electrons can leave the lower energy levels. The greater the cross-section at a given energy, the higher the probability that photons at that energy threshold are absorbed, resulting in an absorption edge in the observed spectrum. The most prominent and known absorption edge known in Vela X-1 and in accreting neutron stars in general is the Fe K-edge, named after the K-shell ( $n = 1$ ), at 7.1 keV (see Fig. 1.8). A comparison with cross-sections for other elements than Fe is shown in [Wilms et al. \(2000\)](#).

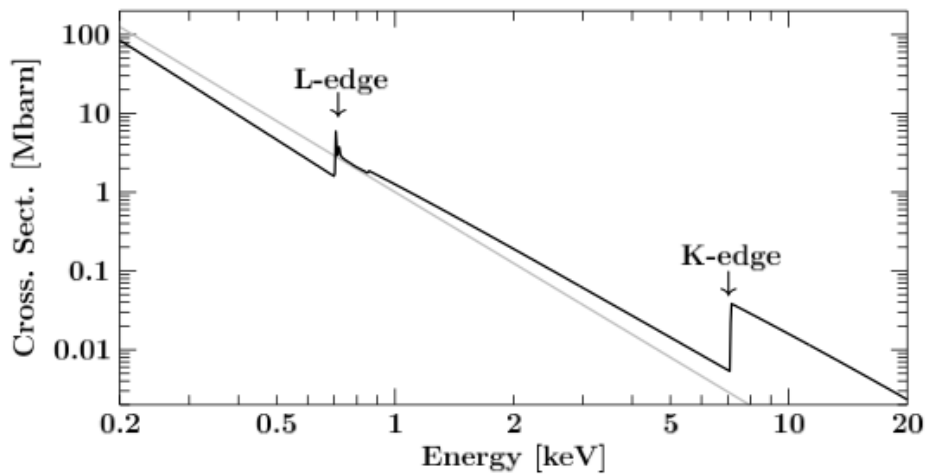


**Fig. 1.8:** Photoelectric cross-section of Fe (black solid line) according to [Verner et al. \(1996\)](#) depending on the energy showing the K- and L-edges. The grey line represents the dependence in  $E^{-3}$ . Figure from [Fürst \(2011\)](#).

### 1.3.5 Line emission

In an ionised atom, if the expelled electron was in a strongly bound shell (the closest ones to the nucleus), the atom is unstable. The gap is filled by an electron from a higher shell thus emitting a photon whose energy corresponds to the difference between the two energy levels. The emitted photon contribute to the so-called fluorescent emission lines in the observed spectrum. The lines are named after the shell (K for  $n = 1$ , L for  $n = 2$ , M for  $n = 3$ , ...) where the electron was ejected from plus a Greek letter corresponding

to the shell where the electron filling the gap is from ( $\alpha$  if from L-shell,  $\beta$  if from M-shell, ...) in the Siegbahn notation. We show in Fig. 1.9 the  $K\alpha$  and  $K\beta$  electronic transitions as examples. In the particular case of hydrogen-like ions (i.e. ionised atoms with only one electron left), the letter preceding the Greek particle in the Siegbahn notation is dropped for the name of the spectral line emissions of the hydrogen atom ("Ly" for Lyman series with transitions from  $n > 1$  to  $n = 1$  i.e. K-shell, "Ba" for Balmer series with transitions from  $n > 2$  to  $n = 2$  i.e. L-shell and so on).

Theoretically in quantum physics, we should consider the fine structure of the atom meaning that the shells are actually divided into sub-structures depending on the quantum numbers (e.g. the 2s and 2p sub-shells for the L-shell). However, the energy difference between the sub-structures in one shell is so small that it cannot be resolved by current X-ray telescopes thus it is commonly adopted in X-ray astronomy to use the simple model of the K-, L- and M-shells.

In the spectrum of Vela X-1, several fluorescent lines are expected. The most prominent ones being the Fe  $K\alpha$  and Fe  $K\beta$  at  $\sim 6.4$  keV and  $\sim 7.1$  keV respectively. The energy of the fluorescent lines changes depending on the ionisation degree of the atom (see e.g. in [Kallman et al., 2004](#), for the Fe  $K\alpha$  and Fe  $K\beta$  lines). Indeed, more energy is needed to detach the electron due to its increasing binding energy as the ionisation degree rises. The ionisation degree is usually marked with a Roman number in X-ray spectroscopy (e.g. HII for  $H^+$ ). The Roman numeral I stands for neutral atom.

A plethora of fluorescent  $K\alpha$  lines (or  $Ly\alpha$  for hydrogen-like ions) from low and high ionisation species of Si, Mg, Ne, S are also expected below 4 keV in the spectrum of Vela X-1 (e.g. [Grinberg et al., 2017](#); [Lomaeva et al., 2020](#); [Amato et al., 2021](#)) as well as Radiative Recombination Continua (RRC) of O ([Lomaeva et al., 2020](#)). RRC emission line features arise as free electrons recombine with ions in the plasma.

Doppler effect is expected in line features due to the motion of the stellar wind whose terminal velocity can reach  $1700 \text{ km s}^{-1}$ . This can cause a broadening of the individual lines, making neighbouring lines difficult to resolve with current X-ray instruments.

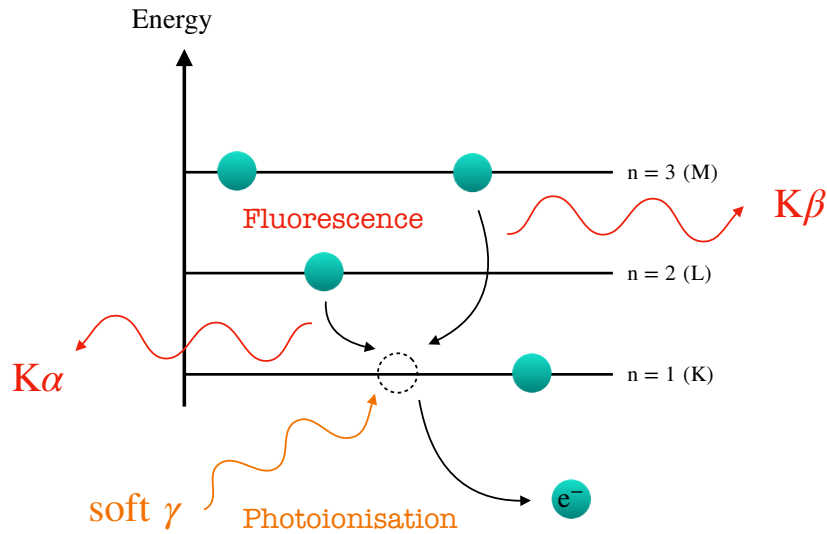


**Fig. 1.9:** Sketch of the photoionisation and fluorescence principles. The orange arrow represents an incoming soft X-ray photon ejecting a bound electron (green sphere) during photoionisation. The red arrows represent two examples of fluorescence: the  $K\alpha$  and  $K\beta$  (or  $Ly\alpha$  and  $Ly\beta$  if hydrogen-like ion) electronic transitions. The K-shell can only hold two electrons, so only one transition is possible in this example.

### 1.3.6 10-keV feature

The spectrum of Vela X-1 exhibits another line feature known as the 10-keV feature. The physical origin for this feature remains unknown (Coburn et al., 2002) and is potentially due to our incomplete comprehension of the continuum. This feature seems to be inherent in the spectra of accreting pulsars (Coburn et al., 2002) but the limitations of the simple phenomenological models usually employed to describe the continuum in X-ray pulsars (e.g. Staubert et al., 2019) may simply result in residuals at 10 keV. In some sources, such as 4U 0115+63 (Ferrigno et al., 2009; Müller et al., 2013) and EXO 2030+375 (Klochkov et al., 2007), it is modelled with a broad Gaussian emission line and is referred to as the "10-keV bump model" by some (Reig & Nespoli, 2013). In other sources, such as XTE J0658-073 (McBride et al., 2006; Nespoli et al., 2012), Cen X-3 (Santangelo et al., 1998), or Vela X-1 (Fürst et al., 2014b), it appears as a broad absorption line. Possible magnetic origin has been associated to the 10-keV bump in KS 1947+300 (Fürst et al., 2014a) and 4U 1901+03 (Reig & Milonaki, 2016).



# Aim of the thesis and open questions

**Context:** Neutron star HMXBs are ideal astrophysical laboratories to understand the matter under extreme conditions and are thus building blocks of star clusters and galaxies. Indeed, we saw in Sect. 1.1.2 that massive stars in HMXBs are meant to undergo gravitational collapse at the end of their life, just like their compact companion. This leads to supernovae whose explosion ionises and enriches the interstellar medium with heavy elements via gas outflows. In order to probe and plan such events for future observations, we need to understand the evolution stages of HMXBs. This can be achieved through the investigation of accretion onto compact objects and of wind structure in massive stars. These two research domains are of great significance for today's and future astrophysics, as evidenced by their prominent inclusion in the science cases for *Athena* ([Barret et al., 2023](#)) and *XRISM* ([XRISM Science Team, 2020](#)).

**Goal:** Using the strong X-ray radiation from the accreting neutron star, we want to study the accretion physics of the material that originates from the stellar wind of the massive companion. Through the measurement of the X-ray spectrum, we can acquire valuable information not only about the X-ray emission region but also about the surrounding material, including its composition and physical state. The archetypical neutron star HMXB Vela X-1 is a perfect case study for such an analysis with its bright luminosity and convenient physical parameters (see Sect.1.2.1) which allow a complete analysis through time-resolved broadband high-resolution spectroscopy.

## 2.1 Investigation of X-ray emission...

To start with, we need a good description of the continuum emitted from the neutron star in Vela X-1. We saw in Sect. 1.3.2 that X-ray photons originate from blackbody, bremsstrahlung and cyclotron radiation. They are up-scattered to higher energies in the dense accretion columns and the overall spectrum of Vela X-1 is well described by an absorbed power law with a high-energy cutoff (e.g. [Staubert et al., 2019](#)). *NuSTAR* has an energy coverage from 3 keV to 79 keV including both soft and hard X-rays. This makes *NuSTAR* one of the instruments of choice for this study in order to constrain and explore all the aspects of accretion physics in Vela X-1. We explored in [Diez et al. \(2022\)](#) the variability of flux and continuum parameters, in particular the CRSFs to determine the accretion regime of the source. The analysis is described in [Diez et al. \(2022\)](#) and results are discussed in Chap. 5.

## 2.2 ... and absorption

From the geometry of the Vela X-1 system (see Sect. 1.2.1), we expect strong changes in absorption along the orbital phase  $\phi_{\text{orb}}$  due to moving accretion and photoionisation wakes intercepting our line of sight (Fig. 1.3). [Doroshenko et al. \(2013\)](#) showed in particular a decrease in  $N_{\text{H}}$  after the eclipse followed by a strong increase around  $\phi_{\text{orb}} \approx 0.5$  when averaged among multiple orbits. Nevertheless, measurements of absorption at the same orbital phase during different observation times are heterogeneous (see Fig. 5 in [Kretschmar et al., 2021](#)). Variations in flux, mass-accretion and mass loss rates have been observed too but the results are difficult to compare since the spectral models used are different (e.g. [Sako et al., 1999](#); [Fürst et al., 2014b](#); [Martínez-Núñez et al., 2014](#)). The presence of clumps together with a complex and turbulent wind geometry could explain the observed variations even though the exact description of the wind in Vela X-1 is still poorly understood. Hence, we need high resolution absorption variability studies covering crucial orbital phases (e.g. wakes passing in front of our line



of sight) on short timescales to describe the material present in the wind and determine the accretion geometry in the clumpy wind scenario. Soft X-ray photons are the most affected by absorption from the stellar wind thus making the *XMM-Newton* observatory an instrument of choice for such study since it has an energy coverage from 0.1 keV to 12 keV. We performed in [Diez et al. \(2023\)](#) a broadband and high-resolution spectroscopy combining the *NuSTAR* data we analysed previously in [Diez et al. \(2022\)](#). The results and discussion are presented in Chap. 5.



# X-ray observatories

To study the properties of Vela X-1 and other HMXBs, X-ray telescopes are essential. Because X-rays are blocked by the Earth's atmosphere, it is necessary to use space-based telescopes to detect and study celestial X-ray sources. In this thesis, we will focus on the X-ray instruments used to observe Vela X-1, which include *NuSTAR* and *XMM-Newton*. These telescopes provide high-resolution imaging and spectroscopy essential to perform a detailed analysis of the Vela X-1 system. We give in the following sections a brief overview of the detectors of interest we used for this study.

## 3.1 *NuSTAR*

The *Nuclear Spectroscopic Telescope ARray (NuSTAR)* ([Harrison et al., 2013](#)) is a NASA small explorer mission launched on 13 June 2012 into a low-Earth, near-equatorial orbit. In order to fit in the low-cost Pegasus launch vehicle, its stowed mast extended upon entry into space to its full length of 10 m. A metrology system on board consisting of two lasers mounted on the optics (see Fig. 3.1) assure that the detectors are always aligned with the optics. Due to the Earth passage in the *NuSTAR* field of view, observations have to be regularly interrupted for about 2 ks. We refer to ([Harrison et al., 2013](#)) as the main source for the following discussion about the instrument properties.

The *NuSTAR* optics consist of 133 concentric coated mirror shells in a Wolter type-I design (see Fig 3.2) operating in the 3 to 79 keV energy range. In this configuration, the incoming X-ray light is reflected twice: once off of an upper mirror section shaped as a parabola and a second time off of a lower mirror section shaped as a hyperbola.

*NuSTAR* carries on board two detector units called Focal Plane Module (FPM) A and B at the focus of each of the two co-aligned optics units (see Fig. 3.1). Each detector unit

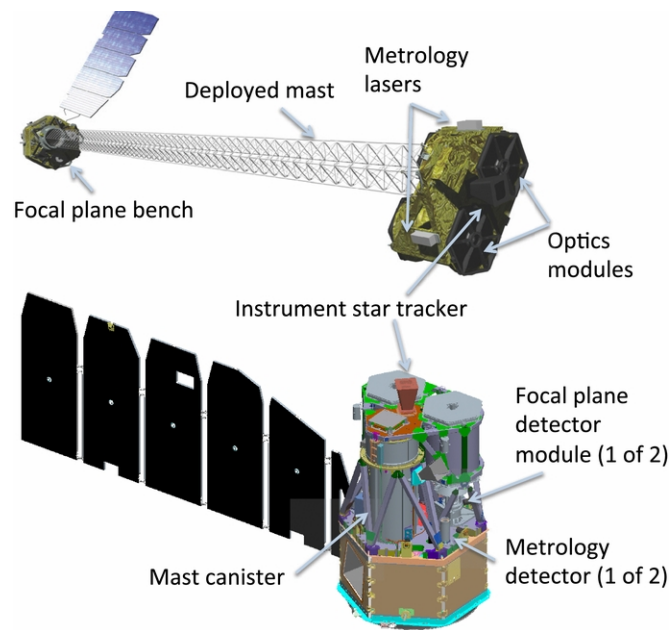


**Fig. 3.1:** Sketch of the *NuSTAR* payload. All modules are indicated by a grey arrow. Figure from [Harrison et al. \(2013\)](#).

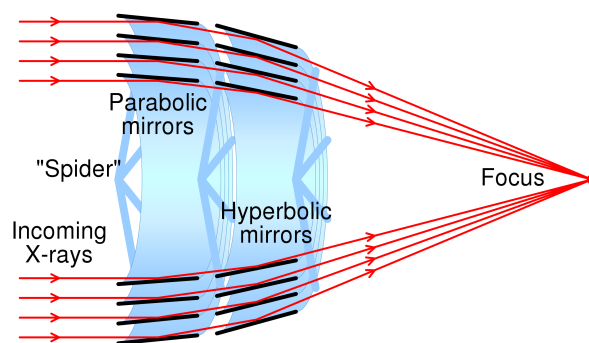


**Fig. 3.2:** Sketch of a Wolter type-I telescope showing incoming X-ray light converging to the focal point. Credits: <https://commons.wikimedia.org/wiki/user:Cmglee>.

(or focal plane) consists of four detectors made of crystals of Cadmium-Zinc-Telluride divided up into pixels. This semiconductor material has the ability to absorb high-energy X-rays creating an electronic signal in the process. One FPM is built in a two-by-two array of detectors subtending  $32 \text{ pix} \times 32 \text{ pix}$  and a  $6' \times 6'$  region of the sky. The time resolution is of  $\sim 0.1 \text{ ms}$ .

## 3.2 *XMM-Newton*

The *X-ray Multi-Mirror (XMM)-Newton* ([Jansen et al., 2001](#)) is a European Space Agency (ESA) 10-m long observatory launched on 10 December 1999 from French Guyana with an Ariane 504 launcher. Initially planned for a three-year mission, the satellite is still operating up to now 20 years later. Due to highly elliptical orbit, *XMM-Newton* is able to make long and uninterrupted observations. In the following, we refer to the *XMM-Newton* Users' Handbook ([XMM-Newton SOC, 2022](#)) for the instrumental characteristics and properties.

It carries on board three Wolter type-I X-ray telescopes with different X-ray detectors in their foci, described below, and a 30-cm optical monitor. We present in Fig. 3.3 a sketch of the *XMM-Newton* payload. The three focal-plane CCD cameras comprise the European Photon Imaging Camera (EPIC), which consists of two Metal Oxide Semiconductor (MOS) CCD arrays (referred to as MOS1 and MOS2; [Turner et al., 2001](#)) and the pn camera ([Strüder et al., 2001](#)). With a field of view of  $30'$ , the EPIC cameras provide the opportunity to conduct imaging observations with remarkable sensitivity in the energy range from 0.1 to 12 keV with moderate spectral resolution ( $E/\Delta E \sim 20\text{--}50$ ). The MOS cameras are installed behind the Reflection Grating Spectrometer (RGS) ([den Herder et al., 2001](#)) whose grating assemblies 1 and 2 divert about half of the telescope incident flux towards the RGS1 and RGS2 readout cameras.

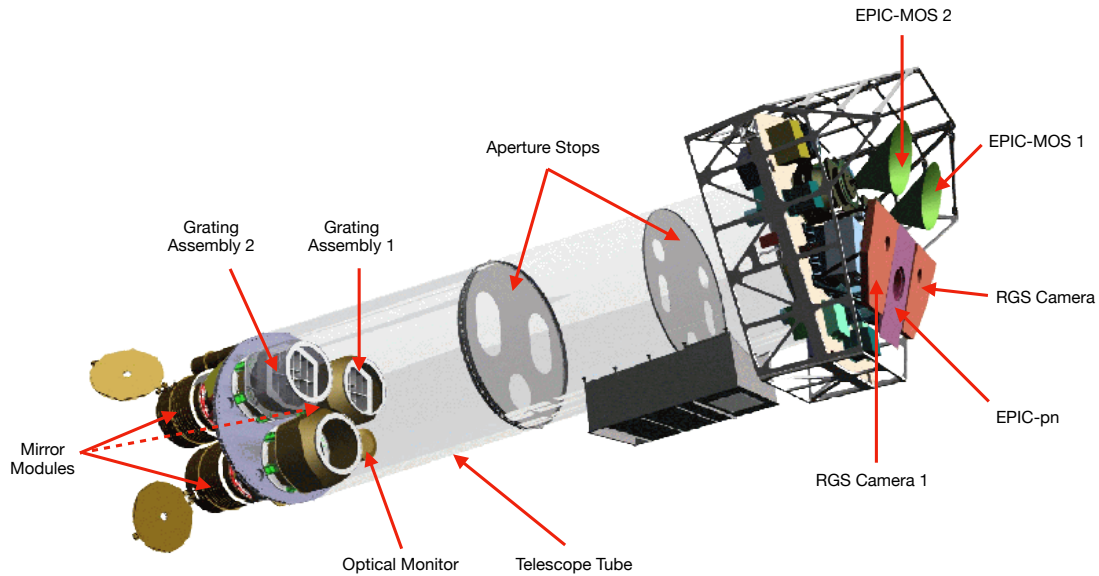


**Fig. 3.3:** Sketch of the *XMM-Newton* payload. All modules are indicated by a red arrow. Credits: ESA, figure courtesy of Dornier Satellitensysteme GmbH.

### 3.2.1 EPIC-pn

The pn camera (as all EPIC CCDs) operates in photon counting mode with a fixed, mode dependent frame readout frequency. The produced event lists are tables containing a listing of the detected events with information about the position at which they were detected, their arrival times and energies.

The pn camera consists of twelve individual  $3 \times 1$  cm pn-CCDs on a single wafer and allows several modes of data acquisition. In the full frame and extended full frame mode, all pixels of all CCDs are read out ( $376 \text{ pix} \times 384 \text{ pix}$ ) and thus the full field of view is covered. In the large window mode (also available with MOS), only half of the area of all twelve CCDs is read out whereas in small window mode only the CCD at the focal point is used to collect data. Finally, in timing mode (also available with MOS), imaging is made only in one dimension, along the column axis. Along the row direction, data from a predefined area on one CCD chip are collapsed into a one-dimensional row to be read out at high speed ( $0.03 \text{ ms}$ ). A special flavour of the timing mode of the pn camera is the burst mode which offers very high time resolution ( $7 \mu\text{s}$ ) but a low duty cycle of 3%.

## Pile-up

When too many incoming photons hit the CCDs of a detector, two or more independent photons arriving at neighbouring pixels during one read-out cycle can be interpreted as a single event with a higher energy being the sum of the energies of the independent photons (Jethwa et al., 2015). This is a common phenomenon to the observation of very bright sources with the *XMM-Newton* EPIC cameras, particularly for Vela X-1 (Martínez-Núñez et al., 2014). This effect can be responsible for photon loss or energy distortion when photons are moved to higher energies.

To test and evaluate for pile-up, the `epatplot` task from the Science Analysis System (SAS) software can be used to read the pattern information statistics of the input EPIC-pn set as function of PI channel. If the derived single and double event fractions differ too much from the model curves, the observation is affected by pile-up and pixels have to be excluded from the Point Spread Function (PSF).

The source of study for this work, Vela X-1, is too bright to exploit MOS data so we exclusively analyse EPIC-pn in timing mode and corrected for pile-up. RGS data of our Vela X-1 observation are also available but their analysis is beyond the scope of this thesis.





# Summary of the original publications

In this Chapter, we summarise the analyses performed in [Diez et al. \(2022\)](#) and [Diez et al. \(2023\)](#), provided in Appendix. The reader is referred to those two publications for more information about the data reduction, observations (light curves, spectra...) and methods used. The main results will be presented and discussed in Chap. 5.

## 4.1 Continuum, cyclotron line, and absorption variability in the high-mass X-ray binary Vela X-1 ([Diez et al., 2022](#))

The aim of this paper is to probe the accretion and X-ray production mechanisms of Vela X-1 by modelling with high precision its spectral continuum. We analysed two observations of Vela X-1 taken with *NuSTAR* in January and May 2019. The first observation, referred to as observation I, covers orbital phases from  $\phi_{\text{orb}} \approx 0.68$  to  $\phi_{\text{orb}} \approx 0.78$ . The second observation, referred to as observation II, has been interrupted by issues with the ground station causing a partial loss of the data. We thus named observation IIa the part covering from  $\phi_{\text{orb}} \approx 0.36$  to  $\phi_{\text{orb}} \approx 0.44$  and observation IIb the part covering from  $\phi_{\text{orb}} \approx 0.46$  to  $\phi_{\text{orb}} \approx 0.52$ , see Fig. 4.1. It has to be noted that observation II is simultaneous with *XMM-Newton* observation that is discussed in [Diez et al. \(2023\)](#).

The spectral analysis consists of two parts. We started with a time-averaged spectroscopy, meaning we extracted a spectrum covering the total exposure time of each

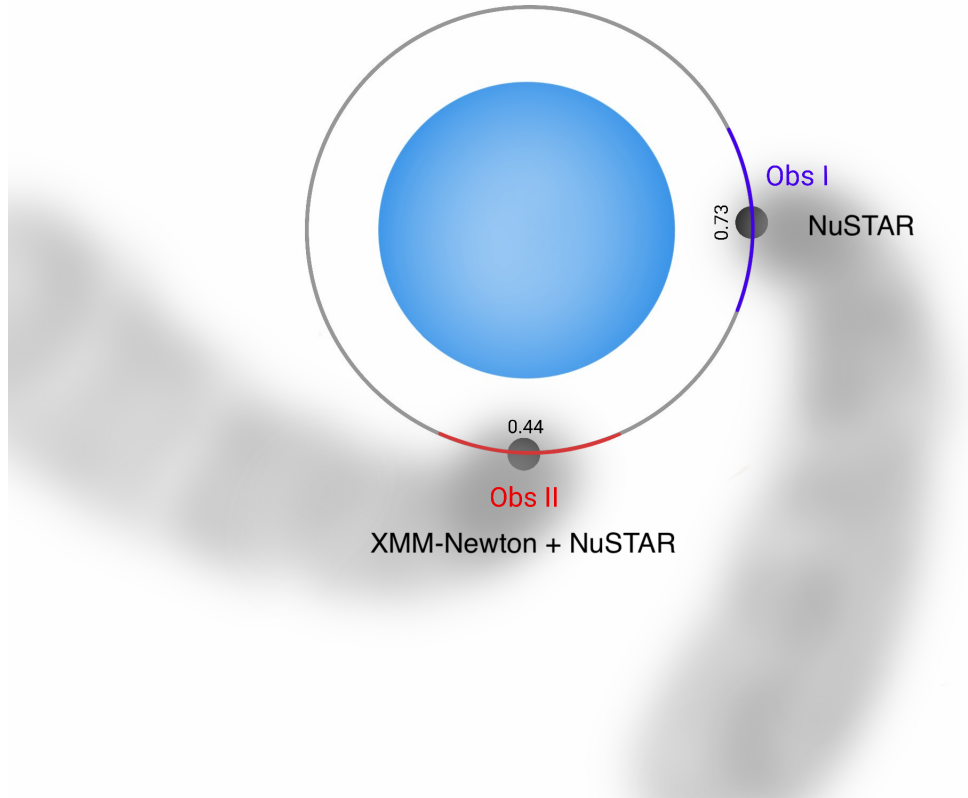


**Fig. 4.1:** Sketch of Vela X-1 showing the positions of the wake structure and the orbital phases covered with corresponding instruments during observation I and II. The observer's point of view is located facing the system at the bottom of the picture.

observation (I, IIa and IIb) in order to elaborate a good continuum model that can describe the data. Our best-fit model is a partial covering model accounting for both absorption from the interstellar medium and the stellar wind. This model has the advantage of isolating the individual contributions of each absorber by two different absorption column densities:  $N_{H,1}$  for the stellar wind and  $N_{H,2}$  for the interstellar medium (see Fig. 4.2). The covering fraction CF gives the percentage of the emitted radiation that is absorbed by the stellar wind. The continuum is a power law with a photon index  $\Gamma$  modified by a high-energy Fermi-Dirac cutoff (FDcut; Tanaka, 1986) with two multiplicative absorption lines accounting for the fundamental and harmonic CRSFs and two additional Gaussian components for the 10-keV feature and for the Fe  $K\alpha$  fluorescent line. Our best-fit model can be written as:

$$F(E) = (CF \times N_{H,1} + (1 - CF)) \times N_{H,2} \times (E^{-\Gamma} \times \text{FDcut} \times \text{CRSF}, F \times \text{CRSF}, H + \text{Fe K}\alpha + 10\text{keV}) \quad (4.1)$$

We then extracted a spectrum for each orbit of *NuSTAR* around the Earth ( $\sim 5.8$  ks), called *NuSTAR*-orbit for the remainder of this thesis, and for each pulse of the neutron star ( $\sim 283$  s). We fitted the data using our best-fit partial covering model from Eq. 4.1 and explored the variability of parameters of interest for the study of the continuum shape.

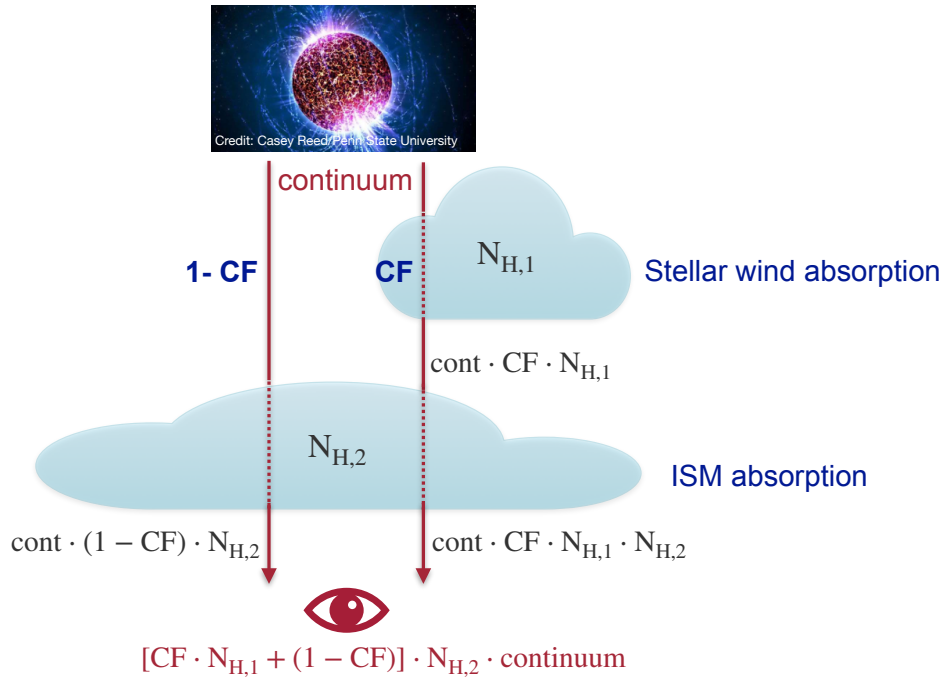


**Fig. 4.2:** Sketch of the partial covering model. The continuum emitted from the neutron star and its vicinity is described in Eq. 4.1. The observer (represented by an eye) is located at the bottom of the picture. Figure from [Diez et al. \(2022\)](#).

## 4.2 Observing the onset of the accretion wake in Vela X-1 (Diez et al., 2023)

In this paper, we wanted to use the low-energy coverage from *XMM-Newton* to probe the internal structure and variability of the stellar wind of Vela X-1 that could not be assessed with *NuSTAR*. We analysed a simultaneous *XMM-Newton* EPIC-pn and *NuSTAR* observation of Vela X-1. This observation corresponds to observation II in Diez et al. (2022). The advantage of these new EPIC-pn data is that we have now the information about the physical events which happened during the loss of the previous *NuSTAR* data between  $\phi_{\text{orb}} \approx 0.44$  to  $\phi_{\text{orb}} \approx 0.46$ .

We built on the previous work in Diez et al. (2022) by employing the same partial covering model we first developed for the *NuSTAR* analysis, with additional fluorescent emission lines below 4 keV (see Table 5.1 in Sect. 5.2.2 for a list of the observed soft emission lines). We again extracted an *XMM-Newton* EPIC-pn for each *NuSTAR*-orbit and each pulse of the neutron star in order to allow for direct combined analysis with the previous *NuSTAR* data. However, we faced calibration issues when combining both instruments as well as different exposure times in the selected time intervals of extraction due to misaligned start/stop times and *NuSTAR* loss of data. We performed an extensive set of tests to assess, quantify and where possible, alleviate, calibration problems and discuss them in detail in the Appendices to Diez et al. (2023). We proceeded to the *NuSTAR*-orbit-by-orbit and pulse-by-pulse analyses with combined *XMM-Newton* EPIC-pn and *NuSTAR* datasets taking into account the calibration issues and we extracted the fitting parameters of interest for the study of the stellar wind structure. We also compared our results to previous measurements and theoretical predictions.

# Results & Discussion

## 5.1 Continuum shape and accretion regime in Vela X-1

In this Section, we focus on our results with *NuSTAR* only (Diez et al., 2022) since the continuum shape of the spectrum of Vela X-1 is mainly constrained by the wide energy range covered by *NuSTAR*. The additional *XMM-Newton* data in the 0.5–3 keV energy range do not impact the continuum shape but rather the absorption and stellar wind structure at very low energies (cf. Sect. 1.3.4) and will be discussed in Sect. 5.2

### 5.1.1 Spectral shape

#### Photon index

In Fig. 5.1, we show the evolution of the photon index  $\Gamma$  with the luminosity of Vela X-1 resulting from the orbit-by-orbit ("orbit" refers to a *NuSTAR*-orbit) spectral analysis for our two observations with *NuSTAR*. We also include previous measurements from Fürst et al. (2014b) at  $\phi_{\text{orb}} \approx 0.655\text{--}0.773$ , re-scaled to the updated distance to the source, for direct comparison. A negative correlation between  $\Gamma$  and the luminosity in the 3–79 keV energy band is clearly visible, as already spotted in Vela X-1 by Odaka et al. (2013) and Fürst et al. (2014b). For low luminosities, the high values of  $\Gamma$  indicate that bulk Comptonisation dominates. However, as the photon index decreases with rising luminosity, the thermal Comptonisation becomes dominant. This could be explained by higher accretion rates during flaring episodes leading to more efficient thermal Comptonisation in the accreted plasma (e.g. Odaka et al., 2013). More up-scattered photons are produced and thus flatten the continuum shape.

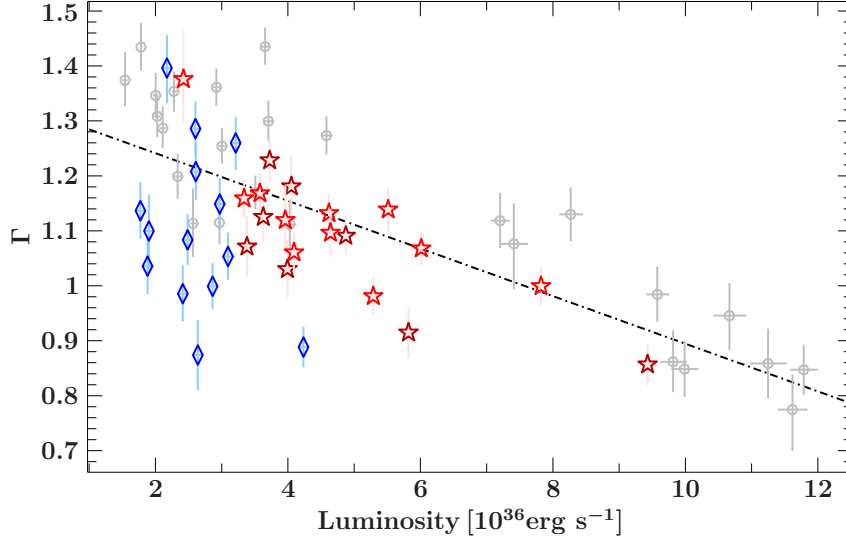


**Fig. 5.1:** Photon index  $\Gamma$  as function of the 3–79 keV luminosity from our orbit-by-orbit results together with ks-integrated spectral fits from Fig. 7 in Fürst et al. (2014b). The blue diamonds represent observation I, bright red stars observation IIa and dark red stars observation IIb. The dot-dashed black line is a linear regression through all the data points. Figure from Diez et al. (2022).

This behaviour is typical for a source in the subcritical accretion regime such as Her X-1 (Staubert et al., 2007) and other Be/X-ray pulsars in Reig & Nespoli (2013). Thus, Vela X-1 appears to be a subcritical source, too. However, uncertainties on this statement will be raised in Sect. 5.1.2.

## Folding energy

As seen in Sect. 4 Eq. 4.1, we used FDcut to model the high-energy cutoff in the spectrum of Vela X-1 as it is commonly done for this source (e.g. Kreykenbohm et al., 1999; Fürst et al., 2014b). The FDcut component is characterised by the cutoff energy  $E_{\text{cut}}$  and the folding energy  $E_{\text{fold}}$  such that an absorbed power law modified by a high-energy Fermi-Dirac cutoff can be written as:

$$F(E) \propto N_{\text{H}} \times E^{-\Gamma} \times \left( 1 + \exp\left(\frac{E - E_{\text{cut}}}{E_{\text{fold}}}\right) \right)^{-1} \quad (5.1)$$

The folding energy  $E_{\text{fold}}$  describes the steepness of the continuum after the high-energy cutoff (see Fig. 5.2). Low  $E_{\text{fold}}$  implies a steeper cutoff, i.e. a softer spectrum caused by less high-energy photon flux. In other words, changes in the folding energy, caused by variable luminosity for example, would indicate changes in the underlying Comptonisation in the accretion column of the neutron star.

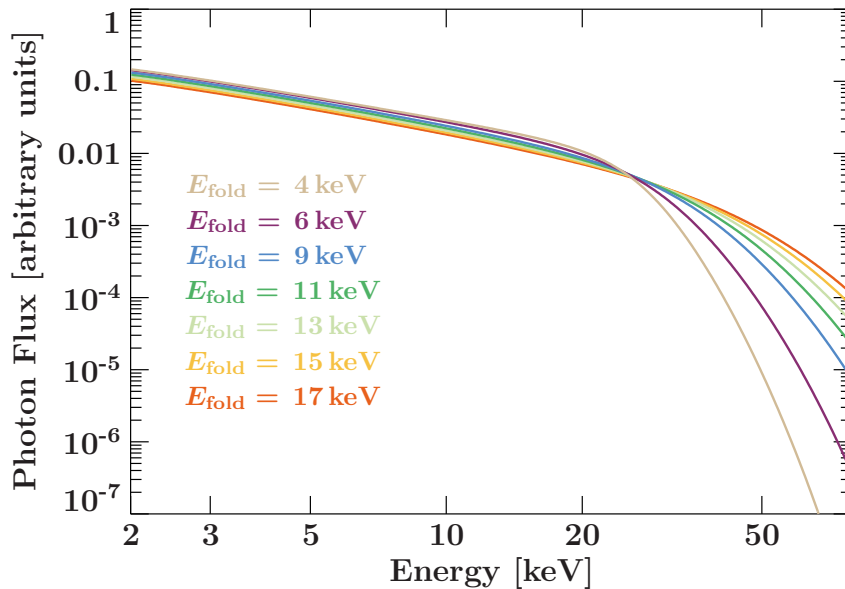


**Fig. 5.2:** Examples of absorbed power laws modified by a FDcut at  $\sim 24$  keV with varying  $E_{\text{fold}}$ .

Model degeneracies have to be considered before investigating possible physical correlations of  $E_{\text{fold}}$  with other spectral parameters. Due to the underlying shape of our model, we expect a positive degeneracy between  $E_{\text{fold}}$  and the X-ray flux  $\mathcal{F}$  (or luminosity since  $\mathcal{F} = L/4\pi d^2$ ). Confidence maps calculated for folding energy and flux confirmed this expectation. We show the confidence map for the time-averaged spectrum of observation I in Fig. 5.3. The same trend has been observed for observations IIa and IIb.

In Fig. 5.4, we present the results of the orbit-by-orbit and pulse-by-pulse analyses for the folding energy  $E_{\text{fold}}$  as function of the luminosity. We observe a negative correlation between those two parameters for  $L \lesssim 4 \times 10^{36} \text{ erg s}^{-1}$  followed by a stabilisation of  $E_{\text{fold}}$  around  $\sim 10$  keV for higher luminosities.

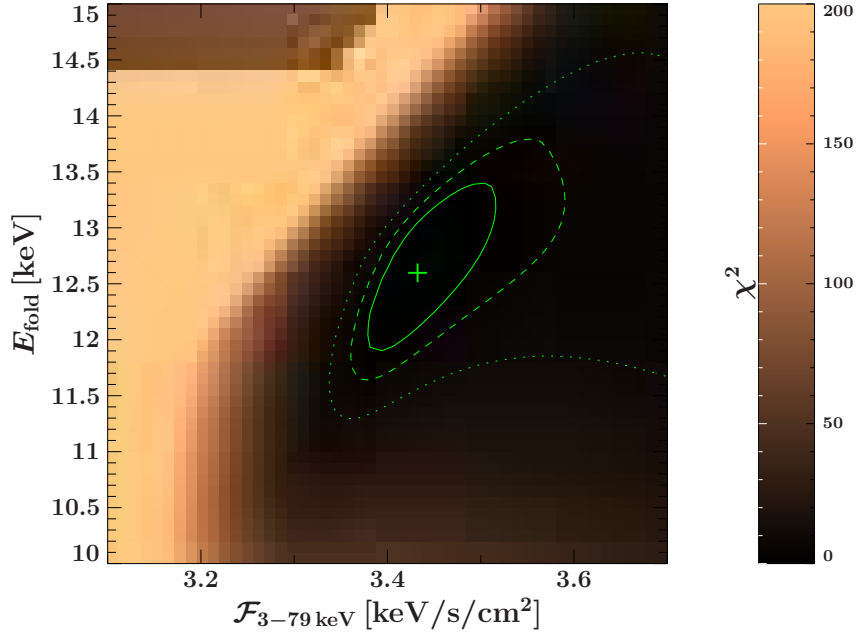


**Fig. 5.3:** Confidence map for  $E_{\text{fold}}$  against flux  $\mathcal{F}_{3-79 \text{ keV}}$  in the 3 to 79 keV energy band obtained with the time-averaged spectrum of observation I. The solid, dashed and dotted green lines show the contours for 68%, 90% and 99% confidence levels respectively. The green cross shows the best-fit couple of parameters.

[Odaka et al. \(2013\)](#) also found the same trend between  $E_{\text{fold}}$  and flux with *Suzaku* data even though our values for folding energy cannot be directly compared with theirs since they used a NPEX model. In a sample of Be/X-ray binaries in the subcritical accretion regime, [Reig & Nespoli \(2013\)](#) also found a similar behaviour of the cutoff.

This negative correlation between  $E_{\text{fold}}$  and the luminosity is opposed to the expected positive model degeneracy we saw in Fig. 5.3 thus confirming the real observed event in our data. When the luminosity increases,  $E_{\text{fold}}$  decreases leading to a softening of the spectrum due to a steeper cutoff. This would indicate a higher temperature of the plasma causing more efficient Compton down-scattering of high-energy photons via electron recoil.



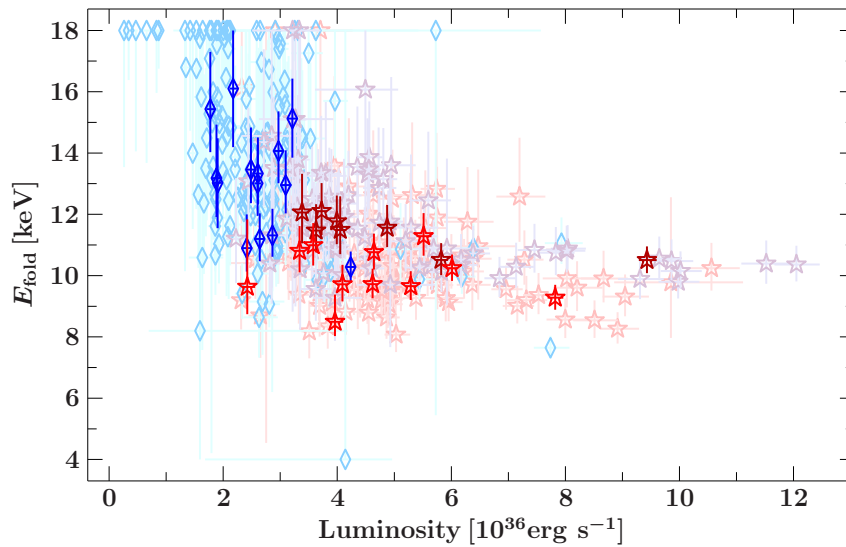


**Fig. 5.4:** Folding energy  $E_{\text{fold}}$  as function of the luminosity in the 3 to 79 keV energy band resulting from our orbit-by-orbit and pulse-by-pulse spectral analyses. Dark blue diamonds are the results of the orbit-by-orbit analysis for observation I, light blue diamonds are the results of the pulse-by-pulse spectroscopy for observation I, bright red stars are the results of the orbit-by-orbit spectroscopy for observation IIa, pink stars are the results of the pulse-by-pulse spectroscopy for observation IIa, dark red stars are the results of the orbit-by-orbit spectroscopy for observation IIb, and lavender stars are the results of the pulse-by-pulse spectroscopy for observation IIb. Figure from [Diez et al. \(2022\)](#).

## 5.1.2 Accretion regime

### CRSF variability

We saw previously that the negative correlation we observed between  $\Gamma$  and the luminosity puts Vela X-1 in the subcritical sources. Following [Becker et al. \(2012\)](#) (cf Sect. 1.3.3), in subcritical sources the characteristic emission height  $h_c$  at which Coulomb interactions are dominant in stopping the infalling gas is anti-correlated with the luminosity (see Fig. 1.7). As this emission region get closer to the neutron star's surface, the strength of the magnetic field  $B$  increases. Additionally, the CRSF energy  $E_{\text{CRSF}}$  is positively correlated with the magnetic field such that:

$$E_{\text{CRSF},n} = n \times \frac{\hbar e B}{m_e c} \approx n \times 11.57 \times \frac{B}{10^{12} \text{ G}} \text{ keV} \quad (5.2)$$

where  $\hbar = h/2\pi$  with  $h$  the Planck constant,  $e$  and  $m_e$  the electron charge and mass,  $c$  the speed of light,  $n = 1$  corresponds to the fundamental Landau level,  $n > 1$  for harmonics. In presence of a strong gravitational potential of the neutron star, the cyclotron line energy is modified by the redshift as  $E_{\text{CRSF},n} \times (1 + z)^{-1}$ .

Therefore, since  $h_c$  is anti-correlated with the luminosity  $L$ , we expect a positive correlation between  $E_{\text{CRSF},n}$  and  $L$  in subcritical sources. Another scenario that could explain the positive correlation between the cyclotron line energy and the luminosity is Doppler effect in the accretion channel moderated by the luminosity-dependent velocity profile ([Mushtukov et al., 2015](#)). It was indeed observed in several accreting X-ray pulsars that the correlation of the cyclotron energy with the luminosity and the correlation of the photon index with luminosity were inverse to each other, that is, if one was positive, the other was negative ([Staubert et al., 2007](#); [Klochkov et al., 2011](#)). [Fürst et al. \(2014b\)](#) computed the theoretical CRSF energy-luminosity relation in subcritical sources based on the derivations made in [Becker et al. \(2012\)](#):

$$E_{\text{theo},n} = n \times \left[ 1 + 0.6 \left( \frac{R_{\text{NS}}}{10 \text{ km}} \right)^{-\frac{13}{14}} \left( \frac{\Lambda}{0.1} \right)^{-1} \left( \frac{\tau_*}{20} \right) \left( \frac{M_{\text{NS}}}{1.4 M_{\odot}} \right)^{\frac{19}{14}} \right. \\ \left. \times \left( \frac{E_{\text{NS},1}}{1 \text{ keV}} \right)^{-\frac{4}{7}} \left( \frac{L_X}{10^{37}} \right)^{-\frac{5}{7}} \right]^{-3} \times E_{\text{NS},1}, \quad (5.3)$$

where  $\tau_*$  is the Thomson optical depth set to 20 for typical X-ray pulsars (Becker et al., 2012) in order to stop the accretion flow via Coulomb interactions,  $R_{\text{NS}}$  and  $M_{\text{NS}}$  the radius and mass of the neutron star respectively.  $E_{\text{NS},1}$  is the surface energy of the fundamental cyclotron line and is equal to  $11.57 \text{ keV} \times B_{\text{NS}}/10^{12} \text{ G}$  with  $B_{\text{NS}}$  the magnetic field strength at the surface of the neutron star in G. We considered a radius of  $\sim 10 \text{ km}$ , a mass of  $\sim 1.7\text{--}2.1 M_{\odot}$  (Kretschmar et al., 2021) and  $E_{\text{NS},1} = 30 \text{ keV}$  (as in Fürst et al., 2014b). The parameter  $\Lambda$  is used to explain how the location of the Alfvén surface differs between predominantly orbital or radial inflow scenarios. It depends on the ratio of the radial velocity of the flow to the free-fall velocity and the thickness of the accretion disc. In Lamb et al. (1973), Eq. 18 demonstrates this relationship. However, even for extreme values of these parameters, such as small radial velocities and a thin accretion disc, the reduction in the Alfvén radius is only by a factor of approximately 10 ( $\Lambda \approx 0.1$ ) compared to the radius corresponding to a fully radial inflow. For spherical accretion,  $\Lambda = 1$ , while for disc accretion,  $\Lambda < 1$ , as noted in Becker et al. (2012). For Vela X-1, we use  $\Lambda = 1$  to account for the stellar wind accretion.

In Fig. 5.5, we present the fundamental and first harmonic cyclotron line energies as function of the luminosity. We also plotted the theoretical CRSF positive correlation calculated from Eq. 5.3. Even though there is an intrinsic variability in the CRSF energies, contrary to Fürst et al. (2014b) (grey datapoints) it does not seem to be correlated with the luminosity in our data (coloured datapoints). This may be due to the fact that our observations do not cover a large enough range of luminosities to observe any correlation. Hence, we cannot draw any conclusions from those results regarding the accretion regime of Vela X-1.

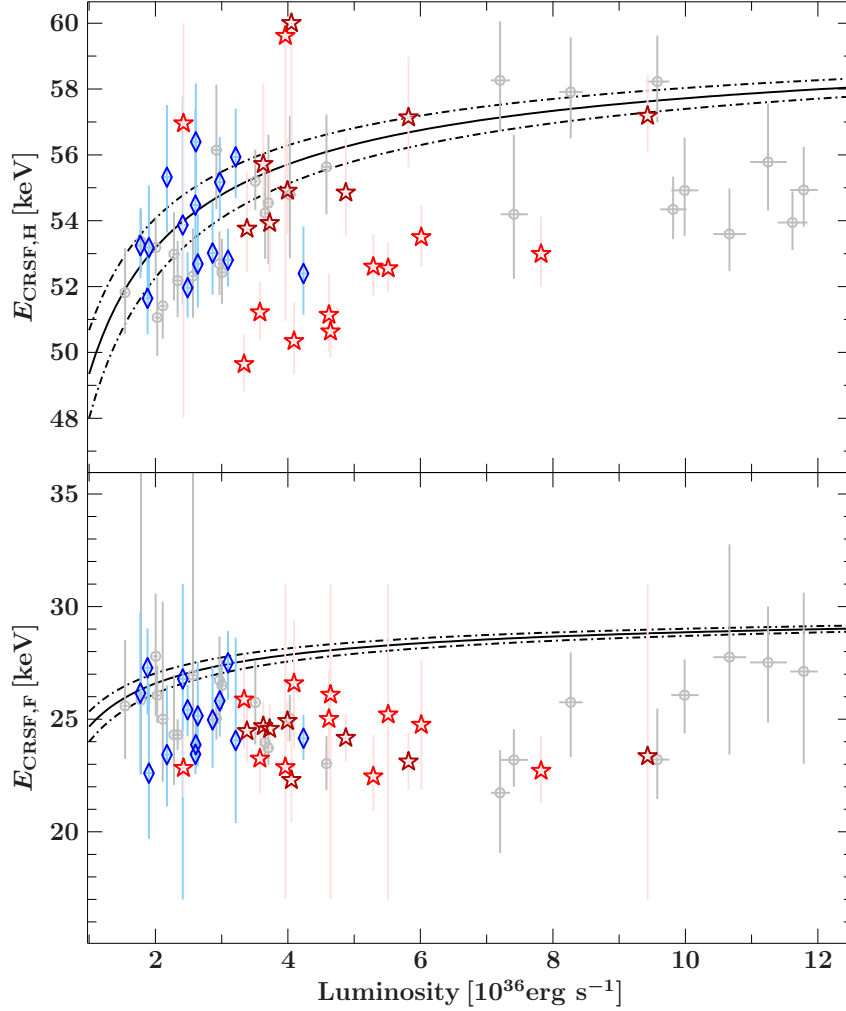


**Fig. 5.5:** Cyclotron line energy for the fundamental  $E_{\text{CRSF,F}}$  (bottom panel) and first harmonic  $E_{\text{CRSF,H}}$  (top panel) as function of the luminosity in the 3 to 79 keV energy band resulting from our orbit-by-orbit spectral analysis together with ks-integrated spectral fits from Fig. 7 in Fürst et al. (2014b). Colours and symbols as in Fig. 5.1. The solid black lines are the theoretical predictions for  $\Lambda = 1$ ,  $E_{\text{NS}} = 30$  keV and  $M_{\text{NS}} = 1.9 M_{\odot}$ . The dot-dashed lines above and below the solid lines are for  $M_{\text{NS}} = 1.7 M_{\odot}$  and  $M_{\text{NS}} = 2.1 M_{\odot}$  respectively. Figure from Diez et al. (2022).

## Critical luminosity

In order to disentangle this, we now compute the critical luminosity  $L_{\text{crit}}$  of Vela X-1. According to Eq. 32 in [Becker et al. \(2012\)](#):

$$L_{\text{crit}} = 1.49 \times 10^{37} \text{ erg s}^{-1} \left( \frac{\Lambda}{0.1} \right)^{-7/5} \omega^{-28/15} \times \left( \frac{M_{\text{NS}}}{1.4 M_{\odot}} \right)^{29/30} \left( \frac{R_{\text{NS}}}{10 \text{ km}} \right)^{1/10} \left( \frac{E_{\text{NS},n}}{n \times 11.57 \text{ keV}} \right)^{16/15}, \quad (5.4)$$

where  $\omega$  is a parameter describing the spectral shape inside the column and is equal to 1 assuming Bremsstrahlung-dominated emission in the accretion column.  $E_{\text{NS},n}$  is the surface cyclotron fundamental ( $n = 1$ ) or harmonic ( $n = 2$ ) energy of the neutron star.

Taking into account the uncertainties on the mass, we obtain  $L_{\text{crit}} \approx 1.98\text{--}2.43 \times 10^{36} \text{ erg s}^{-1}$  for Vela X-1. Following the observed range of luminosities in our data, Vela X-1 seems to belong to the supercritical sources. This goes against the expected subcritical accretion regime from the anti-correlation between the photon index and  $L$  we saw in Fig. 5.1 and the positive correlation between  $E_{\text{CRSF,H}}$  and  $L$  observed in [Fürst et al. \(2014b\)](#). To explain the discrepancies, we need to explore the uncertainties on the parameters we used.

Recent studies ([Legred et al., 2021](#)) assumed a typical neutron star radius of 12 km but this changes by only  $\sim 2\%$  the value of  $L_{\text{crit}}$ . The value of the fundamental cyclotron line at the surface of the neutron star  $E_{\text{NS},1}$  is conservative and likely to be lower than 30 keV. For  $E_{\text{NS},1} = 20 \text{ keV}$ , we have  $L_{\text{crit}} \approx 1.28\text{--}1.57 \times 10^{36} \text{ erg s}^{-1}$  thus confirming the supercritical accretion regime for Vela X-1. We considered a spherical accretion (i.e.  $\Lambda = 1$ ) to describe the geometry of the stellar wind in Vela X-1 even though there are theoretical predictions ([El Mellah et al., 2019](#)) and observational hints ([Liao et al., 2020](#)) of possible accretion disc. Moreover, the complexity of the disturbed and clumpy wind cannot be simply described by a spherical accretion case. In [Fürst et al. \(2014b\)](#), the

value of  $L_{\text{crit}}$  has been computed with  $\Lambda = 0.1$  (pure disc accretion case), which we question. Thus, the value of  $\Lambda$  is more likely to lie between 0.1 and 1. In Fig. 5.6, we show the fundamental cyclotron line energy as function of luminosity with the  $L_{\text{crit}}$  for both extreme values allowed for  $\Lambda$ . The choice of  $\Lambda$  is critical since Vela X-1 goes from being a supercritical source for the spherical wind accretion scenario to being a subcritical source in the disc accretion scenario. This may simply imply that Vela X-1 could lie between the two accretion regimes explaining discrepancies between observed behaviours corresponding to subcritical accretion regime (see Fig. 5.1) and computed critical luminosity. Moreover, direct comparisons with previous observational work has to be taken with caution since different publications use different spectral models.

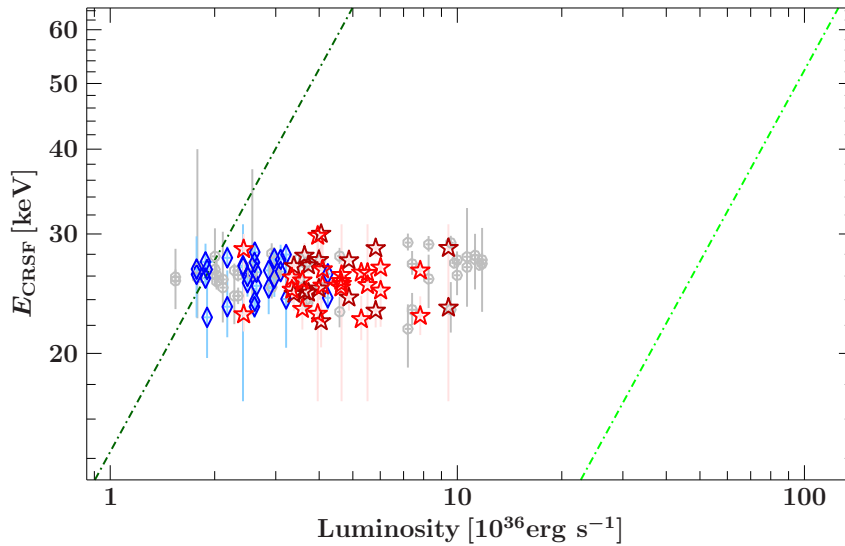


**Fig. 5.6:** Fundamental cyclotron line energy as function of luminosity in the 3–79 keV range. The energy of the harmonic line has been divided by a factor of two. The dot-dashed lines show the critical luminosity for different values of  $E_{\text{NS},1}$  with  $M_{\text{NS}} = 1.9 M_{\odot}$  and  $R_{\text{NS}} = 10$  km. Dark green is for  $\Lambda = 1$  (spherical accretion geometry) and light green is for  $\Lambda = 0.1$  (disc accretion geometry).

## 5.2 Variable absorber

In this Section, we focus on the absorption variability and the stellar wind structure in Vela X-1. In particular, the observation II was simultaneously covered by *XMM-Newton* (see Fig. 4.1) enabling us to perform a high-resolution spectroscopic study of

the stellar wind at low-energies combining the good constraints on the high-energy continuum derived from our *NuSTAR* analysis, whose results were described in the previous section.

## 5.2.1 Large-scale changes

### Onset of the wakes

In Fig. 5.7, we present the *XMM-Newton* EPIC-pn hardness ratios between different energy bands calculated as  $HR = (\text{Hard} - \text{Soft})/(\text{Hard} + \text{Soft})$  for observation II. We can observe a gradual increase of the hardness ratios between the soft 3–6 keV and the hard 8–10 keV bands starting from  $\phi_{\text{orb}} \approx 0.44$  happening simultaneously with a gradual increase of the absorption column density of the stellar wind  $N_{\text{H},1}$  (see Fig. 5.8). Indeed, as described in Sect. 1.3.4, the X-ray absorption from the stellar wind mainly impacts the soft photons. Thus, as  $N_{\text{H},1}$  increases (resp. decreases), the spectral shape will become harder (resp. softer)

The rise of  $N_{\text{H},1}$  at  $\phi_{\text{orb}} \approx 0.44$  appears at the moment where the wakes are intercepting our line of sight (see Fig. 4.1). This result is the direct measurement of the onset of the wakes in Vela X-1, which we are able to trace for the first time with high time-resolution.  $N_{\text{H},1}$  variations on shorter time-scales will be discussed in Sect. 5.2.2.

The hardness ratios between the highest energy bands on the last panel of Fig. 5.7 is constant implying a stable behaviour of the continuum emission from the neutron star as observed in [Martínez-Núñez et al. \(2014\)](#). This implies that observed variations in the spectral shape of Vela X-1 are due to variations in the wind and not from the X-ray source itself.

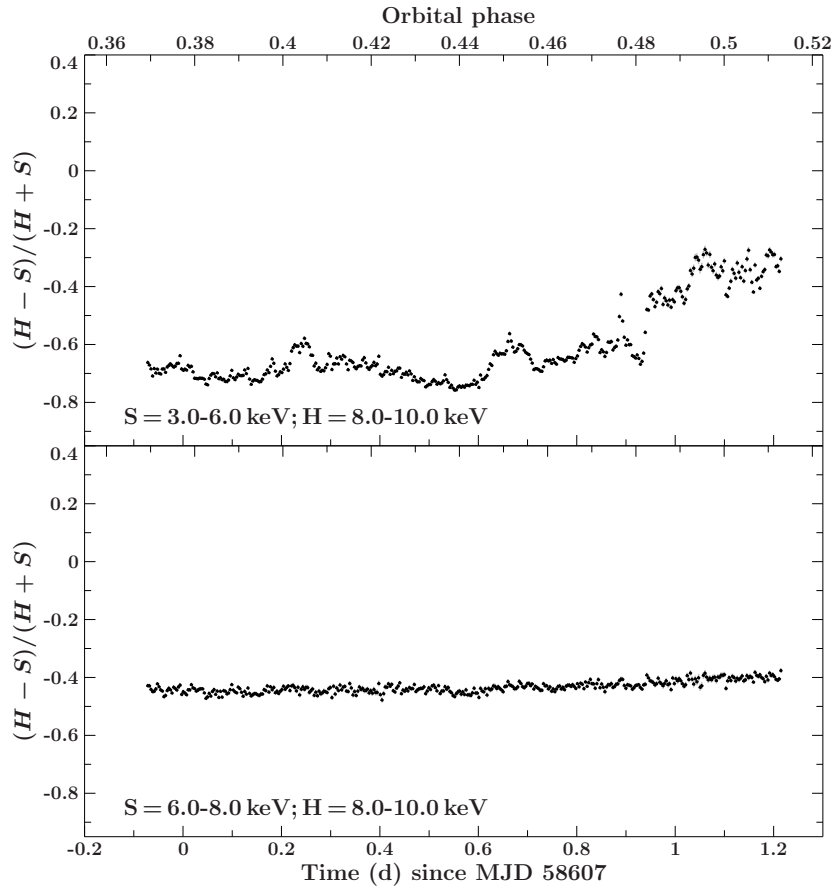


**Fig. 5.7:** Hardness ratios between the mentioned energy bands for observation II with *XMM-Newton* EPIC-pn as function of time (or orbital phase). The time resolution is one pulse period (283.44 sec). Figure from [Diez et al. \(2023\)](#).

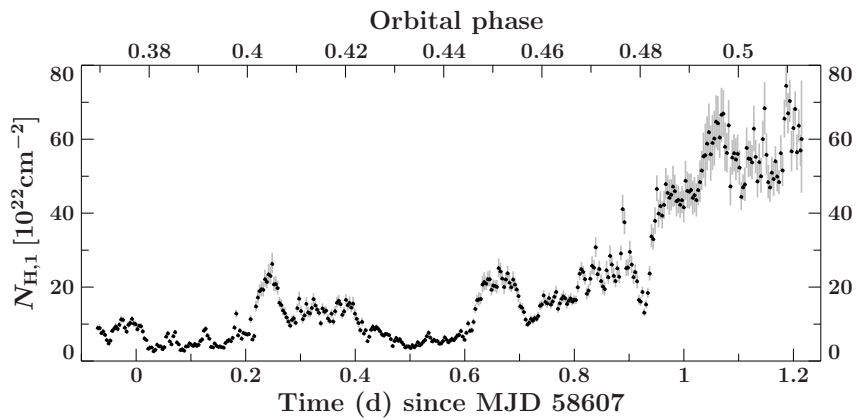


**Fig. 5.8:** Absorption column density of the stellar wind from our pulse-by-pulse analysis of observation II with *XMM-Newton* as function of time (or orbital phase). Figure from [Diez et al. \(2023\)](#).



## Partial coverer

The so-called colour-colour diagram is another tool for the description of the stellar wind absorption variability. In Fig. 5.9, we present the colour-colour diagram of observation II with the bands A (0.5–3 keV), B (3–6 keV) and C (6–10 keV).

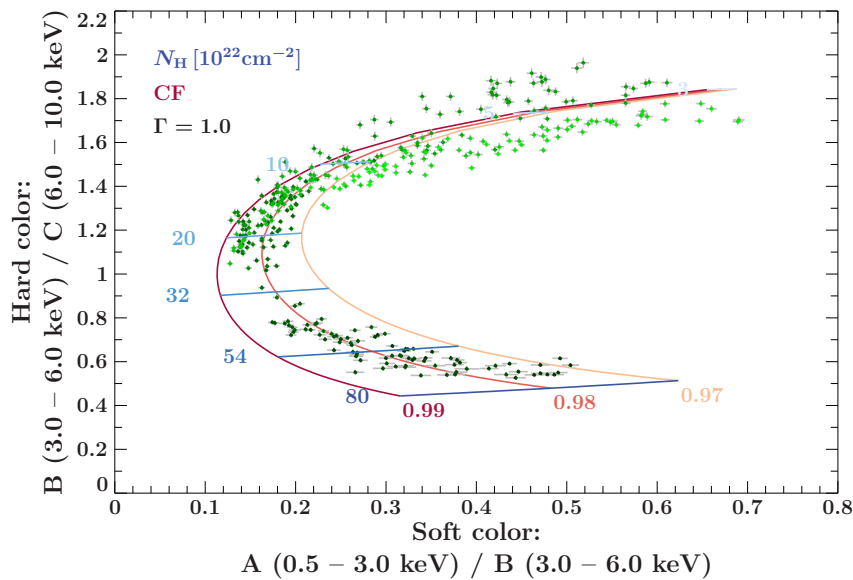


**Fig. 5.9:** Colour-colour diagram of observation II with *XMM-Newton* EPIC-pn. Data points represent the ratio of the light curves in the hard colour depending on the ratio of light curves in the soft colour, from the beginning (light green) to the end (dark green) of the observation. Theoretical expectations for different CF (shades of red) with varying  $N_{H,1}$  (shades of blue) using the partial covering model from Eq. 4.1 are shown. Figure from Diez et al. (2023).

It shows a typical "nose-shape" characteristic of a presence of a partial coverer with variable column density (e.g. Hirsch et al., 2019; Grinberg et al., 2020, in Cyg X-1). The source evolves along the track with time (transition from light green to dark green data points) as expected from the geometrical onset of the wakes. To explain the nose-shape, we show in Fig. 5.10 the impact of varying absorption on the observed spectrum modelled by Eq. 4.1.

Looking at Fig. 5.10, if the coverer fully occults the continuum emitted by the neutron star (CF = 1, dashed lines), both A/B and B/C decrease as  $N_{H,1}$  grows (i.e. as the green data points get darker on Fig. 5.9) since photoabsorption influences the soft energy bands. If the source is partially covered by the absorber (CF < 1, solid lines), the flux in

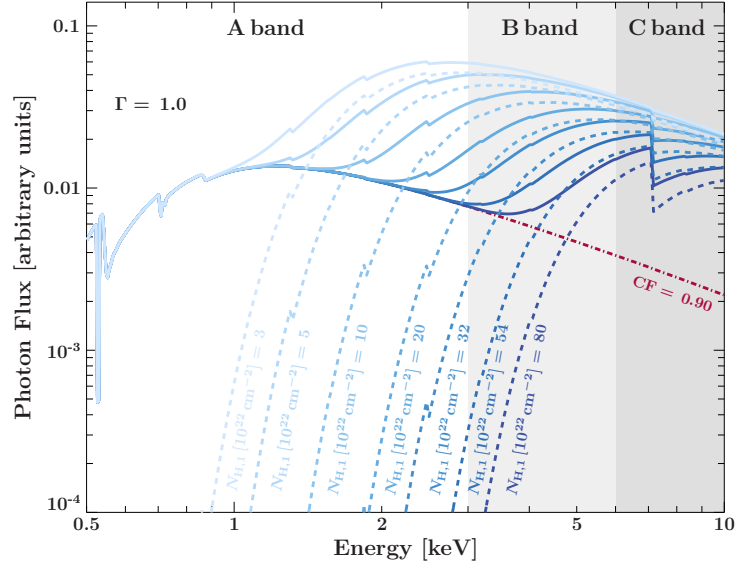


**Fig. 5.10:** Effect of increasing  $N_{\text{H},1}$  on the continuum shape assuming  $\text{CF} = 0.9$ . The shaded grey areas indicate the three energy bands of interest: A (0.5–3 keV), B (3–6 keV) and C (6–10 keV). The resulting observed spectrum (solid lines) is the sum of the uncovered spectrum (dash-dotted line) and the covered spectrum (dashed lines). See Fig. 4.2 for a sketch of the partial covering model. Figure from Diez et al. (2023).

the A band remains constant as  $N_{\text{H},1}$  grows after a certain threshold. For  $\text{CF} = 0.9$ , the threshold is located at  $N_{\text{H},1} = 54 \times 10^{22} \text{ cm}^{-2}$ . However, the fluxes in the B and C bands decrease as  $N_{\text{H},1}$  grows causing the soft colour to become softer as the harder colour does not change. This overall leads to the observed nose-shape in the colour-colour diagram in Fig. 5.9. It directly shows the necessity of using a partial covering model to describe the data.

We also simulate a grid of colour-colour tracks for varying  $N_{\text{H},1}$  and  $\text{CF}$  in Fig. 5.9. Simulations show that the data are well described by high values of  $\text{CF}$  and  $3 \times 10^{22} \text{ cm}^{-2} \lesssim N_{\text{H},1} \lesssim 80 \times 10^{22} \text{ cm}^{-2}$ . This is in agreement with our measurements of  $N_{\text{H},1}$  (Fig. 5.8) and  $\text{CF}$  (Fig. 5.11). The high values of  $\text{CF}$  together with the rise of the  $N_{\text{H},1}$  highlight the presence of a large and thick absorber, identified as the accretion and ionisation wakes, located between the neutron star and the observer.

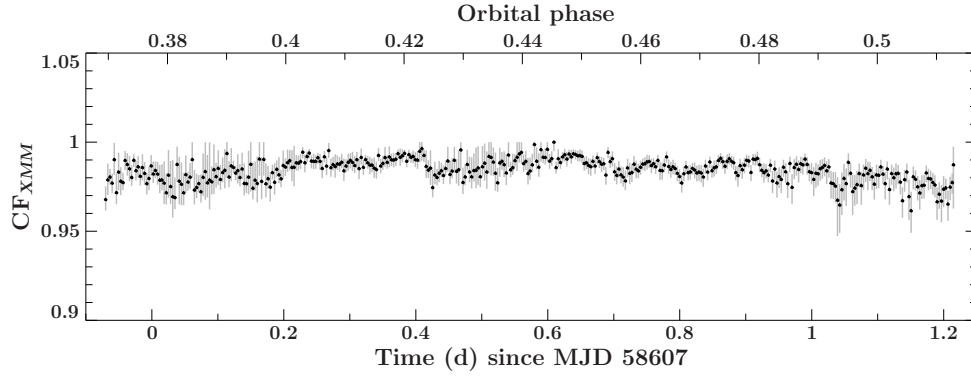


**Fig. 5.11:** Covering fraction from our pulse-by-pulse analysis of observation II with *XMM-Newton* as function of time (or orbital phase). Figure from [Diez et al. \(2023\)](#).

### Comparison with previous observations

Many authors have measured absorption variability with different instruments at different times and orbital phases (see [Kretschmar et al., 2021](#), for an overview). However, studies rarely cover wide orbital phase ranges thus leaving the possibility to mix variability within an individual binary orbit with orbit-to-orbit variations in the structure of the wind. In Fig. 5.12, we compare past  $N_{\text{H},1}$  values with the new ones from this work, accounting for differences in orbital phase definitions with original publications. We can observe a similar rise of  $N_{\text{H},1}$  in past studies although not at the same orbital phase than our observation. This may indicate that the onset of the wakes is not stable in orbital phase. This rise of  $N_{\text{H},1}$  lasts  $\sim 0.02$  in orbital phase which is approximately as long as the rise in  $N_{\text{H},1}$  observed by [Ohashi et al. \(1984\)](#) with *Tenma*. This suggests that similar large-scale structures in the wind may exist between those observations but would have different relative orientation.

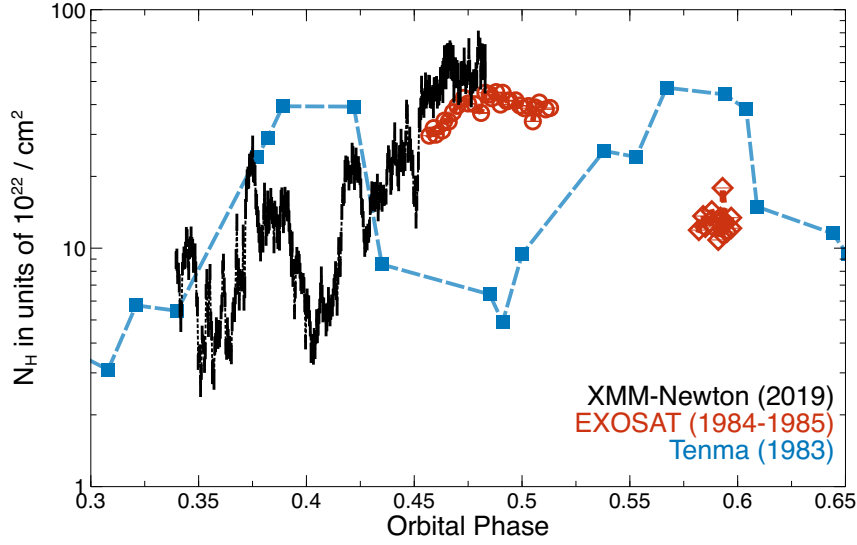


**Fig. 5.12:** Comparison of the *XMM-Newton* EPIC-pn  $N_{\text{H},1}$  values derived for observation II with historical measurements taken during individual binary orbits by *Tenma* (Ohashi et al., 1984) and *EXOSAT* (Haberl & White, 1990). Figure from Diez et al. (2023).

## 5.2.2 Small-scale changes

### Clumpiness of the wind

The hardness ratio of observation II between the softest band (0.5–3 keV) and the hardest band (8–10 keV) in the second panel of Fig. 5.13 appears as a reversed version of the light curve presented in the first panel of the same figure. This is to say that low-states (or at least non-flaring periods) correspond to a hardening of the underlying spectral shape. Simultaneously, local maxima of  $N_{\text{H},1}$  also happen at  $\phi_{\text{orb}} \approx 0.40$ ,  $\phi_{\text{orb}} \approx 0.44$  and  $\phi_{\text{orb}} \approx 0.49$  (see Fig. 5.8). This could be explained by the passage of unaccreted clumps across our line of sight causing absorption of soft photons (i.e. a major contribution of harder photons) as observed in Grinberg et al. (2017) and seen in simulations from El Mellah et al. (2020).

Reciprocally, during flaring periods at  $\phi_{\text{orb}} \approx 0.38$  and  $\phi_{\text{orb}} \approx 0.43$ , the hardness ratio decreases drastically indicating a softening of the underlying spectrum and therefore a major contribution of soft photons. These flaring events also coincide with low  $N_{\text{H},1}$  (see Fig. 5.8), possibly implying accretion of clumps by the neutron star. Indeed, accreted

clumps lead to low  $N_{\text{H},1}$  integrated on our line of sight and expressed through the overall accretion column (see e.g. Fürst et al., 2010; Martínez-Núñez et al., 2014). Clump accretion results in enhanced luminosity as seen in Sect. 1.3.3 due to more efficient Compton up-scattering of cyclotron and bremsstrahlung photons, thus higher X-ray production. Although X-ray flares may be triggered by accretion of clumps, hydrodynamic simulations from El Mellah et al. (2018) showed that the mass of a single clump is likely not enough to trigger a large flare. To establish a correlation between flares and clumpiness of the wind, it is crucial to better understand the entire accretion mechanisms, spanning from the orbital level to the accretion columns scale, which produce a majority of the observed X-rays.

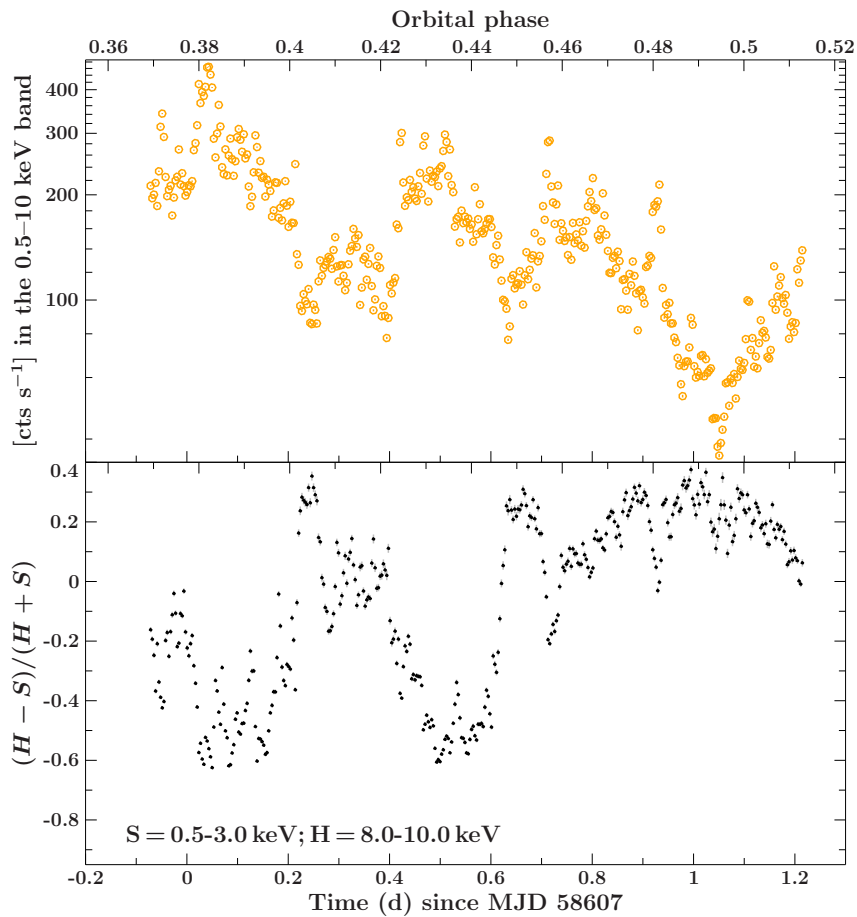


**Fig. 5.13:** Light curve in the 0.5–10 keV band (top panel) and hardness ratio between the 0.5–3 keV and 8–10 keV energy bands of observation II with *XMM-Newton* EPIC-pn as function of time (or orbital phase). The time resolution is one pulse period (283.44 sec). Figure from Diez et al. (2023).

To explore further hints of clumps in the stellar wind of Vela X-1, we explored the dependency between  $N_{\text{H},1}$  and the covering fraction CF. In Fig. 5.14, we can observe a positive correlation for early (in time or in orbital phase) data points in observation II. According to Fig. 4.1, this coincides with the moment when the wakes are starting to enter our line of sight. This positive correlation is well described by accumulation of clumps in the vicinity of the neutron star thus enlarging the amount of material (increase of  $N_{\text{H},1}$ ) and obscuring our line of sight (increase of CF). On the contrary, a negative correlation is observed between those two parameters for later orbital phases in the observation. Due to the geometry and the position of the wakes at late orbital phases for observation II, this could be caused by overlapping of clumps decreasing the CF but increasing  $N_{\text{H},1}$  due to accumulation of material on the integrated line of sight.

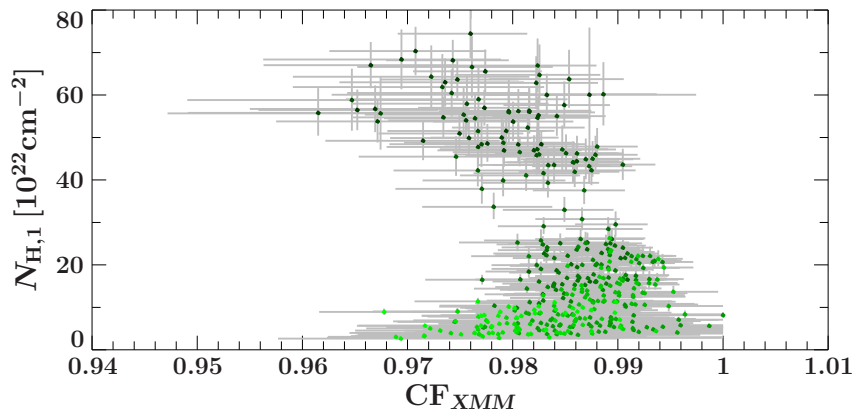


**Fig. 5.14:** Absorption column density  $N_{\text{H},1}$  as function of the covering fraction from our pulse-by-pulse analysis of observation II with *XMM-Newton*, from the beginning (light green) to the end (dark green) of the observation.

### Origin and nature of the absorber

Thanks to the low-energy coverage permitted by *XMM-Newton*, we now have access to a plethora of new soft lines below 4 keV that were not resolved with *NuSTAR* alone. We show in Fig. 5.15 and list in Table 5.1 all the soft lines identified in observation II with *XMM-Newton* EPIC-pn together with a comparison with previous studies and theoretical values. We are also able to resolve the Fe  $K\beta$  line from the Fe  $K\alpha$  line at 7.1 keV and 6.4 keV respectively.

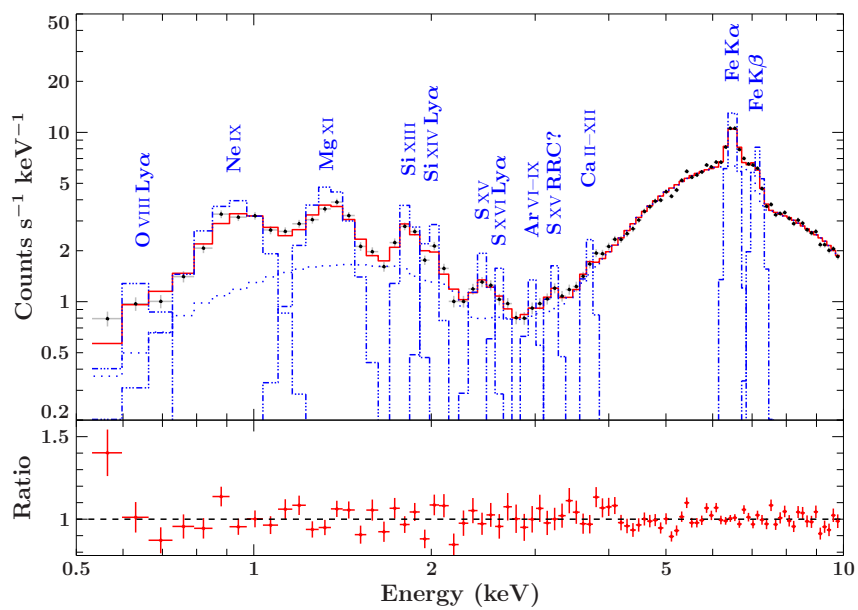


**Fig. 5.15:** Example of a *XMM-Newton* EPIC-pn spectrum (black data points) taken at the most absorbed *NuSTAR*-orbit of observation II. We indicate the individual detected line complexes by blue dot-dashed Gaussians and the absorbed continuum with the blue dotted line. Figure from [Diez et al. \(2023\)](#).

**Tab. 5.1:** Details of soft emission lines between 0.5 keV and 4 keV. Table from [Diez et al. \(2023\)](#).

Line	Detected energy from previous work (keV)	Reference energy (keV)	Identified energy for this work (keV)
O VIII Ly $\alpha$	$0.6538^{+0.0005}_{-0.0011}$ <sup>(a)</sup>	0.6541 <sup>(c)</sup>	$0.6211^{+0.0130}_{-0.0011}$
Ne IX (f, i, r)	$0.90460 \pm 0.00033/0.91454 \pm 0.00034/0.92154 \pm 0.00034$ <sup>(b)</sup>	0.905/0.915/0.922 <sup>(c)</sup>	$0.928^{+0.011}_{-0.012}$
Ne X Ly $\alpha$	$1.02130^{+0.00015}_{-0.00014}$ <sup>(b)</sup>	1.02196 <sup>(d)</sup>	1.02130 (fixed)
Mg XI (f, i, r)	$1.3305 \pm 0.0002/1.3426^{+0.0003}_{-0.0002}/1.3517^{+0.0002}_{-0.0003}$ <sup>(b)</sup>	1.3311/1.3431/1.3522 <sup>(c)</sup>	$1.338^{+0.012}_{-0.019}$
Mg XII Ly $\alpha$	$1.4720 \pm 0.0002$ <sup>(b)</sup>	1.4723 <sup>(d)</sup>	1.4720 (fixed)
Si XIII (f, i, r)	$1.8388 \pm 0.0002/1.8536 \pm 0.0002/1.8643 \pm 0.0002$ <sup>(b)</sup>	1.8382/1.8530/1.8648 <sup>(e)</sup>	$1.823^{+0.014}_{-0.013}$
Si XIV Ly $\alpha$	$2.0049 \pm 0.0003$ <sup>(b)</sup>	2.0056 <sup>(f)</sup>	2.0049 (fixed)
S XV (f, i, r)	$2.4287^{+0.0007}_{-0.0008}/2.4463^{+0.0007}_{-0.0009}/2.4590^{+0.0006}_{-0.0009}$ <sup>(b)</sup>	2.4291/2.4463/2.4606 <sup>(e)</sup>	$2.439^{+0.029}_{-0.027}$
S XVI Ly $\alpha$	$2.6207^{+0.0016}_{-0.0017}$ <sup>(b)</sup>	2.6196 <sup>(f)</sup>	2.6207 (fixed)
Ar VI–IX	$2.9661^{+0.0043}_{-0.0099}$ <sup>(g)</sup>	2.9619 – 2.9675 <sup>(h)</sup>	2.9661 (fixed)
S XV RRC?		3.224 <sup>(c)</sup>	$3.23^{+0.04}_{-0.06}$
Ca II–XII K $\alpha$	$3.6905^{+0.0022}_{-0.0009}$ <sup>(i)</sup>	3.6911 – 3.7110 <sup>(h)</sup>	$3.822^{+0.019}_{-0.102}$

(f, i, r): Referring to forbidden, intercombination and resonance lines respectively. The f, i and r lines due to the fine structure of the atom cannot be resolved with *XMM-Newton* EPIC-pn.

(fixed): to previous detected energies.

Note: To convert from Å in previous works to keV, we compute  $E[\text{keV}] = hc \div \lambda[\text{Å}]$  where  $hc = 12.39842$  (with values for  $h$ ,  $c$  and  $e$  from CODATA 2018, [Tiesinga et al. 2021](#)) and round to relevant significant digits.

<sup>(a)</sup> [Lomaeva et al. \(2020\)](#), <sup>(b)</sup> [Amato et al. \(2021\)](#), <sup>(c)</sup> [Drake \(1988\)](#), <sup>(d)</sup> [Erickson \(1977\)](#), <sup>(e)</sup> [Hell et al. \(2016\)](#), <sup>(f)</sup> [Garcia & Mack \(1965\)](#), <sup>(g)</sup> [Schulz et al. \(2002\)](#), <sup>(h)</sup> [House \(1969\)](#), <sup>(i)</sup> [Watanabe et al. \(2006\)](#)



The Ne IX, Mg XI, Si XIII and S XV are ions with only two remaining electrons on their orbital (He-like ions). The presence of those ions in the spectrum of Vela X-1 shows a strong photoionisation of the wind, further confirmed by the presence of the even more ionised He-like ions O VIII, Ne X, Mg XII, Si XIV and S XVI. The coexistence of both H-/He-like ions with fluorescent emission lines of near-neutral ions (Fe  $K\alpha$  and Fe  $K\beta$ ) can be explained by a warm photoionised wind and smaller cooler gas regions such as clumps as stated by [Grinberg et al. \(2017\)](#) and [Amato et al. \(2021\)](#). According to ([Watanabe et al., 2006](#)), the fluorescent lines are more a result of either the reflection of the stellar photosphere in the extended stellar wind or the accretion wake. They also observed brighter X-ray line emissions at  $\phi_{\text{orb}} \approx 0.5$  than during the eclipse indicating a highly ionised region located between the neutron star and its massive stellar companion that is occulted during the eclipse.

The detected soft emission lines are only visible during the second half of observation II, i.e. starting from  $\phi_{\text{orb}} \approx 0.44$ . Once the neutron star passed this orbital phase, the absorption column density of the stellar wind  $N_{\text{H},1}$  increases (as seen previously in Fig. 5.8) revealing soft emission lines in the extracted spectra of Vela X-1. Those lines appear to be even stronger during late orbital phases as visible in Fig. 5.16 showing line fluxes as function of time. Indeed, we can notice an increase of the Ne IX and S XV line fluxes (among others) towards late orbital phases (and high  $N_{\text{H},1} \gtrsim 50 \times 10^{22} \text{ cm}^{-2}$ ) while they were mostly consistent with 0 before  $\phi_{\text{orb}} \approx 0.44$ .

The apparition of those lines during heavy absorption suggests that they originate from a large scale in the system as seen in [Watanabe et al. \(2006\)](#). Indeed, if they would originate from the vicinity of the neutron star, they should be obscured during heavy absorption by the presence of the local absorber (particularly at  $\phi_{\text{orb}} > 0.44$ ). [Sako et al. \(1999\)](#) with ASCA and [Schulz et al. \(2002\)](#) with *Chandra*/HETGS observed soft emission lines even during eclipse, i.e. when the neutron star and its absorber are outside our line of sight. Hence, lines originate from a larger scale in the wind which we identify to be the ionisation wake. The presence of clumps partially obscuring our line of sight would also allow for partial visibility of lines even during high absorption, as suggested by the negative correlation between  $N_{\text{H},1}$  and CF during late orbital phases in Fig. 5.14.

The Fe  $K\alpha$  and Fe  $K\beta$  line fluxes also show a drastic increase towards late orbital phases. Moreover, they are positive throughout the whole observation. Past studies have also shown the presence of the Fe  $K\alpha$  and Fe  $K\beta$  lines at various orbital phases ( $\phi_{\text{orb}} \approx 0.25$  in Goldstein et al., 2004; Watanabe et al., 2006; Grinberg et al., 2017,  $\phi_{\text{orb}} \approx 0.75$  in Amato et al., 2021; Fürst et al., 2014b; Diez et al., 2022, eclipse in Sato et al., 1986; Sako et al., 1999; Schulz et al., 2002; Watanabe et al., 2006), thus implying that they can be detected at any orbital phase. This is again another observational hint for the presence of the ionisation wake in the stellar wind of the Vela X-1 system.

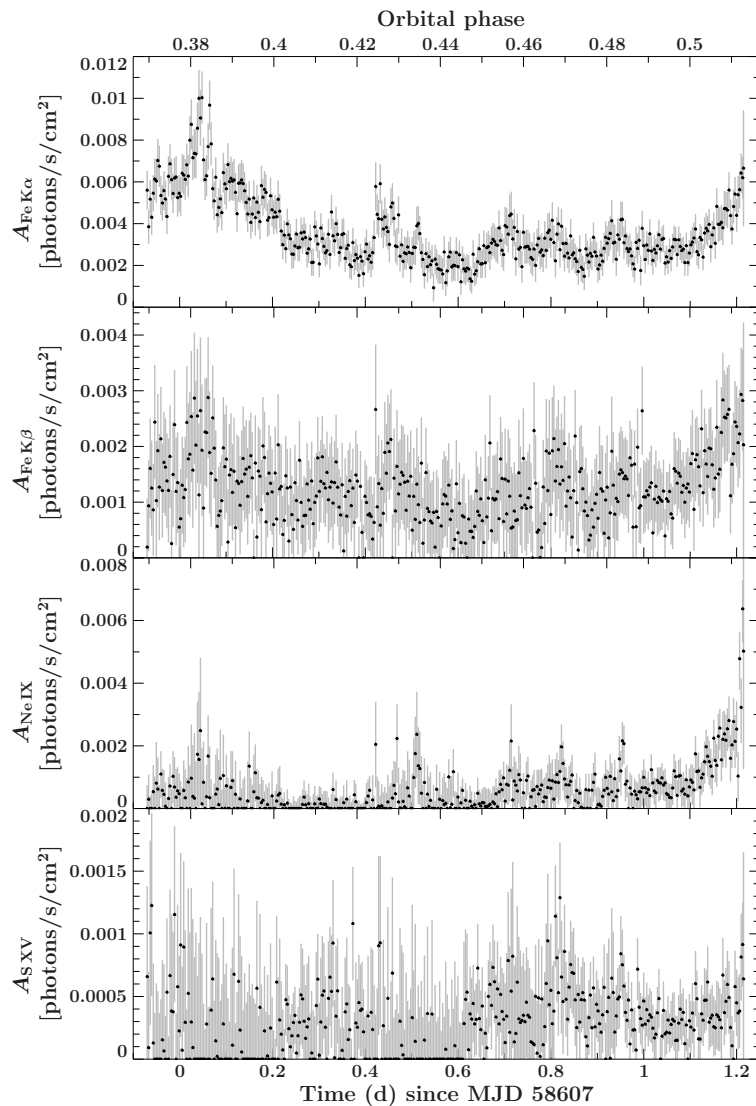


**Fig. 5.16:** Fluxes of some soft lines obtained from the pulse-by-pulse analysis of observation II as function of time (with corresponding orbital phase). From top to bottom: flux of the Fe  $K\alpha$ , Fe  $K\beta$ , Ne IX and S XV line. Figure from Diez et al. (2023).

## Conclusion & Outlook

We analysed new observations of Vela X-1 taken at different orbital phases with *NuSTAR* and *XMM-Newton* thus probing a different line of sight of the system on a wide X-ray energy band. By combining both datasets, the potential degeneracy between the power law slope and absorption strength in our partial covering is minimised. The *NuSTAR* data play a crucial role at high absorption since it is challenging to constrain the continuum with *XMM-Newton* only. Reciprocally, the low-energy coverage and high resolution of the EPIC-pn detector on board *XMM-Newton* revealed the local structure and variability of the wind which is not permitted by *NuSTAR* only.

We have confirmed the anti-correlation of the photon index with flux. However, we strongly question the suggested subcritical accretion regime for Vela X-1 since the expected positive correlation between the energy of the harmonic cyclotron line with flux could not be observed in our data. Moreover, theoretical predictions for the calculation of the critical luminosity are based on inevitable simple and fixed geometries and would require further theoretical exploration of height-scaling of the line forming region.

Our results show the passage of dense and extended wakes when the neutron star is close to inferior conjunction characterised by a strong increase of the stellar wind absorption column density  $N_{\text{H},1}$ . This is the first time that we are able to trace the onset of the wakes with such high-time resolution, i.e. down to the pulse period of the neutron star ( $\sim 283$  s) in this study. Local variability of  $N_{\text{H},1}$ , covering fraction and flux has been associated to accretion, passage and/or overlapping of clumps on our line of sight.




We performed the X-ray photography of the stellar wind in Vela X-1 through high-resolution spectroscopy. The evidence of highly ionised atoms such as Ly $\alpha$  lines of O, Ne, Mg, Si and S suggests a strong photoionisation of the wind. Furthermore, we interpreted the coexistence of highly ionised atoms with near-neutral ions together with the anti-correlation of the folding energy with flux at different absorption phases as

changes in temperature of the plasma. This could be caused respectively by the presence of colder gas regions (clumps) in the photoionised plasma and more efficient Compton down-scattering of high-energy via electron recoil.

Nonetheless, those results have to be considered with caution since the EPIC-pn resolution did not permit to distinguish between individual line contribution in a broad Gaussian line-complex and blending with neighbouring atoms can happen. This aspect was beyond the scope of this thesis but future work on the simultaneous available *XMM-Newton* RGS data would disentangle this. Finally, analyses on a sample of HMXBs together with simulations of *Athena* ([Barret et al., 2023](#)) and *XRISM* ([XRISM Science Team, 2020](#)) data would be beneficial for such high-resolution studies.

# Appendix

# Continuum, cyclotron line, and absorption variability in the high-mass X-ray binary Vela X-1

C. M. Diez<sup>1</sup>, V. Grinberg<sup>2,1</sup>, F. Fürst<sup>3</sup>, E. Sokolova-Lapa<sup>4,5</sup>, A. Santangelo<sup>1</sup>, J. Wilms<sup>4</sup>, K. Pottschmidt<sup>6,7</sup>, S. Martínez-Núñez<sup>8</sup>, C. Malacaria<sup>9</sup>, and P. Kretschmar<sup>10</sup>

<sup>1</sup> Institut für Astronomie und Astrophysik, Universität Tübingen, Sand 1, 72076 Tübingen, Germany  
e-mail: [diez@astro.uni-tuebingen.de](mailto:diez@astro.uni-tuebingen.de)

<sup>2</sup> European Space Agency (ESA), European Space Research and Technology Centre (ESTEC), Keplerlaan 1, 2201 AZ Noordwijk, The Netherlands

<sup>3</sup> Quasar Science Resources S.L for European Space Agency (ESA), European Space Astronomy Centre (ESAC), Camino Bajo del Castillo s/n, 28692 Villanueva de la Cañada, Madrid, Spain

<sup>4</sup> Dr. Karl Remeis Sternwarte & Erlangen Centre for Astroparticle Physics, Friedrich-Alexander-Universität Erlangen-Nürnberg, Sternwartstr. 7, 96049 Bamberg, Germany

<sup>5</sup> Sternberg Astronomical Institute, M. V. Lomonosov Moscow State University, Universitetskij pr., 13, Moscow 119992, Russia

<sup>6</sup> CRESST, Department of Physics, and Center for Space Science and Technology, UMBC, Baltimore, MD 21250, USA

<sup>7</sup> NASA Goddard Space Flight Center, Astrophysics Science Division, Greenbelt, MD 20771, USA

<sup>8</sup> Instituto de Física de Cantabria (CSIC-Universidad de Cantabria), 39005 Santander, Spain

<sup>9</sup> Universities Space Research Association, Science and Technology Institute, 320 Sparkman Drive, Huntsville, AL 35805, USA

<sup>10</sup> European Space Agency (ESA), European Space Astronomy Centre (ESAC), Camino Bajo del Castillo s/n, 28692 Villanueva de la Cañada, Madrid, Spain

Received 9 July 2021 / Accepted 23 December 2021

## ABSTRACT

Because of its complex clumpy wind, prominent cyclotron resonant scattering features, intrinsic variability, and convenient physical parameters (close distance, high inclination, and small orbital separation), which facilitate the observation and analysis of the system, Vela X-1 is one of the key systems for understanding accretion processes in high-mass X-ray binaries on all scales. We revisit Vela X-1 with two new observations taken with *NuSTAR* at orbital phases  $\sim 0.68$ – $0.78$  and  $\sim 0.36$ – $0.52$ , which show a plethora of variability and allow us to study the accretion geometry and stellar wind properties of the system. We follow the evolution of spectral parameters down to the pulse period timescale using a partially covered power law continuum with a Fermi-Dirac cutoff to model the continuum and local absorption. We are able to confirm anti-correlations between the photon index and the luminosity and, for low fluxes, between the folding energy and the luminosity, implying a change of properties in the Comptonising plasma. We were not able to confirm a previously seen correlation between the cyclotron line energy and the luminosity of the source in the overall observation, but we observed a drop in the cyclotron line energy following a strong flare. We see strong variability in absorption between the two observations and within one observation (for the  $\sim 0.36$ – $0.52$  orbital phases) that can be explained by the presence of a large-scale structure, such as accretion and photoionisation wakes in the system, and our variable line of sight through this structure.

**Key words.** stars: neutron – X-rays: binaries – stars: winds, outflows – accretion, accretion disks

## 1. Introduction

Vela X-1 is an eclipsing high-mass X-ray binary (HMXB) that consists of a B0.5 Ib supergiant, HD 77581 (Hiltner et al. 1972), and an accreting neutron star with a pulse period of  $\sim 283$  s (McClintock et al. 1976) in an  $\sim 8.964$  d orbit around this supergiant (Kreykenbohm et al. 2008). A thorough review of the Vela X-1 system is given by Kretschmar et al. (2021), who also discussed the role of this system in understanding HMXB systems in general. Here, we limit ourselves to points that are of immediate relevance for this work. The radius of HD 77581 is  $30 R_{\odot}$  and the orbital separation  $\sim 1.7 R_{*}$  (van Kerkwijk et al. 1995; Quaintrell et al. 2003). The neutron star is thus embedded in the dense wind of the supergiant companion, which has a mass loss rate of  $\sim 10^{-6} M_{\odot} \text{ yr}^{-1}$  (Watanabe et al. 2006). The source is located at  $1.99^{+0.13}_{-0.11}$  kpc (Kretschmar et al. 2021) and is therefore one of the brightest persistent point sources in the X-ray sky despite a moderate mean luminosity of  $5 \times 10^{36} \text{ erg s}^{-1}$

(Fürst et al. 2010). The mass of the neutron star is estimated to be  $\sim 1.7$ – $2.1 M_{\odot}$  (Kretschmar et al. 2021).

The system is highly inclined ( $>73^{\circ}$ ; van Kerkwijk et al. 1995), which facilitates the study of the accretion and wind physical properties through observations at different orbital phases (e.g., Haberl & White 1990; Goldstein et al. 2004; Watanabe et al. 2006; Fürst et al. 2010). Doroshenko et al. (2013) showed a systematic change in the absorption along the orbit when averaged among multiple orbits: in particular, average absorption decreased after the eclipse, reached a minimum at the orbital phase of  $\phi_{\text{orb}} \approx 0.3$ , and grew afterwards, with a strong increase around  $\phi_{\text{orb}} \approx 0.5$ . However, measurements of absorption at the same orbital phase are often different during different orbits of the system (Kretschmar et al. 2021). Fürst et al. (2010) also found deviations from a log-normal distribution in the histogram of the orbital phase averaged brightness distribution of Vela X-1 that could be due to the complex and turbulent accretion geometry of the system.

The overall large-scale wind structure in Vela X-1 has been investigated in different publications over the years. [Odaka et al. \(2013\)](#) interpreted the strong changes in absorption of Vela X-1 on short timescales observed with Suzaku as being due to the compact object's motion in the supersonic stellar wind forming a bow shock. [Eadie et al. \(1975\)](#) suggested an accretion wake in Vela X-1 based on the absorption dips that appeared in the light curve of the Ariel V Sky Survey Experiment. Accretion and photoionisation wakes, and possibly a tidal stream, have also been suggested as causes (see e.g., [Nagase et al. 1983](#); [Sato et al. 1986](#); [Blondin et al. 1990](#); [Kaper et al. 1994](#); [van Loon et al. 2001](#); [Malacaria et al. 2016](#)).

An accretion wake forms through the focussing of the stellar wind due to the influence of the gravitational field of the neutron star, leading to an unsteady bow shock in the vicinity of the neutron star ([Blondin et al. 1991](#); [Manousakis & Walter 2015](#); [Malacaria et al. 2016](#)). A photoionisation wake is formed when the wind interacts with the Strömgen sphere, which is created around the neutron star because of the photoionisation of the wind material (see Fig. 2 in [Watanabe et al. 2006](#)).

Hydrodynamical simulations optimised for Vela X-1 have been conducted in [Blondin et al. \(1990\)](#) and [Manousakis \(2011\)](#), who showed the formation of the wakes and an overall complex large-scale structure in the wind. [Grinberg et al. \(2017\)](#) illustrated the accretion and photoionisation wakes in the Vela X-1 system in their Fig. 1 based on the simulations published in [Manousakis \(2011\)](#).

Even beyond the variable absorption, Vela X-1 is known to be an intrinsically highly variable source. It has shown bright flares ([Martínez-Núñez et al. 2014](#); [Kreykenbohm et al. 2008](#); [Lomaeva et al. 2020](#)) and off-states ([Kreykenbohm et al. 2008](#); [Doroshenko et al. 2011](#)) where the observed flux decreased to less than 10% of its normal value ([Kreykenbohm et al. 2008](#); [Sidoli et al. 2015](#)).

The off-states have been interpreted in the context of a highly structured wind of the companion by some authors ([Kreykenbohm et al. 2008](#); [Ducci et al. 2009](#); [Fürst et al. 2010](#)). For [Manousakis & Walter \(2015\)](#), hydrodynamic instabilities are sufficient to explain the origin of the off-states without the need for intrinsic inhomogeneities in the stellar wind. Another theory to explain the origin of the off-states in Vela X-1 is the interaction of the neutron star's magnetosphere with the plasma ([Doroshenko et al. 2011](#)). Beyond the off-states, variations in the mass-accretion rate that lead to the observed flares and the variable absorption require, at least to some degree, a clumpy structure of the wind ([Kreykenbohm et al. 2008](#); [Fürst et al. 2010](#); [Martínez-Núñez et al. 2014](#)).

Vela X-1 shows various features in its X-ray spectrum that are typical for accreting neutron stars. One such feature is a prominent fluorescent emission line associated with FeK $\alpha$  around 6.4 keV, which was first reported in [Becker et al. \(1978\)](#). Some previous analyses with high resolution instruments (e.g., [Watanabe et al. 2006](#)) have also detected FeK $\beta$ , while others, at different orbital phases, struggled to constrain this feature ([Amato et al. 2021](#)). [Watanabe et al. \(2006\)](#) stated there are three possible explanations for the presence of these lines in Vela X-1: the extended stellar wind, reflection off the stellar photosphere, and the accretion wake. Another observed line-like feature in the spectrum of X-ray pulsars is the so-called 10 keV feature. The physical origin of this feature is still unknown ([Coburn et al. 2002](#)), which may be due to our incomplete understanding of the continuum spectrum; it is usually modelled with simple phenomenological models. It appears to be an inherent feature in the spectra of accreting pulsars ([Coburn et al. 2002](#))

and probably reflects the limitations of the simple phenomenological models used ([Staubert et al. 2019](#)). It may appear in emission in some sources, such as 4U 0115+63 ([Ferrigno et al. 2009](#); [Müller et al. 2013](#)) and EXO 2030+375 ([Klochkov et al. 2007](#)). It is then modelled with a broad Gaussian emission component and is often referred to as the '10 keV bump' model ([Reig & Nespoli 2013](#)). In other sources, it has been found in absorption, such as in XTE J0658-073 ([McBride et al. 2006](#); [Nespoli et al. 2012](#)), Cen X-3 ([Santangelo et al. 1998](#)), or Vela X-1 ([Fürst et al. 2014b](#)), and modelled with a broad Gaussian absorption component ([Fürst et al. 2014b](#)). In 4U 1901+03 ([Reig & Milonaki 2016](#)) and KS 1947+300 ([Fürst et al. 2014a](#)), similar features have been interpreted as being of possible magnetic origin.

Cyclotron resonant scattering features (CRSFs, or cyclotron lines) appear as broad absorption lines in the X-ray spectra of highly magnetised neutron stars whose magnetic field strength can be then directly measured from the CRSF energy. The fundamental CRSF is the result of resonant scattering of photons by electrons in strong magnetic fields from the ground level to the first excited Landau level followed by radiative decay (see [Staubert et al. 2019](#), and references therein, for a review). At higher excited Landau levels, the resulting CRSFs are called harmonics. The spectrum of Vela X-1 has been confirmed to show two CRSFs ([Kreykenbohm et al. 2002](#)): a prominent harmonic line at  $\sim 55$  keV and a weaker fundamental at  $\sim 25$  keV ([Kendziorra et al. 1992](#); [Kretschmar et al. 1997](#); [Orlandini et al. 1998](#); [Kreykenbohm et al. 1999, 2002](#); [Fürst et al. 2014b](#)). In Vela X-1, the harmonic line is broader and deeper than the fundamental line, which can be so weak that it cannot be significantly detected in some observations ([Odaka et al. 2013](#)). The study of the CRSF energy variability with luminosity is important for determining the physical properties of the source (see Sect. 6.1.2).

In several accreting X-ray pulsars, it was observed that the correlation of the CRSF energy with the luminosity and the correlation of the photon index with luminosity were inverse to each other, that is, if one was positive, the other was negative (e.g., [Klochkov et al. 2011](#), for a sample study). There are theoretical expectations for a correlation between the CRSF energy and luminosity.

Following [Becker et al. \(2012\)](#), the variation in the CRSF energy with luminosity is due to the variation in the emission height within the accretion column that characterises the line-forming region. They define a source as being in the supercritical accretion regime when the radiation field has a dynamic effect on the infalling plasma. In this regime, the accretion flow is decelerated in the extended radiative shock, the height of which increases with the mass-accretion rate. It can move the line-forming region away from the surface of the neutron star to the higher altitudes corresponding to the lower magnetic field, though not necessarily up to the shock height (see e.g., [Nishimura 2014](#)). This can explain the negative correlation of the CRSF centroid energy with luminosity. An alternative model has been suggested by [Poutanen et al. \(2013\)](#) based on the reflection of the radiation from the neutron star surface at different altitudes. The so-called critical luminosity,  $L_{\text{crit}}$ , is associated with the transition from the negative correlation of the CRSF energy and luminosity to the positive one. It is understood that in the subcritical regime (the X-ray luminosity  $L_X < L_{\text{crit}}$ ), the role of the radiation in the stopping of the accretion flow becomes negligible. There are several mechanisms proposed to explain the matter deceleration in the subcritical regime that can also explain the observed positive correlation of the CRSF energy with the

**Table 1.** Observation details.

Name	Obs ID	Time start MJD (day) binarycor	Time stop MJD (day) binarycor	Exposure (ks)	Orbital phase (with $T_{90}$ )	Orbital phase (with $T_{ecl}$ )
Obs I	90402339002	58493.1813	58494.0910	36.086	0.68–0.78	0.65–0.75
Obs II	30501003002	58606.8688	58608.2465	40.562	0.36–0.52	0.34–0.49
<i>Obs IIa</i>	<i>30501003002</i>	<i>58606.8688</i>	<i>58607.5660</i>	<i>22.557</i>	<i>0.36–0.44</i>	<i>0.34–0.42</i>
<i>Obs IIb</i>	<i>30501003002</i>	<i>58607.7625</i>	<i>58608.2465</i>	<i>18.005</i>	<i>0.46–0.52</i>	<i>0.44–0.49</i>

**Notes.** As observation II is divided into two parts, observations IIa and IIb, for the analysis, we list the details for both sub-observations above.

luminosity. The matter can be fully decelerated (i.e. stopped) by Coulomb collisions in the accretion channel. The height at which the effective stopping occurs decreases with the increasing luminosity (Staubert et al. 2007; Becker et al. 2012), causing the positive correlation. Another scenario (Mushtukov et al. 2015b) suggests that the shift in the CRSF energy to lower values with the decreasing luminosity can also be explained by the Doppler effect in the accretion channel moderated by the luminosity-dependent velocity profile. Another possibility at low mass-accretion rates is the origination of the collisionless shock above the surface (Langer & Rappaport 1982). The height of this shock decreases with increasing mass-accretion rate (Shapiro & Salpeter 1975), thus moving the line-forming region closer to the surface of the neutron star and resulting in the positive correlation of the CRSF energy and luminosity (Rothschild et al. 2017; Vybornov et al. 2017).

The value  $L_{crit}$ , corresponding to the transition between the subcritical and supercritical regimes, is dependent on the magnetic field of the source and the geometry of the accretion channel. The analytical expressions were obtained, for example, by Basko & Sunyaev (1976) and Becker et al. (2012) under different considerations. The critical luminosity was calculated numerically as a function of the magnetic field of the neutron star for different types of accretion (disc or wind) by Mushtukov et al. (2015a), taking the resonance in the Compton scattering cross-sections and the possible mixture of polarisation modes into account. It was shown that the critical luminosity is not a monotonic function of the magnetic field strength.

For Vela X-1, a tentative detection of such a correlation between CRSF energy and luminosity has been presented in Fürst et al. (2014b). It was also found that  $\Gamma$  was anti-correlated with the luminosity (e.g., Odaka et al. 2013; Fürst et al. 2014b), indicating that the source was in a subcritical accretion regime, behaving similarly to sources such as Her X-1 (Staubert et al. 2007) and GX 304–1 (Yamamoto et al. 2011).

Given the importance of Vela X-1 for the study of wind-accreting neutron stars, we use two further observations with *NuSTAR*, taken at different orbital phases of the source, to map the accretion environment and the structure of the stellar wind in the source and to further investigate possible correlations of the CRSF with other spectral parameters. First, we describe the two datasets and the analysis software used in Sect. 2. We then present the light curves and timing results of those observations in Sect. 3. We proceed to time-averaged spectroscopy in Sect. 4 and to time-resolved spectroscopy in Sect. 5. We discuss the results in Sect. 6, focussing on the wind structure and the CRSFs, and give a summary and an outlook in Sect. 7.

## 2. Observation and data reduction

*NuSTAR* (Harrison et al. 2013) observed Vela X-1 on 10–11 January 2019 and on 3–5 May 2019 as science target using the

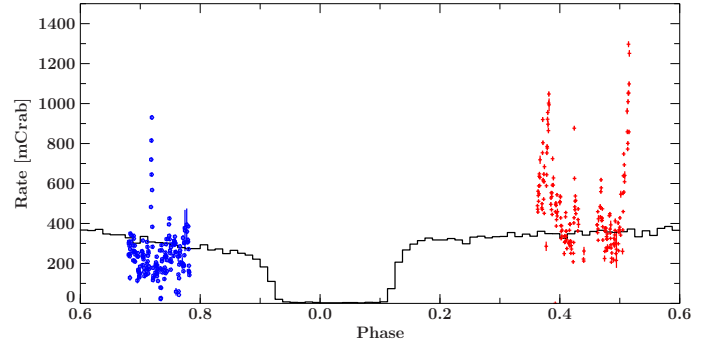


**Fig. 1.** *NuSTAR* 3–79 keV flux for observation I (blue) in January 2019 and observation II in May 2019 (red) with a time resolution of  $P_I = 283.4532$  s and  $P_{II} = 283.4447$  s, respectively, and *Swift*/BAT 15–50 keV flux averaged over all data since 2005 (solid black line) plotted over the neutron star’s orbital phase, where  $\phi_{orb} = 0$  is defined with  $T_{90}$ .

focal plane modules A and B (FPMA and FPMB). We then have two datasets with an exposure of  $\sim 36$  ks and  $\sim 40$  ks, referred as observation I and observation II, respectively. Details about the observations are given in Table 1 and Fig. 1 shows the count rate of the Vela X-1 system against the orbital phase. As can be seen from Fig. 1, observation II consists of two parts. The interruption is due to data loss caused by problems with the ground station and the corresponding data cannot be recovered. This sketch also includes the *Swift*/BAT 15–50 keV light curve averaged over all data since 2005 and therefore representing the averaged behaviour of the source smoothing out the variability on shorter timescales (Fürst et al. 2010; Kretschmar et al. 2021). The eclipse is clearly visible around  $\phi_{orb} = 0$ .

The orbital phases  $\phi_{orb}$  are derived from the ephemeris from Kreykenbohm et al. (2008) and Bildsten et al. (1997) (see Table 2). Several definitions of the time of phase zero can be found in the literature. The most common are  $T_{ecl}$  and  $T_{90}$ .  $T_{ecl}$  is the mid-eclipse time whereas  $T_{90}$  is the time when the mean longitude  $l$  is equal to  $90^\circ$ . For the particular case of Vela X-1, those two points are very close to each other, the difference is of the order of  $\Delta\phi \approx 0.02$ . Nonetheless, in soft X-rays the eclipse boundaries can be hard to define and considering that the orbit is elliptical, defining  $T_{ecl}$  is not always that clean. Explanations on how to convert  $T_{90}$  to  $T_{ecl}$  can be found in Kreykenbohm et al. (2008). In this work, we exclusively use  $T_{90}$ .

The two observations are carried out at different orbital phases. At the orbital phase of observation I that is at  $\phi_{orb} \approx 0.75$ , the accretion and photoionisation wakes are placed along the line of sight of the observer (see Fig. 1 in Grinberg et al. 2017). Thus, a different behaviour of the absorption is expected compared to observation II at  $\phi_{orb} \approx 0.4–0.5$ , where the wakes may be starting to pass through the observer’s line of sight.



**Table 2.** Ephemeris used.

References	Orbital parameter	Value	Units
<a href="#">Kreykenbohm et al. (2008)</a>	Time of mean longitude equal to $\pi/2$ ( $T_{90}$ )	$52974.001 \pm 0.012$	MJD (day)
<a href="#">Kreykenbohm et al. (2008)</a>	Mid-eclipse time ( $T_{\text{ecl}}$ )	$52974.227 \pm 0.007$	MJD (day)
<a href="#">Kreykenbohm et al. (2008)</a>	Orbital period ( $P_{\text{orb}}$ )	$8.964357 \pm 0.000029$	day
<a href="#">Bildsten et al. (1997)</a>	Semi-major axis ( $a \sin i$ )	$113.89 \pm 0.13$	lt-sec
<a href="#">Bildsten et al. (1997)</a>	Eccentricity ( $e$ )	$0.0898 \pm 0.0012$	
<a href="#">Bildsten et al. (1997)</a>	Longitude of periastron ( $\omega$ )	$152.59 \pm 0.92$	
<a href="#">van Kerkwijk et al. (1995)</a>	Inclination ( $i$ )	$>73$	°

We use the NUSTARDAS pipeline v2.0.0 and HEASOFT v6.28 with *NuSTAR* CALDB (calibration database) v20200826 applied with the clock correction to extract spectra and light curves for the time-averaged observations and we also proceed to extract spectra orbit-by-orbit and pulse-by-pulse, necessary for a time-resolved analysis of this highly variable source (see Sect. 5). For the orbit-by-orbit spectroscopy, we extract a spectrum for each *NuSTAR* orbit around the Earth. That leads to 14 spectra for observation I and 19 spectra for observation II. For the pulse-by-pulse spectroscopy, we extract a spectrum for each rotation of the neutron star, with the corresponding integration pulse period derived for this observation (see Sect. 3). That leads to 168 spectra for observation I and 209 spectra for observation II. The event times are barycentred using the `barycorr` tool from NUSTARDAS pipeline and corrected for the binary orbit using the ephemeris from Table 2. We use the Interactive Spectral Interpretation System (ISIS) v1.6.2-47 ([Houck & Denicola 2000](#)) to analyse the data and note that ISIS allows access to XSPEC ([Arnaud 1996](#)) models that are referenced later in the text.

We extracted source spectra from a region with a radius of  $\sim 82$  arcsec for observation I and  $\sim 67$  arcsec for observation II around Vela X-1's FK5 coordinates, separately for FPMA and FPMB. As Vela X-1 is very bright, it illuminates the whole focal plane, and we thus extract background spectra circular regions with  $\sim 63$  arcsec radius for observation I and  $\sim 67$  arcsec radius for observation II as far away from the source as possible for both observations to minimise source influence on background estimation. Since the background changes over the field-of-view of the instrument, systematic uncertainties are formally introduced by this method. Vela X-1, however, is about a factor of 5 brighter than the background even at the highest energies used here, such that the effect of residual uncertainties is negligible.

Due to a thermal blanket tear, the detector focal plane module FPMA requires a low energy effective area correction ([Madsen et al. 2020](#)). Such a correction is automatically applied in all *NuSTAR* CALDB releases starting with the 20200429 CALDB. However, for some sources the automatic procedure results in an over-correction. This is the case for our observation II, where the automatic procedure results in stark differences between the focal plane modules. After consulting with the *NuSTAR* calibration team (K. Madsen, priv. comm.), it was decided that the best approach was to revert to the old FPMA ARF<sup>1</sup> for this observation, which results in an agreement between the modules.

All spectra were re-binned within ISIS to a minimal signal to noise of 5, adding at least 2, 3, 5, 8, 16, 18, 48, 72, and 48 channels for energies between 3.0–10, 10–15, 15–20, 20–35, 35–45,

45–55, 55–65, 65–76, and 76–79 keV, respectively. Uncertainties are given at the 90% confidence ( $\Delta\chi^2 = 2.7$  for one parameter of interest), unless otherwise noted.

### 3. Light curves and timing

#### 3.1. Pulse period

The pulse period of Vela X-1 shows strong variations on all timescales mainly due to a highly variable accretion rate. It varies in a way mostly consistent with random-walk ([de Kool & Anzer 1993](#)). To measure this period accurately to do the pulse-by-pulse analysis in Sect. 5, we perform epoch-folding ([Leahy 1987](#)) on the FPMA extracted light curve with 1 sec binning. A pulse period of  $P_{\text{I}} = 283.4532 \pm 0.0008$  s for observation I and of  $P_{\text{II}} = 283.4447 \pm 0.0004$  s for observation II are found, which is consistent with the overall pulse period history of Vela X-1 from *Fermi* Gamma-ray Burst Monitor<sup>2</sup>. The pulse period changes by such a small fraction ( $\pm \sim 0.06\%$  at most) within one observation that it is not enough to induce significant shifts in the pulse phase in the pulse-by-pulse analysis. The uncertainties were estimated using a Monte Carlo simulation ([Larsen & Monakhov 1996](#)) with 2000 runs.

#### 3.2. Light curves

Vela X-1 is known to be a highly variable source, and thus we present the light curves of observations I and II in the top panels of Fig. 2 to investigate the relevant features. We bin the light curves to the spin period of the neutron star to avoid the intra-pulse variability.

In observation I, at  $T_{\text{obs}} \approx 58493.53$  MJD, we can observe a large flare indicated in the left upper panel of Fig. 2 where the source flux increases to  $\sim 200$  counts  $\text{s}^{-1}$  per module, from an average of  $\sim 60$  counts  $\text{s}^{-1}$  during the whole observation. Moreover, two off-states are detected at  $T_{\text{obs}} \approx 58493.66$  MJD and  $T_{\text{obs}} \approx 58493.93$  MJD. Here, the source flux drops to  $\sim 6$ – $7$  counts  $\text{s}^{-1}$  for the first off-state and  $\sim 10$  counts  $\text{s}^{-1}$  for the second one.

In observation II, the average source flux is  $\sim 118$  counts  $\text{s}^{-1}$  about twice as much as during observation I. At  $T_{\text{obs}} \approx 58606.95$  MJD,  $T_{\text{obs}} \approx 58607.03$  MJD,  $T_{\text{obs}} \approx 58607.42$  MJD and  $T_{\text{obs}} \approx 58608.23$  MJD four major flares indicated in the right upper panel of Fig. 2 are detected reaching  $\sim 220$  counts  $\text{s}^{-1}$ ,  $\sim 275$  counts  $\text{s}^{-1}$ ,  $\sim 228$  counts  $\text{s}^{-1}$  and  $\sim 238$  counts  $\text{s}^{-1}$ , respectively. However, this time no off-state is detected. The big gap in observation II between  $T_{\text{obs}} \approx 58607.57$  MJD and  $T_{\text{obs}} \approx 58607.76$  MJD is due to the loss of data.

<sup>1</sup> [https://nustarsoc.caltech.edu/NuSTAR\\_Public/NuSTARoperationSite/ml1.php](https://nustarsoc.caltech.edu/NuSTAR_Public/NuSTARoperationSite/ml1.php)

<sup>2</sup> <https://gamma-ray.nsstc.nasa.gov/gbm/science/pulsars/lightcurves/velax1.html>

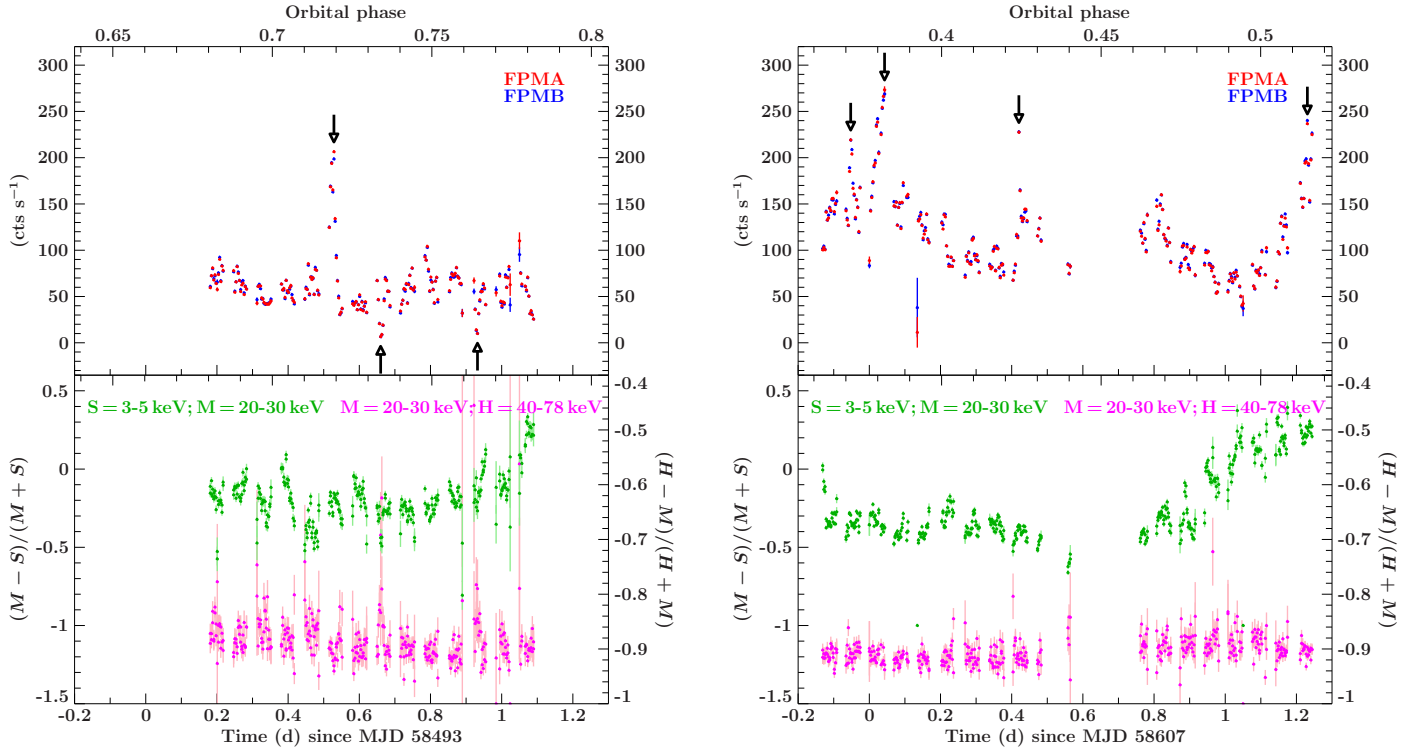


**Fig. 2.** Light curves and hardness ratios for observations I (*left panel*) and II (*right panel*) with a time resolution of  $P_I = 283.4532$  s and  $P_{II} = 283.4447$  s, respectively. Major off-states and major flares are indicated by arrows. Green points show the hardness ratio between the 3–5 keV and the 20–30 keV bands using the left-hand y axis. Magenta points show the hardness ratio between the 20–30 keV and the 40–78 keV bands using the right-hand y axis.

### 3.3. Hardness ratios

In the bottom panels of Fig. 2, we present the hardness ratios calculated as  $HR = (\text{Medium} - \text{Soft})/(\text{Medium} + \text{Soft})$  (left-hand y axis) and  $HR = (\text{Hard} - \text{Medium})/(\text{Hard} + \text{Medium})$  (right-hand y axis) with three different energy bands. The low-energy ratio (in green) covers the energy region where most of the absorption from the stellar wind happens, and thus, we tried to compare it to the high-energy ratio (in magenta), which is less impacted by the effect of the stellar wind absorption and instead more representative of the true underlying continuum shape.

In observation II, we observe that the 3–5 keV to 20–30 keV hardness behaves differently before and after the data loss period: it is roughly constant before and rising after, while the 20–30 keV to 40–78 keV hardness shows no such trends. This motivated us to divide observation II into two parts to be analysed separately: observation IIa and observation IIb, which correspond to the data before and after the loss, respectively (details can be found in Table 1). Moreover, the time-averaged modelling of the spectrum of observation II leads to a bad description of the data, supporting the choice of a separate analysis (see Sect. 4).

In observation I, there are two changes, at  $T_{\text{obs}} \approx 58493.67$  MJD and  $T_{\text{obs}} \approx 58493.92$  MJD, that correspond to the location of the two off-states. However, there is no change associated with the flare in any of both hardness ratios. This has already been observed in the flares analysed in Kreykenbohm et al. (2008) or Fürst et al. (2014b). The spectrum becomes slightly harder in the low-energy ratio towards the end of the observation, but the hardness shows no other strong overall trends.

In observation II, the high-energy hardness ratio shows the exact same behaviour than during observation I. However, this

time we do not see any strong change as no off-state was observed during this observation. Again, no significant change in both hardness ratios is shown at the location of the flares. The spectrum in the low-energy ratio remains roughly flat for the first part of the observation but becomes suddenly harder starting from  $T_{\text{obs}} \approx 58607.75$  MJD, which corresponds to the end of the period where the data were lost.

The changes in the hardness ratios observed during the off-states and the time variability of Vela X-1 during observations I and II require a spectral analysis of the source on shorter timescales. To achieve this goal, we start by analysing the spectra averaged over the three effective observations (Obs I, Obs IIa, and Obs IIb) as a basis for the further analysis (Sect. 4). We then continue analysing the orbit-by-orbit spectra to have a first overview of the evolution of various spectral parameters over time and use these values as inputs for the pulse-by-pulse spectroscopy. Both analyses are detailed in Sect. 5. This step-by-step time-resolved spectral analysis allows us to have a fine adjustment of the parameters and a follow-up of the parameters along the time at each step of the analysis. Finally, the obtained results are discussed in Sect. 6.

## 4. Time-averaged spectroscopy

### 4.1. Choice of continuum model

We first address the choice of the overall continuum model. Different flavours of power law models with high energy cutoffs are used in the literature to empirically describe the continuum spectral shape of accreting neutron stars (e.g., Staubert et al. 2019).

The Fermi-Dirac cutoff (FDcut; Tanaka 1986) is the most widely used continuum model for Vela X-1 (see

Kreykenbohm et al. 1999, 2008; Fürst et al. 2014b). Thus, we used a power law with the photon index  $\Gamma$  and FDCut with the cutoff energy  $E_{\text{cut}}$  and the folding energy  $E_{\text{fold}}$  so that

$$F(E) \propto E^{-\Gamma} \times \left(1 + \exp\left(\frac{E - E_{\text{cut}}}{E_{\text{fold}}}\right)\right)^{-1}. \quad (1)$$

In this model, we constrain  $E_{\text{fold}}$  and  $E_{\text{cut}}$  to 4–18 keV and 18–40 keV, respectively, to avoid model degeneracies. With this model, we are able to achieve a good description of the data (see Sect. 4.2 for an in-depth discussion).

We also investigated several other models to fit all our observations. The same trends have been observed for all of them, but for simplicity we only quote the values for observation I below. The best-fit parameters for the time-averaged tested models can be found in Tables A.1 and A.2.

We attempt to describe the data with a `highcut`<sup>3</sup> model, another often used model for the continuum in accreting neutron stars (Santangelo et al. 1998; Staubert et al. 2019). It results in a statistically worse description of the data than the FDCut model.

We also used the NPEX (Mihara 1995) model for the continuum. This model consists of the sum of a negative and a positive power law, which is then modified by an exponential cutoff that is characterised by a folding energy. This model has previously been used for a number of HMXBs (see e.g., Hemphill et al. 2014; Jaisawal & Naik 2016). We explored the NPEX with the 10 keV feature parameter space (see Sect. 4.2 for a more detailed discussion about the modelling of the 10 keV feature). The combination of two power laws with wide allowed ranges of indices makes the analysis difficult and provides several combinations of good fits. If the positive power law is fixed to 2, the function is known to be a good approximation of the unsaturated Comptonisation spectrum in neutron stars (Makishima et al. 1999; Odaka et al. 2013; Hemphill et al. 2014). This results in a good fit ( $\chi^2/\text{d.o.f.} \approx 604.15/456$ ), with both power law components of NPEX contributing to the continuum, but both CRSFs are very broad and deep (see Sect. 4.2 for a more detailed discussion about the modelling of the CRSFs), in particular the strength of the harmonic CRSF reaches  $83 \pm 10$ , effectively altering the continuum. Moreover, the norm of the positive power law index was found close to 0, approaching a single power law with a high energy cutoff. While statistically satisfactory, this model is thus not a good description of the data (see e.g., Bissinger né Kühnel et al. 2020, for discussion of similar problems for a different HMXB). We also explore the NPEX without the 10 keV feature parameter space but it also results in a bad description of the continuum modelled by a too deep harmonic CRSF.

We further explore a Comptonisation continuum, using a single `compTT` (Titarchuk 1994) in a spherical accretion case as done previously in Maitra & Paul (2013) for Vela X-1. This results in a statistically good description of the data for both with and without 10 keV feature cases, but the overly strong CRSFs again effectively alter the continuum. A double `compTT` model has been recently proposed for several X-ray pulsars (see e.g., Doroshenko et al. 2012; Tsygankov et al. 2019), albeit for the low luminosity regime below Vela X-1's luminosity. We also explore this double `compTT` model without the 10 keV feature, as it should in theory get rid of the absorption feature observed in the 10 keV range. We obtain a good fit ( $\chi^2/\text{d.o.f.}$  is 622.53/456, slightly larger but similar to the FDCut best-fit) where the parameters can be constrained and the CRSFs behave as expected (if

both  $T_0$  are tied and allowed to vary up to 1 keV, otherwise if they are free to vary in a wider range of values then the CRSFs become very strong again), showing around the same values as our FDCut best-fit model. However, the behaviour of the Comptonisation components does not agree with expectations from previous applications of this model and defies previous physical interpretation. Tsygankov et al. (2019), who introduced this model for the low luminosity state of GX 304-1, discuss that the components are likely to be independent. In particular, the low-energy component ( $kT \lesssim 2$  keV) can be explained as radiation from hotspots at the neutron star's surface heated up by the accretion process. However, in our analysis, this component is much hotter, with  $kT \approx 6.9$  keV. Additionally, in the low luminosity case, the two Comptonisation continua are of equal strength, while in our model the hotter component dominates the overall flux and spectral shape.

Overall, we conclude that the FDCut model offers the best empirical description of the continuum that we can obtain. Since it also allows us direct comparison with previous results, especially Fürst et al. (2014b) because different continua may lead to shifts in derived CRSF positions (e.g., Müller et al. 2013), we decide to adopt it for further modelling.

## 4.2. Modelling

We introduced a floating cross-normalisation parameter,  $C_{\text{FPMB}}$ , in order to give the relative normalisation between *NuSTAR*'s two detectors: FPMA and FPMB.

We try modelling the fluorescent emission lines features associated with  $\text{FeK}\alpha$  and  $\text{FeK}\beta$  with narrow Gaussian components. The  $\text{FeK}\beta$  line cannot be constrained because of the limited energy resolution of *NuSTAR* and the overlapping Fe K-edge at 7.1 keV. Thus we only include the  $\text{FeK}\alpha$  line around 6.4 keV in our final model.

For our analysis, we modelled the CRSFs using two multiplicative Gaussian absorption lines (`gabs` in XSPEC<sup>3</sup>) corresponding to the fundamental CRSF (CRSF,F) and to the harmonic CRSF (CRSF,H) with

$$\text{CRSF}(E) = \exp\left[-\left(\frac{d}{\sigma\sqrt{2\pi}}\right)\exp\left[-0.5\left(\frac{E - E_{\text{cyc}}}{\sigma}\right)^2\right]\right], \quad (2)$$

where  $d$  is the line depth and  $\sigma$  the line width.

We described the 10 keV feature with a broad Gaussian line in absorption, as also done in Fürst et al. (2014b). We first tried to describe the spectrum without this feature. However, the analysis leads to visible residuals in absorption in the 10 keV region for observation IIa and a bad description of the overall continuum, which is compensated for by deeper and broader CRSFs that effectively alter the continuum for all observations. We therefore conclude that the feature is necessary for a good description of our data. The physical origin of this 10 keV feature is unclear. The 10 keV feature in absorption has been found in other sources (McBride et al. 2006; Nespoli et al. 2012; Santangelo et al. 1998) and only sometimes tentatively associated with a CRSF (Reig & Milonaki 2016; Fürst et al. 2014a). In Vela X-1, it has so far never been interpreted as a CRSF, although we cannot definitely exclude such an origin currently.

We further had to constrain the width of the fundamental line, setting it ad hoc to  $\sigma_{\text{CRSF,F}} = 0.5 \times \sigma_{\text{CRSF,H}}$ , following previous work (Fürst et al. 2014b). This value is based on the fact that the width of the CRSF is dominated by thermal broadening, for which  $\sigma/E$  is independent of energy (Schwarm et al. 2017). As  $E_{\text{CRSF,F}}/E_{\text{CRSF,H}}$  is roughly 0.5, we used 0.5 for the width

<sup>3</sup> <https://heasarc.gsfc.nasa.gov/xanadu/xspec/manual/node129.html>

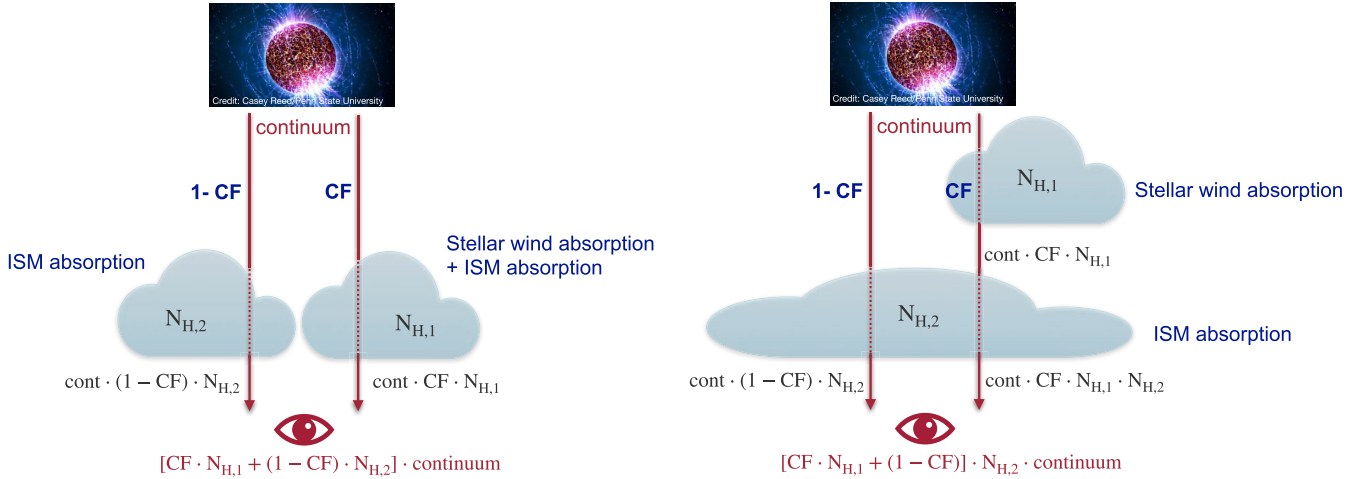


**Fig. 3.** Comparison of the partial covering model from Fürst et al. (2014b) (left side) and the partial covering model from this work (right side). The continuum corresponds to  $(F(E) \times \text{CRSF}, F \times \text{CRSF}, H + \text{FeK}\alpha + 10 \text{ keV})$  in both cases.

ratio as well. Letting the width free results in an overly wide fundamental CRSF that effectively describes the continuum in the 10–30 keV range. We do, however, verify that when the line width is free, the best-fit CRSF energies, especially for the harmonic line, do not change significantly. Further, freezing the line width to a slightly larger value does not change the resulting best fit significantly. However, much narrower fundamental line (0.2 of the harmonic) leads to an increase in the reduced chi-square ( $\chi^2/\text{d.o.f.} \approx 716.96/456$  for observation I) explained by a too narrow fundamental line shifting down the line energy of  $\sim 1$  keV.

To describe the different absorption components surrounding the neutron star, we use the `tbabs` model (Wilms et al. 2000) and the corresponding abundances and cross-sections (Verner et al. 1996). We first try a single-absorption model but the spectrum is not well described at low energies, as can be seen on the example of observation I (Fig. 4c). This can be understood as a high contribution of the absorption from the stellar wind at low energies. Therefore, we use a partial covering model with the covering fraction  $CF$  to take into account the clumpy structure of the stellar wind. The allowed values for  $CF$  range between 0 and 1. Different setups of a partial covering model or equivalent models have previously been shown to be necessary to describe the spectrum of Vela X-1 well (e.g., Martínez-Núñez et al. 2014; Fürst et al. 2014b; Malacaria et al. 2016).

Therefore, our final and best-fit model can be written as

$$I(E) = (CF \times N_{H,1} + (1 - CF)) \times N_{H,2} \times (F(E) \times \text{CRSF}, F \times \text{CRSF}, H + \text{FeK}\alpha + 10 \text{ keV}). \quad (3)$$

This partial covering model is equivalent to the partial covering model used in Fürst et al. (2014b) and allows for an easier comparison of the spectral parameters. The only difference lies in the description of the absorption components (see Fig. 3) that are differently parametrised between the two models. In Fürst et al. (2014b), they split the absorption component into two absorption columns: one corresponding to the absorption from the interstellar medium and the other one corresponding to both the absorption from the interstellar medium and from the stellar wind. In this work, we used two distinct absorption columns to describe the stellar wind and the absorption from the interstellar medium in order to have access to both parameters separately.

The absorption  $N_{H,1}$  corresponding to the stellar wind embedding the neutron star is free and the absorption from the interstellar medium  $N_{H,2}$  has been fixed to  $3.71 \times 10^{21} \text{ cm}^{-2}$  based

on NASA’s HEASARC  $N_H$  tool website<sup>4</sup> (HI4PI Collaboration 2016). We also tested to leave  $N_{H,2}$  as free parameter of the fit. For observation I, we obtain a high upper limit, consistent with the fixed value. For both parts of observation II, we obtain higher values that also lead to a systematic decrease in the photon index  $\Gamma$ . Given that *NuSTAR* does not cover the range below 3 keV, it is challenging to constrain low values of  $N_{H,2}$ , especially for a partial coverer. We thus decide to fix the  $N_{H,2}$  to the theoretical galactic column density value for the following analysis.

We first show the contribution from the broad line components in Figs. 4 and 5. We observe a broad, strong contribution of the harmonic CRSF at around 54 keV and a much weaker fundamental CRSF at  $\sim 25$  keV (residual panel b), as commonly found for this source (Kreykenbohm et al. 2002; Fürst et al. 2014b). There is also a visible contribution of the 10 keV feature (residual panel c).

The best-fit parameters for the three observations are presented in Table 3. There is an increase in the stellar wind absorption  $N_{H,1}$  between observations IIa and IIb together with an increase in the covering fraction  $CF$ . Even though the energy of the fundamental CRSF  $E_{\text{CRSF},F}$  remains almost constant, we can notice variability in the energy of the harmonic CRSF  $E_{\text{CRSF},H}$  between the three observations. The folding energy  $E_{\text{fold}}$  remains constant within the uncertainties between the three observations whereas we can observe a variable cutoff energy  $E_{\text{cut}}$ . The unabsorbed flux  $\mathcal{F}_{3-79 \text{ keV}}$  is higher by a factor of 2 in observations IIa and IIb than in observation I, following the higher count rates observed. The comparatively poor fit in observation IIa is driven by the low energies, where the spectrum appears even more complex than the model assumes (Fig. 5).

## 5. Time-resolved spectroscopy

Now that we have a good description of the average continuum of Vela X-1 for our observations, we can use the model to access the variability of the source on shorter timescales. The good sensitivity of *NuSTAR* enables us to extract a spectrum for each *NuSTAR* orbit and also for each rotation of the neutron star. However, an analysis on a shorter timescale than the pulse period

<sup>4</sup> <https://heasarc.gsfc.nasa.gov/cgi-bin/Tools/w3nh/w3nh.pl>

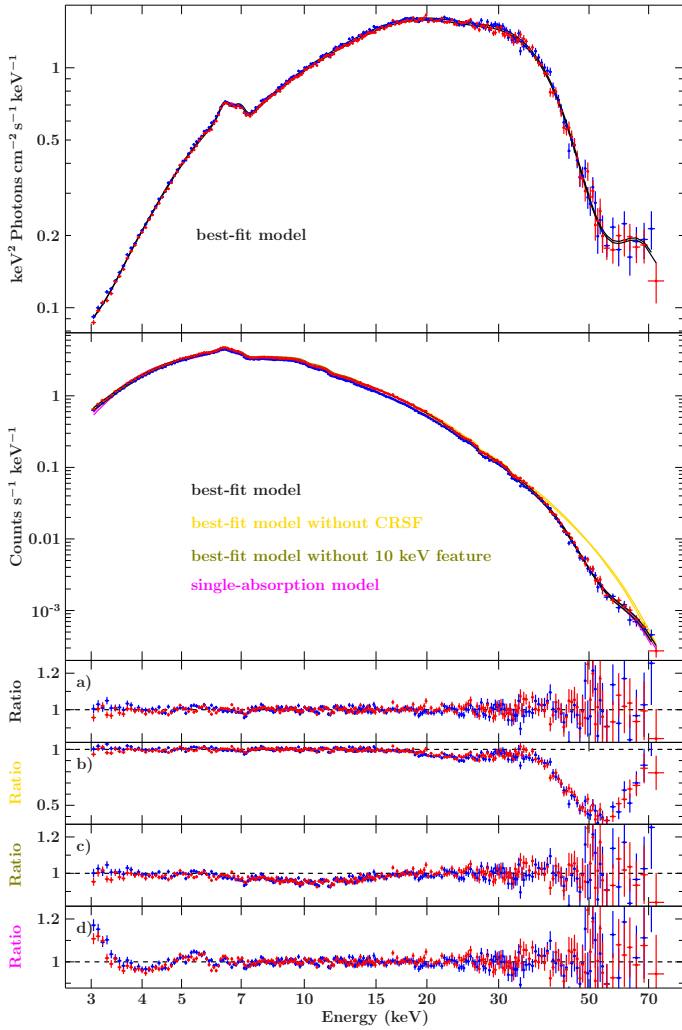


**Fig. 4.** Time-averaged spectrum for observation I. The FPMA data are in red and FPMB data in blue, and models for both focal plane modules are shown in the same colour and are hardly distinguishable with the naked eye. The first two panels show, respectively, the unfolded spectrum and the count spectrum. The residual panels are (from top to bottom): (a) best-fit model (black), (b) best-fit model with CRSFs (yellow) turned off but not fitted again, (c) best-fit model with 10 keV feature (green) turned off but not fitted again, and (d) single-absorption model (magenta). Green and magenta lines are almost hidden by the data and the best-fit model in the data panel.

is not expedient because the spectrum is highly variable with the pulse phase (see Kreykenbohm et al. 2002; La Barbera et al. 2003; Maitra & Paul 2013).

We used the model in Eq. (3) for the time-resolved spectroscopy, employing the same parameter ranges that we used for the time-averaged spectroscopy. However, given the shorter exposure time per spectrum and consequently lower signal-to-noise ratio, we have to fix some more parameters (see Table 3) to their time-averaged values to obtain meaningful constraints on our model parameters. As the background is stable during the observation, we use the time-averaged background for all of the sliced-data since it provides a better estimate of the true background spectrum due to the higher signal-to-noise.

Due to its proximity to and thus degeneracy with  $E_{\text{CRSF,F}}$ , the  $E_{\text{cut}}$  parameter has to be fixed for the orbit-by-orbit analysis. We further fix the line widths of both harmonic and fundamental

CRSFs,  $\sigma_{\text{CRSF,H}}$  and  $\sigma_{\text{CRSF,F}}$ , the line width of the  $\text{FeK}\alpha$  line,  $\sigma_{\text{FeK}\alpha}$ , the energy of the 10 keV feature,  $E_{10\text{keV}}$ , the line width of the 10 keV feature,  $\sigma_{10\text{keV}}$ , and the floating cross-normalisation parameter,  $C_{\text{FPMB}}$ , to their respective time-averaged values.

For the pulse-by-pulse spectroscopy, we start with the same settings and fixed parameters as for the orbit-by-orbit spectroscopy. However, several of the remaining parameters are not well constrained by these data. Thus, we have to fix the strengths  $d_{\text{CRSF,H}}$  and  $d_{\text{CRSF,F}}$  and energies  $E_{\text{CRSF,H}}$  and  $E_{\text{CRSF,F}}$  of both harmonic and fundamental CRSFs to their respective orbit-wise values. We show the results of both orbit-by-orbit and pulse-by-pulse spectral analyses as functions of time and orbital phase for observations I and II (IIa–IIb) in Figs. 6 and 7, respectively.

Some of the individual values presented correspond to observations with very short exposures and can be usually recognised as outliers with large uncertainties. This is in particular the case for orbit-wise spectra at orbits 10, 11, and 12. These data have been affected by the loss of data due to ground station problems. Several pulse-wise outliers are located at the edges of the individual orbits where the data covers only a part of a given pulse. When discussing possible parameter correlations, these measurements have to be treated with caution. The off-states can be clearly seen in our data, but are too short for a detailed spectral analysis.

A significant variability of the presented parameters with time and orbital phase is observed in observations I and II. In particular, during the flare in observation I (at  $T_{\text{obs}} \approx 58493.53$  MJD),  $\Gamma$  reaches its minimal value while the energy of the  $\text{FeK}\alpha$ , which is rather stable otherwise, increases.

Significant variations in the energy of CRSFs and especially  $E_{\text{CRSF,H}}$  can be observed in both datasets for the orbit-by-orbit spectral analysis. In observation IIb the values of  $E_{\text{CRSF,H}}$  are higher than during observation IIa. In observation I,  $E_{\text{CRSF,H}}$  is at higher energies before than after the flare. The fundamental line is much weaker than the harmonic and thus the uncertainties on the values are much larger, preventing us from drawing conclusions on any correlations.

The stellar wind absorption is high in both observations.  $N_{\text{H,1}}$  in observation I averages around  $\sim 40 \times 10^{22} \text{ cm}^{-2}$ . In observation II, it is more variable, in particular during observation IIb: it shows a rapid increase to more than  $\sim 50 \times 10^{22} \text{ cm}^{-2}$ .

The covering fraction CF remains stable around 0.9 for observation I. In observation II, CF is more variable, ranging between  $\sim 0.3$  and  $\sim 1$  and is higher during observation IIb than during observation IIa. During flares, the covering fraction tends to decrease on the pulse-by-pulse timescale as visible in observation I at  $T_{\text{obs}} \approx 58493.53$  MJD or in observation II at  $T_{\text{obs}} \approx 58606.95$  MJD, at  $T_{\text{obs}} \approx 58607.03$  MJD and at  $T_{\text{obs}} \approx 58607.42$  MJD. During off-states ( $T_{\text{obs}} \approx 58493.66$  MJD and at  $T_{\text{obs}} \approx 58493.93$  MJD in observation I), which corresponds to a minimum in  $\mathcal{F}_{3-79\text{keV}}$ , the CF tends to reach its maximal value of 1.

The folding energy  $E_{\text{fold}}$  seems to show distinct behaviour during both the flare and the off-states, but a correlation cannot be easily concluded without further investigation (see Sect. 6).

## 6. Discussion

### 6.1. Spectral shape and CRSF variability with luminosity

In this subsection, to compare our results to previous work and to other sources, we have to convert our observed 3–79 keV flux,

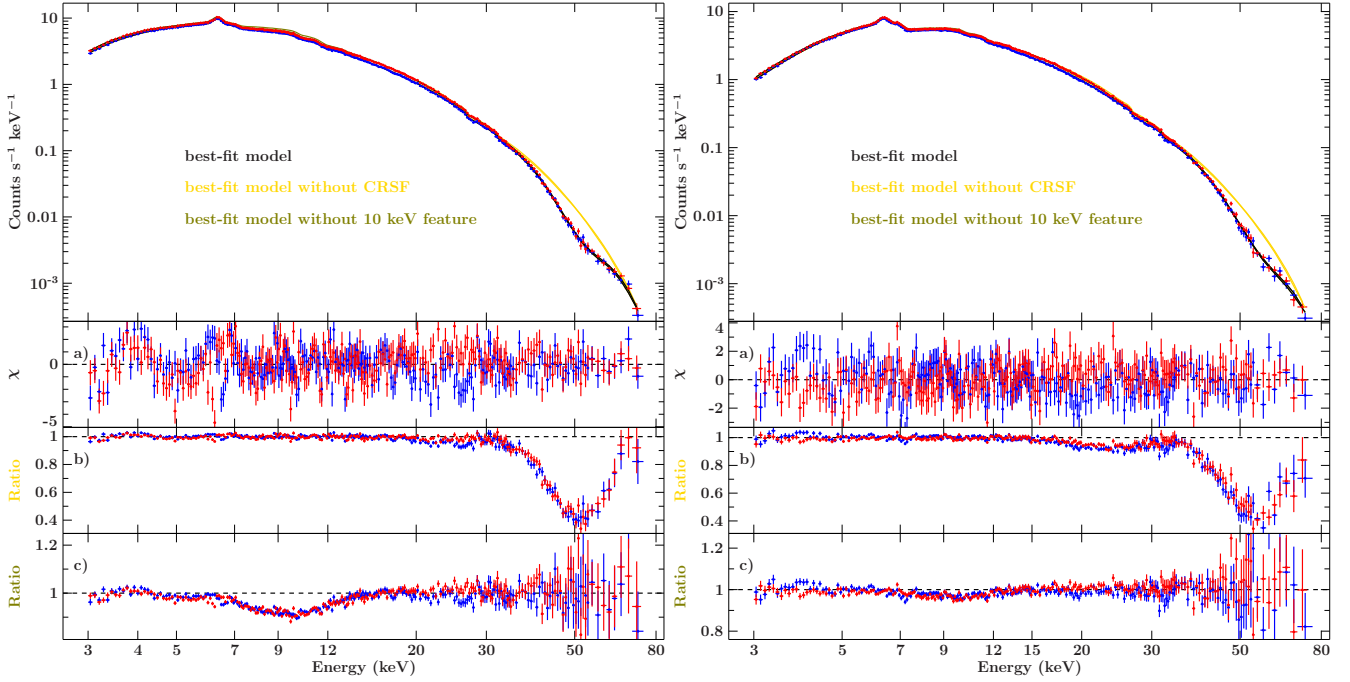


**Fig. 5.** Time-averaged spectrum for observations IIa (left panel) and IIb (right panel). The FPMA data are in red and the FPMB data in blue. Models for both focal plane modules are shown in the same colour and are hardly distinguishable with the naked eye. The residual panels are (from top to bottom): (a) best-fit model (black), (b) best-fit model with CRSFs (yellow) turned off but not fitted again, (c) best-fit model with 10 keV feature (green; this line is almost hidden by the data and the best-fit model in the data panel) turned off but not fitted again.

**Table 3.** Best-fit parameters for the time-averaged final model.

Parameter	Obs I	Obs IIa	Obs IIb	Orbit-by-orbit	Pulse-by-pulse
$C_{\text{FPMA}}$	1	1	1	1	1
$C_{\text{FPMB}}$	$1.0203 \pm 0.0021$	$1.0142 \pm 0.0018$	$1.0204 \pm 0.0022$	$\Rightarrow$ fixed	$\Rightarrow$ fixed
$N_{\text{H},1}$ ( $10^{22}$ cm $^{-2}$ )	$34.0 \pm 1.0$	$32.1 \pm 1.9$	$42.8^{+1.2}_{-1.3}$	fitted	fitted
$N_{\text{H},2}$ ( $10^{22}$ cm $^{-2}$ )	fixed to 0.371	fixed to 0.371	fixed to 0.371	fixed to 0.371	fixed to 0.371
$\Gamma$	$1.09 \pm 0.05$	$1.084^{+0.024}_{-0.025}$	$1.01^{+0.04}_{-0.05}$	fitted	fitted
$E_{\text{cut}}$ (keV)	$19.9^{+3.5}_{-2.0}$	$26.1^{+1.1}_{-1.2}$	$21 \pm 4$	$\Rightarrow$ fixed	$\Rightarrow$ fixed
$E_{\text{fold}}$ (keV)	$12.6^{+0.9}_{-0.8}$	$10.2^{+0.5}_{-0.4}$	$11.2^{+1.1}_{-2.1}$	fitted	fitted
$E_{\text{CRSF,F}}$ (keV)	$24.7^{+1.0}_{-0.9}$	$24.3^{+1.0}_{-1.1}$	$24.0^{+0.0}_{-0.8}$	fitted	$\Rightarrow$ fixed
$\sigma_{\text{CRSF,F}}$ (keV)	fixed to $0.5 \times \sigma_{\text{CRSF,H}}$	fixed to $0.5 \times \sigma_{\text{CRSF,H}}$	fixed to $0.5 \times \sigma_{\text{CRSF,H}}$	$\Rightarrow$ fixed	$\Rightarrow$ fixed
$d_{\text{CRSF,F}}$ (keV)	$0.75^{+0.00}_{-0.19}$	$0.31^{+0.16}_{-0.11}$	$0.86^{+0.00}_{-0.24}$	fitted	$\Rightarrow$ fixed
$E_{\text{CRSF,H}}$ (keV)	$53.8^{+1.1}_{-0.9}$	$51.8 \pm 0.7$	$56.0^{+2.0}_{-1.2}$	fitted	$\Rightarrow$ fixed
$\sigma_{\text{CRSF,H}}$ (keV)	$7.9^{+1.3}_{-0.9}$	$7.4^{+0.8}_{-0.6}$	$8.8^{+6.6}_{-1.2}$	$\Rightarrow$ fixed	$\Rightarrow$ fixed
$d_{\text{CRSF,H}}$ (keV)	$18^{+6}_{-4}$	$16.5^{+3.1}_{-2.5}$	$18.58^{+0.00}_{-4.65}$	fitted	$\Rightarrow$ fixed
$E_{\text{FeK}\alpha}$ (keV)	$6.364 \pm 0.012$	$6.357 \pm 0.006$	$6.356 \pm 0.008$	fitted	fitted
$A_{\text{FeK}\alpha}$ (ph s $^{-1}$ cm $^{-2}$ )	$(1.35 \pm 0.11) \times 10^{-3}$	$(4.04^{+0.17}_{-0.16}) \times 10^{-3}$	$(4.50^{+0.23}_{-0.22}) \times 10^{-3}$	fitted	fitted
$\sigma_{\text{FeK}\alpha}$ (keV)	$0.070^{+0.029}_{-0.045}$	$0.045^{+0.023}_{-0.045}$	$0.074^{+0.021}_{-0.025}$	$\Rightarrow$ fixed	$\Rightarrow$ fixed
$E_{10\text{keV}}$ (keV)	$9.5^{+0.6}_{-1.0}$	$9.13^{+0.14}_{-0.17}$	$9.2^{+0.5}_{-0.6}$	$\Rightarrow$ fixed	$\Rightarrow$ fixed
$A_{10\text{keV}}$ (ph s $^{-1}$ cm $^{-2}$ )	$(-4.8^{+2.2}_{-4.8}) \times 10^{-3}$	$-0.0125^{+0.0017}_{-0.0023}$	$(-4.5^{+1.6}_{-2.4}) \times 10^{-3}$	fitted	fitted
$\sigma_{10\text{keV}}$ (keV)	$3.2^{+1.0}_{-0.7}$	$2.34^{+0.22}_{-0.18}$	$2.1^{+0.6}_{-0.5}$	$\Rightarrow$ fixed	$\Rightarrow$ fixed
$\mathcal{F}_{3-79\text{keV}}$ (keV s $^{-1}$ cm $^{-2}$ )	$3.43^{+0.10}_{-0.05}$	$6.35^{+0.09}_{-0.00}$	$6.24^{+2.89}_{-0.10}$	fitted	fitted
$\mathcal{F}_{3-79\text{keV}}$ (erg s $^{-1}$ cm $^{-2}$ )	$(5.49^{+0.17}_{-0.08}) \times 10^{-9}$	$(10.2^{+0.1}_{-0.00}) \times 10^{-9}$	$(10.0^{+4.4}_{-0.4}) \times 10^{-9}$	fitted	fitted
CF	$0.883 \pm 0.005$	$0.505^{+0.012}_{-0.013}$	$0.852 \pm 0.005$	fitted	fitted
$\chi^2/\text{d.o.f.}$	613.37/456	731.94/456	578.30/456		

**Notes.** In the two right-most columns, we indicate which spectral parameters are fixed to the value found in the corresponding analysis at lower time resolution or still left free during the fit.

$\mathcal{F}_{3-79\text{keV}}$ , to the 3–79 keV luminosity,  $L_{3-79\text{keV}}$ , using  $\mathcal{F}_{3-79\text{keV}} = L_{3-79\text{keV}}/(4\pi d^2)$ , where  $d$  is the distance to the source and is equal to  $1.99^{+0.13}_{-0.11}$  kpc (Kretschmar et al. 2021). Overall, our luminosities are in the range of  $\sim 2\text{--}10 \times 10^{36}$  erg s $^{-1}$  (Fig. 8) and thus slightly but not drastically below the often quoted range of around or a few  $10^{37}$  erg s $^{-1}$  for the critical luminosity (e.g.,

Reig & Nespoli 2013). Uncertainties on the distance lead to systematic uncertainties in the overall luminosity of the source of approximately +15%/–12%. For this work, we chose to use an empirical model to describe the spectrum of Vela X-1 in order to get insights into the underlying physics, which is discussed below.

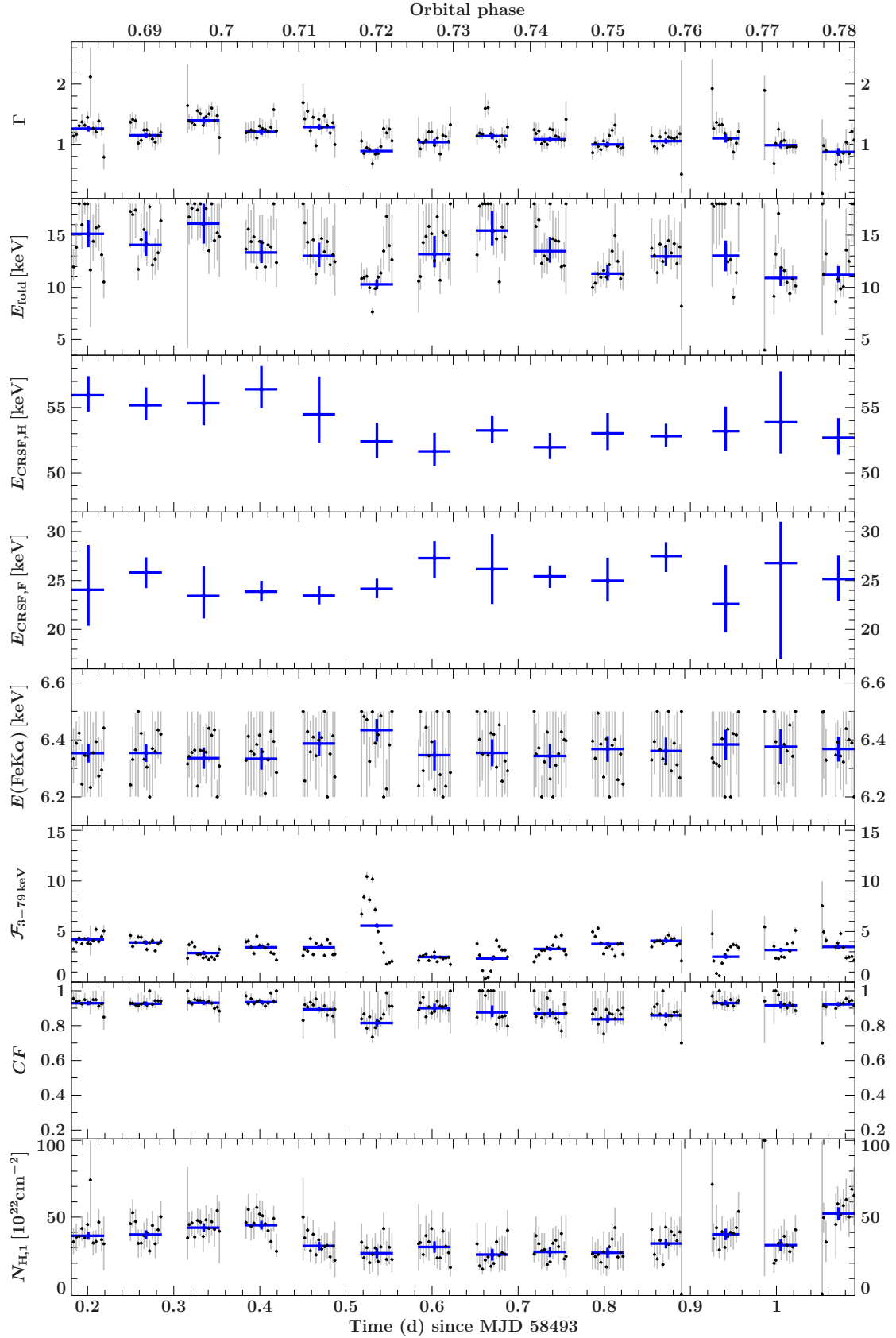


**Fig. 6.** Results of the pulse-by-pulse (black) and orbit-by-orbit (blue) analyses for observation I as functions of time, showing also the corresponding orbital phase. The panels show (from top to bottom): photon index ( $\Gamma$ ), folding energy ( $E_{\text{fold}}$ ) in keV, energy of the harmonic CRSF ( $E_{\text{CRSF,H}}$ ) in keV, energy of the fundamental CRSF ( $E_{\text{CRSF,F}}$ ) in keV, energy of the FeK $\alpha$  line in keV, unabsorbed flux ( $\mathcal{F}_{3-79\text{keV}}$ ) in keV s $^{-1}$  cm $^{-2}$ , covering fraction (CF), and absorption from the stellar wind ( $N_{\text{H},1}$ ) in 10 $^{22}$  cm $^{-2}$ .

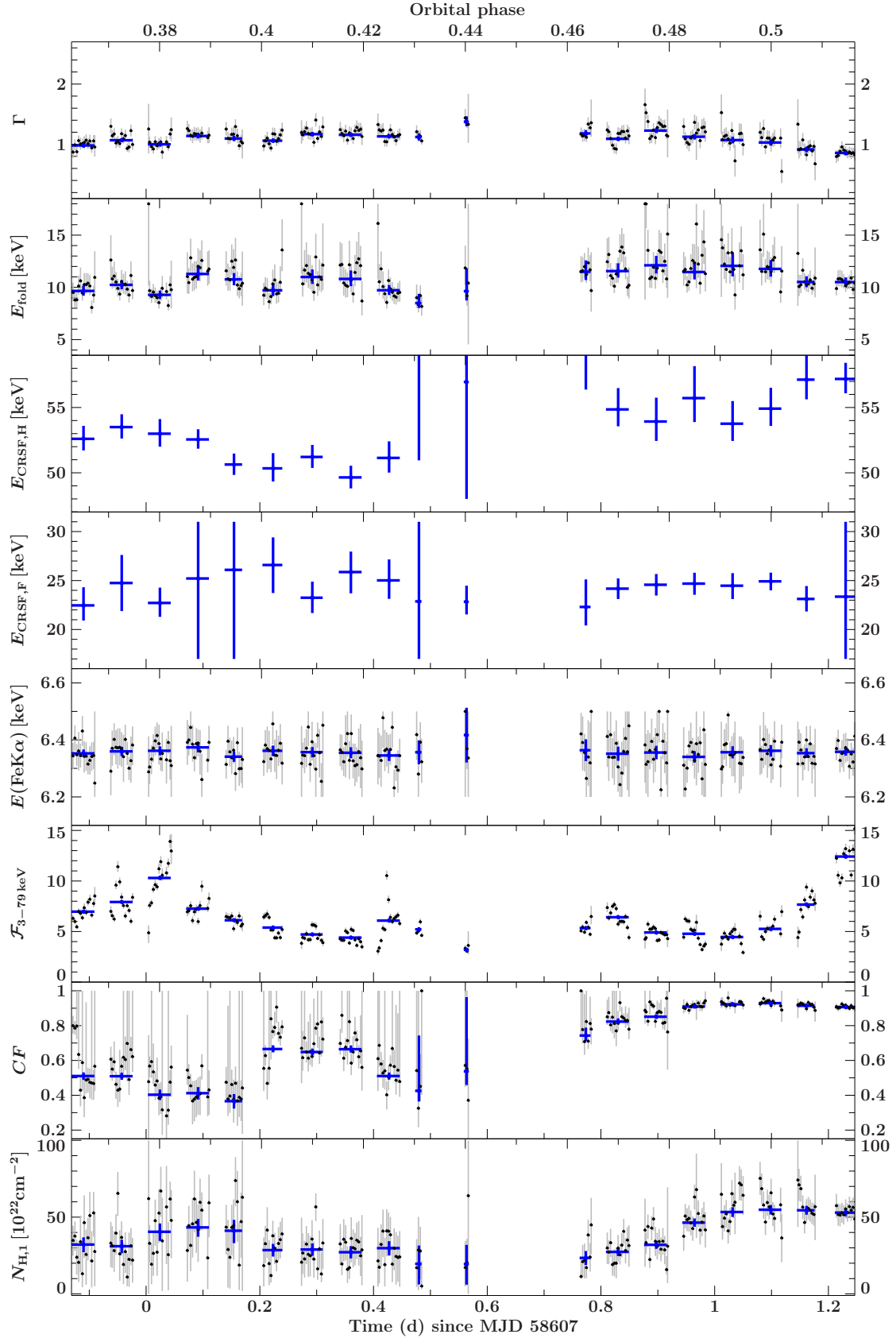


**Fig. 7.** Results of the pulse-by-pulse (black) and orbit-by-orbit (blue) analyses for observation II as functions of time, showing also the corresponding orbital phase. The panels show (from top to bottom): photon index ( $\Gamma$ ), folding energy ( $E_{\text{fold}}$ ) in keV, energy of the harmonic CRSF ( $E_{\text{CRSF,H}}$ ) in keV, energy of the fundamental CRSF ( $E_{\text{CRSF,F}}$ ) in keV, energy of the  $\text{FeK}\alpha$  line in keV, unabsorbed flux ( $\mathcal{F}_{3-79\text{keV}}$ ) in  $\text{keV s}^{-1} \text{cm}^{-2}$ , covering fraction (CF), and absorption from the stellar wind ( $N_{\text{H},1}$ ) in  $10^{22} \text{cm}^{-2}$ .



### 6.1.1. Continuum spectral shape

In the upper panel of Fig. 8, we show our results for the correlation between  $\Gamma$  and the luminosity. We also include previous measurements by Fürst et al. (2014b) at orbital phase 0.655–0.773, re-scaled to the updated distance to the source. We can observe a negative correlation between the spectral slope and the luminosity. This behaviour is typical for a source in the subcritical accretion regime as it has already been found for example for Her X-1 (Staubert et al. 2007), Vela X-1 (Odaka et al. 2013; Fürst et al. 2014b), and several Be/X-ray pulsars in the subcritical accretion regime (Reig & Nespoli 2013). Assuming X-ray radiation dominated by Comptonisation, this correlation can be a consequence of the increase in the accretion rate resulting in an increase in the X-ray luminosity and to a more efficient Comptonisation occurring in the accreted plasma (Odaka et al. 2013).

In Fig. 9 we can also see an anti-correlation between  $E_{\text{fold}}$  and luminosity, as already indicated in Figs. 6 and 7 for lower luminosities ( $\leq 4 \times 10^{36} \text{ erg s}^{-1}$ ). For higher luminosities, the folding energy seems to be constant around  $\sim 10 \text{ keV}$ . Considering the underlying shape of the model we employ, we expect a positive degeneracy between the folding energy  $E_{\text{fold}}$  and the X-ray flux (or luminosity). Confidence maps calculated for folding energy and flux indeed confirm this expectation, implying that the observed opposite trend cannot be explained by modelling degeneracies. Odaka et al. (2013) use a different continuum model (NPEX) when analysing Suzaku data, so that the values of their and our parameters called folding energy cannot be directly compared. The trends, however, are comparable: they also find a negative correlation followed by a stabilisation between folding energy and flux at higher fluxes. Similar behaviour of the cutoff has been observed in a sample of Be/X-ray binaries when modelling their spectra with a cutoff power law in the subcritical accretion regime (Reig & Nespoli 2013). Assuming a significant contribution of not only bulk, but also thermal Comptonisation to the overall emission (Becker & Wolff 2007; Ferrigno et al. 2009), the change in the cutoff would correspond to a change in the temperature of the Comptonising plasma.

### 6.1.2. Accretion regime

To verify the accretion regime of Vela X-1 for our observations, we computed its critical luminosity using Eq. (32) from Becker et al. (2012):

$$L_{\text{crit}} = 1.49 \times 10^{37} \text{ erg s}^{-1} \left( \frac{\Lambda}{0.1} \right)^{-7/5} \omega^{-28/15} \times \left( \frac{M_{\text{NS}}}{1.4 M_{\odot}} \right)^{29/30} \left( \frac{R_{\text{NS}}}{10 \text{ km}} \right)^{1/10} \left( \frac{E_{\text{NS},n}}{n \times 11.57 \text{ keV}} \right)^{16/15}, \quad (4)$$

where  $M_{\text{NS}}$  and  $R_{\text{NS}}$  are the mass and radius of the neutron star and  $\omega$  is a parameter describing the spectral shape inside the column.  $E_{\text{NS},n}$  is the surface cyclotron fundamental ( $n = 1$ ) or harmonic ( $n = 2$ ) energy of the neutron star. We use  $\omega = 1$  (assuming that the spectrum inside the emission region is dominated by Bremsstrahlung). Recent publications (Legred et al. 2021) tend to assume a typical neutron star radius  $R_{\text{NS}}$  around 12 km. However, for this work, we used  $R_{\text{NS}} = 10 \text{ km}$  under the same assumptions as in Becker et al. (2012) for typical neutron star parameters<sup>5</sup>. We considered a mass of  $\sim 1.7\text{--}2.1 M_{\odot}$

<sup>5</sup> The critical luminosity with a neutron star radius of 12 km is  $\sim 2\%$  higher than the critical luminosity using a neutron star radius of 10 km.

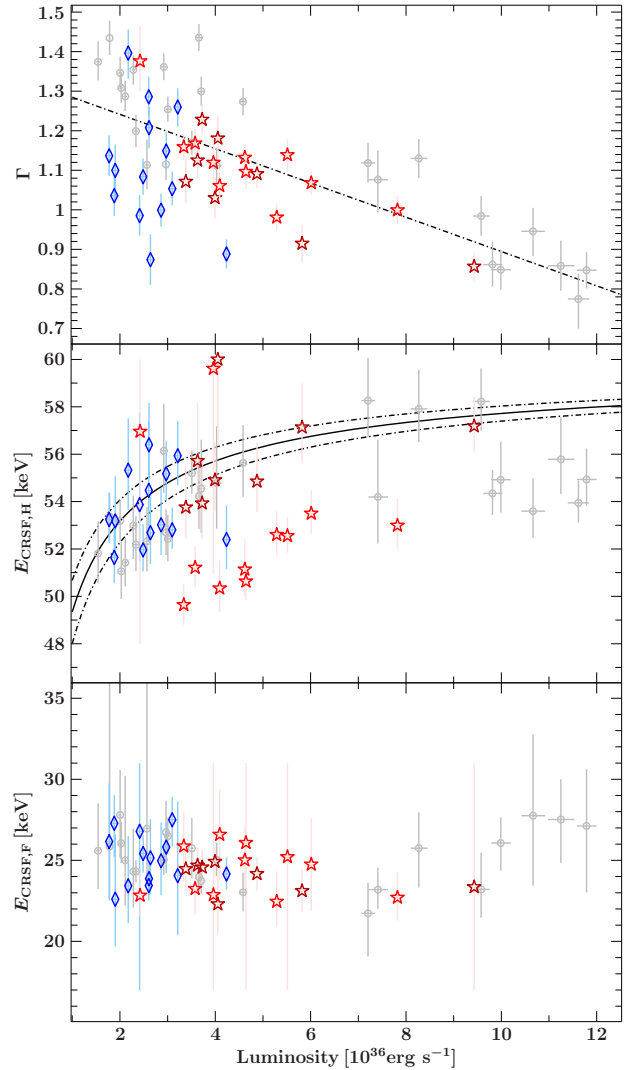


**Fig. 8.** Spectral parameter as a function of the 3–79 keV luminosity based on our orbit-by-orbit spectroscopy results (dark blue diamonds represent observation I, bright red stars observation IIa, and dark red stars observation IIb) together with kilosecond-integrated spectral fits from Fig. 7 in Fürst et al. (2014b) (grey circles). *Upper panel:* photon index ( $\Gamma$ ). The dot-dashed black line is a linear regression through all data points, meant to guide the eye. *Middle panel:* energy of the harmonic CRSF ( $E_{\text{CRSF,H}}$ ). The solid black line is the theoretical prediction for  $\Lambda = 1$ ,  $E_{\text{NS}} = 30 \text{ keV}$ , and  $M_{\text{NS}} = 1.9 M_{\odot}$ . The dot-dashed lines above and below the solid line are for  $M_{\text{NS}} = 1.7 M_{\odot}$  and  $M_{\text{NS}} = 2.1 M_{\odot}$ , respectively. *Lower panel:* energy of the fundamental line ( $E_{\text{CRSF,F}}$ ).

(Kretschmar et al. 2021) and a surface fundamental cyclotron energy of  $E_{\text{NS}} = 20 \text{ keV}$ .

Parameter  $\Lambda$  in Eq. (4) accounts for the difference in location of the Alfvén surface in case of the predominantly orbital or radial inflow (see, for example, Eq. (18) from Lamb et al. 1973). It depends on the ratio of the radial velocity of the flow to the free-fall one and on the thickness of the accretion disc. However, the Alfvén radius is reduced only by a factor of  $\sim 10$  ( $\Lambda \sim 0.1$ ) from the radius corresponding to a fully radial inflow even for the extreme values of these parameters (small radial velocities and a thin accretion disc). For spherical accretion,  $\Lambda = 1$  and for disc accretion  $\Lambda < 1$  (Becker et al. 2012). In the case of Vela X-1, we consider a wind accreting source so the accretion is more likely to be spherical than through an accretion disc, although there are theoretical predictions of possible disc

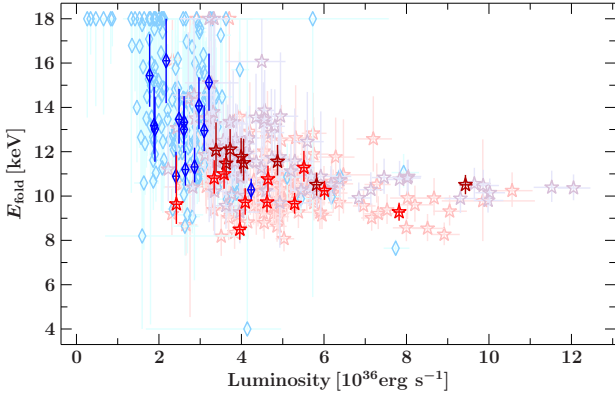


**Fig. 9.** Folding energy ( $E_{\text{fold}}$ ) as a function of the 3–79 keV luminosity based on our orbit-by-orbit and pulse-by-pulse spectroscopy results. Dark blue diamonds are the results of the orbit-by-orbit analysis for observation I, light blue diamonds are the results of the pulse-by-pulse spectroscopy for observation I, bright red stars are the results of the orbit-by-orbit spectroscopy for observation IIa, pink stars are the results of the pulse-by-pulse spectroscopy for observation IIa, dark red stars are the results of the orbit-by-orbit spectroscopy for observation IIb, and lavender stars are the results of the pulse-by-pulse spectroscopy for observation IIb.

formation (El Mellah et al. 2019) and observational hints that temporarily a disc can be formed sometimes (Liao et al. 2020). Additionally, even without the presence of a disc, the accretion from the clumpy, disturbed wind of the companion is more complex than a simple spherical accretion case (e.g., El Mellah et al. 2018).

If we consider a spherical accretion with  $\Lambda = 1$ , then  $L_{\text{crit}} \approx 0.13\text{--}0.15 \times 10^{37} \text{ erg s}^{-1}$  using Eq. (4) and taking uncertainties on the mass into account. This classifies Vela X-1 as a super-critical source. However, in previous works, Vela X-1 has been classified as a subcritical source (Fürst et al. 2014b) assuming  $\Lambda = 0.1$  (thus disc accretion case), also following Becker et al. (2012). Indeed, for  $\Lambda = 0.1$ , we obtain  $L_{\text{crit}} \approx 3.22\text{--}3.95 \times 10^{37} \text{ erg s}^{-1}$ . Our assumption of  $E_{\text{NS}} = 20 \text{ keV}$  is conservative. Given that the measured energy of the fundamental line is above 20 keV, the real value is likely higher and will lead to a higher  $L_{\text{crit}}$ . For instance, assuming  $E_{\text{NS}} = 30 \text{ keV}$ , we obtain a  $L_{\text{crit}} \approx 4.97\text{--}6.10 \times 10^{37} \text{ erg s}^{-1}$ . This approach puts Vela X-1 in the subcritical regime, which is supported by the observed anti-correlation between  $\Gamma$  and luminosity (see Fig. 8) typical for a subcritical source (Staubert et al. 2007; Odaka et al. 2013; Reig & Nespoli 2013; Fürst et al. 2014b). However, the choice of  $\Lambda = 0.1$  assumes a disc accretion case, which we question for our observations.

A further theoretical calculation for the critical luminosity has been presented in Mushtukov et al. (2015a), taking into account the exact Compton scattering cross-section in the high magnetic field and in particular they show the results of their calculations assuming  $\Lambda = 0.5$ . Their critical luminosity for Vela X-1 under these assumptions is of the order of  $\sim 0.1\text{--}1 \times 10^{37} \text{ erg s}^{-1}$ , which is around our measurements (Fig. 8).

For the Be X-ray binary GRO J1008-57, Kühnel et al. (2017) have computed the theoretically expected critical luminosities at the transition between different accretion regimes after Becker et al. (2012), Mushtukov et al. (2015a), and Postnov et al. (2015, see their Appendix A). Uncertainties in the theories and data limitations do not allow them to favour one of the theories for the prediction of the critical luminosity, similar to our inconclusive results.

Given the above and the fact that neither the disc accretion scenario nor the spherical accretion are a good description for the accretion in the highly structured, disturbed wind in the system, estimates on whether Vela X-1 is on sub- or supercritical regime have to be treated with caution. However, for the following section, Sect. 6.1.3, we assume a subcritical accretion regime for Vela X-1 to compare with previous results.

### 6.1.3. CRSFs, luminosity, and flares

As we found a negative correlation between  $\Gamma$  and luminosity for our observations in Sect. 6.1.1, we expect a positive correlation between the CRSF energy and the luminosity (see details in Sect. 1) in the case of a subcritical accretion regime.

The theoretical expected energy of the fundamental CRSF for a subcritical source can be calculated using Eq. (7) from Fürst et al. (2014b) with  $\tau_*$ , the Thomson optical depth, which we set to 20, the estimate by Becker et al. (2012) for the plasma braking by Coulomb collisions in the filled accretion column and  $E_{\text{NS}}$  the energy of the fundamental cyclotron energy:

$$E_{\text{theo}} = \left[ 1 + 0.6 \left( \frac{R_{\text{NS}}}{10 \text{ keV}} \right)^{-\frac{13}{14}} \left( \frac{\Lambda}{0.1} \right)^{-1} \left( \frac{\tau_*}{20} \right) \left( \frac{M_{\text{NS}}}{1.4 M_{\odot}} \right)^{\frac{19}{14}} \times \left( \frac{E_{\text{NS}}}{1 \text{ keV}} \right)^{-\frac{4}{7}} \left( \frac{L_X}{10^{37}} \right)^{-\frac{5}{7}} \right]^{-3} \times E_{\text{NS}}. \quad (5)$$

To draw the prediction for the line energy of the harmonic CRSF ( $n = 2$ ) and to compare our results with Fürst et al. (2014b), we have to use  $2 \times E_{\text{theo}}$ . The black dot-dashed line in Fig. 8 top panel shows the expected positive correlation between  $E_{\text{CRSF,H}}$  and luminosity in the case of a subcritical source using  $\Lambda = 1$ . However, this correlation is hardly visible for our data. This may be explained by the accretion regime of Vela X-1 lying somewhere in between the sub- and super-critical cases and thus yielding to inconclusive results. Vybornov et al. (2017) also obtained inconclusive results for intermediate accretion regime case for Cep X-4 with collisionless shock theoretical study.

Overall, there seems to be an intrinsic variability in the CRSF energies in our observations but they do not appear to be correlated with the luminosity. In particular, in observation I, we observe a clear drop in CRSF energy from  $\sim 55\text{--}56 \text{ keV}$  to  $\sim 52\text{--}53 \text{ keV}$  after the flare even though the flux and other spectral parameters return to the pre-flare level (Fig. 6). A similar decrease is seen in observation IIa (Fig. 7), but here the overall flux also decreases. If confirmed, such a behaviour could be explained by restructuring of the accretion column and thus change in the location of the CRSF producing region following an episode of stronger accretion. To test whether the observed CRSF variability is real, we redid the orbit-by-orbit analysis, fixing the energies of the CRSFs to their respective average value. The overall fit gets worse compared to the analysis with those energies being free, and we have not seen the changes in the trend observed in other parameters.

## 6.2. The variable absorption in the stellar wind

### 6.2.1. Orbital dependency: Wakes crossing our line of sight

Because of the structure of the stellar wind, the amount of material being on our line of sight towards the neutron star can change and thus modifies the shape of the continuum creating variability. This is particularly striking with the covering fraction, CF, and the equivalent absorbing hydrogen column density,  $N_{\text{H},1}$ ,

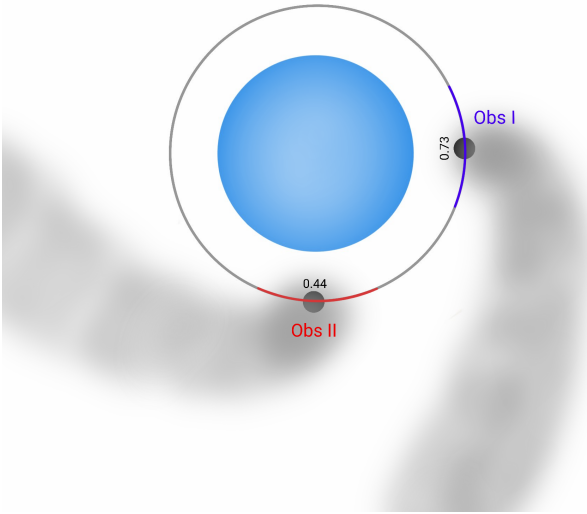


**Fig. 10.** Sketch of Vela X-1 showing possible positions of the wake structure during the two observations at mid-orbital phase. In this image, the observer’s point of view is located facing the system at the bottom of the picture.

showing different behaviours between observations I and II (Figs. 6 and 7) that are taken at different orbital phases when our line of sight crosses different parts of the wind (Fig. 10). The overall structure of the disturbed stellar wind is complex, with both photoionisation and accretion wake present and expected to be variable (Blondin et al. 1990; Malacaria et al. 2016); as our observations cannot distinguish between the components, we refer to them as wakes in general.

Thus, we explore possible correlations between the covering fraction and the column density. Additionally, there are possible modelling degeneracies such as between the slope,  $\Gamma$ , and  $N_{\text{H},1}$ , inherent to the usage of power law models for the continuum modelling of X-ray binaries (e.g., Suchy et al. 2008). We carefully check for such a correlation both with scatter plots of our orbit-by-orbit and pulse-by-pulse fits (Fig. 11) and through calculation of confidence maps for  $\Gamma$  and  $N_{\text{H},1}$  and find that, even if present, it does not significantly contribute to our results.

During observation I, the wakes are located on the line of sight towards the observer. The covering fraction is close to 1, meaning that most of the incoming photons are absorbed through the dense material in the absorption and photoionisation wakes (Blondin et al. 1990; Kaper et al. 1994; Manousakis 2011). This is particularly visible in our time-resolved analysis in Fig. 12 where the orbit-by-orbit and pulse-by-pulse data points of observation I show a positive correlation between the stellar wind absorption  $N_{\text{H},1}$  and the covering fraction CF. Similar high covering fractions and hydrogen column densities have been seen at this orbital phase in both *NuSTAR* (Fürst et al. 2014b) and *Chandra* (Amato et al. 2021) observations.

On the contrary, during observation IIa, the majority of the material in the wakes is not yet on the observer’s line of sight, implying a low covering fraction CF and fewer photons absorbed by the stellar wind (Fig. 10). Indeed, the orbit-by-orbit and pulse-by-pulse data points of observation II in Fig. 12 show a negative correlation between the stellar wind absorption  $N_{\text{H},1}$  and the covering fraction CF.

Finally, during observation IIb, the wakes are starting to pass through the observer’s line of sight and consequently the CF slowly increases to reach the values of observation I (Fig. 7).

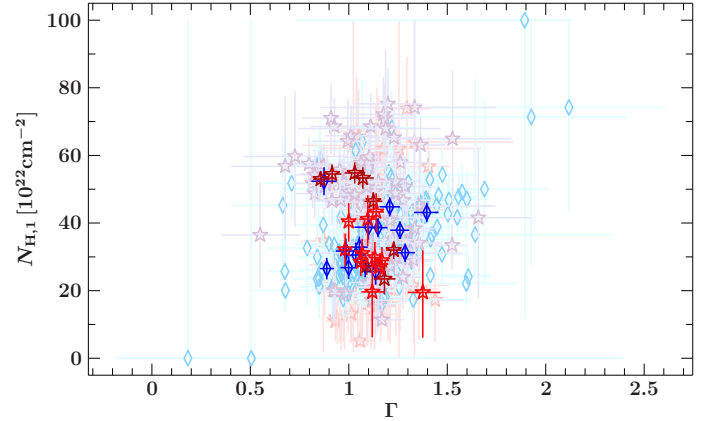


**Fig. 11.** Stellar wind absorption,  $N_{\text{H},1}$ , as a function of the photon index,  $\Gamma$ , based on our orbit-by-orbit and pulse-by-pulse spectroscopy results. Symbols are the same as in Fig. 9.

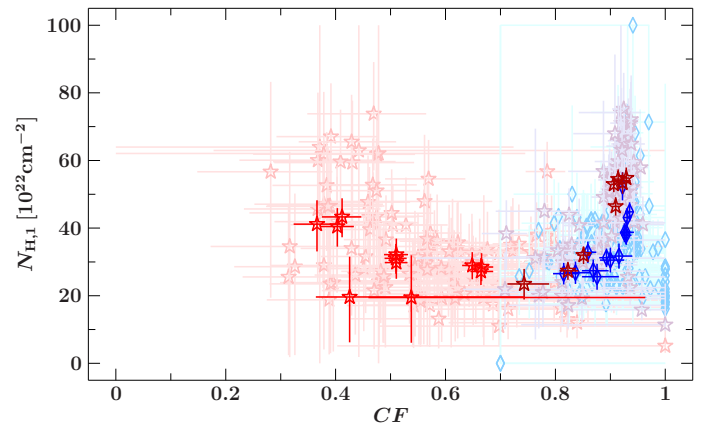


**Fig. 12.** Stellar wind absorption,  $N_{\text{H},1}$ , as a function of the covering fraction, CF, based on our orbit-by-orbit and pulse-by-pulse spectroscopy results. Symbols are the same as in Fig. 9.

This is confirmed by the time-resolved data points in Fig. 12 where the same positive correlation than in observation I is seen.

To confirm the physical origin of these behaviours, we calculate the confidence maps for the two parameters of interest,  $N_{\text{H},1}$  and CF, using the results from the time-averaged spectroscopy for the three observations, I, IIa, and IIb. For observation I, pure modelling degeneracy would lead to a negative correlation between the two parameters, in opposite to what is seen on the scatter plot in Fig. 12, confirming the physical origin to the observed correlation. Similarly, for observation IIa, modelling degeneracy would imply a positive correlation, while the time-resolved data points are showing a negative correlation between  $N_{\text{H},1}$  and CF also confirming the real event. A possible physical explanation is the overlapping of multiple clumps. The stellar wind surrounding Vela X-1 is clumpy (e.g., Oskinova et al. 2007) and most of the mass of the wind is concentrated in clumps (Sako et al. 1999) so that some of them may be located on our line of sight during an observation. If one clump overlaps with another one, the absorption column density  $N_{\text{H},1}$  increases and CF decreases as also observed by Fürst et al. (2014b). For observation IIb, our approach does not detect an explicit modelling degeneracy between  $N_{\text{H},1}$  and CF.

### 6.2.2. Absorption and luminosity

In observations I and IIb, when the wakes are located on the line of sight, Fig. 13 shows that the intrinsic luminosity of the source does not seem to be correlated with the covering fraction CF. Because CF is correlated with  $N_{\text{H},1}$  (Fig. 12) for these observations, we do not expect the luminosity of the source to correlate with  $N_{\text{H},1}$  either. During a flaring or an off-state period, the fraction of photons absorbed through the stellar wind should be independent from the incoming number of photons if the dense and extended wakes are located on our line of sight as we do not expect them to be strongly influenced by the change in irradiation. However, there are some data points of observation I in Fig. 13 with high luminosities ( $\sim 6\text{--}8 \times 10^{36} \text{ erg s}^{-1}$ ) and low CF ( $\sim 0.7\text{--}0.8$ ) that also correspond to a low  $N_{\text{H},1}$ . They correspond to a decrease in CF and  $N_{\text{H},1}$  associated with flares in observations I and IIb (Figs. 6 and 7). This is in agreement with [Odaka et al. \(2013\)](#)<sup>6</sup> who have found with Suzaku observations that the circumstellar absorption does not seem to correlate with the X-ray luminosity except for a strong flare.

[Martínez-Núñez et al. \(2014\)](#) have also observed a decrease in absorption during a giant flare that they attribute to the accretion of a dense clump in the wind. Our observations would support this scenario. Similar changes to the absorbing column density around and during flares have been seen in other wind-accreting sources, including in supergiant fast X-ray transients ([Pradhan et al. 2019](#); [Bozzo et al. 2017](#)).

For observation IIa, the behaviour seems strikingly different (Fig. 13), with possible indications of a negative correlation, although the large uncertainties preclude firm conclusions. Based on our knowledge of the geometry of the system, we interpret this as mainly a spurious correlation, linked to events that happen simultaneously in this particular observation by happenstance. At the beginning of observation IIa, the wakes are located outside our line of sight, which corresponds to a low covering fraction CF. As seen in Fig. 2, the beginning of observation IIa also coincides with the first flaring period, where a deep local short decrease in CF (see Fig. 7) can also be observed for each flare due to the above described theory of accreted clumps. Similarly, while the wakes are starting to get towards our line of sight, the CF increases and this coincides with a decrease in the X-ray luminosity as the flare subsides (Fig. 2).

The observed energy of the iron line is mostly constant throughout all discussed observations and consistent with neutral iron, except for one notable exception: during the bright flare in observation II, it increases (Fig. 6). This could be indicative of increased ionisation during the flare. Interestingly, however, no increase in the iron line energy is seen in either parts of observation I (Fig. 7), nor was an increase in the iron line energy observed in a previous observation of a giant flare by [Martínez-Núñez et al. \(2014\)](#). A careful modelling of our data during the flare does not reveal further possible correlations.

## 7. Summary and outlook

We have analysed two new observations of Vela X-1 taken with *NuSTAR* at different orbital phases, thus probing a different line of sight through the system. For spectral modelling, we used a partial covering model with a power law continuum with a Fermi-Dirac cutoff further modified by CRSFs. We interpreted our observations in the context of a highly magnetised neutron

<sup>6</sup> Using the ephemeris listed in Table 2 and employed throughout this paper, the observation discussed in [Odaka et al. \(2013\)](#) is at  $\phi_{\text{orb}} \approx 0.20\text{--}0.38$ .

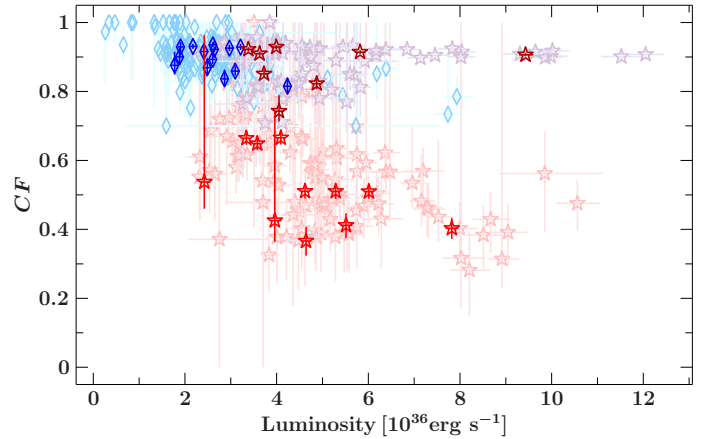


**Fig. 13.** Covering fraction, CF, as a function of the 3–79 keV luminosity based on our orbit-by-orbit and pulse-by-pulse spectroscopy results. Symbols are the same as in Fig. 9.

star accreting from the clumpy, disturbed wind of a companion and draw conclusions about the accretion geometry and stellar wind structure and their interplay.

Our observations can be explained by denser, extended wakes passing through the line of sight starting at orbital phase  $\sim 0.45$ . At lower orbital phases, the continuum is less absorbed by the stellar wind. The observed flares and the absorption variability during and around the flaring episodes can be explained by the accretion of clumps. It would be interesting, in future work, to perform a uniform analysis of Vela X-1 at all available orbital phases in order to draw a more complete picture of the stellar wind at different orbital phases ([Kretschmar et al. 2021](#)).

We have confirmed that the photon index is anti-correlated with luminosity but cannot confirm the suggested correlation of the energy of the harmonic CRSF with flux. While the anti-correlation of the photon index with luminosity points towards subcritical accretion for Vela X-1, theoretical considerations for the critical luminosity are inconclusive and will require further investigation. The theoretical expectations for the evolution of the energy of the harmonic CRSF with luminosity shown in Fig. 8 are based (unavoidably) on rather simple, mostly fixed geometries. The intermediate case between two accretion regimes for Vela X-1 is the most difficult to treat, and it could be interesting in the future to explore more variability than height-scaling in theoretical studies, including full radiation hydro simulations as suggested by [Vybornov et al. \(2017\)](#). Still, we observe variability in CRSF energy and in particular a drop following a flaring episode. Further observations of Vela X-1 and careful analysis of flaring episodes are necessary to test whether this observation was spurious or implies a change in the accretion geometry after a strong flare.

*Acknowledgements.* We thank the anonymous referee whose input helped to strengthen the paper. This work has been partially funded by the Bundesministerium für Wirtschaft und Energie under the Deutsches Zentrum für Luft- und Raumfahrt Grants 50 OR 1915. S.M.N. acknowledges funding under project RTI2018-096686-B-C21 funded by MCIN/AEI/10.13039/501100011033 and by ‘ERDF A way of making Europe’, and by the Unidad de Excelencia María de Maeztu, ref. MDM-2017-0765. E.S.L. acknowledges support by DFG grant 1830Wi1860/11-1 and RFBR grant 18-502-12025. K.P. acknowledges support by NASA under award number 80GSFC17M0002. This work has made use of (1) the Interactive Spectral Interpretation System (ISIS) maintained by *Chandra* X-ray Center group at MIT; (2) the *NuSTAR* Data Analysis Software (*NuSTARDAS*) jointly developed by the ASI Science Data Center (ASDC, Italy) and the California Institute of Technology (Caltech, USA); (3) the of ISIS functions (isiscripts <http://www.sternwarte.uni-erlangen.de/isis/>)

provided by ECAP/Remeis observatory and MIT; (4) NASA's Astrophysics Data System Bibliographic Service (ADS). We thank John E. Davis for the development of the `slxfig` (<http://www.jedsoft.org/fun/slxfig/>) module used to prepare most of the figures in this work.

## References

- Amato, R., Grinberg, V., Hell, N., et al. 2021, *A&A*, **648**, A105
- Arnaud, K. A. 1996, in *XSPEC: The First Ten Years*, eds. G. H. Jacoby, & J. Barnes, *ASP Conf. Ser.*, **101**, 17
- Basko, M. M., & Sunyaev, R. A. 1976, *MNRAS*, **175**, 395
- Becker, P. A., & Wolff, M. T. 2007, *ApJ*, **654**, 435
- Becker, R. H., Rothschild, R. E., Boldt, E. A., et al. 1978, *ApJ*, **221**, 912
- Becker, P. A., Klochkov, D., Schönherr, G., et al. 2012, *A&A*, **544**, A123
- Bildsten, L., Chakrabarty, D., Chiu, J., et al. 1997, *ApJS*, **113**, 367
- Bissinger né Kühnel, M., Kreykenbohm, I., Ferrigno, C., et al. 2020, *A&A*, **634**, A99
- Blondin, J. M., Kallman, T. R., Fryxell, B. A., & Taam, R. E. 1990, *ApJ*, **356**, 591
- Blondin, J. M., Stevens, I. R., & Kallman, T. R. 1991, *ApJ*, **371**, 684
- Bozzo, E., Bernardini, F., Ferrigno, C., et al. 2017, *A&A*, **608**, A128
- Coburn, W., Heindl, W. A., Rothschild, R. E., et al. 2002, *ApJ*, **580**, 394
- de Kool, M., & Anzer, U. 1993, *MNRAS*, **262**, 726
- Doroshenko, V., Santangelo, A., & Suleimanov, V. 2011, *A&A*, **529**, A52
- Doroshenko, V., Santangelo, A., Kreykenbohm, I., & Doroshenko, R. 2012, *A&A*, **540**, L1
- Doroshenko, V., Santangelo, A., Nakahira, S., et al. 2013, *A&A*, **554**, A37
- Ducci, L., Sidoli, L., Mereghetti, S., Paizis, A., & Romano, P. 2009, *MNRAS*, **398**, 2152
- Eadie, G., Peacock, A., Pounds, K. A., et al. 1975, *MNRAS*, **172**, 35P
- El Mellah, I., Sundqvist, J. O., & Keppens, R. 2018, *MNRAS*, **475**, 3240
- El Mellah, I., Sander, A. A. C., Sundqvist, J. O., & Keppens, R. 2019, *A&A*, **622**, A189
- Ferrigno, C., Becker, P. A., Segreto, A., Mineo, T., & Santangelo, A. 2009, *A&A*, **498**, 825
- Fürst, F., Kreykenbohm, I., Pottschmidt, K., et al. 2010, *A&A*, **519**, A37
- Fürst, F., Pottschmidt, K., Wilms, J., et al. 2014a, *ApJ*, **780**, 133
- Fürst, F., Pottschmidt, K., Wilms, J., et al. 2014b, *ApJ*, **784**, L40
- Goldstein, G., Huenemoerder, D. P., & Blank, D. 2004, *AJ*, **127**, 2310
- Grinberg, V., Hell, N., El Mellah, I., et al. 2017, *A&A*, **608**, A143
- Haberl, F., & White, N. E. 1990, *ApJ*, **361**, 225
- Harrison, F. A., Craig, W. W., Christensen, F. E., et al. 2013, *ApJ*, **770**, 103
- Hemphill, P. B., Rothschild, R. E., Markowitz, A., et al. 2014, *ApJ*, **792**, 14
- HI4PI Collaboration (Ben Bekhti, N., et al.) 2016, *A&A*, **594**, A116
- Hiltner, W. A., Werner, J., & Osmer, P. 1972, *ApJ*, **175**, L19
- Houck, J. C., & Denicola, L. A. 2000, in *ISIS: An Interactive Spectral Interpretation System for High Resolution X-Ray Spectroscopy*, eds. N. Manset, C. Veillet, & D. Crabtree, *ASP Conf. Ser.*, **216**, 591
- Jaisawal, G. K., & Naik, S. 2016, *MNRAS*, **461**, L97
- Kaper, L., Hammerschlag-Hensberge, G., & Zuiderwijk, E. J. 1994, *A&A*, **289**, 846
- Kendziorra, E., Mony, B., Kretschmar, P., et al. 1992, in *Frontiers Science Series*, eds. Y. Tanaka, & K. Koyama, 51
- Klochkov, D., Horns, D., Santangelo, A., et al. 2007, *A&A*, **464**, L45
- Klochkov, D., Staubert, R., Santangelo, A., Rothschild, R. E., & Ferrigno, C. 2011, *A&A*, **532**, A126
- Kretschmar, P., Pan, H. C., Kendziorra, E., et al. 1997, *A&A*, **325**, 623
- Kretschmar, P., El Mellah, I., Martínez-Núñez, S., et al. 2021, *A&A*, **652**, A95
- Kreykenbohm, I., Kretschmar, P., Wilms, J., et al. 1999, *A&A*, **341**, 141
- Kreykenbohm, I., Coburn, W., Wilms, J., et al. 2002, *A&A*, **395**, 129
- Kreykenbohm, I., Wilms, J., Kretschmar, P., et al. 2008, *A&A*, **492**, 511
- Kühnel, M., Fürst, F., Pottschmidt, K., et al. 2017, *A&A*, **607**, A88
- La Barbera, A., Santangelo, A., Orlandini, M., & Segreto, A. 2003, *A&A*, **400**, 993
- Lamb, F. K., Pethick, C. J., & Pines, D. 1973, *ApJ*, **184**, 271
- Langer, S. H., & Rappaport, S. 1982, *ApJ*, **257**, 733
- Larsen, A. N., & Monakhov, E. V. 1996, *Nucl. Instrum. Methods Phys. Res. B*, **117**, 71
- Leahy, D. A. 1987, *A&A*, **180**, 275
- Legred, I., Chatziioannou, K., Essick, R., Han, S., & Landry, P. 2021, *Phys. Rev. D*, **104**, 063003
- Liao, Z., Liu, J., Zheng, X., & Gou, L. 2020, *MNRAS*, **492**, 5922
- Lomaeva, M., Grinberg, V., Guainazzi, M., et al. 2020, *A&A*, **641**, A144
- Madsen, K. K., Grefenstette, B. W., Pike, S., et al. 2020, *ArXiv e-prints* [arXiv:2005.00569]
- Maitra, C., & Paul, B. 2013, *ApJ*, **763**, 79
- Makishima, K., Mihara, T., Nagase, F., & Tanaka, Y. 1999, *ApJ*, **525**, 978
- Malacaria, C., Mihara, T., Santangelo, A., et al. 2016, *A&A*, **588**, A100
- Manousakis, A. 2011, PhD Thesis, Université de Genève, Switzerland
- Manousakis, A., & Walter, R. 2015, *A&A*, **575**, A58
- Martínez-Núñez, S., Torrejón, J. M., Kühnel, M., et al. 2014, *A&A*, **563**, A70
- McBride, V. A., Wilms, J., Coe, M. J., et al. 2006, *A&A*, **451**, 267
- McClintock, J. E., Rappaport, S., Joss, P. C., et al. 1976, *ApJ*, **206**, L99
- Mihara, T. 1995, PhD Thesis, Dept. of Physics, Univ. of Tokyo, Japan
- Müller, S., Ferrigno, C., Kühnel, M., et al. 2013, *A&A*, **551**, A6
- Mushtukov, A. A., Tsygankov, S. S., Serber, A. V., Suleimanov, V. F., & Poutanen, J. 2015a, *MNRAS*, **454**, 2714
- Mushtukov, A. A., Suleimanov, V. F., Tsygankov, S. S., & Poutanen, J. 2015b, *MNRAS*, **447**, 1847
- Nagase, F., Hayakawa, S., Makino, F., Sato, N., & Makishima, K. 1983, *PASJ*, **35**, 47
- Nespoli, E., Reig, P., & Zezas, A. 2012, *A&A*, **547**, A103
- Nishimura, O. 2014, *ApJ*, **781**, 30
- Odaka, H., Khangulyan, D., Tanaka, Y. T., et al. 2013, *ApJ*, **767**, 70
- Orlandini, M., Dal Fiume, D., Frontera, F., et al. 1998, *A&A*, **332**, 121
- Oskinova, L. M., Hamann, W. R., & Feldmeier, A. 2007, *A&A*, **476**, 1331
- Postnov, K. A., Gornostaev, M. I., Klochkov, D., et al. 2015, *MNRAS*, **452**, 1601
- Poutanen, J., Mushtukov, A. A., Suleimanov, V. F., et al. 2013, *ApJ*, **777**, 115
- Pradhan, P., Bozzo, E., Paul, B., Manousakis, A., & Ferrigno, C. 2019, *ApJ*, **883**, 116
- Quaintrell, H., Norton, A. J., Ash, T. D. C., et al. 2003, *A&A*, **401**, 313
- Reig, P., & Milonaki, F. 2016, *A&A*, **594**, A45
- Reig, P., & Nespoli, E. 2013, *A&A*, **551**, A1
- Rothschild, R. E., Kühnel, M., Pottschmidt, K., et al. 2017, *MNRAS*, **466**, 2752
- Sako, M., Liedahl, D. A., Kahn, S. M., & Paerels, F. 1999, *ApJ*, **525**, 921
- Santangelo, A., del Sordo, S., Segreto, A., et al. 1998, *A&A*, **340**, L55
- Sato, N., Hayakawa, S., Nagase, F., et al. 1986, *PASJ*, **38**, 731
- Schwarm, F. W., Schönherr, G., Falkner, S., et al. 2017, *A&A*, **597**, A3
- Shapiro, S. L., & Salpeter, E. E. 1975, *ApJ*, **198**, 671
- Sidoli, L., Paizis, A., Fürst, F., et al. 2015, *MNRAS*, **447**, 1299
- Staubert, R., Shakura, N. I., Postnov, K., et al. 2007, *A&A*, **465**, L25
- Staubert, R., Trümper, J., Kendziorra, E., et al. 2019, *A&A*, **622**, A61
- Suchy, S., Pottschmidt, K., Wilms, J., et al. 2008, *ApJ*, **675**, 1487
- Tanaka, Y. 1986, in *Radiation Hydrodynamics in Stars and Compact Objects*, eds. D. Mihalas, & K. H. A. Winkler (New York: Springer-Verlag), *Proc. IAU Colloq.*, **255**, 89
- Titarchuk, L. 1994, *ApJ*, **434**, 570
- Tsygankov, S. S., Rouco Escorial, A., Suleimanov, V. F., et al. 2019, *MNRAS*, **483**, L144
- van Kerkwijk, M. H., van Paradijs, J., & Zuiderwijk, E. J. 1995, *A&A*, **303**, 497
- van Loon, J. T., Kaper, L., & Hammerschlag-Hensberge, G. 2001, *A&A*, **375**, 498
- Verner, D. A., Ferland, G. J., Korista, K. T., & Yakovlev, D. G. 1996, *ApJ*, **465**, 487
- Vybornov, V., Klochkov, D., Gornostaev, M., et al. 2017, *A&A*, **601**, A126
- Watanabe, S., Sako, M., Ishida, M., et al. 2006, *ApJ*, **651**, 421
- Wilms, J., Allen, A., & McCray, R. 2000, *ApJ*, **542**, 914
- Yamamoto, T., Sugizaki, M., Mihara, T., et al. 2011, *PASJ*, **63**, S751

## Appendix A: Additional tables

Table A.1. Best-fit parameters for the time-averaged tested models for observation I.

Parameter	FDcut	FDcut (w/o 10 keV)	highcut (w/o 10 keV)	
$C_{\text{FPMA}}$	1	1	1	1
$C_{\text{FPMB}}$	$1.0203 \pm 0.0021$	$1.0203 \pm 0.0021$	$1.0203 \pm 0.0021$	$1.0204 \pm 0.0021$
$N_{\text{H},1}$ ( $10^{22} \text{ cm}^{-2}$ )	$34.0 \pm 1.0$	$34.4 \pm 1.0$	$36.4^{+1.0}_{-1.1}$	$35.2^{+0.9}_{-1.0}$
$N_{\text{H},2}$ ( $10^{22} \text{ cm}^{-2}$ )	fixed to 0.371	fixed to 0.371	fixed to 0.371	fixed to 0.371
$\Gamma$	$1.09 \pm 0.05$	$1.294^{+0.017}_{-0.033}$	$1.373^{+0.015}_{-0.017}$	$1.353 \pm 0.016$
$E_{\text{cut}}$ (keV)	$19.9^{+3.5}_{-2.0}$	$40^{+0}_{-5}$	$25.6^{+0.5}_{-0.4}$	$28.1^{+0.7}_{-1.0}$
$E_{\text{fold}}$ (keV)	$12.6^{+0.9}_{-0.8}$	$10.5^{+1.0}_{-0.7}$	$15.0^{+0.7}_{-0.6}$	$16.0^{+1.2}_{-1.0}$
$E_{\text{CRSF,F}}$ (keV)	$24.7^{+1.0}_{-0.9}$	$27.38^{+0.26}_{-0.29}$	$25.8^{+0.5}_{-0.4}$	$27.6^{+0.5}_{-0.6}$
$\sigma_{\text{CRSF,F}}$ (keV)	$0.5 \times \sigma_{\text{CRSF,H}}$	$0.5 \times \sigma_{\text{CRSF,H}}$	$0.5 \times \sigma_{\text{CRSF,H}}$	$0.5 \times \sigma_{\text{CRSF,H}}$
$d_{\text{CRSF,F}}$ (keV)	$0.75^{+0.00}_{-0.19}$	$2.82^{+0.15}_{-0.61}$	$3.3 \pm 0.4$	$4.9^{+0.4}_{-0.5}$
$E_{\text{CRSF,H}}$ (keV)	$53.8^{+1.1}_{-0.9}$	$53.6 \pm 0.8$	$54.4 \pm 0.5$	$55.3 \pm 0.7$
$\sigma_{\text{CRSF,H}}$ (keV)	$7.9^{+1.3}_{-0.9}$	$10.9^{+0.4}_{-0.8}$	$8.7^{+2.0}_{-0.6}$	$10.7^{+0.5}_{-0.7}$
$d_{\text{CRSF,H}}$ (keV)	$18^{+6}_{-4}$	$38^{+4}_{-9}$	$19.4^{+14.0}_{-2.9}$	$33 \pm 6$
$E_{\text{FeK}\alpha}$ (keV)	$6.364 \pm 0.012$	$6.365 \pm 0.012$	$6.365 \pm 0.012$	$6.367 \pm 0.012$
$A_{\text{FeK}\alpha}$ ( $\text{ph s}^{-1} \text{ cm}^{-2}$ )	$(1.35 \pm 0.11) \times 10^{-3}$	$(1.44 \pm 0.11) \times 10^{-3}$	$(1.39^{+0.13}_{-0.11}) \times 10^{-3}$	$(1.36 \pm 0.11) \times 10^{-3}$
$\sigma_{\text{FeK}\alpha}$ (keV)	$0.070^{+0.029}_{-0.045}$	$0.084^{+0.027}_{-0.033}$	$0.07^{+0.04}_{-0.05}$	$0.067^{+0.029}_{-0.053}$
$E_{10 \text{ keV}}$ (keV)	$9.5^{+0.6}_{-1.0}$	–	$8.00^{+0.27}_{-0.00}$	–
$A_{10 \text{ keV}}$ ( $\text{ph s}^{-1} \text{ cm}^{-2}$ )	$(-4.8^{+2.2}_{-4.8}) \times 10^{-3}$	–	$(4.8^{+2.1}_{-1.1}) \times 10^{-4}$	–
$\sigma_{10 \text{ keV}}$ (keV)	$3.2^{+1.0}_{-0.7}$	–	$0.40^{+0.32}_{-0.11}$	–
$\mathcal{F}_{3-79 \text{ keV}}$ ( $\text{keV s}^{-1} \text{ cm}^{-2}$ )	$3.43^{+0.10}_{-0.05}$	$3.91^{+0.05}_{-0.21}$	$3.642^{+0.012}_{-0.053}$	$3.92^{+0.10}_{-0.11}$
CF	$0.883 \pm 0.005$	$0.898 \pm 0.004$	$0.8979^{+0.0031}_{-0.0030}$	$0.901 \pm 0.004$
$\chi^2/\text{dof}$	613.37/456	692.60/459	617.16/456	698.07/459

**Table A.2.** Best-fit parameters for the time-averaged tested models for observation I.

Parameter	single compTT	single compTT (w/o 10 keV)	double compTT	NPEX (w/o 10 keV)	
$C_{\text{FPMA}}$	1	1	1	1	1
$C_{\text{FPMB}}$	$1.0203 \pm 0.0021$	$1.0203 \pm 0.0021$	$1.0203 \pm 0.0021$	$1.0203 \pm 0.0021$	$1.0203 \pm 0.0021$
$N_{\text{H},1}$ ( $10^{22} \text{ cm}^{-2}$ )	$37.0^{+1.3}_{-1.4}$	$35.8 \pm 1.1$	$35.5 \pm 1.2$	$34.3 \pm 1.1$	$34.3 \pm 1.0$
$N_{\text{H},2}$ ( $10^{22} \text{ cm}^{-2}$ )	fixed to 0.371	fixed to 0.371	fixed to 0.371	fixed to 0.371	fixed to 0.371
$\Gamma_1$	–	–	–	$-0.51 \pm 0.14$	$-0.71 \pm 0.04$
$\Gamma_{1,\text{norm}}$	–	–	–	$0.164^{+0.039}_{-0.030}$	$0.167 \pm 0.010$
$\Gamma_2$	–	–	–	fixed to 2	fixed to 2
$\Gamma_{2,\text{norm}}$	–	–	–	$(1.3^{+0.6}_{-0.5}) \times 10^{-3}$	$(1.07^{+0.11}_{-0.10}) \times 10^{-4}$
$E_{\text{cut}}$ (keV)	–	–	–	$6.33^{+0.38}_{-0.29}$	$7.75^{+0.34}_{-0.30}$
$\text{compTT}_{\text{norm},1}$	$0.0559^{+0.0032}_{-0.0028}$	$0.0541^{+0.0024}_{-0.0023}$	$0.052^{+0.009}_{-0.025}$	–	–
$T_{0,1}$ (keV)	$0.94^{+0.05}_{-0.07}$	$1.000^{+0.000}_{-0.008}$	$1.000^{+0.000}_{-0.018}$	–	–
$kT_1$ (keV)	$8.3^{+0.5}_{-0.4}$	$8.2 \pm 0.5$	$6.9^{+0.4}_{-0.8}$	–	–
$\tau_1$	$10.43 \pm 0.22$	$10.52^{+0.23}_{-0.22}$	$11.9^{+1.2}_{-0.9}$	–	–
$\text{compTT}_{\text{norm},2}$	–	–	$(6^{+25}_{-5}) \times 10^{-3}$	–	–
$T_{0,2}$ (keV)	–	–	fixed to $T_{0,1}$	–	–
$kT_2$ (keV)	–	–	$12.3^{+2.7}_{-4.2}$	–	–
$\tau_2$	–	–	$6.6^{+6.5}_{-1.6}$	–	–
$E_{\text{CRSF,F}}$ (keV)	$26.29^{+0.31}_{-0.00}$	$26.2 \pm 0.4$	$24.9^{+0.8}_{-0.6}$	$27.9 \pm 0.7$	$26.62 \pm 0.29$
$\sigma_{\text{CRSF,F}}$ (keV)	$0.5 \times \sigma_{\text{CRSF,H}}$	$0.5 \times \sigma_{\text{CRSF,H}}$	$0.5 \times \sigma_{\text{CRSF,H}}$	$0.5 \times \sigma_{\text{CRSF,H}}$	$0.5 \times \sigma_{\text{CRSF,H}}$
$d_{\text{CRSF,F}}$ (keV)	$2.7 \pm 0.7$	$2.7 \pm 0.8$	$0.85^{+0.44}_{-0.20}$	$18.7^{+2.4}_{-3.0}$	$3.6^{+0.8}_{-0.7}$
$E_{\text{CRSF,H}}$ (keV)	$54.9 \pm 0.9$	$54.9 \pm 1.0$	$53.6^{+1.0}_{-0.8}$	$51.7^{+1.2}_{-1.0}$	$54.5 \pm 0.8$
$\sigma_{\text{CRSF,H}}$ (keV)	$11.0^{+0.9}_{-1.0}$	$11.0^{+1.0}_{-1.1}$	$7.6^{+1.3}_{-0.8}$	$14.2^{+0.4}_{-0.0}$	$11.5 \pm 0.8$
$d_{\text{CRSF,H}}$ (keV)	$36^{+10}_{-9}$	$35^{+11}_{-10}$	$16.2^{+5.9}_{-3.0}$	$83 \pm 10$	$40^{+10}_{-8}$
$E_{\text{FeK}\alpha}$ (keV)	$6.368 \pm 0.012$	$6.368 \pm 0.012$	$6.368 \pm 0.012$	$6.364 \pm 0.012$	$6.365 \pm 0.012$
$A_{\text{FeK}\alpha}$ ( $\text{ph s}^{-1} \text{ cm}^{-2}$ )	$(1.44^{+0.12}_{-0.11}) \times 10^{-3}$	$(1.37 \pm 0.11) \times 10^{-3}$	$(1.40 \pm 0.11) \times 10^{-3}$	$(1.36 \pm 0.11) \times 10^{-3}$	$(1.40 \pm 0.11) \times 10^{-3}$
$\sigma_{\text{FeK}\alpha}$ (keV)	$0.084^{+0.027}_{-0.034}$	$0.076^{+0.028}_{-0.037}$	$0.082^{+0.027}_{-0.035}$	$0.072^{+0.029}_{-0.042}$	$0.078^{+0.028}_{-0.037}$
$E_{10\text{keV}}$ (keV)	$8.39^{+0.26}_{-0.20}$	–	–	$9.8^{+0.5}_{-0.8}$	–
$A_{10\text{keV}}$ ( $\text{ph s}^{-1} \text{ cm}^{-2}$ )	$(5.3^{+3.1}_{-2.4}) \times 10^{-4}$	–	–	$-0.37 \pm 0.11$	–
$\sigma_{10\text{keV}}$ (keV)	$0.71^{+0.23}_{-0.20}$	–	–	$6.6^{+0.5}_{-0.4}$	–
CF	$0.842^{+0.014}_{-0.012}$	$0.831^{+0.005}_{-0.004}$	$0.830 \pm 0.005$	$0.878 \pm 0.010$	$0.882 \pm 0.005$
$\chi^2/\text{dof}$	604.45/456	630.30/459	622.53/456	604.15/456	644.55/459

# Observing the onset of the accretion wake in Vela X-1

C. M. Diez<sup>1</sup>, V. Grinberg<sup>2</sup>, F. Fürst<sup>3</sup>, I. El Mellah<sup>4</sup>, M. Zhou (周孟磊)<sup>1</sup>,  
A. Santangelo<sup>1</sup>, S. Martínez-Núñez<sup>5</sup>, R. Amato<sup>6</sup>, N. Hell<sup>7</sup>, and P. Kretschmar<sup>8</sup>

<sup>1</sup> Institut für Astronomie und Astrophysik, Universität Tübingen, Sand 1, 72076 Tübingen, Germany  
e-mail: diez@astro.uni-tuebingen.de

<sup>2</sup> European Space Agency (ESA), European Space Research and Technology Centre (ESTEC), Keplerlaan 1, 2201 AZ Noordwijk, The Netherlands

<sup>3</sup> Quasar Science Resources S.L for European Space Agency (ESA), European Space Astronomy Centre (ESAC), Camino Bajo del Castillo s/n, 28692 Villanueva de la Cañada, Madrid, Spain

<sup>4</sup> Université Grenoble Alpes, CNRS, IPAG, 38000 Grenoble, France

<sup>5</sup> Instituto de Física de Cantabria (CSIC-Universidad de Cantabria), 39005, Santander, Spain

<sup>6</sup> IRAP, CNRS, Université de Toulouse, CNES, 9 Avenue du Colonel Roche, 31028 Toulouse, France

<sup>7</sup> Lawrence Livermore National Laboratory, 7000 East Avenue, Livermore, CA 94550, USA

<sup>8</sup> European Space Agency (ESA), European Space Astronomy Centre (ESAC), Camino Bajo del Castillo s/n, 28692 Villanueva de la Cañada, Madrid, Spain

Received 16 December 2022 / Accepted 16 March 2023

## ABSTRACT

High-mass X-ray binaries (HMXBs) offer a unique opportunity to investigate accretion onto compact objects and the wind structure in massive stars. A key source for such studies is the bright neutron star HMXB Vela X-1 whose convenient physical and orbital parameters facilitate analyses and in particular enable studies of the wind structure in HMXBs. Here, we analyse simultaneous *XMM-Newton* and *NuSTAR* observations at  $\phi_{\text{orb}} \approx 0.36\text{--}0.52$  and perform time-resolved spectral analysis down to the pulse period of the neutron star based on our previous *NuSTAR*-only results. For the first time, we are able to trace the onset of the wakes in a broad 0.5–78 keV range with a high-time resolution of  $\sim 283$  s and compare our results with theoretical predictions. We observe a clear rise in the absorption column density of the stellar wind  $N_{\text{H},1}$  starting at orbital phase  $\sim 0.44$ , corresponding to the wake structure entering our line of sight towards the neutron star, together with local extrema throughout the observation, which are possibly associated with clumps or other structures in the wind. Periods of high absorption reveal the presence of multiple fluorescent emission lines of highly ionised species, mainly in the soft-X-ray band between 0.5 and 4 keV, indicating photoionisation of the wind.

**Key words.** X-rays: binaries – stars: neutron – stars: winds, outflows

## 1. Introduction

The prototypical eclipsing high-mass X-ray binary (HMXB) Vela X-1 is one of the brightest persistent point sources in the X-ray sky despite a moderate mean intrinsic luminosity of  $5 \times 10^{36}$  erg s<sup>-1</sup> (Fürst et al. 2010). It lies at a relatively short distance of  $1.99^{+0.13}_{-0.11}$  kpc; see the review by Kretschmar et al. (2021) and references therein for this and other system parameters quoted in Sect. 1. The system consists of a B0.5 Ib supergiant, HD 77581 (Hiltner et al. 1972), orbited by an accreting neutron star with an orbital period of  $\sim 8.964$  days (Kreykenbohm et al. 2008; Falanga et al. 2015). The mass and radius of HD 77581 have been estimated by different authors to be between  $\sim 20$  and  $\sim 26 M_{\odot}$  and between  $\sim 27$  and  $\sim 32 R_{\odot}$  (Table 4 in Kretschmar et al. 2021). A strong stellar wind with a mass-loss rate of  $\sim 10^{-6} M_{\odot} \text{ yr}^{-1}$  (e.g. Watanabe et al. 2006; Falanga et al. 2015; Giménez-García et al. 2016) fuels the accretion of matter onto the neutron star and the pulsating X-ray emission with a fluctuating pulse period of  $\sim 283$  s. The mass of the neutron star is estimated to be  $\sim 1.7\text{--}2.1 M_{\odot}$ , which is on the heavier side of the typical mass distribution; see Table 4 in Kretschmar et al. (2021), and especially the estimates by Rawls et al. (2011) and Falanga et al. (2015).

As the orbital separation of the two components is only  $\sim 1.7 R_{\star}$  (van Kerkwijk et al. 1995; Quaintrell et al. 2003),

the neutron star is deeply embedded in the dense wind of the supergiant and significantly influences the wind flow. Due to the high inclination of the system of  $>73^{\circ}$  (Joss & Rappaport 1984; van Kerkwijk et al. 1995, and others), observations at different orbital phases can sample different structures in the stellar wind as modified by the interaction with the neutron star. One notable feature is the varying absorption as a function of orbital phase, which was detected by many authors (see the overview Fig. 5 of Kretschmar et al. 2021). They found a typical decrease in the absorption after eclipse up to an orbital phase of 0.2–0.3 (Martínez-Núñez et al. 2014; Lewis et al. 1992) followed by a sometimes steep increase in the phase range of 0.4–0.6 (Haberl & White 1990), with a varying location in phase in individual observations and with generally high absorption at later orbital phases (Sato et al. 1986; Haberl & White 1990).

In addition to the variations in observed flux due to X-ray absorption, wind-accreting X-ray pulsars also usually show significant variability of the intrinsic X-ray flux caused by a complex interplay of factors, such as variations in the density of the accreted material and possible inhibition of accretion by interactions at the magnetosphere. (Martínez-Núñez et al. 2017). For individual observations, especially at softer X-ray energies, it is not always evident to distinguish absorption variations from those of the intrinsic emission. A study of variability in Vela X-1 by Fürst et al. (2010) based on INTEGRAL data in the hard



X-ray band, which is only very slightly affected by absorption, found a log-normal distribution of the intrinsic flux values. On various occasions ‘low states’ or ‘off-states’ have been observed (see Table 1 in Kretschmar et al. 2021, with multiple references), but again not always with a clear distinction of intrinsic X-ray brightness versus high absorption.

Early on in the history of observations of this source, X-ray observations and optical-emission-line evidence suggested a wake structure trailing the X-ray source in the binary system (see references in Conti 1978). These structures can be caused by multiple processes. The neutron star moving highly supersonically through the dense stellar wind will lead to a bow shock with a trailing accretion wake. Photoionisation of the wind by the bright X-ray source can lead to the formation of a shock between the accelerating wind and the stalling photoionised plasma (Fransson & Fabian 1980), which can then lead to a trailing spiral structure, the photoionisation wake. X-ray heating and radiative cooling of the wind (Kallman & McCray 1982; Blondin et al. 1990) can create additional instabilities and filamentary structures, leading to stronger short-term variations. Tidal deformation of the mass donor can lead to enhanced wind flux in the direction of the neutron star, even if it does not fill its Roche Lobe. For close systems, this can develop into a dense ‘tidal stream’ (Blondin et al. 1991), which when deflected by coriolis force tends to pass behind the compact object, which explains the high absorption at later orbital phases. The density enhancement from such a tidal stream would be expected to be quite stable in orbital phase, while variations caused by an accretion wake would vary from orbit to orbit. According to Blondin (1994), in a specific system, there would be either a tidal stream between the star and the neutron star, or a photoionisation wake trailing the neutron star.

Vela X-1 has also been studied via X-ray line spectroscopy. Early studies (e.g. Becker et al. 1978; Ohashi et al. 1984) mainly focused on the pronounced iron-line complex visible also very clearly in eclipse. A broad FeK $\alpha$  emission line was also found by Sato et al. (1986), but these authors suspected further contributions to the overall line intensity from FeK $\beta$  as well as from fluorescent K $\alpha$  lines of Si, S, Ar, Ca, and Ni. Further elements have been reported from spectra taken during or close to eclipse (Nagase et al. 1994; Sako et al. 1999; Schulz et al. 2002), including recombination lines and radiative recombination continua (RRC), as well as fluorescence lines. The variety of observed ionisation states is a strong indication of the presence of an inhomogeneous wind with optically thick, less ionised matter coexisting with warm photoionised plasma. *Chandra*/HETGS spectra from three orbital phases (0, 0.25 and 0.5) were analysed by Goldstein et al. (2004) and Watanabe et al. (2006), who found an eclipse-like spectrum around orbital phase 0.5, while the spectrum was dominated by the continuum around phase 0.25. Grinberg et al. (2017) revisited the observation at phase 0.25, analysing time intervals of low and high spectral hardness (i.e. different levels of absorption) separately and detected line features from high- and low-ionisation species of Si, Mg, and Ne, as well as strongly variable absorption. This again implied the presence of both cool and hot gas phases, possibly from the combination of an intrinsically clumpy stellar wind and a highly structured accretion flow close to the compact object. Analysing the grating spectrometer data of a long *XMM-Newton* observation at early orbital phases, Lomaeva et al. (2020) found emission lines corresponding to highly ionised O, Ne, Mg, and Si as well as RRC of O. In addition, these authors found potential absorption lines of Mg at a lower ionisation stage and features identified as iron L lines.

In our targeted observing programme with *XMM-Newton* and *NuSTAR*, we aimed to cover an interesting binary phase range in which we expect strong changes in absorption while the accretion and ionisation wakes are crossing the line of sight of the observer (Grinberg et al. 2017). In our previous work with *NuSTAR* (Diez et al. 2022), we observed strong absorption variability along the orbital phase. However, an in-depth study of the varying absorption cannot be explored with *NuSTAR* alone as we need coverage at lower energies, which is possible with *XMM-Newton*. On the other hand, *XMM-Newton* alone is not sufficient and we need *NuSTAR* to constrain the continuum, hence the necessity for simultaneous observation.

We introduce the datasets and their reduction in Sect. 2 followed by a presentation of the light curves extracted in different relevant energy bands in Sect. 3. Using the results, we proceed to the time-resolved spectral analysis in Sect. 4 and finally discuss our results in Sect. 5, focusing on the absorption variability. A summary is given in Sect. 6 and in Appendix A we describe the calibration issues we faced during this work between *NuSTAR* and *XMM-Newton* in detail.

## 2. Observation and data reduction

Vela X-1 was observed on 3–5 May 2019 as the science target of a simultaneous campaign with *XMM-Newton* and *NuSTAR*. We used the European Photon Imaging Camera pn-CCDs (EPIC-pn; Strüder et al. 2001), the EPIC Metal Oxide Semiconductor (EPIC-MOS; Turner et al. 2001), and the Reflection Grating Spectrometers (RGS; den Herder et al. 2001) on board *XMM-Newton* (Jansen et al. 2001) under Obs ID 0841890201. The *NuSTAR* data under Obs ID 30501003002 were analysed in Diez et al. (2022). In the present paper, we focus on the simultaneous analysis of the new EPIC-pn data with our previous *NuSTAR* work (updated with the current calibration files and software) in order to obtain a broadband mapping of the stellar wind along the orbital phase of the neutron star around the companion star. The simultaneous RGS data will be explored in a later work. Details about the observation are given in Table 1 and a sketch of the system during this observation is shown in Fig. 1. We note the much larger net *XMM-Newton* EPIC-pn exposure due to the low Earth orbit (LEO) of *NuSTAR*.

The orbital phases  $\phi_{\text{orb}}$  are obtained with the ephemeris in Table 2 from Diez et al. (2022), which is derived from Kreykenbohm et al. (2008) and Bildsten et al. (1997) and where  $\phi_{\text{orb}} = 0$  is defined as  $T_{90}$ . The time of phase zero is usually defined using  $T_{90}$  (the time when the mean longitude  $l$  is equal to  $90^\circ$ ) or by  $T_{\text{ecl}}$  (the mid-eclipse time). Explanations on how to convert  $T_{90}$  to  $T_{\text{ecl}}$  can be found in Kreykenbohm et al. (2008). Table 1 also provides orbital phases with  $T_{\text{ecl}}$ . In this work, we exclusively use  $T_{90}$  and all the mentioned times are corrected for the binary orbit.

We use HEASOFTv6.30.1, and to analyse the data, we use the Interactive Spectral Interpretation System (ISIS) v1.6.2-51 (Houck & Denicola 2000). ISIS provides access to XSPEC (Arnaud 1996) models that are referenced later in the text.

### 2.1. *NuSTAR*

We used the NuSTARDAS pipeline (nupipeline) v2.1.2 with the calibration database (CALDB) v20220608 applied with the clock correction. We proceeded to the extraction of the products as in Diez et al. (2022), using the updated pipeline and

**Table 1.** Observations log.

Instrument	Obs ID	Time start		Time stop		Exposure (ks)	Orbital phase (with $T_{90}$ )	Orbital phase (with $T_{\text{ecl}}$ )
		MJD (day)	binarycor <sup>(a)</sup>	MJD (day)	binarycor <sup>(a)</sup>			
<i>NuSTAR</i>	30501003002	58606.8688		58608.2465		40.562	0.36–0.52	0.34–0.49
<i>XMM-Newton</i>	0841890201	58606.9283		58608.2146		109.311	0.37–0.51	0.34–0.48

**Notes.** <sup>(a)</sup>Stands for ‘binary-corrected’ times. The BinaryCor tool in ISIS removes the influence of the double-star motion for circular or elliptical orbits. The Git repository of the `isisscripts` where the BinaryCor function is described at <https://www.sternwarte.uni-erlangen.de/gitlab/remeis/isisscripts/-/blame/6216a4ab8307f5825e17109db3cfb5c317a7ab08/share/isisscripts.sl>. The start and stop times are given as modified Julian dates (MJD).

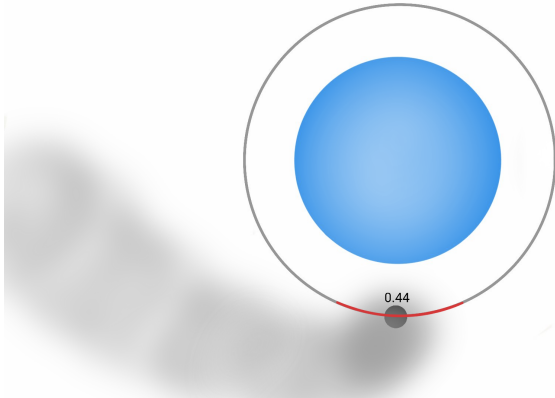


**Fig. 1.** Sketch of Vela X-1 showing the orbital phases covered during this *XMM-Newton* EPIC-pn observation. In this image, the observer is located facing the system at the bottom of the picture.

calibration files mentioned above. Briefly, we extracted a spectrum for every orbit of *NuSTAR* around the Earth and for every rotation of the neutron star with the previously derived pulse period of  $\sim 283$  s. For the extraction of the source region, we used a smaller radius of  $\sim 60$  arcsec to minimise the impact of the background. The uncertainties are given at 90% confidence and the events were barycentred using the `barycorr` tool from the NUSTARDAS pipeline. The spectra were rebinned within ISIS to a minimal signal-to-noise ratio (S/N) of 5, adding at least 2, 3, 5, 8, 16, 18, 48, 72, and 48 channels for energies in the ranges 3.0–10, 10–15, 15–20, 20–35, 35–45, 45–55, 55–65, 65–76, and 76–79 keV, respectively, as in our previous work.

## 2.2. *XMM-Newton*

The observation was setup in pn-timing mode with a thin filter. For the generation of the event lists file, we used the Science Analysis System (SAS) software v20.0 with the Current Calibration Files (CCF) as of April 2022 starting from Observation Data Files (ODFs) level running `epproc`<sup>1</sup>.

The default calibration uses `withrdpha='Y'` and `runepfast='N'` as of SASv14.0<sup>2</sup>. However, this default timing mode calibration led us to an offset of the instrumental and physical lines of the source towards higher energies of

<sup>1</sup> <https://xmm-tools.cosmos.esa.int/external/sas/current/doc/epproc/node8.html>

<sup>2</sup> See the *XMM-Newton* CCF Release Note 0369 (Migliari S., Smith M., 2019, XMM-CAL-SRN-0369) <https://xmmweb.esac.esa.int/docs/documents/CAL-SRN-0369-0-0.pdf>

$\sim +140$  eV (see Appendix A.1). Therefore, after consulting with the *XMM-Newton* calibration team (S. Migliari, priv. comm.), we decided to instead turn off the Rate-Dependent PHA (RDPHA) correction (`withrdpha='N'`) and apply the Rate-Dependent CTI (RDCTI) correction using `epfast` (`runepfast='Y'`), resulting in satisfactory spectra.

No filtering for flaring particle background was necessary. Because the source was so bright that it illuminated the whole CCD detector, no background was extracted. The event times were barycentred using the `barycen` tool from the SAS pipeline and were deleted if found to be on bad pixels with the `#XMMEA_EP` argument in the `evselect` step.

As *XMM-Newton* EPIC-pn and *NuSTAR* observations were simultaneous, we were able to reuse the pulse period previously derived on the FPMA light curve,  $P = 283.4447 \pm 0.0004$  s (Diez et al. 2022), to extract the *XMM-Newton* light curves in order to avoid intrinsic pulse variability. For a sanity check, we still performed epoch folding on the *XMM-Newton* light curve with 1 s binning and indeed derived the exact same pulse period as in our previous work.

We selected single and double pixel events (`PATTERN<=4` in the `evselect` step) in the source region from `RAWX=32` to `RAWX=44`. We removed the outermost parts of the point spread function (PSF) wings to reduce the influence of background noise or possible dust scattering effects. The count rate of the overall observation on different energy bands was sufficiently high to select a region of only 13 pixels centred around the maximum of the PSF. We applied the task `epic1ccorr` to perform absolute and relative corrections.

## 2.3. Spectrum extraction and pile-up

For the extraction of the spectra, we performed the same selection of events as above, but we also deleted events close to CCDs gaps or bad pixels (`FLAG==0` in the `evselect` step). An update to the EPIC effective area was made available in April 2022 to improve the cross-calibration between *XMM-Newton* and *NuSTAR* as of April 5, 2022<sup>3</sup>. As we want to compare our *XMM-Newton* results to our previous *NuSTAR* ones, we activated this correction using the `applyabsfluxcorr=yes` argument in the `arfgen` step. All spectra were rebinned using the optimal rebinning approach of Kaastra & Bleeker (2016).

Because of the high count rate (see Sect. 3), the data were strongly affected by pile-up (Jethwa et al. 2015), in particular at the centre of the PSF. To test and evaluate for pile-up in our observation, we used the `epatplot` task to read the

<sup>3</sup> See the *XMM-Newton* Science Operations Team Calibration Technical Note 0230 (Fürst F., 2022, XMM-SOC-CAL-TN-0230) <https://xmmweb.esac.esa.int/docs/documents/CAL-TN-0230-1-3.pdf>

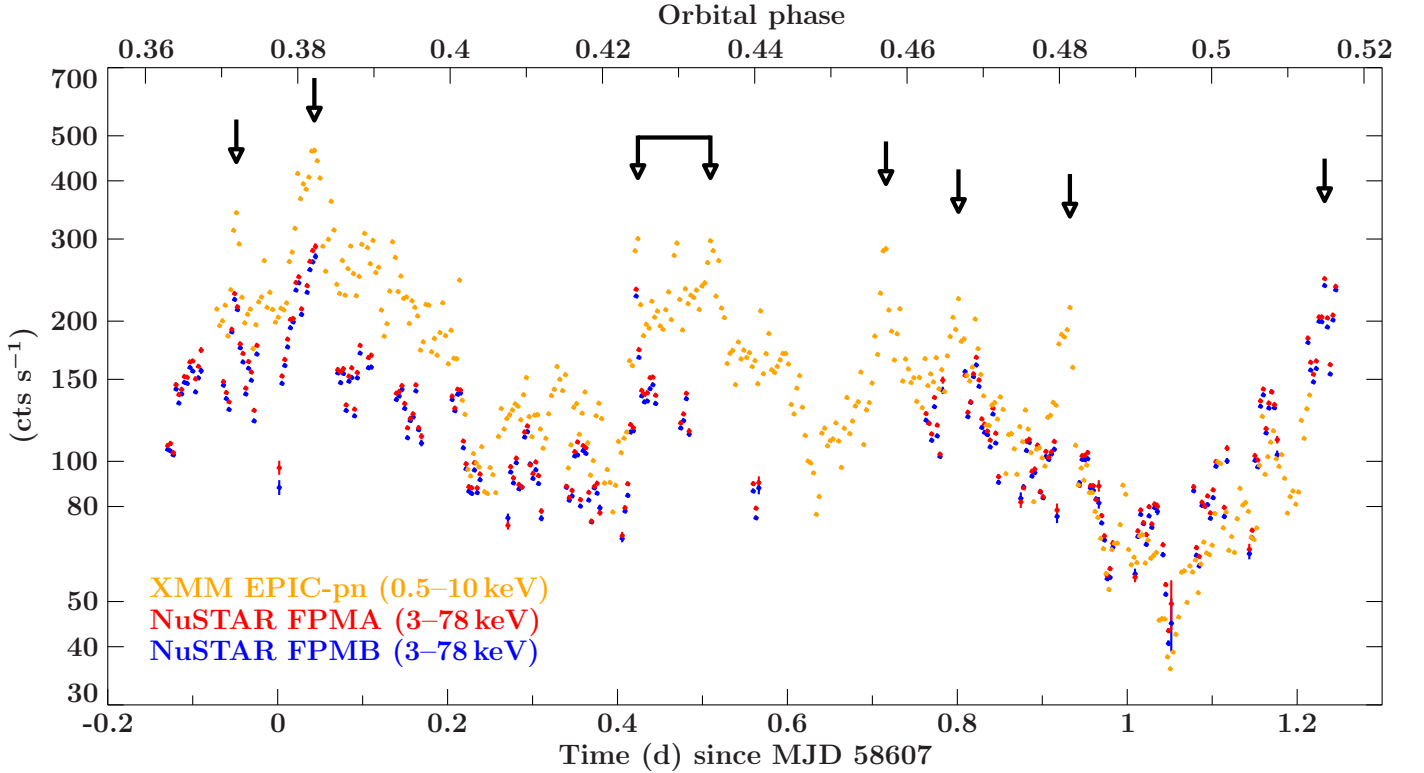


**Fig. 2.** Light curves for *XMM-Newton* EPIC-pn (orange), *NuSTAR* FPMA (red), and FPMB (blue) with a time resolution of  $P = 283.44$  s. The count rate is plotted on the y-axis in logarithmic scale against the orbital phase (top axis) and the time of the observation (bottom axis). Major short flares are indicated by single arrows. The connected arrows at  $\sim 58607.42$  MJD indicate a flaring episode of  $\sim 8$  ks.

pattern information statistics of the input EPIC-pn set as a function of PI channel. As an additional sanity check, we performed an energy test on the iron line region (for more details, see Appendix A.2). According to the results of these tests, we decided to exclude the three centremost columns of the PSF (RAWX 37–38–39). Moreover, we excluded spectral channels below 0.5 keV and above 10 keV from the analysis where the S/N was very low.

We use this work to also report some cross-calibration issues between *NuSTAR* and *XMM-Newton* EPIC-pn. Cross-calibration issues between *XMM-Newton* EPIC-pn and *NuSTAR* are a known phenomenon when combining datasets from both observatories<sup>3</sup> (see e.g. Gokus 2017) and the *XMM-Newton* Science Operations Centre is working on this issue with an upcoming update of the SAS software (S. Migliari, priv. comm.). At the time of writing, no release is available, and so we describe the cross-instrumental issues in Appendix A.3 and how we coped with them for our analysis in Sect. 4.2.

### 3. Light curves and timing

#### 3.1. Pulse period and average light curves

Strong flux variability was detected in Vela X-1 during this observation with timescales ranging from several kiloseconds down to the pulse period of the neutron star. To study the overall system behaviour, we present the 0.5–10 keV *XMM-Newton* EPIC-pn light curve in Fig. 2 together with the *NuSTAR* FPMA and FPMB 3–78 keV light curves.

The ratio of the *XMM-Newton* EPIC-pn count rate by the *NuSTAR* FPMA-FPMB count rate is not constant. During the first half of the observation (until  $T_{\text{obs}} \approx 58607.60$  MJD),

the average *XMM-Newton* EPIC-pn count rate is  $\sim 30\%$  higher than the *NuSTAR* one. Their ratio stabilises around 1 during the second half of the observation when the wakes are coming through our line of sight (see Fig. 1) and therefore when the absorption from the stellar wind is more prominent. As *XMM-Newton* EPIC-pn covers lower energies than *NuSTAR*, we expect it to be more affected by the absorption due to the stellar wind, explaining this behaviour.

All the major flares detected are indicated by arrows in Fig. 2. We can observe three flares happening simultaneously with both *NuSTAR* and *XMM-Newton* EPIC-pn at  $T_{\text{obs}} \approx 58606.95$  MJD,  $T_{\text{obs}} \approx 58607.04$  MJD, and  $T_{\text{obs}} \approx 58607.42$  MJD, and a fourth flare visible at  $T_{\text{obs}} \approx 58608.23$  MJD covered by *NuSTAR* only, as expected in Diez et al. (2022). With the new addition of EPIC-pn data, we can retrieve the data between  $T_{\text{obs}} \approx 58607.57$  MJD and  $T_{\text{obs}} \approx 58607.76$  MJD, which were lost during the *NuSTAR* campaign, and also retrieve data during the eclipses of the *NuSTAR* instrument. Therefore, we can observe three new flares at  $T_{\text{obs}} \approx 58607.72$  MJD,  $T_{\text{obs}} \approx 58607.80$  MJD, and  $T_{\text{obs}} \approx 58607.93$  MJD, together with the flare at  $T_{\text{obs}} \approx 58607.42$  MJD, which is longer than what was seen with *NuSTAR*. This flare lasts  $\sim 8$  ks and reaches  $\sim 300$  counts  $\text{s}^{-1}$  which is almost as long as but brighter than the flaring period in Martínez-Núñez et al. (2014). The timescales of the flares appear to be from less than a *NuSTAR* eclipse ( $\sim 2.5$  ks) up to  $\sim 8$  ks. The brightest observed flare at  $T_{\text{obs}} \approx 58607.04$  MJD reaches  $\sim 465$  counts  $\text{s}^{-1}$  with EPIC-pn.

#### 3.2. Energy-resolved light curves

To estimate the influence of the stellar-wind absorption on the observed count-rate variations, we extract the light curves in the relevant energy bands. In Diez et al. (2022), we saw a

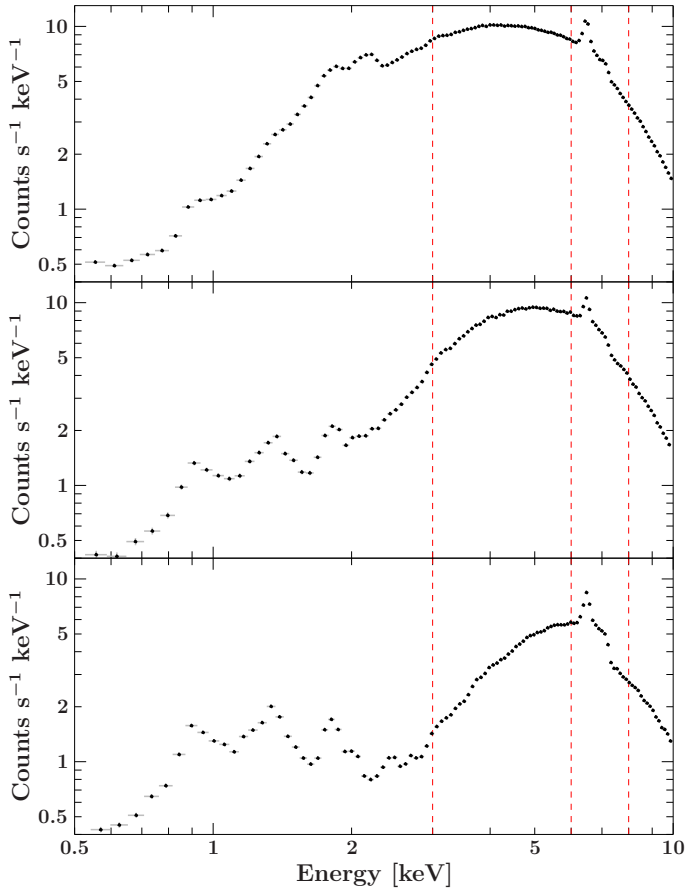


**Fig. 3.** *XMM-Newton* EPIC-pn spectra extracted during the three different phases of the observation. These are shown in chronological order from the top to the bottom panel: Phase of stable hardness ratio ( $0.37 \leq \phi_{\text{orb}} \leq 0.44$ ), phase of the loss of *NuSTAR* data ( $0.44 \leq \phi_{\text{orb}} \leq 0.46$ ), and phase of the rise of the hardness ratio ( $0.46 \leq \phi_{\text{orb}} \leq 0.51$ ), respectively. The vertical red dashed lines indicate the four energy bands we chose for the extraction of the energy-resolved light curves.

change in the hardness ratio between the 3.0–5.0 keV and 20.0–30.0 keV energy bands, roughly separating the observation into three noticeable phases: stable hardness ratio from the beginning of the observation to  $T_{\text{obs}} \approx 58607.57$  MJD, followed by the loss of the *NuSTAR* data until  $T_{\text{obs}} \approx 58607.76$  MJD, and finally the rise of the hardness ratio until the end. Fig. 3 shows three different *XMM-Newton* EPIC-pn spectra taken during the above-mentioned phases of the observation. We can observe low-energy variability towards the end of the observation (last panel of the figure). As expected from the geometry of the system (see Fig. 1), when the wakes occupy most of the line of sight of the observer, the absorption from the wind is so strong that the emission lines of the material become visible (see e.g. Watanabe et al. 2006). From the last spectrum, we can even highlight four energy bands of interest. The first one, from 0.5 keV to 3.0 keV, covers all the low-energy emission lines. We choose the second energy band from 3.0 keV to 6.0 keV to account for the low-energy part of the continuum before the iron-line region from 6.0 keV to 8.0 keV. The last energy band covers the high-energy part of the continuum from 8.0 keV to 10.0 keV. This will help us to compare the photon count rate in different energy bands relative to the continuum to check for variability. We present a more detailed spectral analysis in Sect. 4.

We present the *XMM-Newton* EPIC-pn light curves in the above-mentioned energy bands in Fig. 4. All light curves show the same features and variability in all energy bands, but the flares and low states are more prominent at low energies, particularly in the 0.5–3.0 keV energy band where the brightest flare is approximately five times higher than the average count rate in that band ( $\sim 24$  counts  $\text{s}^{-1}$ ). We notice a corresponding trend for the low state at  $T_{\text{obs}} \approx 58607.24$  MJD, which is roughly five times smaller than the average count rate in the 0.5–3.0 keV band. The long and broad flare is visible in all energy bands but, again, is much more prominent in the 0.5–3.0 keV energy band and shows a rather stable plateau at  $\sim 40$  counts  $\text{s}^{-1}$ . In the two highest energy bands, the overall count rate stays relatively stable around the mean value of each individual light curve. This phenomenon was observed in a similar energy band, 1.0–3.0 keV, in Martínez-Núñez et al. (2014) and was associated with a stable spectral shape from the unabsorbed source.

### 3.3. Hardness ratios

For a more quantitative study of the source variability and in particular in an attempt to determine the origin of the variability shown in Vela X-1, we present the *XMM-Newton* EPIC-pn hardness ratios in Fig. 5. In the second panel, we observe a mirrored version of the light curve for the hardness ratio between the  $S = 0.5$ –3.0 keV and  $H = 8.0$ –10.0 keV bands. The minima of the hardness ratio correspond to the maxima of the light curve and vice versa. This shows that the observed flares of the light curve happen during the softening of the spectral shape, suggesting a contribution mainly from low-energy photons, as seen in Fig. 4. On the contrary, low states correspond to a hardening of the spectral shape, suggesting the major contribution is from high-energy photons. In the third panel, the hardness ratio between the  $S = 3.0$ –6.0 keV and  $H = 8.0$ –10.0 keV bands remains relatively constant until  $T_{\text{obs}} \approx 58607.60$  MJD ( $\phi_{\text{orb}} \approx 0.44$ ), with a local maximum at  $T_{\text{obs}} \approx 58607.24$  MJD ( $\phi_{\text{orb}} \approx 0.40$ ). The overall hardness ratio starts to increase after  $T_{\text{obs}} \approx 58607.60$  MJD ( $\phi_{\text{orb}} \approx 0.44$ ) until  $T_{\text{obs}} \approx 58607.93$  MJD ( $\phi_{\text{orb}} \approx 0.48$ ) followed by a steeper increasing slope until the end of the observation. This was expected from Diez et al. (2022) as we analysed similar energy bands for the hardness ratio: the 3.0–5.0 keV and 20.0–30.0 keV bands which also correspond to the low-energy and continuum parts of the spectrum, respectively. Finally, in the last panel of Fig. 5, the hardness ratio between the 6.0–8.0 keV and 8.0–10.0 keV bands is constant throughout the whole observation, showing no variation in the continuum as in Diez et al. (2022) and Martínez-Núñez et al. (2014).

In summary, it seems that the spectral shape gradually changes at low energies, which is particularly evident between 0.5 keV and 3.0 keV. This could be associated to changes in the behaviour of the absorbing material while the continuum emission from the neutron star seems to be stable.

Further insights into the role played by wind absorption come from a colour–colour diagram (Fig. 6) that shows a typical ‘nose’-like shape that has previously been associated with variable absorption in stellar wind, especially in Cyg X-1 (Nowak et al. 2011; Hirsch et al. 2019; Grinberg et al. 2020; Lai et al. 2022). We further discuss our modelling of the colour–colour diagram and its implications for the wind properties in Sect. 5.1.1. To further explore the behaviour of the source, a spectral analysis of the absorption column density on shorter timescales is necessary.

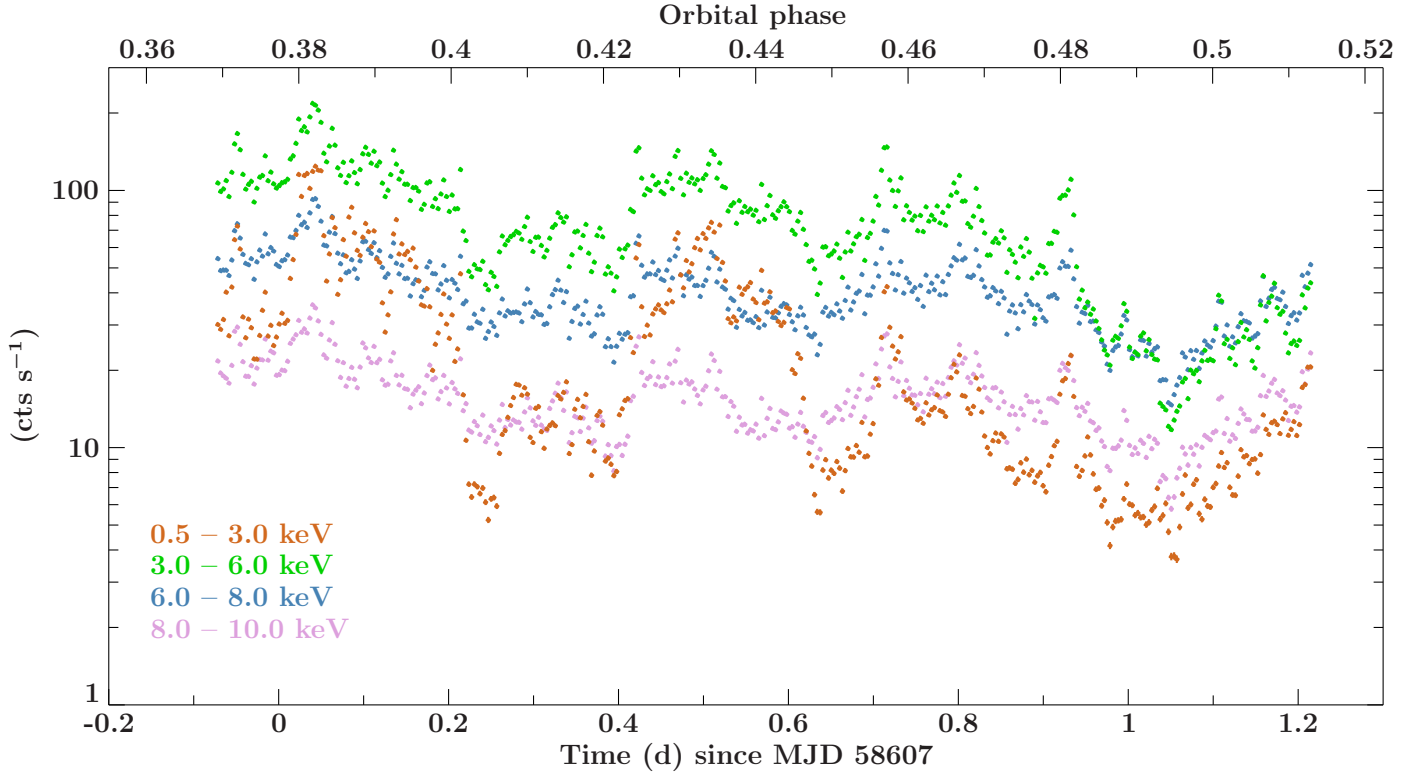


**Fig. 4.** Light curves for *XMM-Newton* EPIC-pn in different energy bands with a time resolution of  $P = 283.44$  s. The count rate shown on the y-axis in logarithmic scale is plotted against the orbital phase and the time of the observation. The energy bands are 0.5–3.0, 3.0–6.0, 6.0–8.0, 8.0–10.0 keV.

## 4. Spectral analysis

### 4.1. Definition of the spectral model

#### 4.1.1. Continuum shape

As this current *XMM-Newton* EPIC-pn work follows results from simultaneous observations analysed in our previous *NuSTAR* work, we decided to use the same continuum model for direct comparisons and homogeneous continuity of the work. The final continuum model we obtained is the following and we refer to Diez et al. (2022) for a detailed discussion on how this model was obtained:

$$I(E) = N_{\text{H},2} \times (\text{CF} \times N_{\text{H},1} + (1 - \text{CF})) \times (F(E) \times \text{CRSF}, F \times \text{CRSF}, \text{H} + \text{FeK}\alpha + 10 \text{ keV}). \quad (1)$$

The parameter  $N_{\text{H},2}$  accounts for the absorption column density from the interstellar medium and is fixed to  $3.71 \times 10^{21} \text{ cm}^{-2}$  using the NASA HEASARC  $N_{\text{H}}$  tool website<sup>4</sup> (HI4PI Collaboration 2016). The absorption  $N_{\text{H},1}$  corresponds to the stellar wind embedding the neutron star and is a free parameter. Those two absorption components are described by the tbabs model (Wilms et al. 2000) with the corresponding abundances and cross-sections from Verner et al. (1996).

The covering fraction (CF) quantifies the clumpy structure of the stellar wind and ranges between 0 (the obscurer does not cover the source) and 1 (the obscurer is fully covering the source). This is characteristic of a partial covering model, of which several flavours can be found in the literature (e.g. Martínez-Núñez et al. 2014; Fürst et al. 2014a; Malacaria et al.

2016), and was found to provide the best description of the clumpy absorber in Vela X-1.

The function  $F(E)$  describes the spectral continuum of the accreting neutron star and is empirically described by a power law with a high-energy cutoff (see e.g. Staubert et al. 2019). Several models from the literature may account for the description of the high-energy cutoff. Our best results were obtained with the FDcut high-energy cutoff, whereby

$$F(E) \propto E^{-\Gamma} \times \left( 1 + \exp\left(\frac{E - E_{\text{cut}}}{E_{\text{fold}}}\right) \right)^{-1}, \quad (2)$$

where  $\Gamma$ ,  $E_{\text{cut}}$ , and  $E_{\text{fold}}$  stand for the photon index, the cutoff energy, and the folding energy, respectively.

In the spectrum of Vela X-1, two cyclotron resonant scattering features (CRSFs, or cyclotron lines) are present with a prominent harmonic line at  $\sim 55$  keV and a weaker fundamental at  $\sim 25$  keV (Kendziorra et al. 1992; Kretschmar et al. 1997; Orlandini et al. 1998; Kreykenbohm et al. 1999, 2002; Fürst et al. 2014b; Diez et al. 2022). These features are typical of highly magnetised neutron stars and can be observed in the source X-ray spectrum as broad absorption lines. CRSFs result from resonant scattering of photons by electrons in strong magnetic fields from the ground level to higher excited Landau levels followed by radiative decay (see Staubert et al. 2019, for a review). We describe the CRSFs using two multiplicative Gaussian absorption lines with the gabs parameter in XSPEC, corresponding to the fundamental and harmonic CRSF, meaning that:

$$\text{CRSF}(E) = \exp\left[-\left(\frac{d}{\sigma\sqrt{2\pi}}\right)\exp\left[-0.5\left(\frac{E - E_{\text{cyc}}}{\sigma}\right)^2\right]\right], \quad (3)$$

where  $d$  is the line depth and  $\sigma$  the line width.

<sup>4</sup> <https://heasarc.gsfc.nasa.gov/cgi-bin/Tools/w3nh/w3nh.pl>

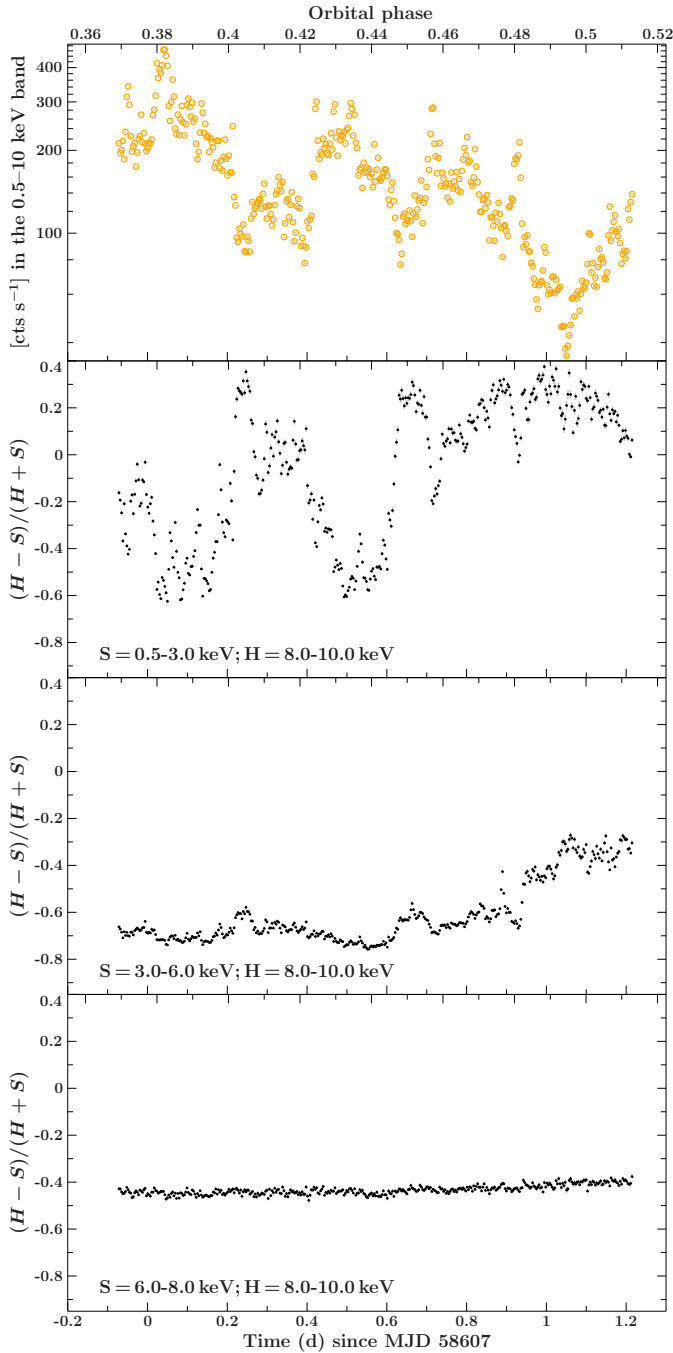


**Fig. 5.** Light curve and hardness ratios for *XMM-Newton* EPIC-pn. The first panel shows the overall count rate in the 0.5–10 keV energy band as in Fig. 2. The following panels show the hardness ratios between the mentioned energy bands. The time resolution is  $P = 283.44$  s.

The fluorescent emission line associated with  $\text{FeK}\alpha$  is modelled with a narrow Gaussian line component with the `egauss` parameter in XSPEC around 6.4 keV, with width and flux left to vary. The 10 keV feature is described by a broad Gaussian line component in absorption. The physical origin of this feature is still unknown, but in Diez et al. (2022) we discussed the presence of this feature in Vela X-1.

#### 4.1.2. Line emission

Thanks to the low-energy coverage permitted by *XMM-Newton* EPIC-pn and a better resolution than *NuSTAR* between 3 and

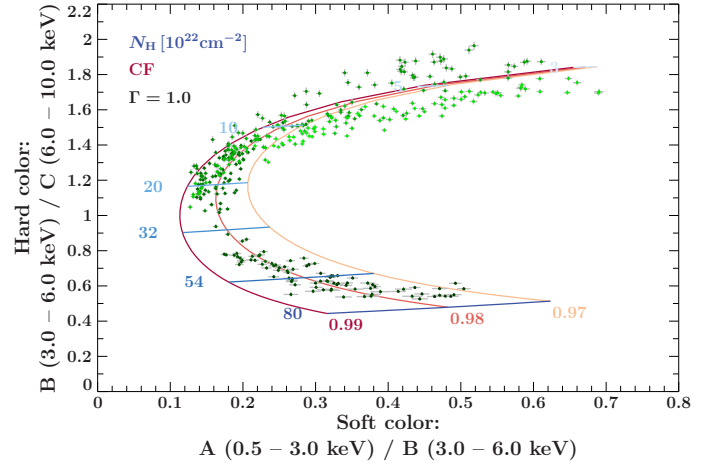


**Fig. 6.** *XMM-Newton* EPIC-pn colour-colour diagram. The data points represent the ratios of the light curves in hard colour depending on soft colour, from beginning (light green) to end (dark green) of the observation. We also show the theoretical expectation for different covering fractions CF (shades of red, varying from 0.97 to 0.99) and absorption column densities  $N_{\text{H},1}$  (shades of blue, varying from  $3 \times 10^{22} \text{ cm}^{-2}$  to  $80 \times 10^{22} \text{ cm}^{-2}$ ) using our partial covering model from Eq. (4). We used a photon index  $\Gamma$  of 1.0. More details about the simulation and its interpretation are given in Sect. 5.1.1.

10 keV, we now have access to new features that we need to include in our model. In our previous analysis, the fluorescent emission line associated with the  $\text{FeK}\beta$  could not be resolved from the  $\text{FeK}\alpha$  emission line. This is now possible with the *XMM-Newton* EPIC-pn energy resolution and we model it with a Gaussian component around 7.1 keV, with flux left free to vary but with fixed width.

Particularly in the most absorbed spectra of our observation, we can now also identify multiple emission lines between 0.5 keV and 4 keV (see last panel of Fig. 3). The absorption from the stellar wind is very strong towards the end of the observation (i.e. towards late orbital phases; see Diez et al. 2022), and therefore the strong continuum emitted by the neutron star is heavily absorbed and reveals the emission lines normally subsumed in the continuum when the absorption is less strong.

To help us to identify the energy of individual observed features, we based our search on *Chandra*/HETGS results of Amato et al. (2021), who analysed Vela X-1 at orbital phase  $\phi_{\text{orb}} \approx 0.75$ , which is even more affected by the stellar wind (see Fig. 1). Because of the limited energy resolution of EPIC-pn, Doppler shifts with orbital phase and triplets or faint lines cannot be resolved in this work. To search for the lines in EPIC-pn spectra, we had to fix the features (such as the CRSFs and the 10 keV feature) and continuum parameters (such as  $E_{\text{cut}}$  and  $E_{\text{fold}}$ ) that are not covered by the EPIC-pn instrument. We fixed them to the average *NuSTAR* values from Diez et al. (2022) for highly absorbed spectra to have an accurate description of the continuum in order to focus on the line description. We performed this search ‘by hand’, fitting Gaussian components to observed line features in the most absorbed time-resolved spectra of the observation until we obtained a satisfactory reduced chi-square. An example of such a spectrum is shown in Fig. 7. The energies of the narrowest lines ( $\text{Ne x Ly}\alpha$ ,  $\text{Mg x II Si x IV Ly}\alpha$ ,  $\text{S x VI Ly}\alpha$ ,  $\text{Ca II–XII K}\alpha$ ) have to be fixed to previous studies and their widths to  $10^{-6}$  keV.

A list of the soft lines identified in this work and a comparison with previous studies is shown in Table 2. We note that, here

**Table 2.** Details of soft emission lines between 0.5 keV and 4 keV.

Line	Detected energy from previous work (keV)	Reference energy (keV)	Identified energy for this work (keV)
O VIII Ly $\alpha$	0.6538 <sup>+0.0005 (a)</sup> <sub>-0.0011</sub>	0.6541 <sup>(c)</sup>	0.6211 <sup>+0.0130</sup> <sub>-0.0011</sub>
Ne IX (f, i, r)	0.90460 $\pm$ 0.00033/0.91454 $\pm$ 0.00034/0.92154 $\pm$ 0.00034 <sup>(b)</sup>	0.905/0.915/0.922 <sup>(c)</sup>	0.928 <sup>+0.011</sup> <sub>-0.012</sub>
Ne X Ly $\alpha$	1.02130 <sup>+0.00015 (b)</sup> <sub>-0.00014</sub>	1.02196 <sup>(d)</sup>	1.02130 (fixed)
Mg XI (f, i, r)	1.3305 $\pm$ 0.0002/1.3426 <sup>+0.0003</sup> <sub>-0.0002</sub> /1.3517 <sup>+0.0002 (b)</sup> <sub>-0.0003</sub>	1.3311/1.3431/1.3522 <sup>(c)</sup>	1.338 <sup>+0.012</sup> <sub>-0.019</sub>
Mg XII Ly $\alpha$	1.4720 $\pm$ 0.0002 <sup>(b)</sup>	1.4723 <sup>(d)</sup>	1.4720 (fixed)
Si XIII (f, i, r)	1.8388 $\pm$ 0.0002/1.8536 $\pm$ 0.0002/1.8643 $\pm$ 0.0002 <sup>(b)</sup>	1.8382/1.8530/1.8648 <sup>(e)</sup>	1.823 <sup>+0.014</sup> <sub>-0.013</sub>
Si XIV Ly $\alpha$	2.0049 $\pm$ 0.0003 <sup>(b)</sup>	2.0056 <sup>(f)</sup>	2.0049 (fixed)
S XV (f, i, r)	2.4287 <sup>+0.0007</sup> <sub>-0.0008</sub> /2.4463 <sup>+0.0007</sup> <sub>-0.0009</sub> /2.4590 <sup>+0.0006 (b)</sup> <sub>-0.0009</sub>	2.4291/2.4463/2.4606 <sup>(e)</sup>	2.439 <sup>+0.029</sup> <sub>-0.027</sub>
S XVI Ly $\alpha$	2.6207 <sup>+0.0016 (b)</sup> <sub>-0.0017</sub>	2.6196 <sup>(f)</sup>	2.6207 (fixed)
Ar VI–IX	2.9661 <sup>+0.0043 (g)</sup> <sub>-0.0099</sub>	2.9619–2.9675 <sup>(h)</sup>	2.9661 (fixed)
S XV RRC?		3.224 <sup>(c)</sup>	3.23 <sup>+0.04</sup> <sub>-0.06</sub>
Ca II–XII K $\alpha$	3.6905 <sup>+0.0022 (i)</sup> <sub>-0.0009</sub>	3.6911–3.7110 <sup>(h)</sup>	3.822 <sup>+0.019</sup> <sub>-0.102</sub>

**Notes.** To convert from Å in previous works to keV, we compute  $E[\text{keV}] = hc \div \lambda[\text{Å}]$  where  $hc = 12.39842$  (with values for  $h$ ,  $c$  and  $e$  from CODATA 2018, [Tiesinga et al. 2021](#)) and round to relevant significant digits. (f, i, r): referring to forbidden, intercombination, and resonance lines respectively. (fixed): to previous detected energies.

**References.** <sup>(a)</sup>[Lomaeva et al. \(2020\)](#), <sup>(b)</sup>[Amato et al. \(2021\)](#), <sup>(c)</sup>[Drake \(1988\)](#), <sup>(d)</sup>[Erickson \(1977\)](#), <sup>(e)</sup>[Hell et al. \(2016\)](#), <sup>(f)</sup>[Garcia & Mack \(1965\)](#), <sup>(g)</sup>[Schulz et al. \(2002\)](#), <sup>(h)</sup>[House \(1969\)](#), <sup>(i)</sup>[Watanabe et al. \(2006\)](#).

we do not aim to perform an in-depth study of the emission-line variability but rather an absorption study of the stellar wind in Vela X-1. The instrumental issues described in Sect. 2 with the limited energy resolution of EPIC-pn can explain the discrepancies obtained for some lines in comparison with previous work, in particular for O VIII Ly $\alpha$  and Ca II–XII K $\alpha$ . The Ar VI–IX and Ca II–XII K $\alpha$  lines were not detected in [Amato et al. \(2021\)](#). However, those lines were identified in [Schulz et al. \(2002\)](#), [Goldstein et al. \(2004\)](#), and [Watanabe et al. \(2006\)](#) for Vela X-1 and in [Fürst et al. \(2011\)](#) for the HMXB GX 301–2. The different charge states of Ca and Ar cannot be resolved, and so in Table 2 we give the potential candidates as in [Schulz et al. \(2002\)](#) and [Watanabe et al. \(2006\)](#).

We also detect a 3.2 keV line that has not been reported in previous work. This feature can most likely be attributed to the S XV RRC, with its ionisation potential of 3.224 keV ([Drake 1988](#)). While lower charge states of Ar are present (2.9661 keV), the line energies for both He-like Ar XVII r at 3.140 keV ([Drake 1988](#)) and H-like Ar XVIII Ly $\alpha$  at 3.321 keV ([Garcia & Mack 1965](#)) are too far away to reasonably match the fitted line energy. The same is true for the H-like S XVI Ly $\beta$  and Ly $\gamma$  lines at 3.106 and 3.276 keV ([Garcia & Mack 1965](#)), respectively, even though the S XVI Ly $\alpha$  feature is clearly detected. If this feature were indeed caused by the S XV RRC, we would expect RRC features from the more abundant ions as well. However, at the low resolution of the CCD spectra, many of the other RRC candidates are too blended to allow for a clear detection; for instance, the Si XIII RRC at 2.438 keV ([Drake 1988](#)) blends with the S XV He $\alpha$  complex, the Ne X RRC at 1.362 keV ([Garcia & Mack 1965](#)) blends Mg XI He $\alpha$ , and the O VIII RRC at 0.871 keV ([Garcia & Mack 1965](#)) with the Ne IX He $\alpha$  lines (see e.g. [Sako et al. 1999](#)).

Finally, our final and best-fit model, which we use for the time-resolved spectroscopy in this work, is:

$$I(E) = N_{\text{H},2} \times [(CF \times N_{\text{H},1} + (1 - CF)) \times (F(E) \times \text{CRSF}, F \times \text{CRSF}, H) + \text{FeK}\alpha + \text{FeK}\beta + 10 \text{ keV} + \text{Soft lines}]. \quad (4)$$

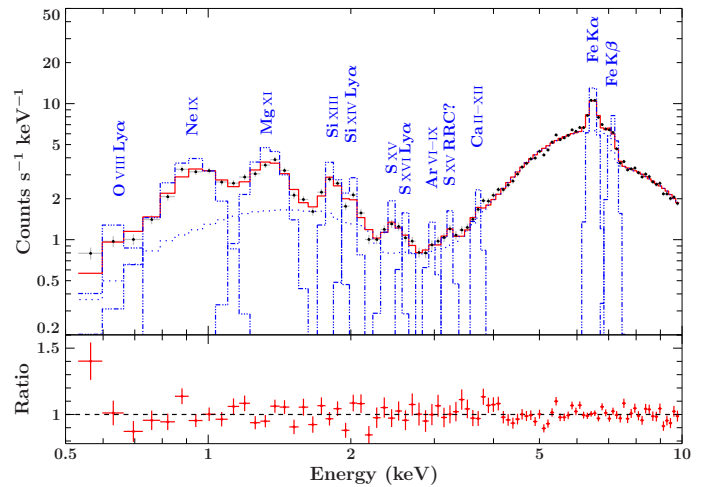


**Fig. 7.** Example *XMM-Newton* EPIC-pn spectrum (black datapoints). We show the last and most absorbed *NuSTAR*-orbit of our observation. We indicate the individual model components including all lines detected in this dataset (blue dot-dashed Gaussians) and the absorbed continuum (blue dotted line). We refer to Sect. 4.2 for a detailed description of the model and to Table 2 for the soft lines.

#### 4.2. *NuSTAR*-orbit-by-orbit analysis

We can now perform the analysis on shorter timescales with both *XMM-Newton* EPIC-pn and *NuSTAR* to access the variability of the stellar wind at low energies. Combining both datasets – and thus increasing the covered spectral range – limits the impact of possible degeneracy between the power-law slope and absorption strength. *NuSTAR* data are especially crucial at high absorption, when it is especially difficult to constrain the continuum with *XMM-Newton* only.

In [Diez et al. \(2022\)](#), we extracted a spectrum for every orbit of *NuSTAR* around the Earth, which is referred to here as ‘*NuSTAR*-orbit’ for the remainder of the paper. This should

not be confused with the duration of a binary orbit of the neutron star around its companion. For the simultaneous *XMM-Newton* EPIC-pn data, we decided to extract a spectrum using the same good time intervals (GTIs) used for the *NuSTAR*-orbit-by-orbit analysis with *NuSTAR* data in order to have a broad X-ray band description of the stellar wind on the same timescale. Due to the different start and stop times of the observations, there are *NuSTAR*-orbits without simultaneous *XMM-Newton* EPIC-pn data (see Fig. 2). Moreover, during the *NuSTAR* campaign, data were lost because of ground-station issues, resulting in no or limited *NuSTAR* coverage for parts of our *XMM-Newton* observation. For the ‘missing’ *NuSTAR*-orbits, we took the average duration of a *NuSTAR*-orbit, which lasts  $\sim 0.067$  MJD ( $\sim 5.8$  ks), in order to extract *XMM-Newton* EPIC-pn spectra. Overall, we have 1 *NuSTAR*-orbit covered by *NuSTAR* only, 2 *NuSTAR*-orbits covered by *XMM-Newton* EPIC-pn only, 4 *NuSTAR*-orbits partially covered by one of the two instruments, and 14 *NuSTAR*-orbits fully covered by both instruments (Fig. 8). We fit the data using the model from Eq. (4), with adaptations as necessitated by the different instrumental coverage as discussed in the following.

Firstly, for the *NuSTAR*-orbits covered by both *NuSTAR* and *XMM-Newton* EPIC-pn, we use a floating cross-normalisation parameter,  $C_{\text{NuSTAR}}$ , in order to give the relative normalisation between the two *NuSTAR* detectors FPMA and FPMB with the *XMM-Newton* EPIC-pn instrument. The difference between FPMA and FPMB is of the order of  $\sim 2\%$ , and so we can safely assume one normalisation constant to account for both focal plane modules for simplicity.

As discussed in Sect. 2, cross-calibration issues between *NuSTAR* and *XMM-Newton* EPIC-pn are impacting the analysis. To correct the observed up-turn in the *NuSTAR* data at  $\sim 3$  keV, we applied two different CFs,  $CF_{\text{XMM}}$  and  $CF_{\text{NuSTAR}}$ , for *XMM-Newton* EPIC-pn and *NuSTAR*, respectively. We do not fix  $CF_{\text{NuSTAR}}$  to previous values from Diez et al. (2022) as this current work benefits from low-energy coverage with *XMM-Newton*, which gives us better constraints on  $N_{\text{H},1}$ , and therefore on  $CF_{\text{NuSTAR}}$ , because those two parameters were found to be strongly correlated, as shown in Fig. 7 of Diez et al. (2022). To correct the shift in the  $\text{FeK}\alpha$  emission line, we apply a gain shift to the *NuSTAR* data in order to align on the iron line energy found with *XMM-Newton* EPIC-pn.

We also introduce another cross-normalisation constant  $C_{\text{Fe}}$  to account for the flux difference observed in *NuSTAR* relative to *XMM-Newton* EPIC-pn in the emission lines that are covered by both observatories:  $\text{FeK}\alpha$  and  $\text{FeK}\beta$ . We fix the soft-emission-line energies and widths to the values estimated when analysing the *XMM-Newton* EPIC-pn spectrum at high absorption (see Table 2) as they are not expected to change significantly with time, even if the source is highly variable (Grinberg et al. 2017). The fluxes of the emission lines are left free as their prominence changes depending on the local absorption.

We fix the CRSF parameters and the energy of the 10 keV feature to the values of their corresponding *NuSTAR*-orbit – which we obtained in our previous analysis in Diez et al. (2022) – to help to constrain the low-energy part of the continuum. Degeneracies between  $E_{\text{CRSF}}$  and  $E_{\text{cut}}$  are expected due to their proximity as seen in Diez et al. (2022); therefore, we also fix the cutoff energy in the same way.

Secondly, for the two *NuSTAR*-orbits only covered by *XMM-Newton* EPIC-pn (*NuSTAR*-orbits number 12 and 13), we fix the CRSFs parameters, the energy of the 10 keV feature  $E_{10\text{keV}}$ , and the cutoff energy  $E_{\text{cut}}$  to the closest *NuSTAR*-orbit values. These parameters cannot be ignored during the fitting because they

modify the shape of the broadband continuum, and therefore fixing them to the values of the closest *NuSTAR*-orbit is the most accurate and meaningful solution. We do not use  $C_{\text{NuSTAR}}$ , gain shift,  $CF_{\text{NuSTAR}}$ , or  $C_{\text{Fe}}$  as there is no need to correct for cross-calibration because no coverage from *NuSTAR* is available for those *NuSTAR*-orbits.

Thirdly, for the *NuSTAR*-orbit that is covered by *NuSTAR* only (*NuSTAR*-orbit number 1), the multiple soft emission lines and the  $\text{FeK}\beta$  line identified with *XMM-Newton* EPIC-pn are not resolved by *NuSTAR* alone. However, those emission lines do not impact the shape of the overall continuum of Vela X-1, and therefore they can be safely ignored for fitting the data for simplicity. We tried to fix them to the values of the closest following *NuSTAR*-orbit but no significant difference could be highlighted when comparing the residuals.

We present the results of the *NuSTAR*-orbit-by-orbit analysis in Fig. 8, focusing on the parameters of interest. An example of a fitted spectrum extracted during one *NuSTAR*-orbit with both *XMM-Newton* EPIC-pn and *NuSTAR* is given in Fig. A.4. However, we caution that the different instrumental coverage of individual spectra may result in artificial parameter behaviour, such as outliers.

Discrepancies between *NuSTAR* and *XMM-Newton* EPIC-pn are visible in the cross-normalisation parameter  $C_{\text{NuSTAR}}$ , reaching  $\sim 20\%$  (not considering outliers), which can be explained by the low-energy up-turn in *NuSTAR* (see Fig. A.4). Moreover, the average energy gainshift of *NuSTAR* relative to *XMM-Newton* EPIC-pn is of  $-87$  eV. This particularly impacts the iron line region as it is covered by both instruments. Therefore, the energy of the iron line shown in the third panel of Fig. 8 is given with respect to the *XMM-Newton* EPIC-pn values, and the gainshift has to be added to retrieve the *NuSTAR* values, with the exception of the magenta triangle outlier of *NuSTAR*-orbit 1, which is only covered by *NuSTAR*.

Significant variability can be observed in the presented parameters. In particular,  $N_{\text{H},1}$  increases by a factor of 6 between the beginning and the end of the observation, showing a very clear rise of the stellar-wind absorption at  $\phi_{\text{orb}} \approx 0.44\text{--}0.49$ . The energy of the iron line remains relatively stable around  $\sim 6.48$  keV, but shows local minima, which seem to be anti-correlated with the flux in the 3–10 keV energy band. This anti-correlation with flux appears to be similar for the photon index, which also shows local dips during flares. The photon index varies overall between 0.8 and 1.2, the change of spectral shape being associated with changes in absorption density in the stellar wind and possible degeneracy with the amount of absorption. We discuss the details of these relationships and a further investigation of them in Sect. 5.

While the CF with *XMM-Newton* EPIC-pn  $CF_{\text{XMM}}$  remains very stable around 0.98, the CF with *NuSTAR* is much more variable, ranging between 0.3 and 0.98 (we note the different y-axis range compared to  $CF_{\text{XMM}}$ ) as in Diez et al. (2022) when analysing *NuSTAR* data alone. This is due to the up-turn in *NuSTAR* data at low energies (see Fig. A.4). We discuss tests performed to assess some possible sources of this effect in Appendix A.3, and in particular a possible contribution from dust scattering. We are unable to find a plausible physical explanation and therefore conclude that the problem is due to some remaining calibration effects. In Diez et al. (2022), we discussed the problems encountered with the low-energy effective area correction for FPMA (Madsen et al. 2020) in our observation. While these problems should not affect FPMB, together with the high variability of the CF as deduced from the *NuSTAR* data alone, they imply a reduced reliability of the *NuSTAR*



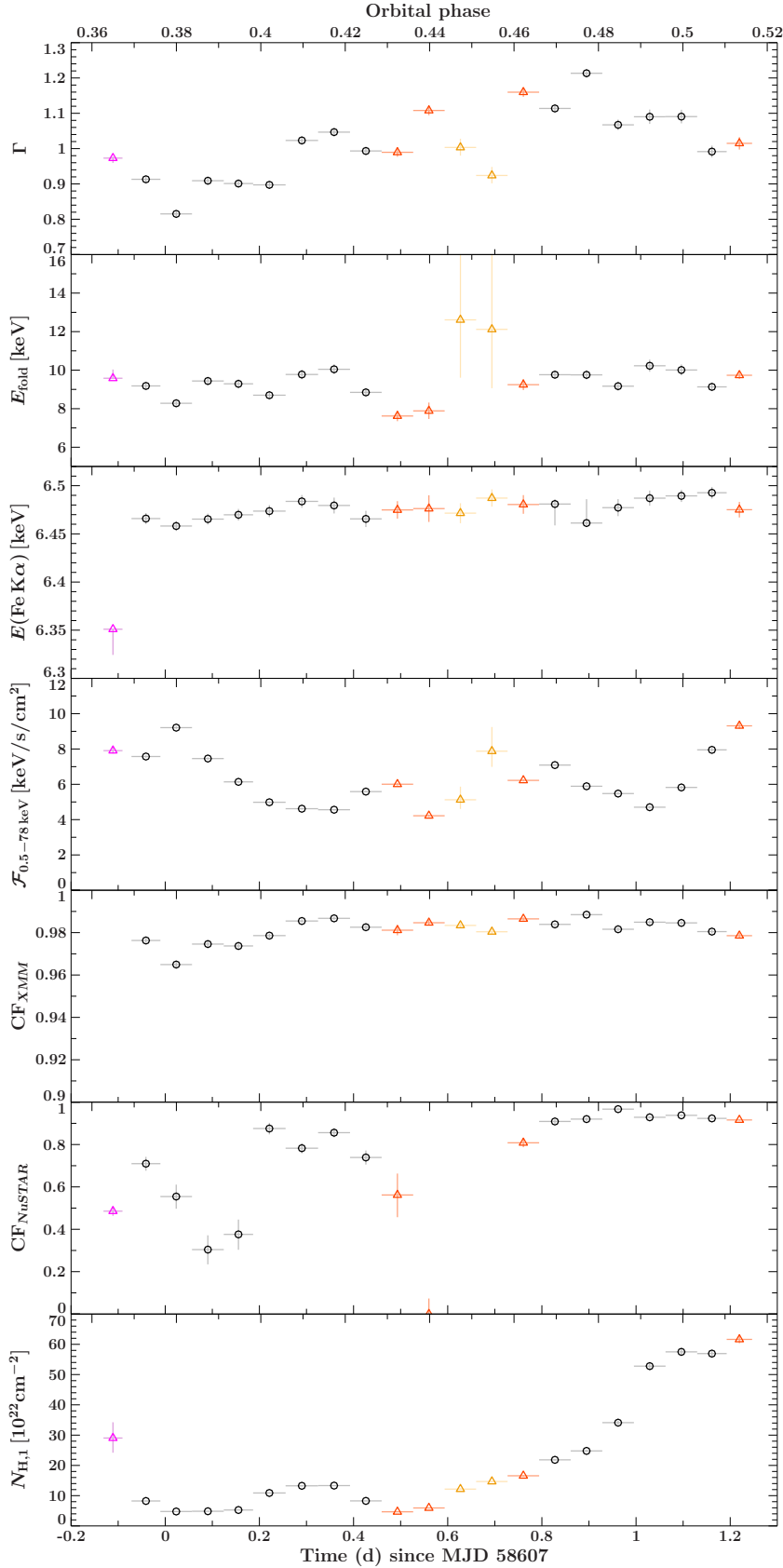


**Fig. 8.** Results of the *NuSTAR*-orbit-by-orbit analysis with *NuSTAR* and *XMM-Newton* as a function of time, together with the corresponding binary orbital phase. From top to bottom: Photon index ( $\Gamma$ ), folding energy ( $E_{\text{fold}}$ ) in keV, energy of the FeK $\alpha$  line in keV, unabsorbed flux  $\mathcal{F}_{0.5-78.\text{keV}}$  in  $\text{keV s}^{-1} \text{cm}^{-2}$ , CFs with *NuSTAR* ( $\text{CF}_{\text{NuSTAR}}$ ) and *XMM-Newton* EPIC-pn ( $\text{CF}_{\text{XMM}}$ ), absorption from the stellar wind  $N_{\text{H},1}$  in  $10^{22} \text{cm}^{-2}$ . Circles show data fully covered by both *XMM-Newton* EPIC-pn and *NuSTAR*. Triangles show data missing coverage from one of the two instruments. Magenta marks the data only covered by *NuSTAR* (*NuSTAR*-orbit 1) and orange the data fully covered by one instrument but partially by the second one (*NuSTAR*-orbits 10, 11, 14 and 21). Finally, yellow is used to denote data only covered by *XMM-Newton* EPIC-pn (*NuSTAR*-orbits 12 and 13).

data for our observation in this energy range. Moreover, looking at Fig. 6, it is obvious that a CF of less than 0.97 would not describe the data. We therefore decide to focus our discussion on *XMM-Newton*-driven CF values for the remainder of the paper.

#### 4.3. Pulse-by-pulse: *XMM-Newton* only

The sensitivity of *XMM-Newton* EPIC-pn allows us to extract a spectrum down to the pulse period of the neutron star (283 s).

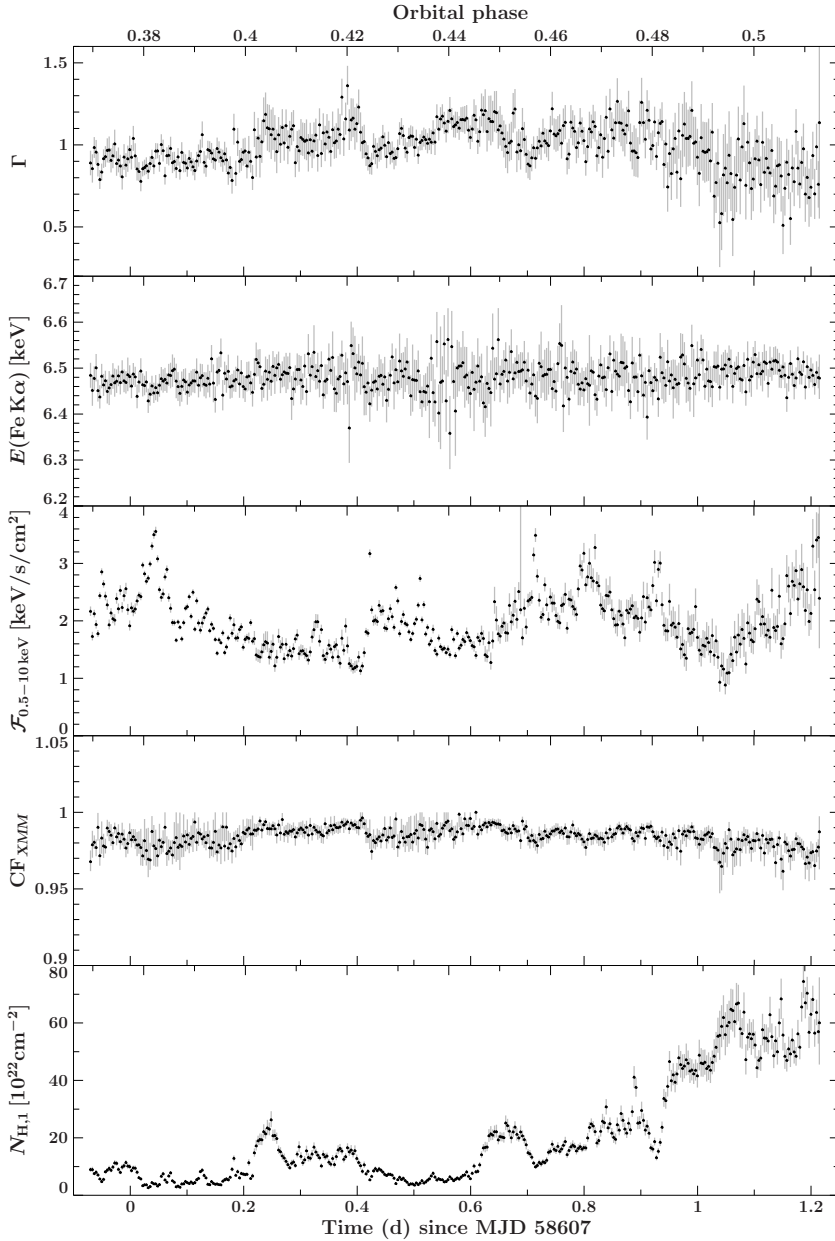


**Fig. 9.** Results of the pulse-by-pulse analysis as a function of time, together with the corresponding binary orbital phase. The panels show (from top to bottom) photon index ( $\Gamma$ ), energy of the FeK $\alpha$  line in keV, unabsorbed flux  $\mathcal{F}_{0.5-10\text{keV}}$  in  $\text{keV s}^{-1} \text{cm}^{-2}$ , CF with *XMM-Newton* EPIC-pn ( $\text{CF}_{\text{XMM}}$ ), and absorption from the stellar wind  $N_{\text{H},1}$  in  $10^{22} \text{cm}^{-2}$ .

We performed a spectral analysis for every pulse of the neutron star to explore further variability on shorter timescales.

Given the cross-instrumental issues between *XMM-Newton* and *NuSTAR* and the different coverage of the overall observation (due to both LEO of *NuSTAR* and the loss of data), this analysis is performed on *XMM-Newton* data only. While for the *NuSTAR*-orbit-by-orbit analysis it was still possible to safely determine the individual contribution of each instrument for each GTI and exclude outliers when needed, such an approach is not feasible for the pulse-by-pulse analysis. The pulse-by-pulse results for this observation with *NuSTAR* only are presented in Diez et al. (2022).

We again use the model from Eq. (4), setting up the initial parameters for each pulse spectrum from the results of the corresponding *NuSTAR*-orbit of the *NuSTAR*-orbit-by-orbit spectral analysis. Given the low signal of the individual datasets, we fix all parameters but the photon index  $\Gamma$ , the covering fraction  $\text{CF}_{\text{XMM}}$ , the absorption column density from the stellar wind  $N_{\text{H},1}$ , the energy of the fluorescent FeK $\alpha$  line, and the flux of all the emission lines.

In Fig. 9, we present the results of the pulse-by-pulse analysis for the *XMM-Newton* EPIC-pn data. The typical reduced chi-square  $\chi_{\text{red}}^2$  of the fittings is  $\sim 1.20$  and the time resolution of  $\sim 283$  s gives us access to much more parameter variability along the orbital phase than in Fig. 8. Again, the rise of the absorption column density  $N_{\text{H},1}$  is clearly visible but with much more local instability, such as two local episodes of high absorption at orbital phases  $\sim 0.40$  and  $\sim 0.44$ . The overall track is very similar to the hardness ratio between the 3–6 keV and 8–10 keV energy bands shown in the third panel of Fig. 5 and is even more amplified on the second panel of the same figure for the hardness ratio between the softest and hardest energy bands. This is expected as mainly low-energy photons are absorbed by the stellar wind, and therefore the underlying spectral shape becomes harder during those high-absorption episodes, as explained in Sect. 3. On the other hand, episodes of low absorption seem to be associated with flaring periods according to Fig. 9, which could be explained by accretion of clumps on the line of sight of the observer, as described in Diez et al. (2022). In Diez et al. (2022), we observed a correlation between  $\text{CF}_{\text{NuSTAR}}$  and  $N_{\text{H},1}$ , but also

with flux. However, there does not seem to be any correlation between *XMM-Newton*-driven CF values and  $N_{\text{H},1}$  or flux  $\mathcal{F}$  for this work. The photon index  $\Gamma$  is relatively variable, particularly towards the end of the observation. This should be taken with caution as the error bars get larger and the absorption is so strong that there may be some degeneracy between  $N_{\text{H},1}$  and  $\Gamma$ .

## 5. Discussion: The variable absorber

### 5.1. Evolution of absorption along the binary orbital phase: the onset of wakes

The main finding of our paper is the detailed analysis of the rise of the  $N_{\text{H},1}$  value and therefore of the absorption in the stellar wind, which we interpret as the onset of the wakes. This is the first time this orbital period and the corresponding wind structure are probed in a time-resolved way with a modern X-ray instrument (see Fig. 5 in [Kretschmar et al. 2021](#)).

#### 5.1.1. X-ray colour evolution with orbital phase

We observe an interesting gradual increase in the hardness ratio between the 3.0–6.0 keV and 8.0–10.0 keV energy bands (see third panel of Fig. 5). This is more a consequence of a general geometric change in the stellar wind than of the local accretion of clumps. When the wakes are coming through our line of sight (see Fig. 1), the absorption in the stellar wind increases, preferentially absorbing low-energy photons emitted in the vicinity of the neutron star starting from  $\phi_{\text{orb}} \approx 0.44$ . In our pulse-by-pulse analysis, this rise in the absorption column density  $N_{\text{H},1}$  can be directly measured from Fig. 9.

On the other hand, the hardness ratio of high-energy bands is constant (last panel of Fig. 5), implying a stable behaviour of the continuum emission from the neutron star. [Martínez-Núñez et al. \(2014\)](#) observed similar behaviour – spectral changes at low energies due to increasing absorption but stable overall source continuum – during their observation, which covered eclipse egress and a major flare.

The above is supported by the behaviour of the source on the colour–colour diagram (Sect. 3.3) where it describes a nose shape (Fig. 6). This is typical of the presence of a partial coverer with variable column density in the system (e.g. [Hirsch et al. 2019](#); [Grinberg et al. 2020](#), in Cyg X-1). As would be expected given the onset of the wake, the source evolves along the track with time, as indicated by transition from light (early in the observation) to dark green (late in the observation) data points in the figure.

Figure 10 shows how absorption impacts the observed spectrum modelled by Eq. (4), which consists of a power-law continuum with a high-energy cutoff, assuming a certain CF. In the case of a continuum fully covered by the obscurer (CF = 1, dashed lines), the flux ratios in the soft colour (A/B) and in the hard colour (B/C) decrease as  $N_{\text{H},1}$  grows, leading to a positive correlation between those ratios for the covered spectrum. On the other hand, if we consider a spectrum where this time only a certain fraction CF < 1 of the continuum is absorbed by the stellar wind (solid lines), the flux in the A band will remain constant as  $N_{\text{H},1}$  grows after a certain threshold. In the example of a covering fraction of 0.9, this happens at  $N_{\text{H},1} = 54 \times 10^{22} \text{ cm}^{-2}$  according to expectations from Fig. 10. Simultaneously, the fluxes in the B and C bands continue to decrease together as  $N_{\text{H},1}$  grows. Hence, the softer colour becomes softer as the harder colour does not change, leading to the observed nose-shape colour–colour

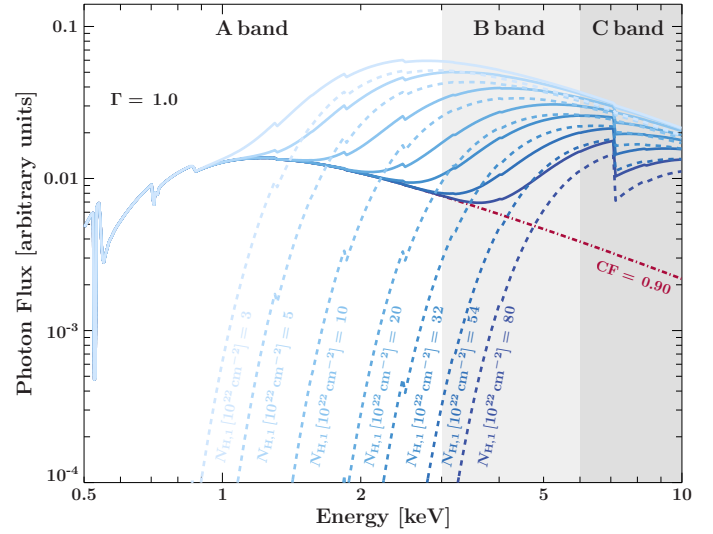


**Fig. 10.** Effect of increasing absorption on our model from Eq. (4) with photon index  $\Gamma = 1.0$  and without emission lines to focus on the evolution of the continuum shape. We assume a CF of 0.9 and a varying absorption column density  $N_{\text{H},1}$  from  $3 \times 10^{22} \text{ cm}^{-2}$  to  $80 \times 10^{22} \text{ cm}^{-2}$  covering the range obtained in Fig. 9. The shaded grey areas indicate three energy bands of interest: The A band from 0.5 to 3 keV, B band from 3 to 6 keV, and C band from 6 to 10 keV. The resulting observed spectrum (solid lines) is the sum of the spectrum not covered by the stellar wind (dash-dotted line) and the covered spectrum (dashed lines). See Fig. 3 of [Diez et al. \(2022\)](#) for an illustrated picture of the partial covering model.

diagram in Fig. 6. This probes the necessity of a partial covering model to describe the data. A higher CF leads to a less elongated curve.

We use an averaged  $\Gamma$  over the values obtained in Fig. 8 for our observation. We simulate a grid of colour–colour tracks for varying values of  $N_{\text{H}}$  and covering fraction and include the results in Fig. 6. Data and simulations agree very well, supporting our interpretation.

#### 5.1.2. Comparison with previous observations and model descriptions

While absorption values have been determined by many authors with various different satellites (see [Kretschmar et al. 2021](#), for an overview), there are few data sets that cover a significant range in orbital phase within an individual binary orbit and therefore that do not mix potential binary orbit-to-orbit variations in wake structures. After correcting for differences in orbital phase definitions in the original papers, in Fig. 11 we compare the absorption values we derived with data points from [Ohashi et al. \(1984\)](#) and [Haberl & White \(1990\)](#). Different spectral models used to fit spectra and to derive  $N_{\text{H}}$  may introduce systematic shifts in the obtained values. Still, the data taken over many years appear to cover a similar range, but sometimes with quite different values at the same orbital phase, as seen already in [Kretschmar et al. \(2021\)](#), indicating that the structures causing these variations are not stable in orbital phase. On the other hand, the duration of the overall rising trend from low absorption to a highly absorbed ‘plateau’ is rather similar in slope –  $N_{\text{H}}$  values double over a time range of 0.02 in orbital phase or  $\sim 15.4 \text{ ks}$  – suggesting that similar larger structures in the wind exist, which may differ somewhat in their relative orientation.

**Table 3.** Parameters used in the model curves shown in Fig. 12.

System discussed	Donor star		Stellar wind		Neutron star		Ref. and Notes
	Mass ( $M_{\odot}$ )	Radius ( $R_{\odot}$ )	Mass loss ( $M_{\odot} \text{ yr}^{-1}$ )	$v_{\text{esc}}$ (km s $^{-1}$ )	$M_{\text{X}}$ ( $M_{\odot}$ )	Distance ( $R_{\star}$ )	
Generic HMXB	22	35.2	$5.8 \times 10^{-6}$	1300	1.4	1.59	[B91]
Vela X-1	23.1	30	$4 \times 10^{-6}$	1400	1.86	1.77	[MW15b]
EXO 1722–363	15	29	$1 \times 10^{-6}$	500	1.9	1.75	[MWB12]
Vela X-1	21–28	27–32	$0.4\text{--}2 \times 10^{-6}$	380–750	1.8–2.1	1.56–2	[K21]

**Notes.** All the simulations use circular binary orbits with a fixed distance of the neutron star from the stellar surface. The last row shows parameter ranges found by more recent studies of the Vela X-1 system (since the year 2000), as compiled by Kretschmar et al. (2021). [B91] Blondin et al. (1991). Showing the ‘full simulation’, Fig. 8 in the publication. [MW15b] Manousakis & Walter (2015b). Stellar parameters from Manousakis & Walter (2015a). [MWB12] Manousakis et al. (2012). [K21] Kretschmar et al. (2021). Distance variation from eccentricity, ‘;’ the binary orbit is very well known.

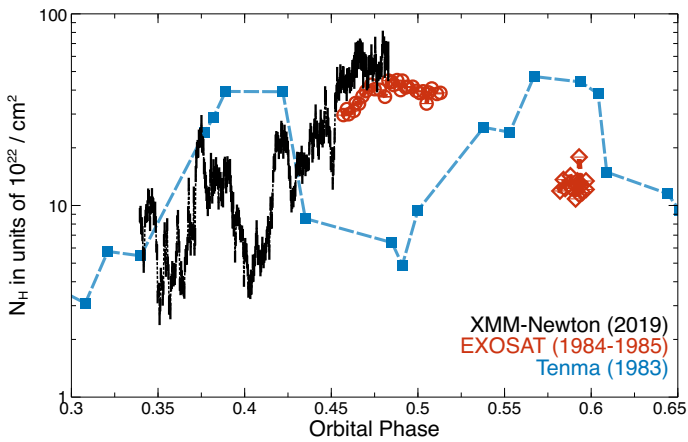


**Fig. 11.** Comparison of the  $N_{\text{H}}$  values determined in this study with historical measurements taken during individual binary orbits by Tenma (Ohashi et al. 1984) and EXOSAT (Haberl & White 1990). We highlight the overall similar slope of the different rising curves. See text for details.

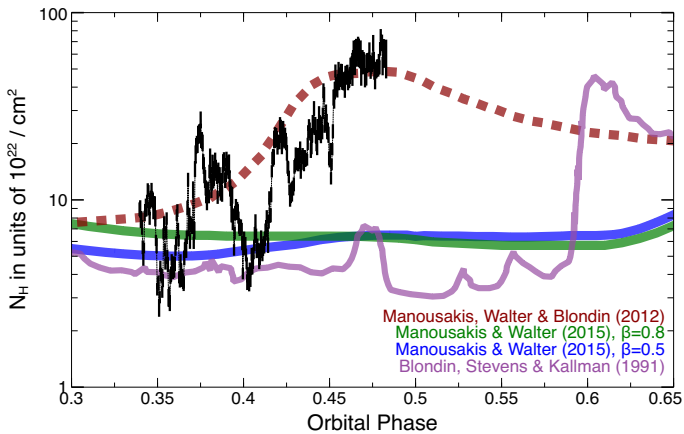


**Fig. 12.** Comparison of the  $N_{\text{H}}$  values determined in this study with a range of model results for  $N_{\text{H}}$  from hydrodynamic simulations for Vela X-1 or similar, but not identical model systems. See the main text and Table 3.

In Fig. 12, we compare our derived  $N_{\text{H}}$  values with some of the few examples of column densities derived from hydrodynamical model calculations. However, it is important to note that these models start from quite different assumptions (see also

Table 3) and were not made for direct comparison. First of all, the curves shown for the models of Manousakis & Walter (2015b) and Manousakis et al. (2012) are time-averaged values of column density over orbital phase, smoothing out the expected significant  $N_{\text{H}}$  variability from binary orbit to binary orbit, while the result from Blondin et al. (1991) is taken from the simulation of a single binary orbit in a model including a tidal stream. It is evident that neither this last model nor the relatively low and little varying average column density predicted by Manousakis & Walter (2015b) shows a marked rise at early orbital phases as found in the data. One of the reasons for this may be the rather high wind velocities and mass-loss rates assumed in these studies, and certainly found in earlier studies of Vela X-1, while more modern studies assume lower wind velocities (see Table 7 and Fig. 19 in Kretschmar et al. 2021). The visually best matching curve from Manousakis et al. (2012) was, on the other hand, calculated for a different system, EXO 1722–363, albeit with relatively similar system parameters to Vela X-1, and assuming a relatively slow wind. Updated hydrodynamical simulations accounting for the current best knowledge of orbital and wind parameters of the system, and taking the non-negligible eccentricity into account, would be very welcome.

## 5.2. Origin and nature of the absorber

The continuum from the neutron star dominates the emission in the spectrum of Vela X-1 until  $\phi_{\text{orb}} \approx 0.44$ . At this orbital phase, the absorption column density increases together with the strength of soft emission lines between 0.5 and 4 keV. Figure 13 shows the evolution of the flux of some lines with time. In particular, we can see the fluxes of the Ne IX and S XV are mostly consistent with 0 at the beginning of the observation but start to increase towards the end, revealing the corresponding elements in the spectrum of Vela X-1. The presence of strong lines during heavy absorption from the stellar wind suggests that the absorber is localised and the lines originate from a larger scale in the system, as in Watanabe et al. (2006). If these lines originated from the local absorber or close to the vicinity of the neutron star, they would be completely absorbed by the stellar wind and would not appear in the resultant spectrum. Another argument in the favour of this statement is that those soft emission lines are also present in the spectrum of Vela X-1 during the eclipse (Sako et al. 1999), which is when the neutron star and its local absorber are outside the line of sight of the observer.

In Fig. 13, the fluxes of the fluorescent FeK $\alpha$  and FeK $\beta$  lines are positive throughout the whole observation, meaning

that those lines are visible at all observed orbital phases here and therefore also originate from a larger scale in the system. The situation is less evident for the fluorescent  $\text{Ca II-XII K}\alpha$  line, which was more difficult to constrain because of blending with neighbouring lines.

The  $\text{Ne IX}$ ,  $\text{Mg XI}$ ,  $\text{Si XIII}$ , and  $\text{S XV}$  complexes are evidence of ionisation of the absorber in the system, as those ions only have two remaining electrons on their orbital. Furthermore, the presence of  $\text{O VIII}$ ,  $\text{Ne X}$ ,  $\text{Mg XII}$ ,  $\text{Si XIV}$ , and  $\text{S XVI Ly}\alpha$  lines also indicates ionisation in the system as they are emitted when the last atomic electron transitions from an  $n = 2$  orbital to the ground state. According to Amato et al. (2021), the warm photoionised wind of the companion star and smaller cooler regions or clumps of gas can explain the simultaneous contribution of H- and He-like emission lines and fluorescent lines of near-neutral ions. Comparing *Chandra*/HETGS data of Vela X-1 with simulations of propagation of X-ray photons in a smooth and undisturbed wind, Watanabe et al. (2006) stated that fluorescent lines originate from reflection of the stellar photosphere in the extended stellar wind or simply from the accretion wake. Additionally, these authors observed brighter soft emission lines at  $\phi_{\text{orb}} = 0.5$  than during the eclipse. This indicates a higher production of X-ray line emission caused by highly ionised ions in a region between the neutron star and its massive stellar companion, which is occulted during eclipse. However, this is difficult to confirm with our data and further studies at higher spectral resolution are necessary.

### 5.3. Short-term absorption variability

#### 5.3.1. Search for characteristic timescales in absorption variability

Theoretical predictions show that variability in a clumpy material can result in typical variability timescales that will depend on the properties of the structures in the stellar wind and/or in the tidal streams in correlation with the orbital parameters of the system (El Mellah et al. 2020). In this section, we therefore present a search for possible indications of such a timescale. To perform this analysis, we used the Stingray: A Modern Python Library for Spectral Timing (Bachetti et al. 2022; Huppenkothen et al. 2019a,b) Python library. Our pseudo-light curve of  $N_{\text{H}}$  contains 392 bins with a binning size equal to the pulse period of the neutron star ( $\sim 283$  s). We used different techniques implemented in Stingray, which are:

- average power spectrum using Leahy normalisation and dividing our data into 11 subsets. This technique allows the search for periodicities in the frequency range between 0.0002 and 0.00175 Hz (see panel a of Fig. 14);
- z-search and chi-search techniques to search for periodicity in the frequency range between 0.006 and 0.0033 (see panels b and c of Fig. 14 respectively).

Neither of the techniques detects a significant periodic or quasi-periodic signal in the evolution of  $N_{\text{H}}$  in the range of frequencies accessible with our data. The simulations of El Mellah et al. (2020) predict a clear signal in the autocorrelation function equivalent to a cutoff in the power spectrum. Given the quality of our data, the presence of such a feature cannot be assessed. Still, the spectrum presented above is, to our knowledge, the first absorption power spectrum calculated for Vela X-1 in an attempt to obtain such timescales.

To expand the frequency search range to larger values, we also performed a Lomb-Scargle periodogram using the routine of Astropy v5.1 Timeseries software (Astropy Collaboration

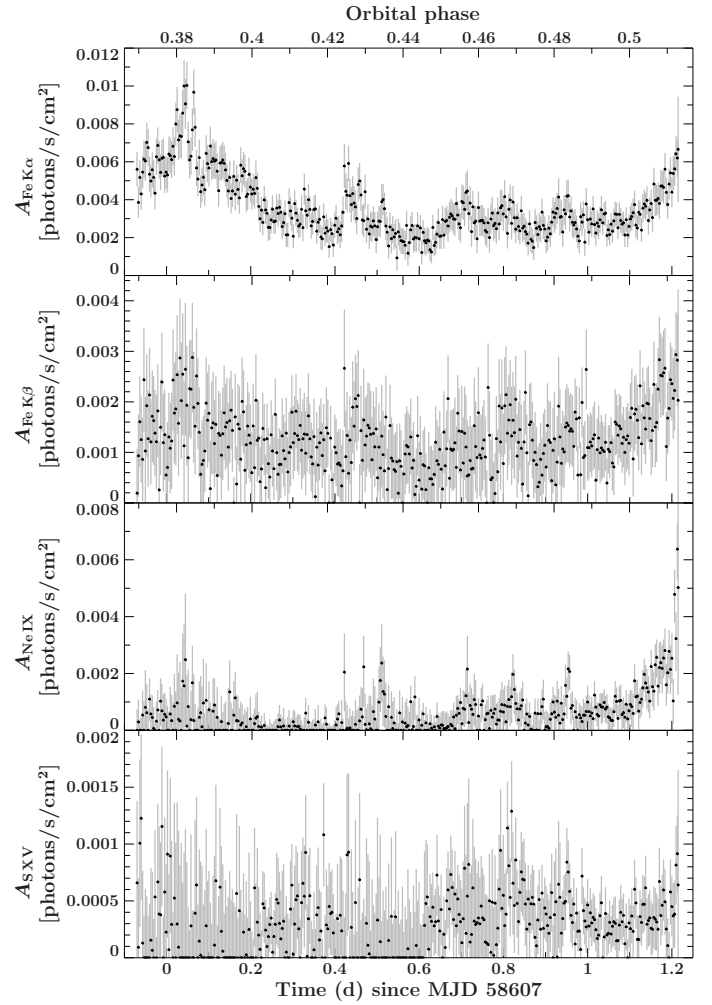


**Fig. 13.** Fluxes in photons  $\text{s}^{-1} \text{cm}^{-2}$  of some soft lines obtained within the pulse-by-pulse analysis as functions of time, together with the corresponding binary orbital phase. The panels show (from top to bottom) the flux of the  $\text{Fe K}\alpha$ , the  $\text{Fe K}\beta$ , the  $\text{Ne IX}$ , and the  $\text{S XV}$  line.

2022) (see panel d of Fig. 14). This technique only finds the binning size of our database (and following harmonics) as a possible period but no other periodicity could be found. It does not allow the shape of the power spectrum to be assessed. This search could be enhanced with an extended sample of the  $N_{\text{H}}$  along one or more binary orbits.

#### 5.3.2. Absorption during flares

During the first two flaring episodes at  $\phi_{\text{orb}} \approx 0.38$  and  $\phi_{\text{orb}} \approx 0.43$ , we saw in the second panel of Fig. 5 that the hardness ratio between the continuum band and the softest band decreases dramatically, indicating a softening of the underlying spectrum. This is also confirmed in Fig. 8 with the local decreases in photon index during flaring episodes. Therefore, more low-energy photons are detected compared to before the flaring episodes. If more low-energy photons reach the detector plane, this suggests that there is less material on the line of sight of the observer (otherwise they would have been absorbed by the wind), and therefore less absorption from the stellar wind. This is confirmed by our time-resolved spectral analysis in Fig. 8 and in Fig. 9, where the absorption column density of the stellar wind  $N_{\text{H},1}$  reaches its minimum during those two flaring episodes.

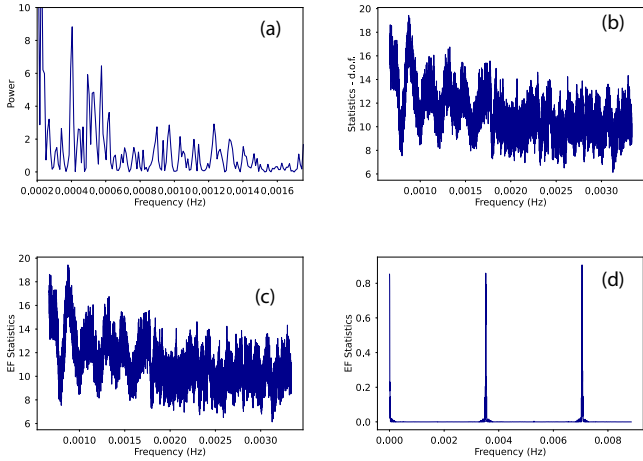


**Fig. 14.** Timing analysis of  $N_{\text{H}}$  evolution: (a) Stingray average power spectrum; (b) Stingray z-square function; (c) Stingray chi-square function; (d) Astropy v5.1 Lomb-Scargle Periodogram.

This is also visible during later short flares with strong but brief softening of the spectral shape together with local minima of  $N_{\text{H},1}$  and CF. These short-timescale events could be associated with the accretion of clumps in the vicinity of the neutron star, as already suggested in Martínez-Núñez et al. (2014) and Diez et al. (2022) for Vela X-1. As material falls onto the surface of the neutron star through the accretion column, photons are produced through bremsstrahlung and cyclotron emission. Those photons are then up-scattered through inverse Compton and more X-rays are produced. The more material falls into the neutron star, the more the temperature increases, favouring interactions and X-ray production. Clumps just passing in front of the source on the line of sight of the observer could explain the local maxima in  $N_{\text{H},1}$  that are not happening simultaneously with flux changes.

## 6. Summary and outlook

We analysed simultaneous *XMM-Newton* and *NuSTAR* data of Vela X-1 covering a broad X-ray range at orbital phase  $\sim 0.36$ – $0.52$ . For the spectral modelling, we used our partial covering model first described in Diez et al. (2022). Thanks to the hard X-ray coverage permitted by *NuSTAR* and our results from previous work, we were able to constrain the continuum in order to focus on the absorption variability at lower energies with *XMM-Newton* EPIC-pn for this work.

This is the first time that such a high-time-resolution absorption study of Vela X-1 has been carried out on a broad X-ray range from 0.5 to 78 keV. We traced the onset of the wakes, which are characterised by a rise in the absorption column density  $N_{\text{H},1}$  starting at orbital phase  $\sim 0.44$  as well as local absorption variability due to the accretion of clumps. The slope of the  $N_{\text{H},1}$  rise is comparable, and is similar to previous observations, albeit with an orbital-phase lag indicating similar large-scale structures in the wind but with different orientation at different times of observation. We also compared our data with simulations from previous works in the literature but no strong match between observations and theoretical models could be found. This reflects the necessity for further and updated hydrodynamical simulations that account for the latest orbital parameter values (for example: eccentricity  $>0$ ) and the complexity of the wind parameters (such as wind velocities and mass-loss rates).

Through high-resolution spectroscopy of the multiple fluorescent lines present in Vela X-1, we performed X-ray

photography of the material in the system. The evidence of those lines at different absorption phases suggests sources of emission from local absorber to large-scale structures. This analysis also reveals strong photoionisation of the wind with the presence of highly ionised elements such as Ly $\alpha$  lines of O, Ne, Mg, Si, and S. However, these results have to be considered with caution as the *XMM-Newton* EPIC-pn energy resolution is not sufficient to perform an accurate spectral analysis of individual lines and blending with neighbouring elements can happen. This aspect is beyond the scope of this paper and the analysis of simultaneous *XMM-Newton* RGS data in a future work is needed to disentangle this. Moreover, we used a neutral absorber to describe the absorption from the wind, but the use of warmabs<sup>5</sup> for warm absorbers and photoionised emitters would be better suited, as would a higher resolution instrument (such as *Chandra*/HETGS). The upcoming XRISM and *Athena* (Barret et al. 2020) are of utmost importance for such a study, as high-resolution spectral analysis is one of their main science goals (XRISM Science Team 2020).

*Acknowledgements.* This work has been partially funded by the Bundesministerium für Wirtschaft und Energie under the Deutsches Zentrum für Luft- und Raumfahrt Grants 50 OR 1915. The research leading to these results has received funding from the European Union’s Horizon 2020 Programme under the AHEAD2020 project (grant agreement no. 871158) and from the ESA Archival Research Visitor Programme. SMN acknowledges funding under project PID2021-122955OB-C41 funded by MCIN/AEI/10.13039/501100011033 and by ‘ERDF A way of making Europe’. RA acknowledges support by the CNES. Work at LLNL was performed under the auspices of the US Department of Energy under contract no. DE-AC52-07NA27344 and supported through NASA grants to LLNL. This work has made use of (1) the Interactive Spectral Interpretation System (ISIS) maintained by *Chandra* X-ray Center group at MIT; (2) the *NuSTAR* Data Analysis Software (NuSTARDAS) jointly developed by the ASI Science Data Center (ASDC, Italy) and the California Institute of Technology (Caltech, USA); (3) the ISIS functions (isisscripts) (<http://www.sternwarte.uni-erlangen.de/isis/>) provided by ECAP/Remeis observatory and MIT; (4) NASA’s Astrophysics Data System Bibliographic Service (ADS); (5) the User’s Guide to the *XMM-Newton* Science Analysis System, Issue 17.0, 2022 (ESA: *XMM-Newton* SOC). We thank John E. Davis for the development of the slxfig (<http://www.jedsoft.org/fun/slxfig/>) module used to prepare most of the figures in this work. Others were created with the Veusz (<https://veusz.github.io/>) package. WebPlotDigitizer (<https://automeris.io/WebPlotDigitizer/>) (© Ankit Rohatgi) has been used to digitise data from figures in older publications.

## References

- Amato, R., Grinberg, V., Hell, N., et al. 2021, *A&A*, 648, A105  
 Arnaud, K. A. 1996, *ASP Conf. Ser.*, 101, 17  
 Astropy Collaboration (Price-Whelan, A. M., et al.) 2022, *ApJ*, 935, 167  
 Bachetti, M., Huppenkothen, D., Khan, U., et al. 2022, *StingraySoftware/stingray: v1.0-beta*  
 Barret, D., Decourchelle, A., Fabian, A., et al. 2020, *Astron. Nachr.*, 341, 224  
 Becker, R. H., Rothschild, R. E., Boldt, E. A., et al. 1978, *ApJ*, 221, 912  
 Bildsten, L., Chakrabarty, D., Chiu, J., et al. 1997, *ApJS*, 113, 367  
 Blondin, J. M. 1994, *AIP Conf. Ser.*, 308, 578  
 Blondin, J. M., Kallman, T. R., Fryxell, B. A., & Taam, R. E. 1990, *ApJ*, 356, 591  
 Blondin, J. M., Stevens, I. R., & Kallman, T. R. 1991, *ApJ*, 371, 684  
 Conti, P. S. 1978, *A&A*, 63, 225  
 den Herder, J. W., Brinkman, A. C., Kahn, S. M., et al. 2001, *A&A*, 365, L7  
 Diez, C. M., Grinberg, V., Fürst, F., et al. 2022, *A&A*, 660, A19  
 Drake, G. W. 1988, *Can. J. Phys.*, 66, 586  
 El Mellah, I., Grinberg, V., Sundqvist, J. O., Driessen, F. A., & Leutenegger, M. A. 2020, *A&A*, 643, A9  
 Erickson, G. W. 1977, *J. Phys. Chem. Ref. Data*, 6, 831  
 Falanga, M., Bozzo, E., Lutovinov, A., et al. 2015, *A&A*, 577, A130  
 Fransson, C., & Fabian, A. C. 1980, *A&A*, 87, 102  
 Fürst, F., Kreykenbohm, I., Pottschmidt, K., et al. 2010, *A&A*, 519, A37

<sup>5</sup> <https://heasarc.gsfc.nasa.gov/xstar/docs/html/node102.html>

- Fürst, F., Suchy, S., Kreykenbohm, I., et al. 2011, *A&A*, **535**, A9
- Fürst, F., Pottschmidt, K., Wilms, J., et al. 2014a, *ApJ*, **784**, L40
- Fürst, F., Pottschmidt, K., Wilms, J., et al. 2014b, *ApJ*, **780**, L33
- García, J. D., & Mack, J. E. 1965, *J. Opt. Soc. Am.*, **55**, 654
- Giménez-García, A., Shenar, T., Torrejón, J. M., et al. 2016, *A&A*, **591**, A26
- Gokus, A. 2017, Master's thesis, (Universität Erlangen-Nürnberg, Germany)
- Goldstein, G., Huenemoerder, D. P., & Blank, D. 2004, *AJ*, **127**, 2310
- Grinberg, V., Hell, N., El Mellah, I., et al. 2017, *A&A*, **608**, A143
- Grinberg, V., Nowak, M. A., & Hell, N. 2020, *A&A*, **643**, A109
- Haberl, F., & White, N. E. 1990, *ApJ*, **361**, 225
- Heinz, S., Burton, M., Braiding, C., et al. 2015, *ApJ*, **806**, 265
- Hell, N., Brown, G. V., Wilms, J., et al. 2016, *ApJ*, **830**, 26
- HI4PI Collaboration (Ben Bekhti, N., et al.) 2016, *A&A*, **594**, A116
- Hiltner, W. A., Werner, J., & Osmer, P. 1972, *ApJ*, **175**, L19
- Hirsch, M., Hell, N., Grinberg, V., et al. 2019, *A&A*, **626**, A64
- Houck, J. C., & Denicola, L. A. 2000, *ASP Conf. Ser.*, **216**, 591
- House, L. L. 1969, *ApJS*, **18**, 21
- Huppenkothen, D., Bachetti, M., Stevens, A., et al. 2019a, *J. Open Source Softw.*, **4**, 1393
- Huppenkothen, D., Bachetti, M., Stevens, A. L., et al. 2019b, *ApJ*, **881**, 39
- Jansen, F., Lumb, D., Altieri, B., et al. 2001, *A&A*, **365**, L1
- Jethwa, P., Saxton, R., Guainazzi, M., Rodriguez-Pascual, P., & Stuhlinger, M. 2015, *A&A*, **581**, A104
- Joss, P. C., & Rappaport, S. A. 1984, *ARA&A*, **22**, 537
- Kaastra, J. S., & Bleeker, J. A. M. 2016, *A&A*, **587**, A151
- Kallman, T. R., & McCray, R. 1982, *ApJS*, **50**, 263
- Kendziorra, E., Mony, B., Kretschmar, P., et al. 1992, in *Frontiers Science Series*, eds. Y. Tanaka, & K. Koyama, 51
- Kretschmar, P., Pan, H. C., Kendziorra, E., et al. 1997, *A&A*, **325**, 623
- Kretschmar, P., El Mellah, I., Martínez-Núñez, S., et al. 2021, *A&A*, **652**, A95
- Kreykenbohm, I., Kretschmar, P., Wilms, J., et al. 1999, *A&A*, **341**, 141
- Kreykenbohm, I., Coburn, W., Wilms, J., et al. 2002, *A&A*, **395**, 129
- Kreykenbohm, I., Wilms, J., Kretschmar, P., et al. 2008, *A&A*, **492**, 511
- Lai, E. V., De Marco, B., Zdziarski, A. A., et al. 2022, *MNRAS*, **512**, 2671
- Lewis, W., Rappaport, S., Levine, A., & Nagase, F. 1992, *ApJ*, **389**, 665
- Lomaeva, M., Grinberg, V., Guainazzi, M., et al. 2020, *A&A*, **641**, A144
- Madsen, K. K., Grefenstette, B. W., Pike, S., et al. 2020, ArXiv e-prints, [arXiv:2005.00569]
- Malacaria, C., Mihara, T., Santangelo, A., et al. 2016, *A&A*, **588**, A100
- Manousakis, A., & Walter, R. 2015a, *A&A*, **575**, A58
- Manousakis, A., & Walter, R. 2015b, *A&A*, **584**, A25
- Manousakis, A., Walter, R., & Blondin, J. M. 2012, *A&A*, **547**, A20
- Martínez-Núñez, S., Torrejón, J. M., Kühnel, M., et al. 2014, *A&A*, **563**, A70
- Martínez-Núñez, S., Kretschmar, P., Bozzo, E., et al. 2017, *Space Sci. Rev.*, **212**, 59
- Nagase, F., Zylstra, G., Sonobe, T., et al. 1994, *ApJ*, **436**, L1
- Nowak, M. A., Hanke, M., Trowbridge, S. N., et al. 2011, *ApJ*, **728**, 13
- Ohashi, T., Inoue, H., Koyama, K., et al. 1984, *PASJ*, **36**, 699
- Orlandini, M., Dal Fiume, D., Frontera, F., et al. 1998, *A&A*, **332**, 121
- Pintore, F., Sanna, A., Di Salvo, T., et al. 2014, *MNRAS*, **445**, 3745
- Quaintrell, H., Norton, A. J., Ash, T. D. C., et al. 2003, *A&A*, **401**, 313
- Rawls, M. L., Orosz, J. A., McClintock, J. E., et al. 2011, *ApJ*, **730**, 25
- Sako, M., Liedahl, D. A., Kahn, S. M., & Paerels, F. 1999, *ApJ*, **525**, 921
- Sato, N., Hayakawa, S., Nagase, F., et al. 1986, *PASJ*, **38**, 731
- Schulz, N. S., Canizares, C. R., Lee, J. C., & Sako, M. 2002, *ApJ*, **564**, L21
- Staubert, R., Trümper, J., Kendziorra, E., et al. 2019, *A&A*, **622**, A61
- Strüder, L., Briel, U., Dennerl, K., et al. 2001, *A&A*, **365**, L18
- Tiesinga, E., Mohr, P. J., Newell, D. B., & Taylor, B. N. 2021, *Rev. Mod. Phys.*, **93**, 025010
- Tsygankov, S. S., Rouco Escorial, A., Suleimanov, V. F., et al. 2019, *MNRAS*, **483**, L144
- Turner, M. J. L., Abbey, A., Arnaud, M., et al. 2001, *A&A*, **365**, L27
- van Kerkwijk, M. H., van Paradijs, J., & Zuiderwijk, E. J. 1995, *A&A*, **303**, 497
- Verner, D. A., Ferland, G. J., Korista, K. T., & Yakovlev, D. G. 1996, *ApJ*, **465**, 487
- Watanabe, S., Sako, M., Ishida, M., et al. 2006, *ApJ*, **651**, 421
- Wilms, J., Allen, A., & McCray, R. 2000, *ApJ*, **542**, 914
- XRISM Science Team 2020, ArXiv e-prints, [arXiv:2003.04962]

## Appendix A: Calibration of *XMM-Newton* EPIC-pn timing mode

In this section, we discuss the calibration of the *XMM-Newton* EPIC-pn timing mode and the tests we performed to justify our choice of calibration and data extraction for this work. We discuss our tests and their implications to conclude with the possible caveats.

### A.1. Test for RDCTI and RDPHA correction in the iron line region

When processing the ODFs to obtain calibrated and concatenated event lists to later generate scientific products, one has to use the `eproc` task. The default calibration of this task for timing mode data<sup>1</sup> uses `withrdpha='Y'`, `withxrlcorrection='Y'`, `runepreject='Y'`, `runepfast='N'`; Y and N standing for YES and NO, respectively.

The Rate-Dependent PHA (RDPHA) correction was introduced with SASv13 as a more robust method than the Rate-Dependent CTI (RDCTI) correction to rectify count-rate-dependent effects on the energy scale of EPIC-pn exposures in timing mode<sup>10</sup>. Thus, the task `epfast`, which applies the RDCTI correction, does not run on data that have been already corrected with the RDPHA correction, and vice versa. This explains why `runepfast` is set to 'N', because `withrdpha` is set to 'Y' by default in the timing mode.

However, when extracting the *XMM-Newton* EPIC-pn spectra for this Vela X-1 observation with the timing mode default RDPHA correction, we obtained higher energies than expected for the line features in the 0.5–10 keV energy range covered by EPIC-pn. This is particularly visible for the fluorescent emission line associated with  $\text{FeK}\alpha$  as it is the most prominent emission feature in the spectrum of Vela X-1. Figure A.1 shows an example of a spectrum with the RDPHA correction in the iron line region fitted with a simple power law and a Gaussian component. The  $\text{FeK}\alpha$  line is found at more than 6.53 keV, while it is expected to be located around  $\sim 6.4$  keV according to our results of the simultaneous *NuSTAR* observation (Diez et al. 2022) or in the spectrum of Vela X-1 in general (see e.g. Goldstein et al. 2004; Watanabe et al. 2006; Giménez-García et al. 2016). The energy of the iron line also depends on how much the observation is affected by pile-up; this aspect is discussed in the following section.

In order to perform a sanity check of the RDPHA correction, we decided to revert back to the RDCTI correction (`epfast`), as this latter was usually performed in timing mode before the RDPHA correction got released in SASv13 and later versions (Martínez-Núñez et al. 2014). We therefore tested `eproc` running the `epfast` task, therefore using the parameters `withdefaultcal='N'`, `withrdpha='N'`, `withxrlcorrection='Y'`, `runepreject='Y'`, `runepfast='Y'`. This setting corresponds to the default calibration of the burst mode<sup>1</sup>. This results in an iron line around 6.34 keV as presented in Fig. A.1, which is more consistent with what we expected. The shift we obtained between the two calibrations is of  $\sim 140$  eV, which may impact the quality of our results. It was also seen in the instrumental line features

<sup>10</sup> see the CCF Release Note 0312 (Guainazzi M., 2014a, XMM-CCF-REL-0312) <https://xmmweb.esac.esa.int/docs/documents/CAL-SRN-0312-1-4.pdf> and the Science Operations Team Calibration Technical Note 0083 (Guainazzi M., et al. 2014b, XMM-SOC-CAL-TN-0083) <https://xmmweb.esac.esa.int/docs/documents/CAL-TN-0083.pdf>

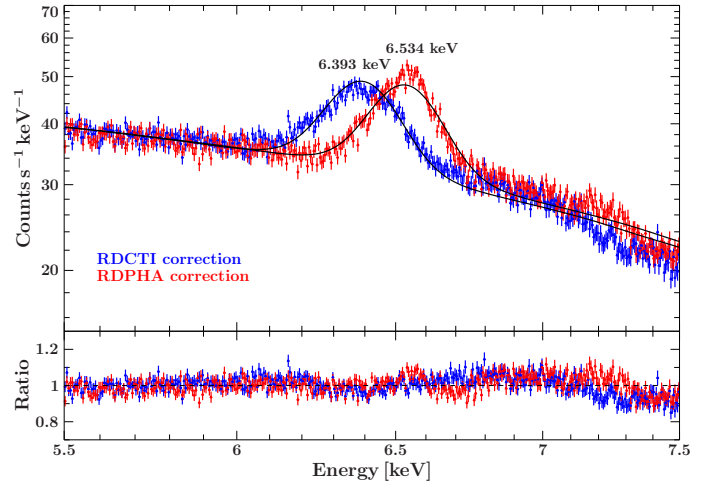


**Fig. A.1.** Example of a spectrum in the iron line region generated with different calibrations. The red spectrum corresponds to events generated applying the RDPHA correction, while the blue spectrum corresponds to the RDCTI correction.

of the detector such as the gold edge region around  $\sim 2.2$  keV. The same behaviour was seen by Pintore et al. (2014) in the spectra of the accreting neutron star GX 13+1, where the authors found a shift of 360 eV in the iron line between the RDCTI and RDPHA corrections.

### A.2. Test for pile-up in the iron line region

As mentioned in Sect. 2, our *XMM-Newton* EPIC-pn observation of Vela X-1 is deeply affected by pile-up. In addition, with the `epatplot` task, we evaluate the pixel columns most affected by pile-up by performing a test in the iron line region. We extract spectra ignoring 1, 3, 5, and 7 columns from the PSF centre (named PSF-#) and then compare the position of the iron line between different extractions. We present example spectra as in Fig. A.1, using the RDPHA correction (see Fig. A.2) and RDCTI correction (see Fig. A.3), where we fitted with a power law and Gaussian component to model the iron line.

We note that with the RDPHA correction, the more the centremost columns are removed, the lower the energy of the iron line is starting from  $\sim 6.54$  keV for one column removed to  $\sim 6.50$  keV for seven ignored columns. However, removing seven columns from the centre of the PSF means ignoring almost the entire available signal, decreasing the S/N. Moreover, the iron line energy is still too high compared to what we expect for this feature as discussed in Sect. A.1. On the contrary, using the RDCTI correction, we obtain the opposite behaviour, with an increase in the iron line energy together with the number of centre columns removed from the PSF. In order to have a good balance between keeping enough signal and having a consistent iron line energy with previous results for Vela X-1, we decided to apply the RDCTI correction and to remove the three centremost columns from the PSF (PSF-3) for this work. Even if we apply those corrections, the energy of the iron line ( $\sim 6.46$  keV) is still higher than what we obtained for the simultaneous *NuSTAR* observation, and so discrepancies between the two instruments are expected for the combined spectral analysis presented in Sect. 4.2.



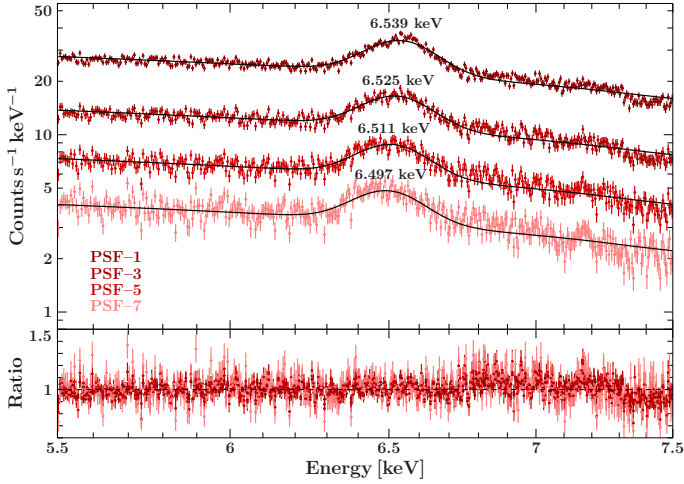


**Fig. A.2.** Example of a spectrum with RDPHA correction as in Fig. A.1, removing 1 (PSF-1), 3 (PSF-3), 5 (PSF-5), and 7 (PSF-7) columns from the centre of the PSF.

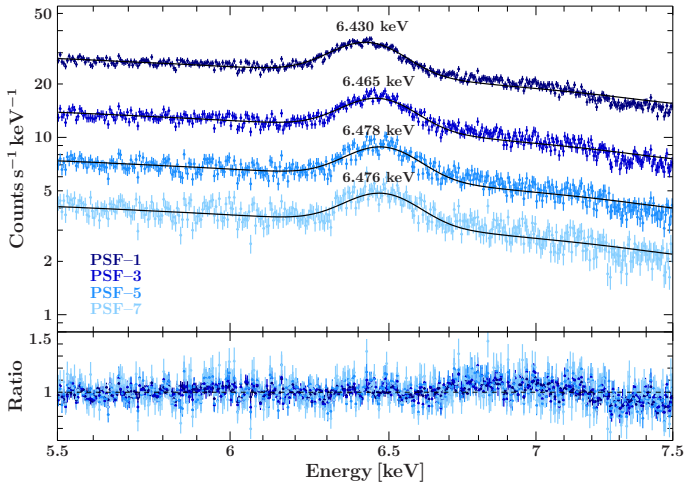


**Fig. A.3.** Example of a spectrum with RDCTI correction as in Fig. A.1 removing 1 (PSF-1), 3 (PSF-3), 5 (PSF-5), and 7 (PSF-7) columns from the centre of the PSF.

### A.3. Cross-instrumental issues

In comparison with *XMM-Newton* EPIC-pn data, we observe a strong soft excess in the *NuSTAR* data (see Fig. A.4). A possible explanation for this is the dust scattering effect. In this scenario, we suppose dense interstellar clouds located between the observer and the source. Those clouds will lead to deviation of the trajectory of low-energy photons that were not supposed to be observed. The low-energy photons will then be scattered towards the observer, producing a soft excess flux at low energy in the spectrum of the source. This scattering leads to the formation of the scattering halo as observed in Circinus X-1 in Heinz et al. (2015). To check for this phenomenon, we extracted source regions of different sizes in the *NuSTAR* data from 10 arcsec to 50 arcsec in steps of 10 arcsec. The smallest source regions account for the maximum of the PSF, though with a possible loss of information from the source. The largest source regions account for the PSF and outside wings, which is where the dust scattering effect is visible and more low-energy photons are present. When comparing the resultant spectra, we cannot see any difference in terms of spectral shape, meaning the soft excess at low energy is always present. Hence, we exclude the

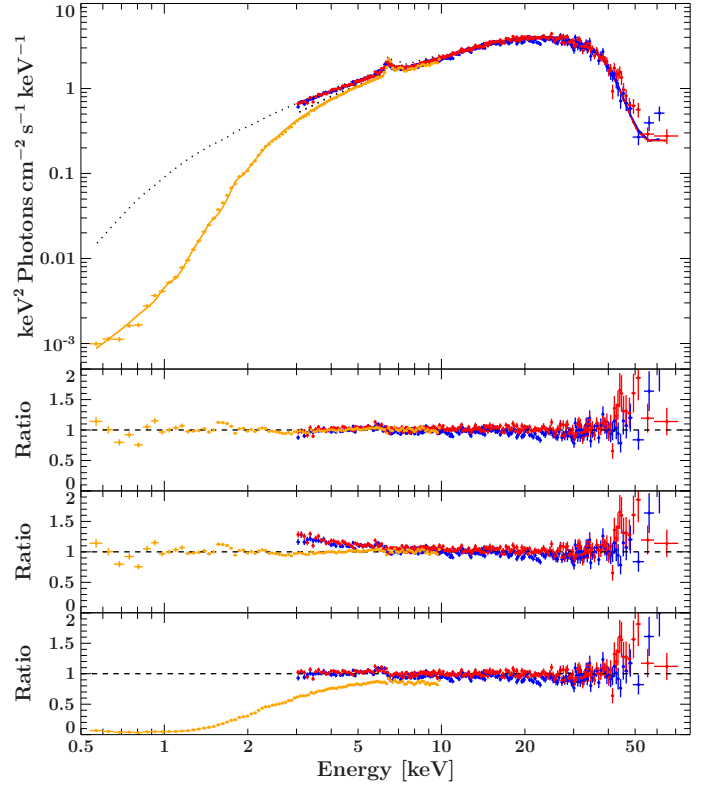


**Fig. A.4.** Example of an unfolded spectrum taken with *XMM-Newton* EPIC-pn (orange), *NuSTAR* FPMA (red), and FPMB (blue) during the fourth *NuSTAR* orbit. Solid lines show the best-fit model with independent  $CF_{XMM}$  and  $CF_{NuSTAR}$ , and dotted lines account for best-fit model with tied CFs. First residual panel: Best-fit model with independent covering fractions. Second residual panel: Best-fit model with  $CF_{NuSTAR}$  tied to  $CF_{XMM}$ . Last residual panel: Best-fit model with  $CF_{XMM}$  tied to  $CF_{NuSTAR}$ . A strong soft excess in the *NuSTAR* data is visible at  $\sim 3$  keV in comparison to the *XMM-Newton* data.

dust scattering effect as a cause for the observed soft excess in our *NuSTAR* data. We also checked for contamination sources in the extracted source region of both instruments but none could be found. As we are unable to find a plausible physical explanation for this phenomenon, we tested our model by tying  $CF_{NuSTAR}$  to  $CF_{XMM}$ . In the second residual panel of Fig. A.4, we observe that the *XMM-Newton* EPIC-pn data are well described, albeit the residuals increase drastically for *NuSTAR* around 3 keV. Reciprocally, we tied  $CF_{XMM}$  to  $CF_{NuSTAR}$  and, as expected, the *NuSTAR* data are well constrained. However, there is a discrepancy up to a factor of 10 between the model and the *XMM-Newton* EPIC-pn data at 0.5 keV as shown on the last residual panel of Fig. A.4. None of the datasets are correctly described by an averaged CF. We conclude that the  $CF_{XMM}$  is the most reliable value for the covering fraction and that the problem may be due to remaining calibration effects from *NuSTAR* at low energies. For the rest of this work, we assumed two independent CFs for each instrument as this is the best way to empirically compensate for the observed difference (see the first residual panel of Fig. A.4). In Tsygankov et al. (2019), an offset between *Swift*/XRT and *NuSTAR* has also been reported. The *Swift*/XRT normalisation was about 1.3 times lower than *NuSTAR* FPMA/FPMB, which is possibly due to the fact that their *NuSTAR* and *Swift* observations were not strictly simultaneous.



# Bibliography

- Amato, R., Grinberg, V., Hell, N., et al. 2021, A&A, 648, A105, Looking through the photoionisation wake: Vela X-1 at  $\varphi_{orb} \approx 0.75$  with Chandra/HETG
- Arons, J., Klein, R. I., & Lea, S. M. 1987, ApJ, 312, 666, Radiation Gas Dynamics of Polar CAP Accretion onto Magnetized Neutron Stars: Basic Theory
- Barret, D., Albuys, V., Herder, J.-W. d., et al. 2023, Experimental Astronomy, The Athena X-ray Integral Field Unit: a consolidated design for the system requirement review of the preliminary definition phase
- Basko, M. M. & Sunyaev, R. A. 1976, MNRAS, 175, 395, The limiting luminosity of accreting neutron stars with magnetic fields.
- Becker, P. A., Klochkov, D., Schönherr, G., et al. 2012, A&A, 544, A123, Spectral formation in accreting X-ray pulsars: bimodal variation of the cyclotron energy with luminosity
- Becker, P. A. & Wolff, M. T. 2007, ApJ, 654, 435, Thermal and Bulk Comptonization in Accretion-powered X-Ray Pulsars
- Bhattacharya, D. & van den Heuvel, E. P. J. 1991, Phys. Rep., 203, 1, Formation and evolution of binary and millisecond radio pulsars
- Bildsten, L., Chakrabarty, D., Chiu, J., et al. 1997, ApJS, 113, 367, Observations of Accreting Pulsars
- Blondin, J. M., Stevens, I. R., & Kallman, T. R. 1991, ApJ, 371, 684, Enhanced Winds and Tidal Streams in Massive X-Ray Binaries
- Brice, N., Zane, S., Turolla, R., & Wu, K. 2021, MNRAS, 504, 701, Super-eddington emission from accreting, highly magnetized neutron stars with a multipolar magnetic field

- Burnard, D. J., Arons, J., & Klein, R. I. 1991, *ApJ*, 367, 575, Accretion Powered Pulsars: Continuum Spectra and Light Curves of Settling Accretion Mounds
- Castor, J. I., Abbott, D. C., & Klein, R. I. 1975, *ApJ*, 195, 157, Radiation-driven winds in Of stars.
- Chandrasekhar, S. 1931a, *MNRAS*, 91, 456, The highly collapsed configurations of a stellar mass
- Chandrasekhar, S. 1931b, *ApJ*, 74, 81, The Maximum Mass of Ideal White Dwarfs
- Coburn, W., Heindl, W. A., Rothschild, R. E., et al. 2002, *ApJ*, 580, 394, Magnetic Fields of Accreting X-Ray Pulsars with the Rossi X-Ray Timing Explorer
- Colgate, S. A. & White, R. H. 1966, *ApJ*, 143, 626, The Hydrodynamic Behavior of Supernovae Explosions
- dal Fiume, D., Orlandini, M., Cusumano, G., et al. 1998, *A&A*, 329, L41, The broad-band (0.1-200 keV) spectrum of HER X-1 observed with BeppoSAX
- Davidson, K. 1973, *Nature Physical Science*, 246, 1, Accretion at a Magnetic Pole of a Neutron Star
- den Herder, J. W., Brinkman, A. C., Kahn, S. M., et al. 2001, *A&A*, 365, L7, The Reflection Grating Spectrometer on board XMM-Newton
- Diez, C. M., Grinberg, V., Fürst, F., et al. 2023, *A&A*, accepted, Observing the onset of the accretion wake in Vela X-1
- Diez, C. M., Grinberg, V., Fürst, F., et al. 2022, *A&A*, 660, A19, Continuum, cyclotron line, and absorption variability in the high-mass X-ray binary Vela X-1
- Doroshenko, V., Santangelo, A., Nakahira, S., et al. 2013, *A&A*, 554, A37, Footprints in the wind of Vela X-1 traced with MAXI
- Drake, G. W. 1988, *Canadian Journal of Physics*, 66, 586, Theoretical energies for the  $n = 1$  and  $2$  states of the helium isoelectronic sequence up to  $Z = 100$

- Driessen, F. A., Sundqvist, J. O., & Kee, N. D. 2019, *A&A*, 631, A172, Theoretical wind clumping predictions of OB supergiants from line-driven instability simulations across the bi-stability jump
- El Mellah, I., Grinberg, V., Sundqvist, J. O., Driessen, F. A., & Leutenegger, M. A. 2020, *A&A*, 643, A9, Radiography in high mass X-ray binaries. Micro-structure of the stellar wind through variability of the column density
- El Mellah, I., Sander, A. A. C., Sundqvist, J. O., & Keppens, R. 2019, *A&A*, 622, A189, Formation of wind-captured disks in supergiant X-ray binaries. Consequences for Vela X-1 and Cygnus X-1
- El Mellah, I., Sundqvist, J. O., & Keppens, R. 2018, *MNRAS*, 475, 3240, Accretion from a clumpy massive-star wind in supergiant X-ray binaries
- Erickson, G. W. 1977, *Journal of Physical and Chemical Reference Data*, 6, 831, Energy levels of one-electron atoms
- Falanga, M., Bozzo, E., Lutovinov, A., et al. 2015, *A&A*, 577, A130, Ephemeris, orbital decay, and masses of ten eclipsing high-mass X-ray binaries
- Feldmeier, A., Puls, J., & Pauldrach, A. W. A. 1997, *A&A*, 322, 878, A possible origin for X-rays from O stars.
- Ferrigno, C., Becker, P. A., Segreto, A., Mineo, T., & Santangelo, A. 2009, *A&A*, 498, 825, Study of the accreting pulsar 4U 0115+63 using a bulk and thermal Comptonization model
- Fowler, R. H. 1926, *MNRAS*, 87, 114, On dense matter
- Fransson, C. & Fabian, A. C. 1980, *A&A*, 87, 102, X-ray induced shocks in stellar winds.
- Fürst, F. 2011, PhD thesis, Der Naturwissenschaftlichen Fakultät der Friedrich-Alexander-Universität Erlangen-Nürnberg
- Fürst, F., Kreykenbohm, I., Pottschmidt, K., et al. 2010, *A&A*, 519, A37, X-ray variation statistics and wind clumping in Vela X-1

- Fürst, F., Pottschmidt, K., Wilms, J., et al. 2014a, *ApJ*, 784, L40, NuSTAR Discovery of a Cyclotron Line in KS 1947+300
- Fürst, F., Pottschmidt, K., Wilms, J., et al. 2014b, *ApJ*, 780, 133, NuSTAR Discovery of a Luminosity Dependent Cyclotron Line Energy in Vela X-1
- Garcia, J. D. & Mack, J. E. 1965, *Journal of the Optical Society of America (1917-1983)*, 55, 654, Energy Level and Line Tables for One-Electron Atomic Spectra
- Giménez-García, A., Shenar, T., Torrejón, J. M., et al. 2016, *A&A*, 591, A26, Measuring the stellar wind parameters in IGR J17544-2619 and Vela X-1 constrains the accretion physics in supergiant fast X-ray transient and classical supergiant X-ray binaries
- Goldstein, G., Huenemoerder, D. P., & Blank, D. 2004, *AJ*, 127, 2310, Variation in Emission and Absorption Lines and Continuum Flux by Orbital Phase in Vela X-1
- Grinberg, V., Hell, N., El Mellah, I., et al. 2017, *A&A*, 608, A143, The clumpy absorber in the high-mass X-ray binary Vela X-1
- Grinberg, V., Nowak, M. A., & Hell, N. 2020, *A&A*, 643, A109, Color-color diagrams as tools for assessment of the variable absorption in high mass X-ray binaries
- Guidry, M. 2019, *Stars and Stellar Processes*, Stars and Stellar Processes (Cambridge University Press)
- Haberl, F. & White, N. E. 1990, *ApJ*, 361, 225, The X-Ray Absorption Spectrum of VELA X-1
- Harding, A. K. 1994, in *American Institute of Physics Conference Series*, Vol. 308, The Evolution of X-ray Binaries, ed. S. Holt & C. S. Day, 429
- Harrison, F. A., Craig, W. W., Christensen, F. E., et al. 2013, *ApJ*, 770, 103, The Nuclear Spectroscopic Telescope Array (NuSTAR) High-energy X-Ray Mission
- Hell, N., Brown, G. V., Wilms, J., et al. 2016, *ApJ*, 830, 26, Laboratory Measurements of the K-shell Transition Energies in L- shell Ions of SI and S

- Hertzsprung, E. 1911, Publikationen des Astrophysikalischen Observatoriums zu Potsdam, 63, Ueber die Verwendung photographischer effektiver Wellenlaengen zur Bestimmung von Farbaequivalenten
- Hessels, J. W. T., Ransom, S. M., Stairs, I. H., et al. 2006, *Science*, 311, 1901, A Radio Pulsar Spinning at 716 Hz
- Hiltner, W. A., Werner, J., & Osmer, P. 1972, *ApJ*, 175, L19, Binary Nature of the B Supergiant in the Error Box of the VELA X-Ray Source
- Hirsch, M., Hell, N., Grinberg, V., et al. 2019, *A&A*, 626, A64, Chandra X-ray spectroscopy of the focused wind in the Cygnus X-1 system. III. Dipping in the low/hard state
- House, L. L. 1969, *ApJS*, 18, 21, Theoretical Wavelengths for Ka-TYPE X-Ray Lines in the Spectra of Ionized Atoms (carbon to Copper)
- Igoshev, A. P., Popov, S. B., & Hollerbach, R. 2021, *Universe*, 7, 351, Evolution of Neutron Star Magnetic Fields
- Jansen, F., Lumb, D., Altieri, B., et al. 2001, *A&A*, 365, L1, XMM-Newton observatory. I. The spacecraft and operations
- Jethwa, P., Saxton, R., Guainazzi, M., Rodriguez-Pascual, P., & Stuhlinger, M. 2015, *A&A*, 581, A104, When is pile-up important in the XMM-Newton EPIC cameras?
- Joss, P. C. & Rappaport, S. A. 1984, *ARA&A*, 22, 537, Neutron Stars in Interacting Binary Systems
- Kallman, T. R., Palmeri, P., Bautista, M. A., Mendoza, C., & Krolik, J. H. 2004, *ApJS*, 155, 675, Photoionization Modeling and the K Lines of Iron
- Kaper, L., van Loon, J. T., Augusteijn, T., et al. 1997, *ApJ*, 475, L37, Discovery of a Bow Shock around VELA X-1
- Klochkov, D., Horns, D., Santangelo, A., et al. 2007, *A&A*, 464, L45, INTEGRAL and Swift observations of EXO 2030+375 during a giant outburst

- Klochkov, D., Staubert, R., Santangelo, A., Rothschild, R. E., & Ferrigno, C. 2011, *A&A*, 532, A126, Pulse-amplitude-resolved spectroscopy of bright accreting pulsars: indication of two accretion regimes
- Kretschmar, P., El Mellah, I., Martínez-Núñez, S., et al. 2021, *A&A*, 652, A95, Revisiting the archetypical wind accretor Vela X-1 in depth. Case study of a well-known X-ray binary and the limits of our knowledge
- Kreykenbohm, I., Coburn, W., Wilms, J., et al. 2002, *A&A*, 395, 129, Confirmation of two cyclotron lines in Vela X-1
- Kreykenbohm, I., Kretschmar, P., Wilms, J., et al. 1999, *A&A*, 341, 141, VELA X-1 as seen by RXTE
- Kreykenbohm, I., Wilms, J., Kretschmar, P., et al. 2008, *A&A*, 492, 511, High variability in Vela X-1: giant flares and off states
- Lada, C. J. & Lada, E. A. 2003, *ARA&A*, 41, 57, Embedded Clusters in Molecular Clouds
- Lamb, F. K., Pethick, C. J., & Pines, D. 1973, *ApJ*, 184, 271, A Model for Compact X-Ray Sources: Accretion by Rotating Magnetic Stars
- Lamers, H. J. G. L. M. & Cassinelli, J. P. 1999, *Introduction to Stellar Winds, Introduction to Stellar Winds* (Cambridge University Press)
- Langer, S. H. & Rappaport, S. 1982, *ApJ*, 257, 733, Low-luminosity accretion onto magnetized neutron stars
- Lattimer, J. M. & Prakash, M. 2007, *Phys. Rep.*, 442, 109, Neutron star observations: Prognosis for equation of state constraints
- Legred, I., Chatziioannou, K., Essick, R., Han, S., & Landry, P. 2021, arXiv e-prints, arXiv:2106.05313, Impact of the PSR J0740+6620 radius constraint on the properties of high-density matter
- Liao, Z., Liu, J., Zheng, X., & Gou, L. 2020, *MNRAS*, 492, 5922, Spectral evidence of an accretion disc in wind-fed X-ray pulsar Vela X-1 during an unusual spin-up period



- Lomaeva, M., Grinberg, V., Guainazzi, M., et al. 2020, *A&A*, 641, A144, High-resolution X-ray spectroscopy of the stellar wind in Vela X-1 during a flare
- Manousakis, A. 2011, PhD thesis, Université de Genève
- Martínez-Núñez, S., Torrejón, J. M., Kühnel, M., et al. 2014, *A&A*, 563, A70, The accretion environment in Vela X-1 during a flaring period using XMM-Newton
- McBride, V. A., Wilms, J., Coe, M. J., et al. 2006, *A&A*, 451, 267, Study of the cyclotron feature in <ASTROBJ>MXB 0656-072</ASTROBJ>
- McClintock, J. E., Rappaport, S., Joss, P. C., et al. 1976, *ApJ*, 206, L99, Discovery of a 283-second periodic variation in the X-ray source 3U 0900-40.
- Meynet, G., Mowlavi, N., & Maeder, A. 2006, arXiv e-prints, astro, Massive star evolution at high metallicity
- Moe, M. & Di Stefano, R. 2017, *ApJS*, 230, 15, Mind Your Ps and Qs: The Interrelation between Period (P) and Mass-ratio (Q) Distributions of Binary Stars
- Müller, S., Ferrigno, C., Kühnel, M., et al. 2013, *A&A*, 551, A6, No anticorrelation between cyclotron line energy and X-ray flux in 4U 0115+634
- Mushtukov, A. A., Tsygankov, S. S., Serber, A. V., Suleimanov, V. F., & Poutanen, J. 2015, *MNRAS*, 454, 2714, Positive correlation between the cyclotron line energy and luminosity in sub-critical X-ray pulsars: Doppler effect in the accretion channel
- Nelson, R. W., Salpeter, E. E., & Wasserman, I. 1993, *ApJ*, 418, 874, Nonthermal Cyclotron Emission from Low-Luminosity Accretion onto Magnetic Neutron Stars
- Nespoli, E., Reig, P., & Zezas, A. 2012, *A&A*, 547, A103, New insights into the Be/X-ray binary system MXB 0656-072
- Odaka, H., Khangulyan, D., Tanaka, Y. T., et al. 2013, *ApJ*, 767, 70, Short-term Variability of X-Rays from Accreting Neutron Star Vela X-1. I. Suzaku Observations
- Ohashi, T., Inoue, H., Koyama, K., et al. 1984, *PASJ*, 36, 699, Properties of the iron line from Vela X-1.

- Oppenheimer, J. R. & Volkoff, G. M. 1939, *Physical Review*, 55, 374, On Massive Neutron Cores
- Oskinova, L., Hamann, W.-R., Ignace, R., & Feldmeier, A. 2011, *Bulletin de la Societe Royale des Sciences de Liege*, 80, 54, X-rays, clumping and wind structures
- Owocki, S. P., Castor, J. I., & Rybicki, G. B. 1988, *ApJ*, 335, 914, Time-dependent Models of Radiatively Driven Stellar Winds. I. Nonlinear Evolution of Instabilities for a Pure Absorption Model
- Özel, F. & Freire, P. 2016, *ARA&A*, 54, 401, Masses, Radii, and the Equation of State of Neutron Stars
- Pauli, W. 1925, *Zeitschrift für Physik*, 31, 765, Über den Zusammenhang des Abschlusses der Elektronengruppen im Atom mit der Komplexstruktur der Spektren
- Quaintrell, H., Norton, A. J., Ash, T. D. C., et al. 2003, *A&A*, 401, 313, The mass of the neutron star in Vela X-1 and tidally induced non-radial oscillations in GP Vel
- Reig, P. & Milonaki, F. 2016, *A&A*, 594, A45, Accretion regimes in the X-ray pulsar 4U 1901+03
- Reig, P. & Nespoli, E. 2013, *A&A*, 551, A1, Patterns of variability in Be/X-ray pulsars during giant outbursts
- Rezzolla, L., Most, E. R., & Weih, L. R. 2018, *ApJ*, 852, L25, Using Gravitational-wave Observations and Quasi-universal Relations to Constrain the Maximum Mass of Neutron Stars
- Romani, R. W., Kandel, D., Filippenko, A. V., Brink, T. G., & Zheng, W. 2022, *The Astrophysical Journal Letters*, 934, L17, PSR J0952-0607: The Fastest and Heaviest Known Galactic Neutron Star
- Rosenberg, H. 1910, *Astronomische Nachrichten*, 186, 71, Über den Zusammenhang von Helligkeit und Spektraltypus in den Plejaden

- Russell, H. N. 1914, *Popular Astronomy*, 22, 275, Relations Between the Spectra and Other Characteristics of the Stars
- Sako, M., Liedahl, D. A., Kahn, S. M., & Paerels, F. 1999, *ApJ*, 525, 921, The X-Ray Spectrum and Global Structure of the Stellar Wind in VELA X-1
- Santangelo, A., del Sordo, S., Segreto, A., et al. 1998, *A&A*, 340, L55, BeppoSAX detection of a Cyclotron Feature in the spectrum of Cen X-3
- Sato, N., Hayakawa, S., Nagase, F., et al. 1986, *PASJ*, 38, 731, X-ray probing of the circumstellar matter in the Vela X-1 system from observations over an eclipse phase.
- Schönherr, G., Wilms, J., Kretschmar, P., et al. 2007, *A&A*, 472, 353, A model for cyclotron resonance scattering features
- Schulz, N. S., Canizares, C. R., Lee, J. C., & Sako, M. 2002, *ApJ*, 564, L21, The Ionized Stellar Wind in Vela X-1 during Eclipse
- Schwarm, F. W., Schönherr, G., Falkner, S., et al. 2017, *A&A*, 597, A3, Cyclotron resonant scattering feature simulations. I. Thermally averaged cyclotron scattering cross sections, mean free photon-path tables, and electron momentum sampling
- Staubert, R., Shakura, N. I., Postnov, K., et al. 2007, *A&A*, 465, L25, Discovery of a flux-related change of the cyclotron line energy in Hercules X-1
- Staubert, R., Trümper, J., Kendziorra, E., et al. 2019, *A&A*, 622, A61, Cyclotron lines in highly magnetized neutron stars
- Strüder, L., Briel, U., Dennerl, K., et al. 2001, *A&A*, 365, L18, The European Photon Imaging Camera on XMM-Newton: The pn-CCD camera
- Sundqvist, J. O. & Owocki, S. P. 2013, *MNRAS*, 428, 1837, Clumping in the inner winds of hot, massive stars from hydrodynamical line-driven instability simulations
- Tanaka, Y. 1986, in *Proc. IAU Colloq. 89, Vol. 255, Radiation Hydrodynamics in Stars and Compact Objects*, ed. D. Mihalas & K.-H. A. Winkler (Springer-Verlag New York)

- Tauris, T. M. & van den Heuvel, E. P. J. 2006, in *Compact stellar X-ray sources*, Vol. 39, 623–665
- Tiesinga, E., Mohr, P. J., Newell, D. B., & Taylor, B. N. 2021, *Rev. Mod. Phys.*, 93, 025010, CODATA recommended values of the fundamental physical constants: 2018
- Titarchuk, L., Mastichiadis, A., & Kylafis, N. D. 1996, *A&AS*, 120, 171, Spherical accretion onto neutron stars and black holes.
- Turner, M. J. L., Abbey, A., Arnaud, M., et al. 2001, *A&A*, 365, L27, The European Photon Imaging Camera on XMM-Newton: The MOS cameras
- van Kerkwijk, M. H., van Paradijs, J., & Zuiderwijk, E. J. 1995, *A&A*, 303, 497, On the masses of neutron stars.
- Verner, D., Yakovlev, D., Band, I., & Trzhaskovskaya, M. 1993, *Atomic Data and Nuclear Data Tables*, 55, 233, Subshell Photoionization Cross Sections and Ionization Energies of Atoms and Ions from He to Zn
- Verner, D. A., Ferland, G. J., Korista, K. T., & Yakovlev, D. G. 1996, *ApJ*, 465, 487, Atomic Data for Astrophysics. II. New Analytic FITS for Photoionization Cross Sections of Atoms and Ions
- Watanabe, S., Sako, M., Ishida, M., et al. 2006, *ApJ*, 651, 421, X-Ray Spectral Study of the Photoionized Stellar Wind in Vela X-1
- Wilms, J., Allen, A., & McCray, R. 2000, *ApJ*, 542, 914, On the Absorption of X-Rays in the Interstellar Medium
- Woosley, S. E., Heger, A., & Weaver, T. A. 2002, *Reviews of Modern Physics*, 74, 1015, The evolution and explosion of massive stars
- XMM-Newton SOC. 2022, *XMM-Newton Users Handbook*, Issue 2.20, XMM-Newton Users Handbook, Issue 2.20
- XRISM Science Team. 2020, arXiv e-prints, arXiv:2003.04962, Science with the X-ray Imaging and Spectroscopy Mission (XRISM)

# Abbreviations

**CRSF** Cyclotron Resonant Scattering Feature

**EPIC** European Photon Imaging Camera

**ESA** European Space Agency

**FPM** Focal Plane Module

**HMXB** High-Mass X-ray Binary

**IMXB** Intermediate-Mass X-ray Binary

**LMXB** Low-Mass X-ray Binary

***NuSTAR*** *Nuclear Spectroscopic Telescope ARray*

**MOS** Metal Oxide Semi-conductor

**PSF** Point Spread Function

**RGS** Reflection Grating Spectrometer

**RRC** Radiative Recombination Continua

**SAS** Science Analysis System

**UV** UltraViolet

***XMM*** *X-ray Multi-Mirror*

# Acknowledgements

This PhD would not have come to an end without the help of wonderful people who crossed my path and who contributed to the successful achievement of these three years.

First of all, I would like to express my heartfelt gratitude to my supervisor Dr. Victoria Grinberg. This has been an incredible journey together: the pandemic and your new job geographically separating us and turning this PhD into an almost fully remote one. This did not prevent us from performing wonderful science and interacting in presence when we had the occasion. You have been more than just a supervisor, you have been a constant source of inspiration, of encouragement and advice when I needed it the most, and guidance towards the long drowning phase of the PhD bathtub (see Fig .1). You always took the right decisions, as difficult as they could be, to make this journey better.

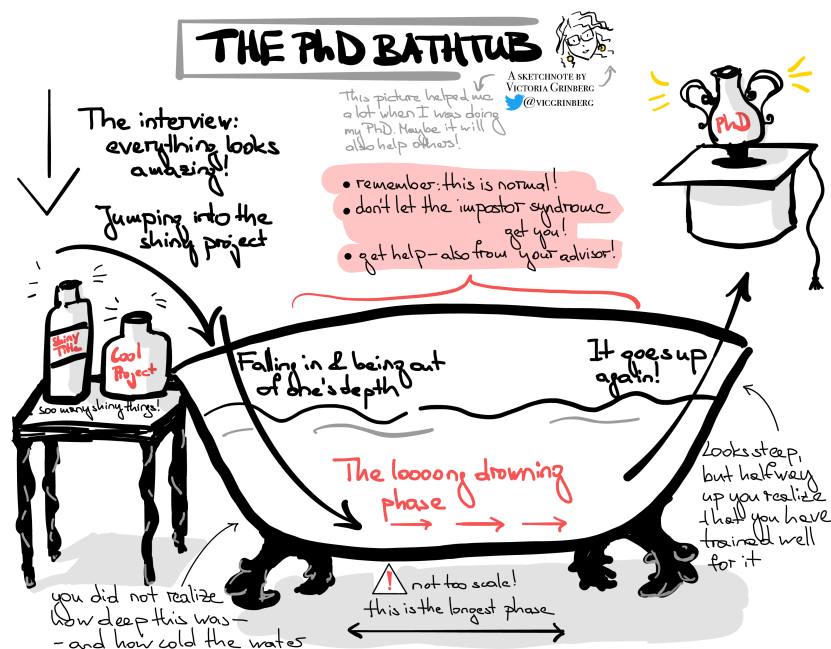


Fig. .1: Illustration of the PhD journey as a bathtub function. Credits: V. Grinberg.

Prof. Dr. Santangelo, I still remember my interview when you asked me if I was ready to move to the little town of Tübingen for the next three years. This has been the best decision I could take and I thank you for trusting me. Being part of the HEA group at the IAAT that you lead shaped my research and personal growth as a young scientist and I am extremely grateful for this. Your help has been crucial, particularly towards the end of the PhD, to do my defence with confidence and serenity.

I would like to thank Prof. Dr. Werner and Prof. Dr. Jäger for being part of my PhD committee, for their valuable contributions and guidance during my defence. Your expertise and thoughtful suggestions broadened my understanding of the subject and enriched the quality of the discussions we had.

My interest in neutron star studies started during my master internship with you Sébastien Guillot. You led me here and I truly hope we will be able to share our interests again for these amazing objects in the future. This research would not have been so fruitful without you, Felix Fürst and Peter Kretschmar. I am beyond happy to be your new colleague at ESAC and I cannot wait for the future in presence interactions and brainstorming (and Spanish restaurants) yet to come.

Margot, everything started during our master. Our PhDs brought us abroad and luckily not too far from each other. Thank you for all the memories, the travels, the pains, the laughs shared together. For being my French reference point when I was feeling home sick. I have no doubt that you will succeed in your scientific career. Even though this time I am going to be further away, I know we will see each other very soon and very often.

Complaining is my national sport and I feel grateful to all the amazing people at the IAAT and their unlimited patience because I could always find an open door to share my thoughts. You were my motivation to come to the office. In particular:

Aafia, I am still mourning the days when we were having our amazing talks with Tübinger tea in my office or hot chocolate with ice creams in town at any season of the year. I am relieved that our careers did not tear us apart on the other side of the world



so I know I will see you very soon. Thank you for sharing with me what seems like just a tiny overview of your amazing home town and family. Enza, for letting me some space in your beautiful heart. Life has not been easy, I am happy to have been your shoulder when you needed it as much as you were mine. You showed that nothing is impossible, whatever the circumstances are. This has been a rather short but intense time with you and I can tell you this is only the beginning. Your endless kindness will bring you the happiness, love and support that you deserve. To all the crazy adventures yet to come. Inga, I still remember that moment more than three years ago in your car when you asked me "how is your first week in Tübingen?" and I replied that it was long, that I was tired of speaking English and just wanted to go home. Thank you for your perseverance with me and always giving me a hand when I needed it the most, it led to a beautiful friendship. I cannot wait to visit you during the hot and dry Spanish summers and you know my door will be open during your snowy Swedish winters. Paul, for the cheerful chats that were ending up in me buying unexpected things on Amazon (such as a sloth tea strainer) and in turning your office into an asylum desk for complaints. Our endless conversations (and cute quokkas) brightened so much my lonely afternoons. Samu, for the bike rides always interrupted by food breaks at the ice cream and burger places to satisfy our infinite appetites, even though we were always going out with enough drink and food supplies to survive an apocalypse. It was an escape to boredom in particular during covid times. Heiko for the last minute planned pizzas which gave me enough reasons to postpone my sports plans. You are a caring person, always available to help and I am very grateful for the emotional support you have shown to me.

Although I cannot thank all my friends individually here, I would be remiss not to mention: Martina, Antonio, Xianqi, Fabian, Marvin, Moritz, Bastian, Berit, Francesco, Gabri, Nadia for being part of this journey. I cherish every moment we spent together and we will for sure meet again wherever we are in the world.

It is important to keep the feet on the ground when you have the head in the stars. Xan, you have been this anchor to the real world. You continuously supported me during those three years (and way before). My ups were as high as my downs were low but you stood under the storm like a rock while you were also having your own PhD to

accomplish. Our escapes to our beloved Basque Country to breathe the fresh air from the ocean and the mountains was enough to charge up my batteries. The list is long but you already know everything.

I would like to thank my uncle for his constant curiosity and for asking me the most obvious (but yet most difficult to answer for me) questions about our Universe. You know you have a special place in my heart.

My last words will go to my beloved father. As far as I can remember, I always told you I wanted to study the stars, but without knowing you would become one of them so early in my life. You were my first support during this long journey that started as a kid. Even though you are not here anymore to witness this important milestone of my scientific career, thanks to you and all the wonderful people I cherish, I can now conclude this incredible chapter of my life.